Title
Consequences of Structure and Composition for Catalysis by Solid and Bronsted Acids

Author
Carr, Robert Ted

Publication Date
2012

Peer reviewed|Thesis/dissertation

Consequences of Structure and Composition for Catalysis by Solid Brønsted Acids

By

Robert Ted Carr

A dissertation submitted in partial satisfaction of the

requirements for the degree of

Doctor of Philosophy

in

Chemical Engineering

in the

Graduate Division

of the

University of California, Berkeley

Committee in charge:

Professor Enrique Iglesia, Chair
Professor Alexis T. Bell
Professor Kenneth N. Raymond

Fall 2012

Consequences of Structure and Composition for Catalysis by Solid Brønsted Acids

by

Robert Ted Carr

Abstract

Consequences of Structure and Composition for Catalysis by Solid Brønsted Acids

by

Robert Ted Carr

Doctor of Philosophy in Chemical Engineering

University of California, Berkeley

Professor Enrique Iglesia, Chair

Unequivocal relations between properties of solid Brønsted acids and their catalytic function must be developed further to provide guidance for their design and application. Structure-function relations for solid Brønsted acid catalysis are developed here on Keggin polyoxometalate (POM) clusters and proton forms of zeolites because their well-defined structures permit reliable calculations of their deprotonation energies (DPE) by theory as measures of acid strength. Keggin POM clusters with W-metal atoms, but different central atoms (P, Si, Al, Co), have a wide range of acid strengths and reactivities without concomitant structural changes. Zeolites also have known structures and DPE values that are accessible to theory, however, their acid sites are located within voids of molecular dimensions, which stabilize confined reactants and transition states via van der Waals interactions. CH_3OH dehydration and isomerization of C_6 alkanes with different backbone structures served as probes of reactivity on these solid acids and provided illustrative examples of how reactions sense the strength and the confining environments of solid acids through the stabilities of intermediates and transition states that mediate them. Rate constants of kinetically-relevant steps in these reactions were obtained from mechanism-based interpretations of rates that were normalized as turnovers by counting the number of accessible protons with 2,6-di-*tert*butyl pyridine titrations during catalysis. These rate constants were correlated with the catalyst DPE values in structure-function relations to determine how reactions "sense" the strength and the solvating environments of solid acids.

Rate constants decrease exponentially with increasing DPE values on POM clusters for all probe reactions; these trends reflect predominantly higher activation energies on weaker acids because ion-pairs at transition states, a ubiquitous feature of Brønsted acid catalysis, contain less stable conjugate anions. The dependences of rate constants on DPE further suggest that activation energies change by much less than the commensurate change in DPE because the higher energy needed to deprotonate weaker acids is largely recovered at transition states via electrostatic interactions between cationic reactants and the conjugate anion. Isomerization rate constants of C_6 alkanes changed similarly with DPE, in spite of large differences in their values. Cyclopropyl carbenium ions mediate each of these isomerizations at transition states of kinetically-relevant steps. Their similar charge distributions interact with conjugate anions equally

via electrostatic interactions at transition states; as a result, they compensate for interactions between protons and anions equally and cause similar sensitivities to acid strength. Reactants with lower rate constants have transition state cations with less stable gas-phase analogs, however, because these are properties of non-interacting cations, they are catalyst independent and do not influence a reaction's sensitivity to DPE. Rate constants for water elimination from H-bonded alkanol intermediates are more sensitive to DPE for bimolecular CH_3OH dehydration than previously reported for unimolecular butanol dehydration. Unimolecular dehydration transition states have more localized charges than bimolecular dehydration transition states where cationic charges are distributed across multiple reactant molecules. The localized cations at unimolecular dehydration transition states more closely resemble protons and are more effective at interacting with conjugate anions, causing weaker effects of DPE. The effects of DPE are weaker for CH_3OH dehydration when rate constants measure transition states from reacting intermediates that are ion-pairs (than from uncharged H-bonded intermediates) because conjugate anions are present at both species and affect their stabilities similarly.

Zeolites are significantly weaker acids than Keggin POM clusters according to their DPE values, yet their reactivities fall within the range of POM clusters for these probe reactions. Larger alkane isomerization rate constants are measured on zeolite BEA than are predicted from its DPE value because significant van der Waals forces stabilize confined cyclopropyl carbenium ions at transition states and overcompensate for any additional entropy loss caused by confinement. Transition state solvation reduces isomerization activation energies because they are measured with respect to gas-phase reactants that are unconfined. Confinement of acid sites within the channels of BEA favors alkyl shift reactions over those that change the degree of hydrocarbon branching and also favor reactions that have less branched transition states. Confinement preferentially stabilizes those transition state cations that best interact with zeolite channel walls via van der Waals contacts. The effects of confinement are weaker for CH_3OH dehydration when bimolecular transition states are measured with respect to intermediates where both CH_3OH reactants are confined than intermediates where one of the CH_3OH is unconfined in the gas-phase.

These relations demonstrate how fundamental properties of solid acids such as their acid strengths and their confining environments, influence stabilities of relevant intermediates and transition states, and by inference influence reactivity, according to their charges and the sizes of confined species. The effects of acid strength are strongest when uncharged reactive intermediates form transition state cations that interact weakly with conjugate anions because of their diffuse charges. The effects of acid strength weaken as transition states become more similar to a proton or as reacting intermediates also become ion-pairs. The effects of confinement are determined by van der Waals stabilization of transition states; these effects are most pronounced when reactants or reacting intermediates are unconfined. The success of these relations indicates the importance of using well-defined acids whose properties can be assessed unambiguously, counting the number of active sites directly during reactions, and interpreting reactivity as chemical events.

The effects of composition on the DPE values and reactivities of Keggin clusters are investigated further using density functional theory (DFT) because their well-defined

structures permit reliable calculations of their properties by theoretical methods. DPE values are dissected into energy terms that reflect covalent and electrostatic interactions between protons and anions by using thermochemical cycles. Similar thermochemical cycles describing interaction energies between conjugate anions and organic cations indicate how catalyst composition influences reactivity through the stabilities of transition states and intermediates, specifically shown here for CH_3OH dehydration. Central atoms of Keggin clusters influence the densities of delocalized electrons in anions, which determine their electrostatic interactions with cations, while addenda atoms influence both covalent and electrostatic interactions between ions. Central atoms influence the stabilization of protons and organic cations because they both interact with the delocalized electrons. The charge distributions of cations determine how strongly changes in the anionic distribution affect electrostatic interactions. Protons are the cation that is most sensitive to changes in the anion because of their localized charges and close proximities to anions. Addenda atoms influence the stabilities protons much more strongly than ion-pair transition states or intermediates, because the latter have much weaker covalent interactions with anions than the former. As a results, solid acids with different covalent contributions to OH bonds cannot be compared directly using DPE values as the descriptor for acid strength in structure-function relations, because ion-pair transition states do not recover covalent interactions that must be overcome to deprotonate the catalyst. H-atom addition energies (HAE), which are also accessible for Keggin clusters from DFT, probe the local abilities of catalysts to accept H-atoms and electrons. HAE values are accurate descriptors of alkane and alkanol oxidative dehydrogenation (ODH) reactions, because H-atom addition and kinetically-relevant H-abstraction steps in ODH reactions both transfer electrons to unoccupied metal atom orbitals, the energies of which are consequential for ODH rates and HAE values.

To my family and friends

Table of Contents

List of Tables

List of Figures

List of Schemes

Acknowledgements

The completion of this thesis not only represents the culmination of my 22 years of schooled education, but also the love and support of the people that I have known, worked, and lived with during that time. I cannot possibly thank everyone that has helped me along the way, but I will try my best. It goes without saying that first and foremost are my parents, Rick and Laura, who were the first and have been the most enduring teachers in my life. They provided me a home where I could learn and grow, and gave me the strength I needed to leave it and take on new challenges when the time came. Thank you also to rest of my family, especially my brother, David, and my grandparents, for encouraging me throughout the years.

Growing up in Michigan, I was lucky enough to be surrounded by people whose support allowed me to succeed and, in their own ways, molded me into the person I am. The Joslins (Mr. and Mrs. J, Jessie, Kevin, and Erica) and Cregeurs (Mr. and Mrs. C, Nate, and Shannon) were second (and third) families to me while growing up (and still are) and often the locations of second (and third) dinners. Eric Heinenger, Nate Cregeur, Kevin Szawala, Marly Maskill, Jennifer Dunifon, Elise Kazmarzcyk, Kate Thiel, Steve Ehlert, Josh Rich, Joe Heathcock, Breanne Baker, Susan Coffin, and Chelsey Williams were great friends and classmates to grow up learning with. A special thank you to Mrs. Hensley, whose own interest in chemistry, sparked mine and started me on this journey. Steve Harrison, Matt Lecureux, The LaChances, The Taulbees, and The Colegroves were also great friends while growing up. Thank you to the Chemical Engineering department and faculty at the University of Michigan for providing an "engaging" curriculum that convinced me to come to grad school and for giving me the skills I needed to survive it. Curt Longcore, Halley Crast, George Cater, Jessie Moreno, and the rest of the class of 2007 made the long, and often very late, hours of studying bearable and oddly, the times I treasure most. Joe DeFrank, Adam Brinckerhoff, Doug Cabell, Eric Jankowski, and Jaime Polan were great people to live, relax, and most importantly, watch Michigan football with. Go Blue!

With exception to my parents, the person I am most indebted to for this thesis is my dissertation advisor, Enrique Iglesia. He provided a lab where "the science" was the only concern and where I was surrounded by talented people. He has taught me to think carefully, to write "clearly, concisely, and thoughtfully", and to always be looking deeper, even when I think that I have reached the limit. I sincerely appreciate the time, effort, and patience he has taken to develop not only my project, but also me as a scientist. Thank you to Josef Macht for beginning the POM project and getting me started and to the rest of "Team POM" (Will Knaeble, John To, Diana Rodriguez-Ortiz, Songhai Chai, Prashant Deshlahra, Wei Qi) for helping me the rest of the way. Much is owed to the rest of the LSAC members, especially Brett Loveless, Raj Gounder, Andrew Jones, Dante Simonetti, Dave Flaherty, Sebastian Kunz, and Carlo Visconti. Thank you also to the many collaborators I have had: Matt Neurock and his group at the University of Virginia for invaluable help with theoretical calculations and Dr. Stuart Soled, Dr. Cindy Yin, and Dr. Stacey Zones for the synthesis of samples. I'd also like to thank the Chemical Sciences Division, Office of Basic Energy Sciences, Office of Science, U.S. Department of Energy under grant number DE-FG02-03ER15479 for financial support

and the Environmental Molecular Science Laboratory, a national scientific user facility sponsored by the Department of Energy's Office of Biological and Environmental Research and located at Pacific Northwest National Laboratory, for supercomputing time. Finally, I'd like to thank my entering classmates, roommates, and friends (Adam Gross, Sean Dee, Ted Amundsen, Megan Hoarfrost, Keith Beers, Bryan McCulloch, Joanna MacKay, Anton Mlinar, Kris Enslow, Dana Nadler, Brett Loveless, Colin Cerretani, Will Vining, Jarred Ghilarducci, Haluna Gunterman, Nisita Wanakule) for keeping me sane in grad school and for making this a cherished experience.

Thank you all so very much.

Chapter 1

Introduction to Understanding Connections Between Structures and Reactivities of Solid Brønsted Acids

Brønsted acids catalyze a broad range of chemical reactions that are relevant to hydrocarbon transformations such as alkane cracking and dehydrogenation, alcohol dehydration, alkene alkyl shifts and isomerization, alkene oligomerization and β-scission, alkylation, aromatization of alkanes and alkenes, and coke formation [1, 2, 3]. Petroleum refining and the chemicals industry employ these reactions routinely with liquid or supported mineral acids that are corrosive, environmentally hazardous, and require complex handling and processing [4]. Solid acid catalysts with a wide range of properties have been developed to replace these less desirable acids; zeolites and silica-alumina are among the most widely used [4, 5], but supported transition metal oxides [6, 7], sulfated oxides [8, 9], and polymer and ion-exchange resins [10] also exist.

Connections between catalyst structure, properties, and how they influence reactivity must be developed further to rationally design new solid acids and to successfully apply available solid acids. Many existing solid acids have active sites with non-uniform and unknown structures, making the determination of direct relationships between catalyst structure and function difficult or equivocal. Various techniques have been developed to characterize solid acids, and specifically to measure the strengths of their acid sites. These include titration methods [11] and temperature-programmed desorption [12], spectroscopy [13, 14], and microcalorimetry [15] of adsorbed molecules, but their results are often convoluted by properties that are unrelated to acid strength and lead to contradictory rankings of solid acids.

The deprotonation energy (DPE) of an acid site is an intrinsic measure of Brønsted acid strength since it only depends on the ability of an acid to donate a proton [16]. Unfortunately, DPE values are inaccessible to direct experimental measurements for relevant solid Brønsted acids; however, theory can reliably estimate DPE values for materials with known structures [17, 18]. Keggin polyoxometalate (POM) clusters (Scheme 1.1) are inorganic solid acids with well-defined isomorphic structures and a wide range of reactivities and acid strengths that can be tuned by their compositions. Keggin POM clusters ($R^{y+}_{(8-n)/y}X^{n+}M_{12}O_{40}$) are metal oxides containing 12 metal addenda atoms (M = W, Mo, V, Nb) that encapsulate a tetrahedrally-coordinated central atom (X^{n+} = P^{5+}, Si^{4+}, Al^{3+}, Co^{2+}), whose valence determines the number of charge-balancing cations (R^{y+}). When protons are the charge-balancing cations (i.e., R^{y+} = H^{+}), such sites are active for Brønsted acid catalysis. Deprotonation energies of W-metal Keggin POM clusters range from 1087 – 1143 kJ mol^{-1} for P, Si, Al, and Co central atoms (in order of increasing DPE) [19]. DPE values of Keggin POM clusters increase with decreasing central atom valence, because their conjugate anions have higher electron densities and are less stable. H-form zeolites are also inorganic solid acids with known structures and have calculated DPE values that range from 1171 – 1200 kJ mol^{-1} (for FAU, MFI, CHA, and MOR frameworks) [17]. Zeolites represent weaker acids (i.e., have larger DPE values) than W-POM clusters and can be used to examine the consequences of confining

acid sites within voids of molecular dimensions. Van der Waals interactions with the zeolite framework stabilize confined molecules and transition states and influence reactivity in ways that are unrelated to acid strength.

Relations between acid strength and reactivity were developed previously on W-Keggin POM clusters and zeolite BEA for butanol dehydration and n-hexene isomerization reactions by using mechanism-based rate expressions and titration site counting methods [19, 20, 21]. H-bonded butanols eliminated water and alkoxides isomerized with rate constants that decreased exponentially with increasing DPE because their transition states featured ion-pairs of cationic reactants and the conjugate anion (Scheme 1.2). Conjugate anions present at these transition states become less stable and lead to higher activation energies as acids weaken. Activation energies were strongly attenuated to changes in DPE because electrostatic interactions between moieties of ion-pairs at transition states recovered most the electrostatic interactions overcome during deprotonation [19, 21]. The sensitivities of rate constants to acid strength depended on the charge localization of transition state cations and how effectively they recovered electrostatic interactions. Dehydration reactions with large differences in rate constants changed similarly with DPE, indicating that more difficult reactions are not necessarily more sensitive to acid strength [21].

These relations on well-defined solid acids are extended here to CH_3OH dehydration and C_6 alkane isomerization probe reactions by employing site counting methods and by interpreting reaction kinetics in chemical terms with mechanism-based rate expressions. Chapter 2 discusses the effects of acid strength and solvation on CH_3OH dehydration to dimethyl ether (DME), which proceeds by a bimolecular mechanism. Density functional theory (DFT) calculations on W-Keggin POM clusters with different central atoms were used to discern the dominant route for DME formation from two competing pathways. The sequence of elementary steps in the preferred route was used to interpret first- and zero-order rate constants measured during kinetic experiments as chemical events. These two kinetic parameters sense acid strength and solvation differently because of the different charges and sizes of reacting intermediates that form ion-pair transition states and are consistent with the calculated effects of DPE on the stabilities of these intermediates. Chapter 3 examines the role of reactant structure in determining C_6 alkane isomerization rate constants and their sensitivities to acid strength and to confinement within zeolite voids. Isomerization rate constants were measured for 2-methylpentane (2MP), 3-methylpentane (3MP), 2,3-dimethylbutane (23DMB), and n-hexane (nH) reactants using bifunctional metal-acid mixtures that equilibrate hydrogenation-dehydrogenation reactions. Alkenes with different backbones subsequently interconvert via similar elementary steps in which alkoxide backbone rearrangements are kinetically-relevant and their isomerization rates are described by similar kinetic expressions. Isomerization rate constants sensed acid strength equally for all reactants, in spite of large differences in their values, because they all proceed via cyclopropyl carbenium ion transition states with similar charge distributions. Solvation preferentially stabilizes alkyl shift transition states over transition states that change the degree of hydrocarbon branching. Deprotonation energies (DPE) and H-atom addition energies (HAE) are calculated for Keggin POM clusters with different central (S, P, Si, Al, Co) and addenda (W, Mo, V) atoms using DFT to develop these probes further as

accurate descriptors of reactivity for Brønsted acid and oxidation catalysis in Chapter 4. The effects of composition on the DPE values of these clusters are examined by using thermochemical cycles that dissect catalyst deprotonation into processes that reflect covalent and electrostatic interactions. Similar thermochemical cycles describing the interactions between conjugate anions and organic cations present as transition states and intermediates during CH_3OH dehydration indicate how reactions sense the abilities of Keggin clusters to delocalize electrons, which are also reflected in their DPE values. These investigations suggest reactions and conditions where DPE values can be used to directly compare the reactivities of different classes of solid acids (e.g., W-POM clusters and zeolites). Finally, HAE values are developed to probe the abilities of Keggin POM clusters to accept H-atoms and electrons at kinetically-relevant steps in oxidative dehydrogenation (ODH) reactions. HAE values depend on the identities of nearby addenda atoms and probe local electronic properties of Keggin clusters that differ from the delocalized properties probed by DPE values.

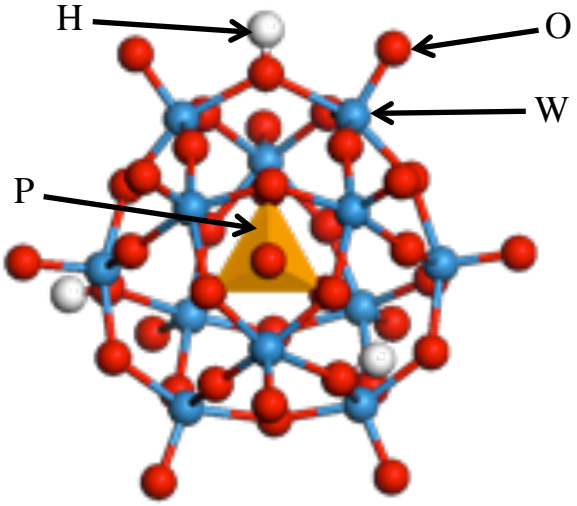

Scheme 1.1. Structure of the Keggin polyoxometalate (POM) cluster, shown specifically for $H_3PW_{12}O_{40}$ (R^{y+} = H^+, X^{n+} = P^{5+}, M = W). The central P-atom is shown as a tetrahedron. Atomic colors correspond to elemental identity (blue = W, red = O, orange = P, white = H).

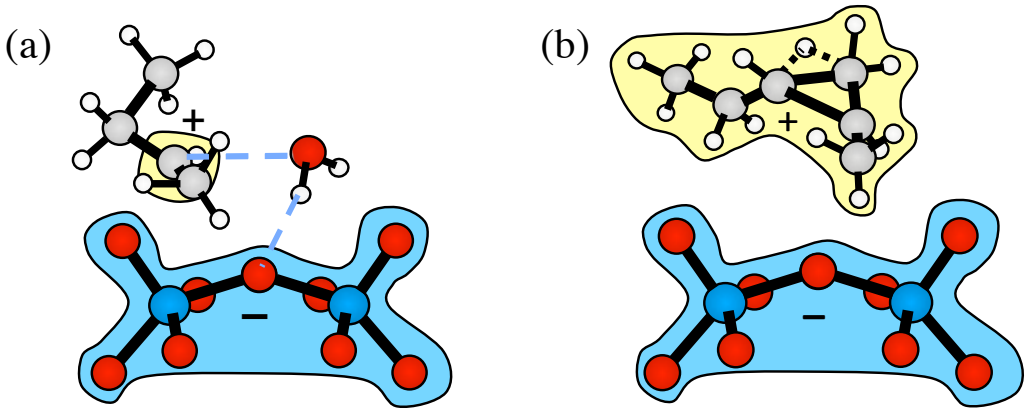

Scheme 1.2. Ion-pair transition states mediating (a) 2-butanol dehydration and (b) n-hexene isomerization on Keggin polyoxometalates. Images of transition state structures were taken from [21] with permission from the authors. Atomic colors correspond to elemental identity (blue = W, red = O, gray = C, white = H).

References

[1] A. Corma, Chem. Rev. 95 (1995) 559.
[2] D. S. Santilli, B. C. Gates. In *Handbook of Heterogeneous Catalysis,* G. Ertl, H. Knözinger, J. Weitkamp, Eds., Wiley-VCH, Weinheim, 1997, Vol.3, p. 1123.
[3] P.B. Venuto, Microporous Mater. 2 (1994) 297.
[4] A. Corma, Curr. Opin. Solid State Mater. Sci. 2 (1997) 63.
[5] A. Corma, Chem. Rev. 97 (1997) 2373.
[6] D.G. Barton, S.L. Soled, G.D. Meitzner, G.A. Fuentes, E. Iglesia, J. Catal. 181 (1999) 57.
[7] T. Okuhara, N. Mizuno, M. Misono, Adv. Catal. 41 (1996) 113.
[8] M. Hino, K. Arata, J. Chem. Soc. Chem. Commun. (1980) 851.
[9] X. Song, A. Sayari, Catal. Rev.- Sci. Eng. 38 (1996) 329.
[10] M.A. Harmer, W.E. Farneth, Q. Sun, J. Am. Chem. Soc. 118 (1996) 7708.
[11] H.A. Benesi, J. Am. Chem. Soc. 78 (1956) 5490.
[12] H. Karge, V. Dondur, J. Phys. Chem. 94 (1990) 765.
[13] A. Zecchina, S. Bordiga, G. Spoto, D. Scarano, G. Spano, F. Geobaldo, J. Chem. Soc., Faraday Trans. 92 (1996) 4863.
[14] M. Hunger, Catal. Rev. – Sci. Eng. 39 (1997) 345.
[15] D. T. Chen, L. Zhang, C. Yi, J.A. Dumesic, J.Catal. 146 (1994) 257.
[16] I.A. Koppel, P. Burk, I. Koppel, I. Leito, T. Sonoda, M. Mishima, J. Am. Chem. Soc. 122 (2000) 5114.
[17] M. Brändle, J. Sauer, J. Am. Chem. Soc. 120 (1998) 1556.
[18] R.A. van Santen, G.J. Kramer, Chem. Rev. 95 (1995) 637.
[19] J. Macht, M.J. Janik, M. Neurock, E. Iglesia, J. Am. Chem. Soc. 130 (2008) 10369.
[20] J. Macht, M.J. Janik, M. Neurock, E. Iglesia, Angew. Chem., Int. Ed. 46 (2007) 7864.
[21] J. Macht, R.T. Carr, E. Iglesia, J. Am. Chem. Soc. 131 (2009) 6554.

Chapter 2

Catalytic Consequences of Acid Strength in the Conversion of Methanol to Dimethyl Ether

Abstract

The effects of acid identity on CH_3OH dehydration are examined here using density functional theory (DFT) estimates of acid strength (as deprotonation energies, DPE) and reaction energies, combined with rate data on Keggin polyoxometalate (POM) clusters and zeolite H-BEA. Measured first-order (k_{mono}) and zero-order (k_{dimer}) CH_3OH dehydration rate constants depend exponentially on DPE for POM clusters; the value of k_{mono} depends more strongly on DPE than k_{dimer} does. The chemical significance of these rate parameters and the basis for their dependences on acid strength were established by using DFT to estimate the energies of intermediates and transition states involved in elementary steps that are consistent with measured rate equations. We conclude from this treatment that CH_3OH dehydration proceeds via direct reactions of co-adsorbed CH_3OH molecules for relevant solid acids and reaction conditions. Methyl cations formed at ion-pair transition states in these direct routes are solvated by H_2O and CH_3OH more effectively than those in alternate sequential routes involving methoxide formation and subsequent reaction with CH_3OH. The stability of ion-pairs, prevalent as intermediates and transition states on solid acids, depend sensitively on DPE because of concomitant correlations between the stability of the conjugate anionic cluster and DPE. The chemical interpretation of k_{mono} and k_{dimer} from mechanism-based rate equations, together with thermochemical cycles of their respective transition state formations, show that similar charge distributions in the intermediate and transition state involved in k_{dimer} cause its weaker dependence on DPE. Values of k_{mono} involve uncharged reactants and the same ion-pair transition state as k_{dimer}; these species sense acid strength differently and cause the larger effects of DPE on k_{mono}. Confinement effects in H-BEA affect the value of k_{mono} because the different sizes and number of molecules in reactants and transition states selectively stabilize the latter; however, they do not influence k_{dimer}, for which reactants and transition states of similar size sense spatial constraints to the same extent. This combination of theory and experiment for solid acids of known structure sheds considerable light on the relative contributions from solvation, electrostatic, and van der Waals interactions in stabilizing cationic transition states and provides predictive insights into the relative contributions of parallel routes based on the size and charge distributions of their relevant intermediates and transition states. These findings also demonstrate how the consequences of acid strength on measured turnover rates depend on reaction conditions and their concomitant changes in the chemical significance of the rate parameters measured. Moreover, the complementary use of experiment and theory in resolving mechanistic controversies has given predictive guidance about how rate and equilibrium constants, often inextricably combined as measured rate parameters, individually depend on acid strength based on the magnitude and spatial distributions of charges in reactants, products, and transition states involved in relevant elementary steps. The unique relations between k_{mono}, k_{dimer}, and DPE developed here for CH_3OH dehydration can be applied in practice to assess the acid strength of any solid acid, many

of which have unknown structures, preventing reliable calculations of their DPE by theory.

2.1. Introduction

Solid Brønsted acids and the reactions that they catalyze represent some of the most important materials and processes for chemical transformations, specifically those involved in the synthesis and conversion of fuels and chemicals. Active site structures in solid acids are often non-uniform and inaccessible to direct measurements of their number and acid strength, especially as they exist and evolve during thermal treatment and catalysis. Thus, the elucidation of specific relations among their structure, acid strength, and function remain challenging and often speculative [1]; yet, such insights are essential to improve existing materials and to guide the design of solid acids for specific catalytic purposes.

Tungsten polyoxometalate (POM) clusters with Keggin structure and charge-balancing protons ($H_{8-n}X^{n+}W_{12}O_{40}$) are Brønsted acids with well-defined connectivity and diverse central atoms ($X^{n+} = P^{5+}$, Si^{4+}, Al^{3+}, and Co^{2+}). The central atoms influence their acid strength, but not their Keggin structure, by changing the number of protons and the anionic charge in the conjugate base [2]; as a result, they enable purposeful compositional and functional modifications without concomitant changes in structural motifs. This compositional diversity causes significant changes in deprotonation energies (DPE), which rigorously reflect Brønsted acid strength.[3,4] DPE is the energy required to separate a proton from a conjugate base to non-interacting distances ($AH \rightarrow A^- + H^+$) and can be estimated from quantum mechanical treatments for known structures such as Keggin clusters.[2] Infrared [5] and nuclear magnetic resonance [6] methods and temperature-programmed desorption [7] and microcalorimetry [8] of adsorbed bases can also be used to infer acid strength, but seldom within reaction environments and often with distracting contributions from van der Waals and H-bonding interactions that do not rigorously reflect acid strength. DPE values for Keggin POM clusters decrease (and acid strength increases) as the valence of the central atom increases because of a concomitant increase in the stability of the anionic conjugate cluster. The DPE values of Keggin cluster in the gas-phase range from 1087 kJ mol^{-1} for $H_3PW_{12}O_{40}$ to 1145 kJ mol^{-1} for $H_6CoW_{12}O_{40}$ [2], making these clusters stronger and more diverse acids than zeolites (1171-1200 kJ mol^{-1} DPE for FAU, CHA, MOR, and MFI) [3] or mineral acids, at least as gas-phase monomers (1249 kJ mol^{-1} to 1359 kJ mol^{-1} for $HClO_4$, H_2SO_4, HNO_3, and H_3PO_4) or dimers (1177 kJ mol^{-1} for $H_2S_2O_7$ and 1274 kJ mol^{-1} for $H_4P_2O_7$) [4] in the latter case.

Measured rate constants, derived from mechanistic interpretations of alkanol dehydration and hexane isomerization rates, decreased exponentially with increasing DPE for Keggin POM and zeolite H-BEA acids.[2,9,48] These trends suggest a proportional relation between DPE and kinetically-relevant activation barriers, in which the "correlation strength" reflects the relative electrostatic stabilization of protons and cationic moieties in ion-pairs of late transition states by the anionic conjugate base. These activation barriers can be dissected into contributions from molecular and active site properties using thermochemical cycles.[9,48] These contributions include (i) adsorption of reactants, (ii) deprotonation of the solid acid, (iii) protonation of reactant(s)

in the gas phase, and (iv) interactions between cationic transition states and the conjugate anion. Hexene isomerization barriers depend more strongly on DPE than those for 1-butanol or 2-butanol dehydration because of the more localized charge at transition states involved in the latter reactions, which recover a larger fraction of the energy required to separate the proton from the conjugate base.

These concepts are extended here to CH_3OH dehydration to dimethyl ether (DME), for which dehydration turnovers require bimolecular events, because the C_1 species involved lack stable gas-phase unimolecular dehydration products (in contrast with the C_n alkoxides formed from C_n alkanols). CH_3OH dehydration and its reverse, DME hydration, occur during homologation to hydrocarbons [10] and DME carbonylation/homologation reactions [11 , 12]. This study resolves long-standing controversies about the mechanism of bimolecular CH_3OH dehydration on solid acid catalysts by combining kinetic data with density functional theory (DFT) calculations. Our results indicate that direct routes, involving reactions between two adsorbed CH_3OH molecules, prevail at all relevant conditions on POM and zeolite acid catalysts. Apparent first- and zero-order rate constants depend differently on DPE values; these differences are explained by the charge distributions of transition states and intermediates involved in their activation barriers. These data and calculations, taken together with previous reports [2,9,48,49] provide predictive guidance for the sensitivity of catalytic reaction rates to acid strength. Mechanistic interpretations of catalytic rates in terms of elementary steps, with rate and equilibrium constants that reflect the chemical properties of the intermediates and transition states involved, are required to rigorously analyze of the effects of catalyst composition on function. The effects of DPE on rate constants are consistent with its inclusion in thermochemical descriptions of activation barriers and show that electrostatic stabilization of intermediates and transition states relative to that of a proton determine their sensitivity to acid strength. For Brønsted acid catalysis, where ion-pair transition states are a ubiquitous feature, the effects of DPE on activation barriers decrease as the reacting intermediate becomes more charged.

2.2. Experimental Methods

2.2.1 Catalyst Synthesis

$H_3PW_{12}O_{40}$ (Sigma-Aldrich; reagent grade; CAS #12501-23-4), $H_4SiW_{12}O_{40}$ (Aldrich; >99.9%; CAS #12027-43-9), $H_5AlW_{12}O_{40}$ [13], and $H_6CoW_{12}O_{40}$ [14,15] were supported on amorphous SiO_2 (Cab-O-Sil HS-5; 310 $m^2 g^{-1}$; 1.5 $cm^3 g^{-1}$ pore volume) by incipient wetness impregnation with their respective ethanol solutions (Sigma-Aldrich; >99.5%; anhydrous) at POM surface densities of 0.04 POM nm^{-2}. SiO_2 was washed three times in 1 M HNO_3 and treated in air (UHP Praxair; 0.5 $cm^3 g^{-1} s^{-1}$) at 573 K for 5 h before impregnation with ethanolic solutions of POM (1.5 cm^3 solution g^{-1} SiO_2). Samples were held in closed vials for 24 h after impregnation to ensure uniform distribution of clusters in SiO_2 pores and then treated in flowing dry air (UHP Praxair; 0.5 $cm^3 g^{-1} s^{-1}$) at 323 K (0.033 K s^{-1} heating rate) for 24 h.

The MAS-^{31}P-NMR spectra of $H_3PW_{12}O_{40}/SiO_2$ confirmed that the Keggin structure was maintained upon dispersion onto SiO_2 (Supporting Information). Transmission electron micrographs showed that POM clusters were present

predominantly as isolated clusters on SiO_2 supports (Supporting Information). H-BEA (Zeolyst; Si/Al =11.8) samples were used as received from the manufacturer. Supported Keggin clusters and H-BEA samples were pressed into wafers, crushed, and sieved to retain 125-180 μm aggregates before catalytic and titration measurements.

2.2.2 Methanol Reaction Rate Measurements

CH_3OH dehydration rates were measured in a differential quartz tubular flow reactor (1.0 cm I.D.) at 373 - 433 K. Catalyst samples (0.01 - 0.2 g) were held on a porous quartz disc and heated with a resistive furnace. Temperatures were measured by a thermocouple (Omega K-type; ± 0.2 K) held within a dimple at the reactor wall and controlled electronically (Watlow; Series 982 controller). Catalyst samples were diluted with washed SiO_2 (pressed and sieved to retain 125-180 μm aggregates) to maintain at least 0.1 g of total mass in all experiments to ensure sufficient bed volume for conductive contact with the reactors walls and the thermocouple well. Keggin POM samples were heated to reaction temperature (0.083 K s^{-1} heating rate) in flowing He (UHP Praxair; 0.83 cm^3 s^{-1}) and held for 1 h before catalytic measurements. H-BEA was heated to 773 K (0.083 K s^{-1} heating rate) in dry air (UHP Praxair) and held for 2.5 h before these measurements. All transfer lines were kept at 393 K to prevent condensation of reactants, products, or titrants. Liquid CH_3OH (Sigma-Aldrich; 99.8%; without additional purification) was mixed with He (UHP Praxair) using a liquid syringe pump (Cole-Palmer 74900 Series). CH_3OH molar flow rates were used to control its partial pressure (0.01-20 kPa) and maintain differential conversions (<10%).

The concentrations of reactants, products, and titrants were determined by gas chromatography using flame ionization detection (Agilent 6890N GC; 50 m HP-1 column). Dimethyl ether was the only product detected during methanol reactions on all catalysts; products were not detected in empty reactors or in reactors containing washed SiO_2 (0.06 g SiO_2; $1x10^{-5}$ moles CH_3OH (g SiO_2)$^{-1}$ s^{-1}). Some deactivation was detected (< 40% of initial rate after 5 h time on stream) on Keggin POM samples, apparently because of slow CH_3OH homologation and alkene oligomerization reactions. The loss of active sites by intervening deactivation were determined by periodic rate measurements at standard conditions (0.3 kPa CH_3OH) and were used to correct rate data so that turnover frequencies were not influenced by such deactivation.

The number of Brønsted acid sites in each sample was measured by titration with 2,6-di-*tert*-butylpyridine during catalytic CH_3OH reactions to report dehydration rates as accurate turnover rates. Titrant mixtures were prepared by dissolving 2,6-di-*tert*-butylpyridine (Aldrich; >97%; CAS #585-48-8) in CH_3OH (Sigma-Aldrich, 99.8%) to give 9×10^{-5} – 1.3×10^{-3} (titrant/CH_3OH) molar ratios. The titrant mixture was introduced into a He gas stream (UHP Praxair) using a syringe pump. Dehydration rates and the number of adsorbed titrant molecules were concurrently measured by gas chromatographic analysis of the reactor effluent using protocols similar to those described above. The number of accessible protons (per POM) was determined from the number of titrant molecules (per POM) required to suppress dehydration catalysis, assuming a 1:1 titrant:H^+ adsorption stoichiometry. Pyridine (Aldrich; anhydrous, 99.8%) was also used for titrations of BEA using concentrations and protocols similar to that of hindered pyridine titration.

2.2.3. Computational Methods

Periodic gradient-corrected density functional theory calculations were carried out using the Vienna ab initio Simulation Package (VASP)[16] to determine optimized structures and energies for all stable intermediates and transition states. The wavefunction was represented by a periodic plane wave basis set expansion (to a cutoff energy of 396.0 eV) and Vanderbilt ultrasoft pseudopotentials to describe electron-core interactions.[17] Exchange and correlation energies were calculated within the generalized gradient approximation using the Perdew-Wang (PW91) form [18] for the exchange and correlation functional. The full Keggin cluster (1.06 nm in diameter) was modeled by placing it in the center of a 20 x 20 x 20 $Å^3$ unit cell to provide a vacuum region that prevents electronic interactions between unit cells. A 1 x 1 x 1 Monkhorst-Pack k-point mesh was used to sample the first Brillioun zone. All structures were converged until forces on all of the atoms were < 0.05 eV $Å^{-1}$. The electronic structures for each structural optimization step were converged self-consistently to < 1 x 10^{-4} eV.

Transition state structures were calculated by combining the nudged elastic band (NEB) method [19], to approximate transition state structures, with the dimer approach of Henkelman [20], used here to converge and isolate the final transition state structure. Initial reaction trajectories in NEB were determined by linear interpolation among 16 equally-spaced images along the reaction coordinate. These images were optimized in the direction perpendicular to the normal vectors connecting images to forces < 0.1 eV $Å^{-1}$ to determine minimum energy reaction paths and the transition state structures and energies. NEB transition state structures and trajectories were used as inputs to dimer calculations. The torque on the dimer was minimized at each of its translational steps to < 1 eV $Å^{-1}$ or up to 8 times per translation. Dimer calculations were optimized until the forces on all atoms were < 0.05 eV $Å^{-1}$ to locate the final transition state.

The optimized $H_3PW_{12}O_{40}$ structure is shown in the Supporting Information (Figure S.2.3) with the O-atoms and the proton labeled in the local active site used for calculations. Surface structures and transition states for all central atoms were calculated at the same proton (H_{C1}) on a bridging O-atom (O_{C1}). Reaction energies (ΔE_{rxn}) were calculated from the product ($E_{prod,i}$) and reactant energies ($E_{react,j}$) using:

$$\Delta E_{rxn} = \sum_i E_{prod,i} - \sum_j E_{react,j} \qquad (2.1)$$

A similar equation was used for activation barriers, for which the transition state replaces the products in Eq. (2.1). Reaction and activation energies were not corrected for zero-point vibrational energies (ZPVE) or entropies, because they are computationally prohibitive for full Keggin structures. ZVPE corrections are not expected to influence reported energies because such corrections are similar for reactants and products (or transition states). Deprotonation energies (DPE) for Keggin POM clusters with different central atoms were previously reported.[2] DPE values are defined as the energy required removing a proton (H^+) from an acid (AH) to distances where interactions with the conjugate base (A^-) are negligible

$$DPE = E_{H+} + E_{A-} - E_{AH} \quad (2.2)$$

Charges on intermediates and transition states were calculated using Bader charge methods [21,22], which formally distribute the electron density between two atoms along a dividing plane of zero flux. This plane is perpendicular to the chemical bond connecting the two atoms and is located where the charge density is a minimum along the bond.

2.3. Results and Discussion

2.3.1 Effects of Methanol Pressure on Dehydration Turnover Rates

Figure 2.1 shows measured CH_3OH dehydration turnover rates per accessible H^+ (Table 2.1) as a function of CH_3OH pressure on Keggin POM clusters ($H_{8-n}X^{n+}W_{12}O_{40}$) with different central atoms (X^{n+} = P^{5+}, Si^{4+}, Al^{3+}, and Co^{2+}) and zeolite H-BEA. Turnover rates initially increased linearly with CH_3OH pressure at all temperatures on all catalysts, but became insensitive to CH_3OH at higher pressures. The shift from linear to zero-order dependence on reactant pressure occurred at higher pressures on Keggin clusters containing central atoms of lower valence (Figure 2.1a) and at higher reaction temperatures for a given POM cluster ($H_4SiW_{12}O_{40}$ in Figure 2.1b). These rate data are consistent with a Langmuir-type rate expression:

$$r = \frac{\alpha P_{MeOH}}{1 + \beta P_{MeOH}} \quad (2.3)$$

and with the elementary steps proposed in Section 2.3.2, which assign specific chemical significance to the kinetic parameters α and β. Accurate values for α and β were estimated by regression of rate data to Eq. (2.3). The dashed curves in Figure 2.1 confirm the accuracy of Eq. (2.3) in describing all rate data.

Turnover rates are normalized by accessible protons, measured here by titration with 2,6-di-*tert*-butylpyridine during CH_3OH dehydration (Table 2.1). Titrant molecules are protonated by Brønsted acid sites, making these sites unavailable for CH_3OH dehydration; these titrants cannot coordinate to Lewis acids because of steric hindrance at their N-atom.[23] In the absence of polar molecules, bulky non-polar titrants cannot penetrate into aggregates of Keggin clusters that form on the support. Polar CH_3OH reactants can expand these agglomerates, however, rendering protons within them accessible to both reactants and titrants.

The number of accessible protons on $H_4SiW_{12}O_{40}$ measured during dehydration catalysis at 413 K was essentially unaffected by the CH_3OH pressure (2.3–2.7 H^+/POM, Supporting Information), indicating that the effects of reactant pressure (Figure 2.1) reflect a kinetic origin instead of concomitant effects of CH_3OH pressure on the accessibility of protons. Figure 2.2a shows dehydration rates on $H_4SiW_{12}O_{40}/SiO_2$ at 413 K before and during introduction of hindered pyridine titrants. CH_3OH dehydration rates became undetectable after adsorption of 2.3 hindered pyridine molecules per POM, indicating that 2,6-di-*tert*-butylpyridine reaches and titrates all reactive protons during

CH_3OH dehydration and that any Lewis acid sites present do not catalyze dehydration at detectable rates.

2,6-di-*tert*-Butylpyridine did not fully suppress CH_3OH dehydration rates on H-BEA (Figure 2.2b) and saturation uptakes were less than the number of framework Al atoms (~0.45 titrants per framework Al; measured from Al-NMR, Supporting Information). Residual rates after saturation with 2,6-di-*tert*-butylpyridine were much smaller (by a factor of 0.15) than initial rates and not much different than those measured after saturation with pyridine (0.5 per framework Al; Supporting Information), which also titrates Lewis acid sites. Thus, we conclude that Lewis acid sites are not responsible for residual dehydration rates after saturation on H-BEA. Residual rates appear to reflect minority protons that CH_3OH can access, but larger organic bases cannot, in spite of the large three-dimensional channels in BEA. The total number of reactive protons accessible to CH_3OH (Table 2.1) was measured from the extrapolation of the titration curve in Figure 2.2b to zero rates (0.55 H^+ per framework Al); these values are used to calculate the dehydration turnover rates reported here.

2.3.2. Direct and Sequential Routes for Methanol Dehydration on Brønsted Acid Sites

Next, we consider sequential and direct routes for CH_3OH dehydration on Brønsted acid sites on Keggin POM clusters and BEA in the context of interpreting measured rate data. CH_3OH dehydration has been proposed to occur on acid-form zeolites and Keggin POM via sequential reactions of CH_3OH through methoxide intermediates [24 - 32] and via a concerted reaction between two adsorbed CH_3OH molecules [33,34]. The sequential route (Scheme 2.1) involves quasi-equilibrated CH_3OH adsorption through interactions with protons (Step 1) to form CH_3OH "monomers" that eliminate H_2O and form methoxide intermediates (Step 2). A second CH_3OH adsorbs at a vicinal O-atom in another quasi-equilibrated step (Step 3) and the methoxide then transfers to the CH_3OH in a step that reforms the proton as DME desorbs (Steps 4 and 5). In direct dehydration routes (Scheme 2.2), CH_3OH monomers form by the same path (Step 1), but a second CH_3OH adsorbs and interacts to form protonated dimers before H_2O elimination forms methoxides (Step 2). These dimers then rearrange to co-adsorbed species (Step 3) with the atomic orientation required to form DME and H_2O in a single, subsequent step (Step 4).

The pseudo-steady-state approximation for all adsorbed species, together with quasi-equilibrated CH_3OH adsorption, irreversible H_2O and DME elimination, and sites predominantly occupied by methoxides and CH_3OH monomers in the sequential dehydration route (Scheme 2.1) give the rate equation (derivation in the Supporting Information):

$$\frac{r_s}{[H^+]} = \frac{k_{DME,s} K_P(CH_3OH)}{1 + \frac{k_{DME,s}}{k_{elim}} K_P(CH_3OH)} \qquad (2.4)$$

in which k_{elim} and $k_{DME,s}$ are the rate constants for H_2O elimination from monomers (Step 2) and for DME formation from methoxide/CH_3OH pairs (Step 4), respectively, and K_P is the equilibrium constant for CH_3OH adsorption next to methoxide species (Step 3). $[H^+]$ is the number of accessible protons, determined by titration with 2,6-di-*tert*-butyl pyridine during CH_3OH dehydration (Section 2.3.1 and Table 2.1). The rate for the direct route (Scheme 2.2) with active sites predominantly occupied by monomers and protonated dimers (derivation in the Supporting Information) is:

$$\frac{r_d}{[H^+]} = \frac{k_{DME,d} K_C K_D (CH_3OH)}{1 + K_D (CH_3OH)} \tag{2.5}$$

in which $k_{DME,d}$ is the rate constant for DME formation from co-adsorbed species (Step 4) and K_D and K_C are the adsorption equilibrium constants for protonated dimers (Step 2) and co-adsorbed species (Step 3), respectively. These treatments give rate equations for the two routes that differ only in the chemical significance of their respective rate parameters; both are consistent with the measured effects of CH_3OH pressure on dehydration rates (Figure 2.1 and Eq. (2.3)). The involvement of these mechanisms can only be discerned by comparing rate and equilibrium constants estimated from the energies of intermediates and transition states derived from DFT calculations.

2.3.3. Energies for Reaction Intermediates and Transition States on Keggin POM from Density Functional Theory

Optimized energies and structures of intermediates and transition states in the sequential and direct routes were calculated for Keggin POM clusters with different central atoms (S, P, Si, Al, Co) and are shown in Figures 2.3a and 2.3b on $H_3PW_{12}O_{40}$, respectively. Keggin clusters with sulfur central atoms were calculated, even though they have not been synthesized in their proton form, so as to examine the catalytic consequences of composition and acid strength over the widest possible range. Corresponding energies for intermediates and transition states on H-BEA were not calculated because they strongly depend on van der Waals forces unrelated to acid strength (or DPE values) and require higher-level theoretical treatments that are computationally prohibitive for these systems.[58] The effects of these additional forces are examined later in Section 2.3.5 by comparing measured rate constants on H-BEA and Keggin POM clusters. The optimized bond lengths and Bader charges for all of the intermediates and transition states on the different Keggin POM clusters are reported in Tables 2.2 and 2.3. Table 2.4 shows energies for all intermediates and transition states relative to two gas-phase CH_3OH molecules and a bare POM cluster. The energies of selected intermediates and of all transition states on POM clusters are shown in Figures 2.4 and 2.5, respectively, as a function of calculated DPE values.

2.3.3.1 Formation of Adsorbed Methanol Monomers

Both routes share the initial adsorption of CH_3OH at protons located on bridging O-atoms in POM clusters to form monomers (A in Figure 2.3a). Monomers at terminal O-atoms were less favorable than on bridging O-atoms by 11 kJ mol^{-1} (Supporting Information). Previous calculations on $H_3PW_{12}O_{40}$ showed that H_2O and CH_3OH assist

"proton-hopping" which greatly increases surface mobility [35] so that protons and monomers reach their equilibrium locations (a bridging to terminal ratio of 20 at 433 K for monomers). The adsorbed CH_3OH structures resemble those proposed for CH_3OH-proton adducts from theoretical [29,31], NMR [36,37], and infrared [25,26,38] evidence. The O-atom in CH_3OH (O_{M1}) is oriented towards the Keggin proton (H_{C1}) and its H-atom (H_{M1}) points towards a vicinal terminal O-atom (O_{C3}). The O_{C1}-O_{M1} distance (0.247 nm) for CH_3OH adsorbed on $H_3PW_{12}O_{40}$, is shorter than for H-bonds among H_2O (0.276 nm) or alkanol (0.274 nm) molecules.[39,40] The H_{C1}-O_{C1} distances (0.108 nm) are similar to those in non-interacting protonated POM clusters (0.098 nm) and the POM proton remains closer to O_{C1} than O_{M1} indicating that protons are not transferred to the adsorbed CH_3OH. Protonated CH_3OH ions (i.e. methyl-oxonium cations $[CH_3OH_2]^+$) relaxed to adsorbed monomers (A in Figure 2.3a) during structure optimization calculations, indicating that the cations are unstable compared to less charged monomer species. $[CH_3OH_2]^+$ ions could only be calculated as transition states in CH_3OH-assisted proton-hopping reactions. The activation barrier for this reaction, which is measured from uncharged monomers, is 15 kJ mol^{-1} on $H_3PW_{12}O_{40}$ (Supporting Information) and indicates that proton transfer to form $[CH_3OH_2]^+$ ions is endothermic.

CH_3OH adsorption energies on Keggin clusters ranged from -62 kJ mol^{-1} to -75 kJ mol^{-1} (Table 2.4 and Figure 2.4), indicative of strong interactions between CH_3OH and protons as a result of the partial charge on H_{C1} (+0.64 to +0.75 e Bader charge). These electrostatic interactions stabilize monomers more effectively than typical intermolecular H-bonds in gaseous H_2O and CH_3OH (18.4 - 20.9 kJ mol^{-1} and 13.4 - 30.5 kJ mol^{-1}, respectively).[41, 42,43] CH_3OH monomers become less stable with increasing DPE (Figure 2.4) because the partial charges on protons, needed for strong adsorption, become less stable on weaker acids. CH_3OH adsorption energies are similar on Keggin clusters and aluminosilicate structures in large-pore zeolites (-63 to -73 kJ mol^{-1})[33,31,44] even though POM clusters are stronger acids, possibly because zeolite frameworks provide additional van der Waals stabilization unrelated to acid strength or DPE.

DME formation from strongly H-bonded CH_3OH species proceeds via the two routes described above (Schemes 2.1 and 2.2). The sequential path involves the elimination of H_2O to form a methoxide (Scheme 2.1, Step 2) that subsequently reacts with another CH_3OH molecule to form DME (Scheme 2.1, Step 4) and restore the proton. The direct route involves a bimolecular reaction between two adsorbed CH_3OH molecules to eliminate H_2O and form protonated DME (Scheme 2.2, Step 4) simultaneously. These routes are examined separately next by calculating the structures and energies of their respective transition states and intermediates on Keggin POM with different central atoms (S, P, Si, Al, Co).

2.3.3.2 Methanol Dehydration by the Sequential Route

The first step in the sequential route is H_2O elimination from monomers, forming covalently-bound methoxides (Scheme 2.1, Step 2). The chemical outcome and the structures along this reaction coordinate are reminiscent of S_N2 reactions in which the POM O-atom (O_{C2}) acts as the nucleophile, H_2O as the leaving group, and the methyl group as the electrophile. The transition state (shown for $H_3PW_{12}O_{40}$ in Figure 2.3a as TS1) involves the transfer of the proton from the POM cluster to the O-atom in adsorbed

CH_3OH (H_{C1}-O_{C1} = 0.398 nm and H_{C1}-O_{M1} = 0.098 nm at TS1 vs. 0.107 nm and 0.140 nm, respectively, in monomers) with the simultaneous elongation and cleavage of the C-O bond in CH_3OH (C_{M1}-O_{M1} = 0.184 nm at TS1 vs. 0.146 nm in the monomer) to form H_2O. The O-atom in the H_2O, the methyl species, and the terminal O-atom of the POM (O_{C2}) are arranged in a straight line at the transition state, consistent with the arrangement required for the proper alignment of orbitals in S_N2-type reactions.[45] The umbrella-like methyl in CH_3OH must invert upon methoxide formation as a planar methyl cation at the transition state (TS1 in Figure 2.3a). Bader charges in the POM cluster (-0.79 e), methyl (+0.59 e), and H_2O (+0.20 e) fragments indicate this is a late ion-pair transition state with the methyl cation stabilized by ion-dipole contact with the H_2O molecule and by electrostatic interactions with neighboring O-atoms in the anionic POM cluster (O_{C2} and O_{C1}).

The corresponding transition state energy relative to gas-phase CH_3OH is 69 kJ mol^{-1} on $H_3PW_{12}O_{40}$ and increases weakly with increasing DPE (Figure 2.5a), because charge separation at the ion-pair transition state requires more energy on weaker acids. The transition state energy for this step on $H_6CoW_{12}O_{40}$ lies above the trend defined the other POM clusters because it occurs earlier along the reaction coordinate, as shown by its bent configuration, which contrasts the linear structures found for other POM clusters (Figure 2.6). The conjugate anion stabilizes the cationic charge on H_2O (+0.20 e) more effectively in this bent conformation than in linear structures because of smaller distances between charged moieties, but it has inappropriate atomic positions for S_N2 reactions. As charge separation becomes more costly on weaker acids, H_2O elimination transition states occur earlier along the reaction coordinate to retain the H_2O fragment near the anionic cluster, but will involve increasingly unstable structures that cannot align their molecular orbitals for S_N2 reactions.

The activation barriers for H_2O elimination (Figure 2.5b) from monomers (A in Figure 2.3a) are significantly higher than their respective transition state energies (measured with respect to gas-phase CH_3OH). They only depend weakly on DPE (140 kJ mol^{-1} except for $H_6CoW_{12}O_{40}$ for the reasons above), because DPE effects on transition state and the monomer energies nearly cancel out. These high barriers for H_2O elimination reflect the unstable nature of methyl cations; they are, however, much smaller than for dehydration of gaseous methyl-oxonium ions (i.e. $[CH_3OH_2]^+_{(g)} \rightarrow CH_3^+{}_{(g)} + H_2O_{(g)}$; E_{dehy} = 290 kJ mol^{-1})[46,51] because electrostatic stabilization by the anionic cluster and ion-dipole interactions with the neighboring H_2O molecule stabilize methyl ions at the elimination transition state. Blaszkowski and van Santen calculated an activation barrier of 215 kJ mol^{-1} for methoxide formation on a small aluminosilicate cluster [34]. This value is significantly higher than the values calculated on POM clusters here, possibly because of the lack of charge screening on small zeolite clusters [47]. H_2O loses its charge upon methoxide formation (-0.01 e Bader charge; Supporting Information) and desorbs subsequently in an endothermic step (19-24 kJ mol^{-1}), whose reaction energy does not depend on the DPE of the POM cluster (Table 2.4).

The transition state involved in H_2O elimination from CH_3OH monomers (TS1) resembles that for H_2O elimination from larger H-bonded alkanols on POM clusters[48,49] and is consistent with the ubiquitous involvement of late ion-pairs at transition states for Brønsted acid catalysis.[9,48] Both transition states have full proton

transfer to the alkanol and cleavage of the alkanol C-O bond to form H_2O interacting with planar carbenium cations. Elimination barriers for CH_3OH (139 to 144 kJ mol^{-1} for all POM clusters) are similar to previous estimates for 2-butanol elimination (127 to 146 kJ mol^{-1})[49] on POM clusters. Thermochemical cycles (discussed in Section 2.3.5 and shown for the comparison of CH_3OH and butanol activation barriers in the Supporting Information) show that the similar activation barriers for CH_3OH and 2-butanol dehydration (for a given acid) reflect compensation between (i) gas-phase alkanol dehydration energies (E_{dehy}; $ROH_{(g)} + H^+_{(g)} \rightarrow R^+_{(g)} + H_2O_{(g)}$), (ii) stabilization of the gas-phase carbenium ion (R^+) by H_2O at the gas-phase transition state analog (E_{water}), and (iii) electrostatic stabilization of this gas-phase analog by the anionic cluster ($E_{ES,POM}$):

$$E_{a,MeOH} - E_{a,BuOH} = (E_{dehy} + E_{water} + E_{ES,POM})_{MeOH} - (E_{dehy} + E_{water} + E_{ES,POM})_{BuOH} \quad (2.6)$$

Gas-phase 2-butanol dehydration is much more exothermic (E_{dehy} = -720 kJ mol^{-1}) than for CH_3OH (E_{dehy} = -485 kJ mol^{-1}),[51,46] because alkyl induction effects stabilize butyl cations. These differences are attenuated, however, by stronger stabilization of methyl cations than butyl cations by H_2O and the conjugate anion (detailed calculations in Supporting Information).[49,50] The distance between the planar C-atom and the O-atom in the eliminated H_2O for TS1 (O_{M1}-C_{M1} = 0.184 nm) is 0.07 nm shorter than in the 2-butanol dehydration transition state (0.26 nm)[49], and as such, methyl cations coordinate more strongly with H_2O to form a carbenium-water complex. Similar activation barriers for H_2O elimination from CH_3OH and 2-butanol, even though butyl cations are much more stable than methyl cations, indicate that the stabilization of methyl groups at CH_3OH transition states is essential for low CH_3OH dehydration activation barriers. These findings suggest, in turn, that routes that do so more effectively, such as the direct dehydration route, may circumvent the high energy barriers associated with the sequential formation and reaction of methoxide intermediates.

Adsorption of a second CH_3OH molecule at a bridging O-atom (O_{C1}) vicinal to a methoxide, leads to methoxide/CH_3OH pairs (Scheme 2.1, Step 3) that form DME by methyl transfer. The hydroxyl H-atom (H_{M2}) of the adsorbed CH_3OH interacts with a bridging POM O-atom (O_{C1}), while its O-atom (O_{M2}) interacts with the C-atom in the methoxide (B in Figure 2.3a). The adsorption energy of this second CH_3OH (-16 to -24 kJ mol^{-1}; Table 2.4) is typical of a H-bond and is weaker than the adsorption of the first CH_3OH at POM protons to form monomers (-77 to -65 kJ mol^{-1}; Table 2.4) because of the absence of electrostatic stabilization. The O-atom separation in this H-bond (O_{M2}-O_{C1} = 0.298 nm on $H_3PW_{12}O_{40}$) is longer than in solid H_2O (0.276 nm)[40] and binding energies resemble those among gas-phase CH_3OH molecules (13 to 30 kJ mol^{-1}).[42,43] These methoxide/CH_3OH pairs react via nucleophilic attack of the methyl by CH_3OH to form DME (Scheme 2.1, Step 4) in a step that resembles the reverse of H_2O elimination (Scheme 2.1, Step 2), except that CH_3OH is present instead of H_2O. The C_{M1}-O_{M2} distance (0.317 – 0.331 nm; Table 2.2) in methoxide/CH_3OH pairs shortens as DME forms (C in Figure 2.3a, C_{M1}-O_{M2} = 0.145 nm). The transition state (TS2 in Figure 2.3a) consists of a planar methyl (+0.57 e Bader charge) stabilized by the O-atom in CH_3OH (+0.20 e Bader charge and O_{M2}–C_{M1} = 0.192 nm) and POM clusters (O_{C2}–O_{M2} = 0.200

nm). Similar to the H_2O elimination transition state, the terminal POM O-atom, methyl, and CH_3OH O-atom are in a linear arrangement that is conducive to S_N2 substitution for all POM central atoms except $H_6CoW_{12}O_{40}$ (Figure 2.6).

The transition state energies to form DME (with respect to two gas-phase CH_3OH) increase slightly with increasing DPE (Figure 2.5a), as in the case of H_2O elimination from CH_3OH monomers. They are consistently smaller, however, because CH_3OH stabilizes cationic methyl fragments via ion-dipole interactions more effectively than H_2O (Scheme 2.3, Supporting Information). DME formation activation barriers (85 kJ mol^{-1} on $H_3PW_{12}O_{40}$), measured with respect to methoxide/CH_3OH pairs, are significantly smaller than for H_2O elimination from monomers (Figure 2.5b), predominantly because methoxide/CH_3OH pairs (and gas-phase H_2O) involved in DME formation are less stable than the monomers (and gas-phase CH_3OH) that precede H_2O elimination (Figure 2.3a). This sequential CH_3OH dehydration catalytic sequence is completed by desorption of DME and the re-protonation of the POM cluster (Scheme 2.1, Step 5), in a concerted step with reaction energies of 65-75 kJ mol^{-1} for these POM clusters (Table 2.4).

2.3.3.3 Direct Route for Methanol Conversion to Dimethyl Ether

Direct CH_3OH dehydration routes involve reactions of gas-phase CH_3OH with monomers to form adsorbed dimers (Scheme 2.2, Step 2); these dimers are stabilized by concerted interactions among POM protons, OH groups in the two CH_3OH molecules, and vicinal POM O-atoms. The two most stable dimers investigated are shown as D and E in Figure 2.3b. In "dimer D", the proton lies between the O-atoms in the two CH_3OH molecules and each CH_3OH molecule acts as a H-bond donor to a vicinal terminal O-atom in the POM cluster (O_{C2} and O_{C3}). The H_{C1}-O_{C1} distance (0.295-0.267 nm vs. 0.097 nm in unreacted POM clusters) is consistent with significant proton transfer in these dimer structures, a conclusion also confirmed by their Bader charges (+ 0.88-0.86 e); thus, we denote these species as protonated dimers. The adsorption energy for this protonated dimer, relative to its CH_3OH monomer and gas-phase CH_3OH precursors, is -85 kJ mol^{-1} on $H_3PW_{12}O_{40}$. This large negative value reflects charge separation in dimers that provides electrostatic stabilization to bind dimers to POM clusters more strongly than H-bonds among CH_3OH (-13 to -30 kJ mol^{-1}).[42,43] Dimers are more stable as DPE decreases because charge separation is less costly for stronger acids. Dimer formation energies (relative to two gas-phase CH_3OH) are more sensitive to DPE than those for less charged CH_3OH monomers (Figure 2.4).

The other stable dimer structure (E in Figure 2.3b) orients the H-atom in the monomer (H_{M1}) directly towards the O-atom in the other CH_3OH (O_{M2}), which itself is H-bonded to a vicinal terminal POM O-atom (O_{C3}) through its H-atom (H_{M2}). The H_{C1}-O_{M1} (0.105 nm) and H_{C1}-O_{C1} (0.148 nm) distances and Bader charges (0.88 – 0.84 e) are also consistent with nearly complete transfer of POM protons to CH_3OH molecules. The formation energies are consequently similar for dimers D and E (-83 kJ mol^{-1} vs. -85 kJ mol^{-1} on $H_3PW_{12}O_{40}$). DPE effects on stability are slightly weaker for E than D structures (Table 2.4), but both structures are much more sensitive to DPE than monomers. The small energy differences between the two dimers for each POM cluster

(< 10 kJ mol^{-1}; Table 2.4) indicates that they co-exist during steady-state CH_3OH dehydration catalysis.

DME formation from protonated dimers requires that the methyl in one CH_3OH molecule approach the O-atom of the other CH_3OH molecule; this requires significant rearrangements of these dimers, in which the two OH groups face each other and the methyl groups point away from each other (D and E in Figure 2.3b). As a result, dimers must first reorient to a structure, denoted here as the "co-adsorbed state" (F in Figure 2.3b), which resembles a CH_3OH monomer interacting weakly with a CH_3OH that is H-bonded to a vicinal terminal POM O-atom (O_{C2}). The monomer methyl group interacts with the O-atom in the other CH_3OH (C_{M1}-O_{M2} = 0.295 – 0.327 nm; Table 2.3) in a configuration that becomes geometrically conducive to methyl transfer. The proton is not transferred from the POM to the co-adsorbed CH_3OH (H_{C1}-O_{C1} = 0.112 to 0.105 nm and H_{C1}-O_{M1} = 0.103 to 0.108 nm; +0.12 e Bader charge); thus, these reactive structures are much less stable than inappropriately oriented protonated dimers (67 to 40 kJ mol^{-1} energy differences for POM with different central atoms (Table 2.4)) because of the resulting absence of electrostatic stabilization.

The rearrangement of protonated dimer D to co-adsorbed species on $H_3PW_{12}O_{40}$ showed no additional barrier above the energy difference between the two intermediates (Supporting Information). The activation barrier to form DME from co-adsorbed species (75 kJ mol^{-1} on $H_3PW_{12}O_{40}$; Table 2.4) is much larger than the barrier to form protonated dimers (< 1 kJ mol^{-1} on $H_3PW_{12}O_{40}$); as a result, co-adsorbed species invariably rearrange to protonated dimers before forming DME. Co-adsorbed species merely represent a small "ledge" along the reaction coordinate that connects protonated dimers to DME formation transition states; these co-adsorbed species avoid the configurational hurdles imposed by inappropriate atomic orientations in protonated dimers. The rapid interconversion of protonated dimers and co-adsorbed species (relative to DME formation rates) cause them to be present at thermodynamic ratios on POM clusters; thus, protonated dimers are much more abundant than co-adsorbed species (by ~10^8 at 433 K) because of their greater stability (Table 2.4). These protonated dimers convert via their sequential rearrangement to properly oriented co-adsorbed species and then DME formation transition states; thus, measured activation barriers for the direct route reflect energy differences between these dimers and DME formation transition states.

Direct methyl transfer between two adsorbed CH_3OH molecules proceeds via a transition state (TS3 in Figure 2.3b) that forms DME and H_2O simultaneously (Scheme 2.2, Step 4). This reaction is an S_N2 substitution in which CH_3OH displaces H_2O at the electrophilic carbon in the methyl group. The proton is transferred to the CH_3OH monomer (H_{C1}-O_{C1} = 0.188 nm; H_{C1}-O_{M1} = 0.098 nm; Table 2.3) and the C-O bond is cleaved at the transition state, forming a planar methyl cation located between H_2O and CH_3OH molecules. The methyl C-atom is nearly equidistant between the O-atoms of H_2O (C_{M1}-O_{M1} = 0.193 nm) and CH_3OH (C_{M1}-O_{M2} = 0.201 nm); these two molecules decrease the methyl charge (from +0.90 e to +0.56 e Bader charge) by delocalizing it (+0.18 e and +0.16 e Bader charges on CH_3OH and H_2O, respectively), while the conjugate base (vicinal O-atoms (O_{C2} and O_{C1}) in the POM) stabilizes these positive charges via electrostatic interactions. The methyl C-atom (C_{M1}), the H_2O O-atom (O_{M1}), and the CH_3OH O-atom (O_{M2}) lie along a line at the direct transition state for all central

atoms including $H_6CoW_{12}O_{40}$, in contrast to the sequential transition states. This is because the organic cation is more stable (relative to smaller ones at both of the sequential transition states) and because the linear structures required for S_N2 reactions do not require significant separations of the cation and conjugate anion. The energy of this transition state is -14 kJ mol^{-1} on $H_3PW_{12}O_{40}$, relative to two gas-phase CH_3OH; it increases as acids weaken (Figure 2.5a) because of the increasing energy cost of separating charges to form ion-pairs. The energy of the direct transition state is much lower than for either of the two transition states in the sequential dehydration route (Scheme 2.3; 69 kJ mol^{-1} and 51 kJ mol^{-1} for TS1 and TS2 on $H_3PW_{12}O_{40}$). These differences predominantly reflect ion-dipole interactions between the methyl and an additional O-atom, which significantly stabilize the direct transition state. Blaszkowski and van Santen calculated a direct DME formation transition state energy (15 kJ mol^{-1} relative to the gas-phase reactants) that lies within the range of the POM clusters and also had an energy that was significantly lower than that of the sequential route (140 kJ mol^{-1} relative to the gas-phase reactants) [34]. The activation barrier for direct DME formation (TS3), measured with respect to its protonated dimer precursor, is much higher than the corresponding energy relative to gas-phase CH_3OH (141 kJ mol^{-1} on $H_3PW_{12}O_{40}$; Figure 2.6b) because the formation of protonated dimers (from two gas-phase CH_3OH) is quite exothermic (-155 kJ mol^{-1} on $H_3PW_{12}O_{40}$; Figure 2.4). Catalytic dehydration turnovers are completed by the sequential desorption of H_2O and DME and the re-protonation of the POM cluster (Scheme 2.2, Step 5) and have combined desorption energies of 94 - 103 kJ mol^{-1} (Table 2.4).

Significantly lower energies (relative to gas-phase CH_3OH) for the direct transition state, compared to those for the sequential transition states (Figure 2.5a and Scheme 2.3), and the very exothermic adsorption of two CH_3OH to form protonated dimers (Figure 2.4) indicate the importance of solvating unstable cations in CH_3OH dehydration reactions (Figure 2.5a). These interactions have been examined among gas-phase cations and H_2O, alkanols, amines or pyridines [51,52,53] to probe the solvation of cations in condensed media. The stability of H^+[51,53] increases monotonically, but less than proportionally, as the number of solvating H_2O or CH_3OH molecules increases. The proton affinity of an isolated CH_3OH is -754 kJ mol^{-1}[54], while the proton affinity of two CH_3OH to form a dimer is -890 kJ mol^{-1} (see Supporting Information). These large differences in stability between $[(CH_3OH)_2H]^+$ and $[CH_3OH_2]^+$ cause the former, but not the latter, to exist as protonated species in contact with POM clusters. The stability gained by solvating a proton between two CH_3OH favors protonated dimers over co-adsorbed species. This additional stability favors high coverages of protonated dimers during catalysis and renders co-adsorbed structures as kinetically-irrelevant minority species. Adsorption of a third CH_3OH molecule near protonated dimers creates CH_3OH trimers, which facilitate DME formation without high energy reorientation (calculation details for $H_3PW_{12}O_{40}$ in the Supporting Information), similar to co-adsorbed species, but do not further solvate the protons. Surface concentrations of trimers are negligible at reaction conditions because the incremental stability from a third CH_3OH (-20 kJ mol^{-1} relative to a protonated dimer and gas-phase CH_3OH) does not offset the large entropy penalty involved in the adsorption step. Thus, CH_3OH trimers do not contribute to measured rates, in spite of their lower activation barriers for DME formation.

2.3.4 Relative Contributions of Sequential and Direct Routes in the Dehydration of Methanol to Dimethyl Ether

Next, we examine the rate equations for sequential and direct routes to determine their respective contributions to CH_3OH dehydration rates and to interpret the chemical significance of the kinetic parameters (α and β; Eq. (2.3)) measured from rate data (Figure 2.1a). Their relative contributions are determined from rate and equilibrium constants estimated from DFT-derived energies for intermediates and transition states in sequential (Scheme 2.1) and direct (Scheme 2.2) routes, taken together with statistical mechanics treatments of activation and reaction entropies[55] (details in Supporting Information). Estimates for rate and equilibrium constants are reported here at the temperature used to measure most of the rate data (433 K; Figure 2.8).

The rate equation for the sequential route (Eq. (2.4)) considers only methoxide and monomer species as surface intermediates, but neglects protonated dimers (Scheme 2.2). The effective stabilization of dimer structures caused by electrostatic interactions (Section 2.3.3.3), however, leads to a significant presence of these species during CH_3OH dehydration catalysis. These protonated dimers are in quasi-equilibrium with monomers (and a gas-phase CH_3OH molecule) because of rapid CH_3OH adsorption-desorption steps; equilibrium constant estimates for dimer formation (4×10^3 kPa^{-1} to 1×10^6 kPa^{-1} at 433 K for all Keggin compositions) indicate that dimers are present at substantial concentrations over all CH_3OH pressures. Thus, contributions from protonated dimers must be included in the site balance of the sequential rate expression, as we describe next.

CH_3OH dehydration rates via sequential pathways, including contributions from protonated dimers, are given by (derivation in Supporting Information):

$$\frac{r_s}{[H^+]} = \frac{k_{DME,s} K_P (CH_3OH)}{1 + \frac{k_{DME,s}}{k_{elim}} K_P (CH_3OH) + \frac{k_{DME,s}}{k_{elim}} K_P K_D (CH_3OH)^2} \quad (2.7)$$

in which rate and equilibrium constants are defined for the elementary steps in Schemes 2.1 and 2.2. Significant dimer coverages (reflected in the magnitude of the third term in the denominator of Eq. (2.7) relative to the others) would cause a negative rate dependence at high CH_3OH pressures, as found at lower temperatures (343-373 K) in 2-butanol dehydration reactions, for which the kinetically-relevant step is also the elimination of H_2O from monomers that compete for protons with unreactive dimers.[2,48] At pressures up to 20 kPa, CH_3OH dehydration rates did not decrease with increasing CH_3OH pressure, an observation that seems inconsistent with Eq. (2.7), given the large equilibrium constants for dimer formation (K_D). We consider this indirect evidence for the lack of involvement of sequential routes in CH_3OH dehydration catalysis, a conclusion confirmed by detailed comparisons of theory and experiment discussed below.

Next, we discuss the contributions of direct and sequential pathways in the context of ratios of their rates using estimates for their respective kinetic and

thermodynamic constants (derivations and calculations in Supporting Information). Rate ratios for the sequential (r_s) and direct (r_d) routes are given by:

$$\frac{r_s}{r_d} = \frac{k_{elim}}{k_{DME,d}K_C K_D(CH_3OH)} \quad (2.8)$$

in which all terms correspond to the elementary steps in Schemes 2.1 and 2.2. The rate constant for H_2O elimination from monomers (k_{elim} in Eq. (2.8) and Scheme 2.1) reflects the difference in free energy between the sequential H_2O elimination transition state (TS1 in Figure 2.3a) and the adsorbed CH_3OH monomer (A in Figure 2.3a). The product $k_{DME,S}K_CK_D$ in the denominator of Eq. (2.8) reflects the difference in free energy between the DME formation transition state in the direct route (TS3 in Figure 2.3b) and the free energy of an adsorbed CH_3OH monomer and a gas-phase CH_3OH. The ratio of the rate constants in Eq. (2.8) merely reflects the free energy difference between the two relevant transition states (TS1 and TS3 in Figure 2.3). These rate ratios range from 6.6 x 10^{-6} to 4.1 x 10^{-4} on all POM clusters at 433 K and 0.01 kPa CH_3OH (Figure 2.7), which are the most favorable conditions for sequential routes. Direct routes are favored even more at the higher CH_3OH pressures required for practical turnover rates (e.g. > 0.5 kPa CH_3OH needed to reach the highest rates; Figure 2.1a). Rate ratio predictions indicate that temperatures well above 700 K are required for detectable contributions from sequential routes, at which point CH_3OH dehydration equilibrium renders the dynamics of this reaction irrelevant and CH_3OH-DME homologation reactions would prevail. As a result, we conclude that CH_3OH dehydration proceeds exclusively via direct routes at all conditions used on Keggin clusters.

Free energy differences between the transition states for H_2O elimination and direct DME formation determine the relative contributions of direct and sequential routes on the various POM clusters. Activation entropies and the "molecularity" of a given transition state are similar on all POM clusters because of their similar structures[9]; thus, free energy differences reflect the corresponding differences in transition state energies among these catalysts. This is consistent with the results in Figure 2.7, where differences in activation barriers of H_2O elimination and direct DME formation (referred in both instances to an adsorbed monomer and a gas-phase CH_3OH molecule) show the opposite dependence on DPE as the ratios of rates via the sequential and direct routes. Activation barriers for the sequential route are 77 - 92 kJ mol^{-1} larger than for the direct route on these POM clusters (Figure 2.7) and this energetic preference of the direct route reflects the stabilization of the methyl cation at its transition state by both H_2O and CH_3OH (Figures 2.3b and Scheme 2.3). The effect of DPE on the differences in activation barriers between the two routes is small (15 kJ mol^{-1} for these clusters; Figure 2.7), however, it causes significant changes in rate ratios as a result of the exponential effects of activation barriers. We do not anticipate that rate ratios will increase above 4 x 10^{-4} (shown for $H_5AlW_{12}O_{40}$ in Figure 2.7) in the DPE range available in solid acids (1087 kJ mol^{-1} for $H_3PW_{12}O_{40}$ to 1200 kJ mol^{-1} for zeolites[3]). Contributions from the sequential route become smaller for acids stronger than $H_5AlW_{12}O_{40}$ because charges in the direct transition state (+0.91 e Bader charge at TS3) are larger and more delocalized than for the sequential H_2O elimination transition state (+0.76 e Bader charge at TS1); as a result,

transition state energies for the direct route (TS3) decrease with increasing acid strength more than for the sequential H_2O elimination counterpart (Figure 2.5a). The expected contributions from sequential pathways also decrease for acids weaker than $H_5AlW_{12}O_{40}$ because their earlier H_2O elimination transition states (shown in Figure 2.6 for $H_6CoW_{12}O_{40}$; Section 2.3.3.2) lead to activation barriers larger than expected based on the effects of DPE found on the other POM compositions (Figure 2.5b).

We also anticipate that DME formation by direct routes will be favored to an even greater extent on zeolites than on POM clusters because of the preferential stabilization of the direct transition states via van der Waals forces within the constrained environments provided by zeolites. Van der Waals forces preferentially stabilize direct DME formation transition states over sequential H_2O elimination transition states because of the larger number of van der Waal contacts introduced by the additional CH_3OH molecule at direct transition states. When spatial constraints favor the smaller transition state in the sequential route (e.g. small-pore zeolites), they do so by inhibition of the facile direct reactions, making these materials much less reactive in CH_3OH dehydration catalysis. Thus, we conclude that the direct route dominates CH_3OH dehydration over the entire range of acid strengths and reaction conditions relevant to solid acids.

For CH_3OH dehydration by the direct route, the chemical origins of measured kinetic parameters (α and β in Eq. (2.3)) can be interpreted by comparison to the rate equation for these elementary steps (Eq. (2.5); Scheme 2.2). The apparent first-order rate constant measured at low CH_3OH pressures (i.e., $\alpha \equiv k_{mono}$) reflects the free energy change between the DME transition state (TS 3 in Figure 2.3b) and a monomer and a gas-phase CH_3OH molecule:

$$k_{mono} = k_{DME,D} K_C K_D = e^{-(\Delta G^* - \Delta G_{monomer} - \Delta G_{MeOH})/RT} \quad (2.9)$$

At high CH_3OH pressures, measured zero-order rate constants (i.e. $\alpha/\beta \equiv k_{dimer}$) reflect the free energy required to form the DME transition state from protonated dimers:

$$k_{dimer} = k_{DME,D} K_C = e^{-(\Delta G^* - \Delta G_{dimer})/RT} \quad (2.10)$$

Estimated values of k_{mono} and k_{dimer} calculated from DFT energies and transition state theory are 50 $(kPa\ s)^{-1}$ and 1 x 10^{-4} s^{-1} on $H_3PW_{12}O_{40}$ at 433 K (calculations included in the Supporting Information). These values are in reasonable agreement with measured apparent rate constants (k_{mono} =0.62 $(kPa\ s)^{-1}$ and k_{dimer} = 4.5x10^{-2} s^{-1}), especially in view of the approximate nature of the theoretical treatments. Theoretical and measured rate constants are also in reasonable agreement for other Keggin clusters; on $H_6CoW_{12}O_{40}$, the weakest acid, measured k_{mono} and k_{dimer} values are 4.7 x 10^{-3} $(kPa\ s)^{-1}$ and 4.7 x 10^{-3} s^{-1} (433 K) and estimated values are 1 $(kPa\ s)^{-1}$ and 3 x 10^{-4} s^{-1}. We confirm with these comparisons that CH_3OH dehydration proceeds via direct routes on POM clusters at temperatures and pressures relevant for its catalytic practice.

2.3.5 Effects of Composition and Deprotonation Energies on Methanol Dehydration Turnover Rates on Solid Acids

Measured rates, accurately described by Eq. (2.3), taken together with theoretical treatments of the direct and sequential dehydration routes (Sections 2.3.3 and 2.3.4) indicate that the direct route is responsible for the formation of DME on POM clusters. As a result, measured first-order (k_{mono}) and zero-order (k_{dimer}) rate constants reflect the free energy of the transition state for these direct pathways (TS3) relative to CH_3OH monomers (A in Figure 2.3a) and protonated dimers (D and E in Figure 2.3b), respectively.

Figure 2.8 shows measured k_{mono} and k_{dimer} values at 433 K (obtained by regressing data to the form of Eq. (2.3)) as a function of DPE estimates for Keggin POM clusters with P, Si, Al, and Co central atoms and zeolite H-BEA. Both rate constants decreased exponentially with increasing DPE (decreasing acid strength) for Keggin POM clusters, as was also found for the rate constants involved in alkanol elimination and alkene isomerization.[9,48] These exponential effects are consistent with the predominant effects of DPE on the energies (instead of the entropies) of intermediates and transition states, whose molecular structures remain similar for all POM clusters. When DPE predominantly influences activation energies, these sensitivities of rate constants can be expressed in terms of the corresponding effects of DPE on measured activation energies [9]:

$$\frac{d(\ln k)}{d(DPE)} = -\frac{1}{RT}\frac{d(E_a)}{d(DPE)} \tag{2.11}$$

The effects of DPE on k_{mono} and k_{dimer} (Figure 2.8) indicate that apparent activation energies increase as acids weaken (DPE increases). The sensitivity of k_{mono} to DPE (-0.093 slope, Figure 2.8, 433 K) is greater than for k_{dimer} (-0.028 slope) and indicates that activation energies for the term k_{mono} are more sensitive to acid strength than for the term k_{dimer}. On H-BEA, k_{dimer} lies along the trend defined by the POM clusters, but k_{mono} is ~100 times larger. This discrepancy in k_{mono} reflects van der Waals contributions, relevant only to k_{mono} because they affect the transition state and adsorbed CH_3OH monomers to different extents, as discussed later in this section.

These trends are consistent with thermochemical cycles that use convenient hypothetical paths to a given transition state structure by exploiting the path independence of free energies, as used previously to describe adsorption in zeolites [56] and the effects of DPE and acid strength in acid catalysis. [9,48,49] In this context, activation energies for steps involving late ion-pair transition states (E_a) depend on the DPE of the acid, the proton affinity of gas-phase reactants (ΔE_{prot}), the interaction energy between the transition state and conjugate base (E_{int}), and the adsorption energy of reactants (ΔE_{ads}, relative to their gas-phase analogs) involved in the formation of the transition state (e.g., CH_3OH monomer for k_{mono}; protonated dimer for k_{dimer}):

$$E_a = DPE + \Delta E_{prot} + E_{int} - \Delta E_{ads} \tag{2.12}$$

The thermochemical cycles for k_{mono} and k_{dimer} (Scheme 2.4) relate the DME formation transition state (TS3) to the monomer and protonated dimer, respectively. ΔE_{prot} is the energy required to add a free proton to two gas-phase CH_3OH molecules to form the gas-phase analog of the transition state (Scheme 2.3). The unstable character of free protons makes these reactions very exothermic, but these energies can be estimated from experiment or DFT calculations.[51,52,54] The protonation of two CH_3OH molecules to form a methyl cation located between the O-atoms in H_2O and CH_3OH (TS3 in Figure 2.3b) gives a ΔE_{prot} value (-693 kJ mol^{-1}) which is much more negative than for the formation of the interacting methyl and H_2O species (-558 kJ mol^{-1}) involved in H_2O elimination to form methoxides (TS1 in Figure 2.3a) or for the interacting methyl and CH_3OH species (-617 kJ mol^{-1}) involved in DME formation via methoxide/CH_3OH pairs in the sequential DME formation route (TS2 in Figure 2.3a) (details of gas-phase calculations are reported in Supporting Information).[46,51] Solvation of methyl cations by concerted dipole-ion interactions with H_2O and CH_3OH (-210 kJ mol^{-1}) significantly stabilize the transition state for the direct route relative to either of the two transition states in the sequential route (Scheme 2.3), which are solvated by one molecule, and favor the direct route as the preferred CH_3OH dehydration pathway.

For full ion-pairs at late transition states, E_{int} predominantly reflects electrostatic interactions[48], but also includes van der Waals forces, whose contributions become significant within constrained spaces, such as those in zeolite micropores, and H-bonding between molecules and framework O-atoms. Activation energies measured with respect to the intermediate directly preceding the transition state along the reaction coordinate, such as the case for k_{dimer}, are typically insensitive to van der Waals and H-bonding interactions, because their respective contributions to E_{int} and ΔE_{ads} tend to cancel out. In such instances, the difference in electrostatic stabilization between the adsorbed intermediate (ΔE_{ads}) and transition state (E_{int}) is the strongest determinant of the dependence of activation energies on DPE. Van der Waals and H-bonding interactions influence activation energies only when intermediates and transitions states are solvated to different extents, as shown later for k_{mono} on H-BEA zeolites where van der Waals interactions are a natural consequence of confinement.

The effects of DPE on E_a reflect the individual sensitivities of each of the terms included in the thermochemical cycle for a given activation energy (Eq. (2.12)):

$$\frac{d(E_a)}{d(DPE)} = 1 + \frac{d(E_{int})}{d(DPE)} - \frac{d(\Delta E_{ads})}{d(DPE)} \tag{2.13}$$

The term corresponding to $d(\Delta E_{prot})/d(DPE)$ has been removed from Eq. (2.13) because ΔE_{prot} depends only on the properties of gaseous molecules. The measured values of k_{mono} and k_{dimer} (Figure 2.8) together with Eq. (2.11) give $d(E_a)/d(DPE)$ values of 0.34 and 0.10, respectively, for these two rate parameters (Table 2.5). Both $d(E_a)/d(DPE)$ values are much smaller than unity, as in the case of alkanol dehydration (0.15) and alkene isomerization (0.32) on POM and H-zeolite catalysts.[9],[48] These small values primarily reflect the stabilization of cationic transition states by the conjugate base ($E_{int} < 0$), which becomes stronger (more negative) as acids weaken ($d(E_{int})/d(DPE) < 0$) and attenuate the effects of DPE on activation energies. Electrostatic stabilization at the

transition state does not fully recover the energy required to overcome electrostatic interactions during the removal of the proton.[9] Protons are the smallest and one of the hardest Lewis acids[57] and consequently, have the strongest electrostatic interactions with anions; thus, $d(E_{int})/d(DPE)$ values lie between 0 and -1 and approach the latter values for small and highly-charged cations at transition states. Smaller cations, with shorter interaction distances and a more concentrated positive charge, recover a larger fraction of the DPE as ion-pairs and weaken the effects of acid strength on activation energies compared with larger cations with more diffuse positive charges.

The effects of DPE on transition state stabilization can be discerned from their DFT-derived energies (relative to two gas-phase CH_3OH molecules and a non-interacting POM cluster) on POM clusters with different central atoms (except for the "bent" sequential transition states found on $H_6CoW_{12}O_{40}$ clusters (Figure 2.6)). The energy of the transition state for direct DME formation (TS3 in Figure 2.3b) increases almost linearly with increasing DPE (Figure 2.5a; 0.39 slope), indicating that stronger acids favor the formation of more stable ion-pairs. As expected from Eq. (2.13), this slope is smaller than unity because electrostatic stabilization of protons (reflected in DPE values) and transition states (reflected in E_{int} values) both increase as acids weaken. Thus, the effects of composition on DPE are compensated by those for E_{int} and energies of transition states are attenuated to DPE. The combined Bader charges on the methyl and on the nearby stabilizing molecules for TS1 (+0.59 e and +0.20 e for the methyl and H_2O) and TS2 (+0.57 e and +0.19 e for the methyl and CH_3OH) are smaller than for TS3 (+0.56 e, +0.17 e, and +0.18 e for the methyl, H_2O, and CH_3OH); they are also less diffuse because the positive charge is delocalized over one fewer molecule the transition state. Thus, transition state energies (relative to two gas-phase CH_3OH) for the sequential H_2O elimination (TS1) and DME formation (TS2) have slopes (0.23 and 0.25, respectively), which are smaller than that for the direct route (0.39) (Figure 2.5a). Activation barriers calculated for sequential and direct routes on aluminosilicate clusters also depended weakly on acid strength [34] as a result of electrostatic interactions at the transition state that compensate for the DPE of the acid.

Next, we consider the effects of adsorption energies (Figure 2.4) in determining DPE effects on activation barriers (Figure 2.5b), which measure transition state energies (Figure 2.5a) relative to reaction intermediates that precede it along the reaction coordinate. Activation barriers for H_2O elimination from adsorbed monomers are much less sensitive to DPE (0.03 slope; Table 2.5) than those for DME formation from methoxide/CH_3OH pairs (0.42 slope; Table 2.5) in the sequential route (Figure 2.5b), even thought their slopes are similar when transition state energies are measured with respect to two gas-phase CH_3OH molecules (Figure 2.5a). These differences in slopes reflect the opposite effects of DPE on monomer and methoxide formation energies (Figure 2.4); adsorbed monomers become less stable (0.16 slope) while methoxide/CH_3OH pairs become more stable (-0.12 slope) with increasing DPE.

The rate equation for the prevailing direct route (Section 2.3.4) shows that the steps responsible for measured k_{mono} and k_{dimer} values (Figure 2.8) share the same DME formation transition state (TS3). Their respective activation energies, however, show different sensitivities to DPE (0.34 and 0.10 slopes, respectively) because of the contrasting effects of DPE on their respective adsorbed intermediates (monomers and

protonated dimers for k_{mono} and k_{dimer}, respectively). Calculated adsorption energies (relative to gas-phase CH_3OH) for monomers (A in Figure 2.3a) and protonated dimers (D and E in Figure 2.3b) become less negative with increasing DPE (Figure 2.4). These DPE effects are stronger for protonated dimers than monomers (slopes of 0.44 and 0.13, respectively) because monomers are less charged than dimers. The O_{C1}-H_{C1} bond distance (0.108 nm) and the Bader charge on the CH_3OH (+0.08 e) in the monomer are only slightly larger than those in non-interacting clusters (O_{C1}-H_{C1} = 0.098 nm) and CH_3OH (+0.00 e Bader charge), indicating that charge separation is not detectable upon forming the monomer, consistent with the weak effects of DPE on monomer formation energies (Figure 2.4). Protonated dimers involve significant proton transfer (O_{C1}-H_{C1} = 0.139 – 0.158 nm), a substantial positive charge (+0.88 to +0.84 e Bader charge), and strong stabilization by the conjugate anion. As a result, dimers become less stable with the conjugate anion as DPE increases (Figure 2.4).

DFT-derived activation barriers for DME formation (TS3) from adsorbed monomers (and a gas-phase CH_3OH molecule) and protonated dimers (Figure 2.5b) correspond to measured activation energies for k_{mono} and k_{dimer}, respectively. The slope of the activation barriers (Table 2.5) for k_{mono} is larger (0.22) than that for k_{dimer} (-0.05) (Figure 2.5b) and shows DPE effects on the stability of the ion-pairs at the transition state are largely offset by the effects of DPE on the stability of charged protonated dimers, but not uncharged monomers. Slopes for measured k_{mono} and k_{dimer} values (Figure 2.8 and Table 2.5; 0.34 and 0.10, respectively) are both higher than predicted by DFT estimates, but the trends confirm that k_{dimer} values are less sensitive to DPE than k_{mono}, in spite of their common transition state, because of the different charges and DPE sensitivities for monomers and protonated dimers. The differences in slopes between measurements and theoretical estimates of activation barriers may reflect the effects of monomers and dimers that are adsorbed on the same POM during catalysis, but not in DFT calculations. The numbers of these co-adsorbed intermediates increases with the proton density of POM clusters and may cause systematic effects with composition that may be misinterpreted as consequences of concomitant changes in DPE with the valence of the central atom and the number of protons per cluster.

The activation energies for k_{mono} depend on DPE more strongly (0.34 slope; Figure 2.8) than those for butanol dehydration rate constants (0.15 slope for both 2-butanol and 1-butanol)[9], for which elimination of H_2O from H-bonded butanols is the kinetically-relevant step and activation energies reflect the energy of late ion-pair transition states relative to adsorbed butanol. The calculated adsorption energies for 2-butanol on POM clusters (X = S, P, Si, Al) show the same sensitivity to DPE ($d(\Delta E_{ads,C4H9OH})/d(DPE)$ = 0.13)[49] as CH_3OH (0.13; Figure 2.4); thus, the weaker effects of DPE on butanol activation energies (compared with those for CH_3OH) must reflect the more effective stabilization of their transition state by POM conjugate anion (Eq. (2.13)). A charge analysis of the 2-butanol dehydration transition state shows a similar, but more localized charge than for the transition state in the direct CH_3OH dehydration route. For butanol, the charge resides entirely on the butyl cation (+0.85 e) without detectable delocalization onto the H_2O molecule (+0.03 e).[49] In contrast, the charge is delocalized over the methyl, H_2O, and CH_3OH moieties (+0.56 e, +0.17 e, and +0.18 e, respectively) in the CH_3OH dehydration transition state; the strong coordination

of methyl cations to H_2O and CH_3OH in CH_3OH dehydration delocalizes the charge at the transition state. The electrostatic stabilization of CH_3OH dehydration transition states by Keggin anions is less effective than for butanol dehydration transition states, thus, the formation of the ion-pair recovers a smaller fraction of the deprotonation energy and k_{mono} is more sensitive to DPE than the corresponding rate constant for butanol dehydration. Similar arguments account for the stronger sensitivity to DPE for transition state energies in the direct route (relative to gas-phase CH_3OH) compared with the two transition states involved in the sequential dehydration pathways (Figure 2.5a).

Next, we consider the chemical significance of the value of k_{mono} measured on BEA, which lies well above the trend defined by the corresponding k_{mono} values on POM clusters, and of its k_{dimer} value, which in contrast with k_{mono}, lies along the trend defined by the POM clusters (Figure 2.8). Brønsted acid sites in zeolites reside within channels of molecular dimensions; these small channels stabilize adsorbed species, such as monomers and protonated dimers, and transition states via van der Waals contacts much more effectively than at surfaces of POM clusters. These van der Waals forces influence activation barriers via their ability to stabilize transition states (E_{int} in Eq. (2.12)) and their precursor reactants (ΔE_{ads} in Eq. (2.12)) to different extents. The DME transition state and its protonated dimer precursor each contain two CH_3OH molecules; as a result, van der Waals forces stabilize both to a similar extent, leading to activation barriers for k_{dimer} that do not sense the confined spaces responsible for van der Waals interactions. Therefore, the values of k_{dimer} on Keggin POM and H-BEA catalysts depend only on acid strength and are not affected by confinement in zeolite channels. In contrast, activation barriers of k_{mono} are influenced by the strength of van der Waals forces because the gas-phase CH_3OH not present in the monomer becomes stabilized within the zeolite at the transition state. The selective van der Waals stabilization of the transition state for k_{mono} leads to a smaller barrier on H-BEA than predicted by the effects of DPE for POM clusters (and to k_{mono} values about 100 larger than expected in Figure 2.8). Calculated corrections for dispersive interactions stabilize CH_3OH adsorbed at a zeolite proton in H-ZSM-5 by 29 kJ mol^{-1}.[58] These interactions would increase rate constant estimates by ~4000-fold (at 433 K) and more than fully account for the observed deviation between the k_{mono} value on BEA and the trend defined by Keggin clusters. This correction over-predicts the k_{mono} value on BEA (by a factor of 40) because it does not account for the reduction in intermediate and transition state entropies that also arise as a consequence of confinement in zeolite channels. The effects of confinement in zeolites are larger for the transition state than for the monomer because two CH_3OH molecules are present at the active site at the transition state and only one CH_3OH molecule is present in the monomer intermediate (the other CH_3OH reactants is in the gas-phase). As a result, the pre-exponential factor for k_{mono} on BEA is lower than on Keggin clusters. Transition states and protonated dimers experience similar extents of confinement because two CH_3OH molecules are at the active site in each. These effects cancel in the pre-exponential factor of k_{dimer} so that it is the same on BEA and Keggin POM.

These data and theoretical treatments suggest that CH_3OH dehydration turnover rates can be used to assess the acid strength of solids acids of unknown structures, for which reliable DPE estimates are inaccessible, as we have shown previously for more complex alkene isomerization and dehydration of larger alkanols.[59] The k_{dimer} values

measured on acids with unknown structure can be compared to the reactivity-DPE relation shown in Figure 2.8 for acids of known structure to estimate DPE values for these solids within reaction environments. Similar assessments using measured values of k_{mono} can be applied, at least for materials lacking constrained environments of molecular dimensions, for which van der Waals effects influence the value of k_{mono}. The different effects of van der Waals forces on k_{mono} and k_{dimer} provide a powerful indicator of the extent to which confinement effects influence measured turnover rates. For instance, when measured k_{mono} values are larger than expected for the DPE values measured from k_{dimer} values on a given solid acid, we conclude that confinement effects significantly influence the reactivity of that solid acid, independently of its specific acid strength.

2.4. Conclusions

The effects of acid identity on CH_3OH dehydration rates are examined using theoretical assessments of acid strength (as deprotonation energies, DPE) and reaction paths, combined with rate constants measured on Keggin polyoxometalate (POM) clusters of varying central atom identity (P, Si, Al, Co) and zeolite H-BEA. Apparent first-order (k_{mono}) and zero-order (k_{dimer}) rate constants, measured from kinetic experiments and titrations of accessible protons, decrease exponentially with increasing DPE on these well-defined Brønsted acids, but with k_{mono} values depending more strongly on DPE than k_{dimer} values. These observations are consistent with the predominant effects of DPE on activation energies found in previous investigations of 2-butanol dehydration and n-hexene isomerization reactions. Measured rates alone are unable to ascertain the chemical significance of these rate constants and their dependences on acid strength because rate expressions based on elementary steps associated with competing direct and sequential dehydration routes both agree with rate dependences. Calculations of structures, energies, and charges of intermediates and transition states involved in these routes by density functional theory (DFT) indicate the ubiquitous involvement of ion-pairs in these and other acid-catalyzed reaction pathways. The stabilities of these ion-pairs depend on DPE sensitively because charge separation required for their formation reflect the stability of the anionic conjugate base formed during deprotonation. Mechanism-based rate expressions for direct and sequential routes and estimates of their rate and equilibrium constants from statistical treatments of entropy and DFT-derived energies indicate that CH_3OH dehydration proceeds exclusively via direct reactions of co-adsorbed CH_3OH, instead of by sequential methoxide formation and reaction with CH_3OH, for all relevant solid acids and reaction conditions. All ion-pair transition states in these paths feature unstable methyl cations interacting with the anionic conjugate base via electrostatic interactions, however, H_2O and CH_3OH molecules at direct transition states solvate methyl cations more effectively than at sequential transition states and lead to the dominant role of direct routes in CH_3OH dehydration.

Measured dependences of k_{mono} and k_{dimer} on DPE indicate their activation barriers change less than commensurate changes in DPE values in agreement with the weak dependence of all calculated transition state energies (measured relative to gas-phase CH_3OH) on DPE. These effects reflect electrostatic interactions at the transition state that partially recover the energy needed to separate the proton from the conjugate

anion during deprotonation and as a result, compensate DPE. Interpretations of k_{mono} and k_{dimer} as chemical events in the direct route and thermochemical descriptions of their respective activation barriers indicate that both rate constants reflect the DME formation transition state and only differ in the identity of the reacting intermediate; k_{mono} and k_{dimer} measure this transition state from uncharged monomers and protonated dimers, respectively. Similar ion-pairs and charge distributions in protonated dimers and the transition state attenuate the effects of DPE on k_{dimer}, while the weak effects of DPE on uncharged monomers leave k_{mono} more sensitive to DPE. These results are consistent with calculated energies and charges of monomers and protonated dimers and their effects on calculated activation barriers for k_{mono} and k_{dimer}. The value of k_{dimer} on BEA agrees with Keggin predictions because confinement in zeolite channels affects protonated dimers and transition states equally, however, the selective stabilization of the transition state over monomers increases k_{mono} on BEA above the trend on Keggin clusters. This study and its analysis indicates the importance of interpreting rates by mechanism-based rate expressions, whose rate and equilibrium constants reflect the properties of their involved reacting intermediates and transition states and the dependence of these constants to acid strength can be interpreted from the changes in charge distributions among them.

2.5. Tables, Figures, and Schemes

2.5.1 Tables

Table 2.1. Number of accessible protons per POM cluster or framework Al measured by chemical titration with 2,6-di-*tert*-butylpyridine[a] during CH_3OH dehydration[b] on SiO_2-supported POM clusters and H-BEA zeolite.

Catalyst	***POM Content (% wt)***	***POM Surface Density (nm^{-2})***	***Accessible H^+ (per POM or framework Al)***
$H_3PW_{12}O_{40}$	5	0.04	2.0
$H_4SiW_{12}O_{40}$	5	0.04	3.0
$H_5AlW_{12}O_{40}$	5	0.04	2.3
$H_6CoW_{12}O_{40}$	5	0.04	2.3
H-BEA[c]	- - -	- - -	0.55

[a] assuming a 1:1 titrant:H^+ stoichiometry
[b] 0.3 kPa MeOH, 433 K
[c] Value listed per framework Al

Table 2.2. Atomic distances (listed in nm) and Bader charges (listed as electron charges) of intermediates and transition states in the sequential route for CH_3OH dehydration (Scheme 2.1).

	Central Atom				
Species[a]	**S**	**P**	**Si**	**Al**	**Co**
Bare Cluster					
H_{C1}-O_{C1}	0.098	0.097	0.097	0.097	0.097
Monomer (A)					
H_{C1}-O_{C1}	0.108	0.107	0.107	0.108	0.104
H_{C1}-O_{M1}	0.141	0.140	0.140	0.139	0.149
C_{M1}-O_{M1}	0.146	0.146	0.146	0.146	0.145
C_{M1}-O_{C2}	0.324	0.333	0.326	0.337	0.350
H_{C1} Bader Charge	0.730	0.730	0.644	0.662	0.750
CH_3OH Bader Charge	0.000	0.116	0.000	0.084	0.089
H_2O Elimination TS (TS1)					
H_{C1}-O_{C1}	0.404	0.398	0.367	0.371	0.182
H_{C1}-O_{M1}	0.098	0.098	0.098	0.098	0.099
C_{M1}-O_{M1}	0.186	0.184	0.183	0.181	0.253
C_{M1}-O_{C2}	0.207	0.208	0.210	0.213	0.250
Methyl Bader Charge	0.580	0.590	0.590	0.580	0.596
Water Bader Charge	0.190	0.200	0.230	0.210	0.250
Methoxide/CH_3OH Pairs (B)					
H_{M2}-O_{C1}	0.205	0.204	0.201	0.213	0.208
H_{M2}-O_{M2}	0.097	0.098	0.098	0.097	0.097
C_{M1}-O_{M2}	0.317	0.327	0.320	0.327	0.331
C_{M1}-O_{C2}	0.144	0.143	0.143	0.143	0.142
DME Formation TS (TS2)					
H_{M2}-O_{C1}	0.473	0.470	0.482	0.395	0.208
H_{M2}-O_{M2}	0.098	0.098	0.098	0.098	0.099
C_{M1}-O_{M2}	0.193	0.192	0.189	0.189	0.202
C_{M1}-O_{C2}	0.199	0.200	0.201	0.203	0.205
Methyl Bader Charge	0.571	0.570	0.570	0.570	0.560
CH_3OH Bader Charge	0.221	0.190	0.230	0.200	0.200
Adsorbed DME (C)					
C_{M1}-O_{M2}	0.144	0.145	0.144	0.144	0.144
C_{M1}-O_{C2}	0.323	0.323	0.323	0.329	0.324

[a]Atomic and structural labels correspond to diagrams in Figure 2.3a

Table 2.3. Atomic distances (listed in nm) and Bader charges (listed as electron charges) of intermediates and transition states in the direct route for CH_3OH dehydration (Scheme 2.2).

	Central Atom				
Species[a]	**S**	**P**	**Si**	**Al**	**Co**
Protonated Dimer D (D)					
H_{C1}-O_{C1}	0.295	0.284	0.275	0.271	0.267
H_{M1}-O_{C3}	0.162	0.154	0.160	0.157	0.148
H_{M2}-O_{C2}	0.173	0.187	0.179	0.181	0.185
Dimer Bader Charge	0.882	0.875	0.876	0.869	0.856
Protonated Dimer E (E)					
H_{C1}-O_{C1}	0.158	0.148	0.148	0.150	0.139
H_{C1}-O_{M1}	0.103	0.105	0.104	0.104	0.108
H_{M2}-O_{C3}	0.175	0.184	0.177	0.169	0.176
Dimer Bader Charge	0.883	0.871	0.866	0.856	0.838
Co-Adsorbed CH_3OH (F)					
H_{C1}-O_{C1}	0.112	0.110	0.110	0.108	0.105
H_{C1}-O_{M1}	0.132	0.134	0.134	0.139	0.144
C_{M1}-O_{M1}	0.147	0.146	0.146	0.146	0.146
C_{M1}-O_{M2}	0.295	0.326	0.289	0.312	0.327
DME Formation TS (TS3)					
H_{C1}-O_{C1}	0.181	0.188	0.180	0.170	0.171
H_{C1}-O_{M1}	0.100	0.099	0.100	0.101	0.101
C_{M1}-O_{M1}	0.193	0.193	0.192	0.193	0.195
C_{M1}-O_{M2}	0.200	0.201	0.199	0.198	0.198
Methyl Bader Charge	0.561	0.559	0.546	0.541	0.538
Water Bader Charge	0.170	0.181	0.181	0.171	0.168
CH_3OH Bader Charge	0.180	0.169	0.171	0.181	0.178
Adsorbed DME + H_2O (G)					
H_{C1}-O_{C1}	0.219	0.211	0.219	0.212	0.209
H_{C1}-O_{M1}	0.098	0.098	0.098	0.098	0.098
H_{M2}-O_{C2}	0.130	0.125	0.119	0.115	0.110
C_{M1}-O_{M1}	0.305	0.302	0.306	0.319	0.312
C_{M1}-O_{M2}	0.147	0.147	0.146	0.146	0.145

[a]Atomic and structural labels correspond to diagrams in Figure 2.3b

Table 2.4. Energies (in kJ mol^{-1}) of intermediates and transition states relative to non-interacting clusters and two gas-phase CH_3OH in CH_3OH dehydration for sequential (Scheme 2.1) and direct (Scheme 2.2) routes

	POM Central Atom				
Species[a]	**S**	**P**	**Si**	**Al**	**Co**
Bare Cluster	0.0	0.0	0.0	0.0	0.0
Monomer (A)	-72.5	-74.6	-66.4	-63.5	-61.7
Sequential Mechanism					
H_2O Elimination TS (TS1)	66.9	68.8	77.7	76.9	104.6
Methoxide + H_2O_{ads}	-31.2	-36.6	-39.6	-39.4	-41.1
Methoxide	-10.4	-17.1	-19.2	-15.5	-18.1
Methoxide/CH_3OH Pairs (B)	-23.6	-34.5	-35.9	-35.9	-34.3
DME Formation TS (TS2)	49.3	50.9	53.5	63.9	84.3
Adsorbed DME (C)	-85.4	-85.2	-84.9	-81.2	-75.8
Direct Mechanism					
Protonated Dimer D (D)	-155.3	-155.1	-143.6	-134.5	-123.2
Protonated Dimer E (E)	-155.2	-153.9	-147.6	-140.5	-130.6
Co-Adsorbed CH_3OH (F)	-88.5	-88.7	-87.6	-99.5	-82.8
DME Formation TS (TS3)	-17.3	-13.7	-10.2	0.0	12.9
Adsorbed DME + H_2O (G)	-113.1	-105.3	-104.6	-107.3	-91.1

[a] Structural labels correspond to diagrams in Figure 2.3

Table 2.5. Dependences of measured and calculated activation barriers on deprotonation energies ($d(E_a)/d(DPE)$) for Keggin polyoxometalates and zeolite BEA.

Reaction	Measured	Calculated[c]
Sequential H_2O Elimination	- - -	0.03
Sequential DME Formation	- - -	0.42
Direct DME Formation		
from Monomers	0.34[a]	0.22
from Protonated Dimers	0.10[a]	-0.05
Butanol Elimination	0.15[b]	- - -
Alkane Isomerization	0.32[b]	- - -

[a] Values taken from slopes of rate constants (at 433 K) shown in Figure 2.8 and Eq. (2.11).
[b] Values for butanol elimination (at 373 K) and n-hexane isomerization (473 K) taken from ref. [9].
[c] Values taken from slopes shown in Figure 2.5b.

2.5.2. Figures

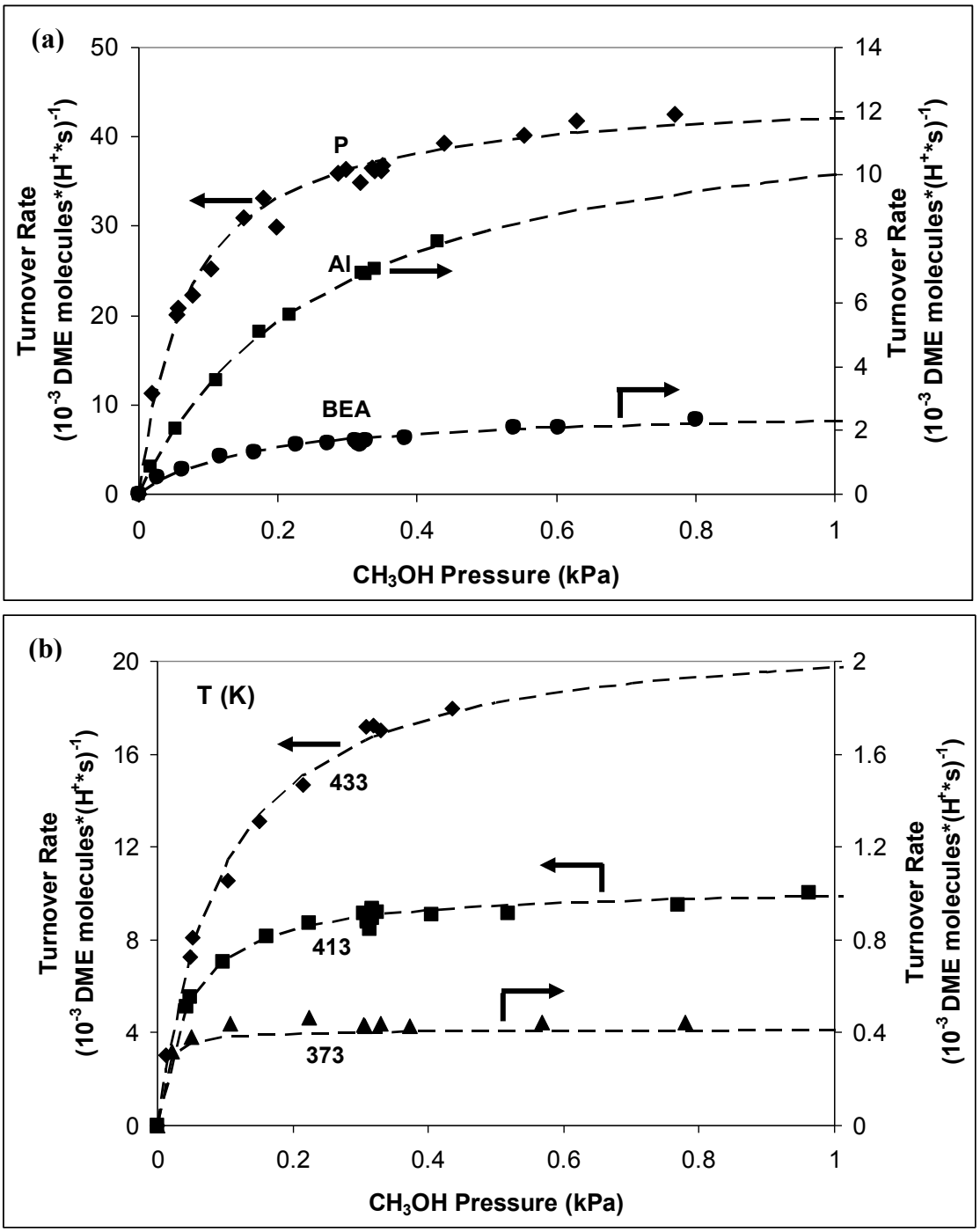

Figure 2.1. (a) DME turnover rates (per accessible proton) as a function of CH_3OH pressure at 433 K on $H_3PW_{12}O_{40}/SiO_2$ (♦), $H_5AlW_{12}O_{40}/SiO_2$ (■), and H-BEA (●). Dashed curves represent the regressed best fits to Eq. (2.3). (b) DME turnover rates (per accessible proton) on $H_4SiW_{12}O_{40}/SiO_2$ as a function of CH_3OH pressure at 373 K (▲), 413 K (■), and 433 K (♦). Dashed curves represent the regressed best fits to Eq. (2.3).

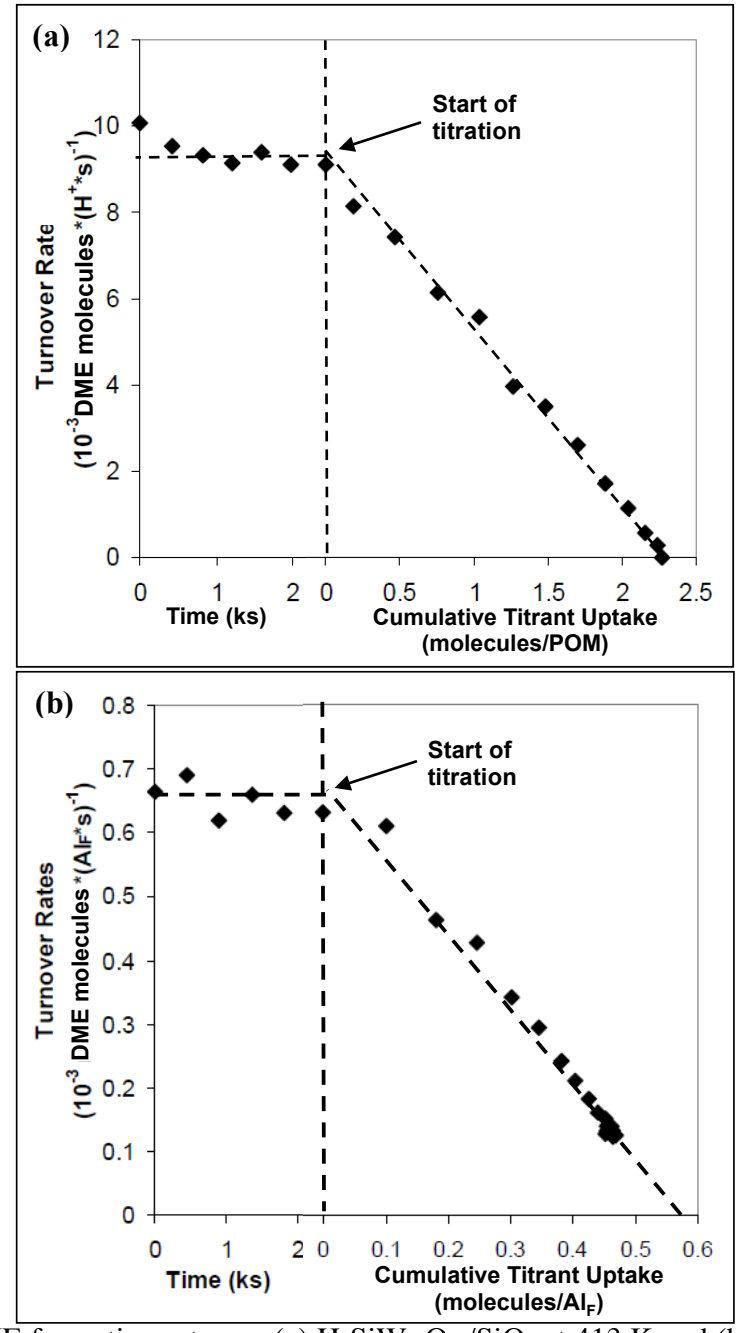

Figure 2.2. DME formation rates on (a) $H_4SiW_{12}O_{40}/SiO_2$ at 413 K and (b) H-BEA at 433 K as a function of time before 2,6-di-*tert*-butylpyridine injection (0.3 kPa CH_3OH) and as a function of cumulative titrant uptake (0.3 kPa CH_3OH, 1.4Pa 2,6-di-*tert*-butylpyridine).

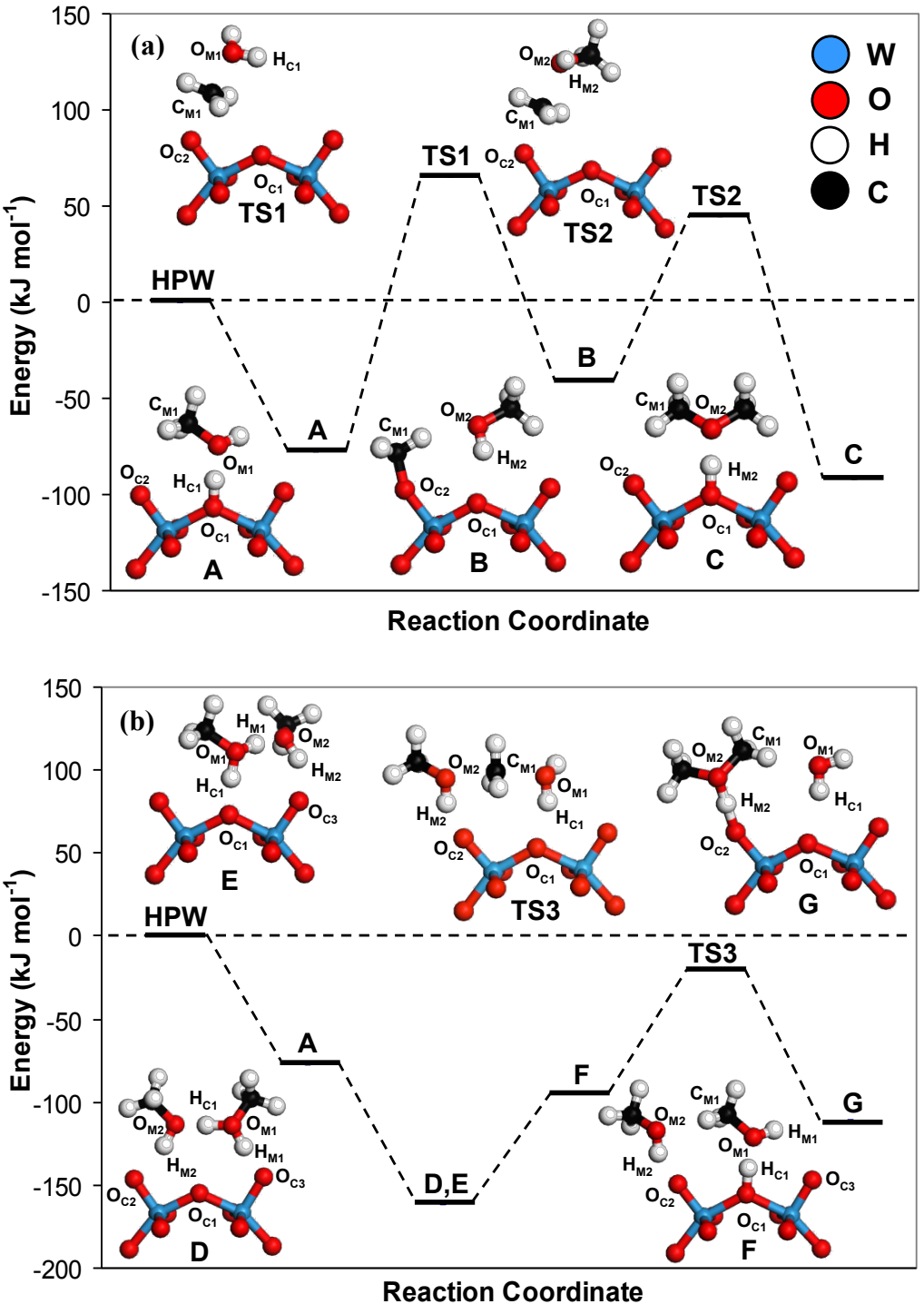

Figure 2.3. Structures and energies of intermediates and transition states calculated for (a) the sequential route and (b) the direct route on $H_3PW_{12}O_{40}$. Atomic labels correspond to those used to report the distances listed in Tables 2.2 and 2.3 for the sequential and direct routes, respectively. Atomic colors correspond to elemental identity (blue = W, red = O, white = H, black = C).

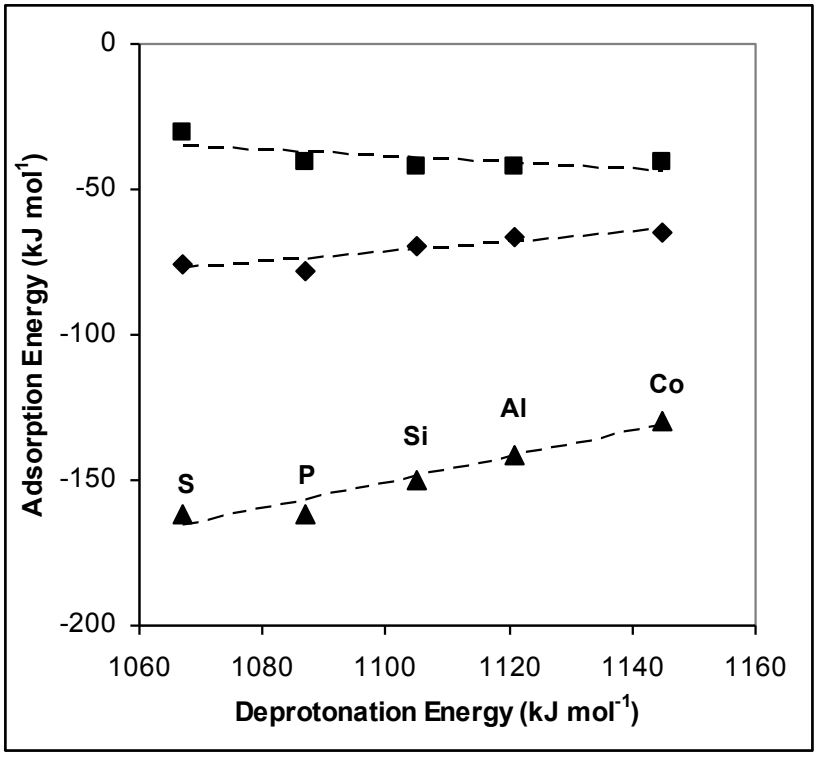

Figure 2.4. Calculated adsorption energies for monomers (A in Figure 2.3a, ♦), methoxide/CH_3OH pairs (B in Figure 2.3a, ■), and protonated dimers (D in Figure 2.3b, ▲) on $H_{8-n}X^{n+}W_{12}O_{40}$ (X = S, P, Si, Al, Co) clusters as a function of deprotonation energies. Adsorption energy values are relative to bare clusters and two gas-phase CH_3OH molecules. Dashed lines are linear best fits of the calculated values.

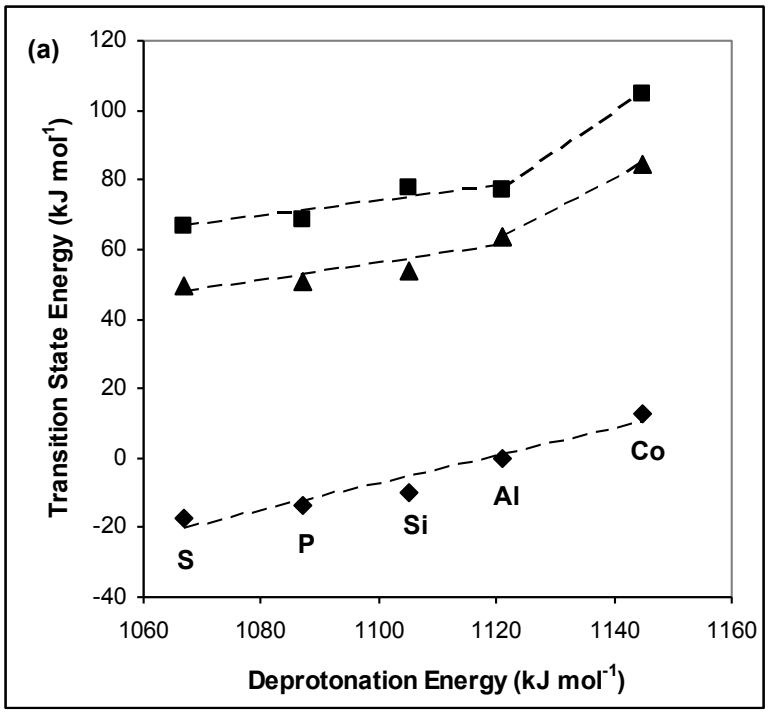

Figure 2.5. (a) Calculated transition state energies relative to two gas-phase CH_3OH for sequential H_2O elimination (TS1 in Figure 2.3a, ■), sequential DME formation (TS2 in Figure 2.3a, ▲), and direct DME formation (TS3 in Figure 2.3b, ♦) on $H_{8-n}X^{n+}W_{12}O_{40}$ (X = S, P, Si, Al, Co) clusters as a function of deprotonation energy. Dashed lines are linear best fits of the calculated values.

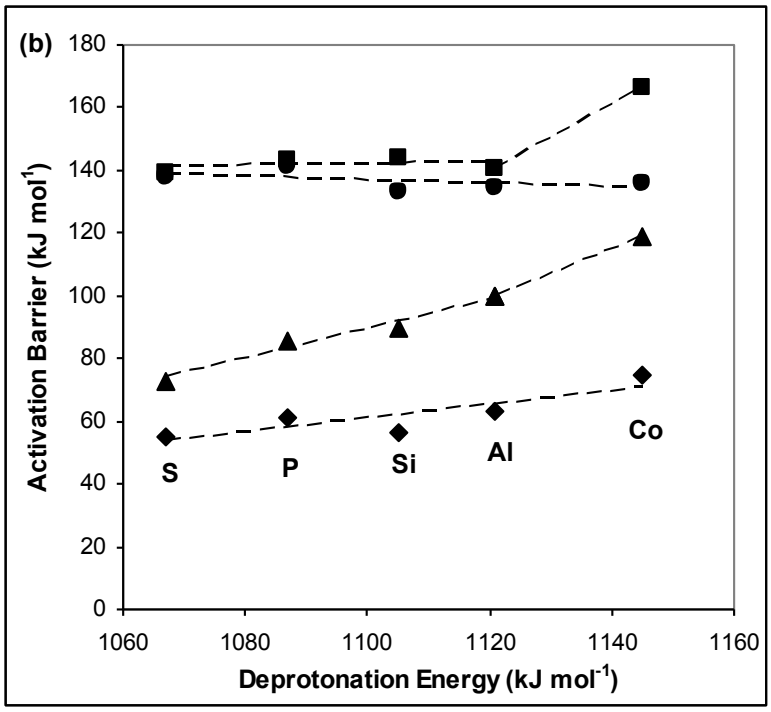

Figure 2.5. (b) Calculated activation barriers for sequential H_2O elimination from monomers (TS1 in Figure 2.3a, ■), sequential DME formation from methoxide/CH_3OH pairs (TS2 in Figure 2.3a, ▲), direct DME formation from monomers and gas-phase CH_3OH (TS3 in Figure 2.3b, ♦), and direct DME formation from protonated dimers (TS3 in Figure 2.3b, ●) on $H_{8-n}X^{n+}W_{12}O_{40}$ (X = S, P, Si, Al, Co) clusters as a function of deprotonation energy. Dashed lines are linear best fits of the calculated values.

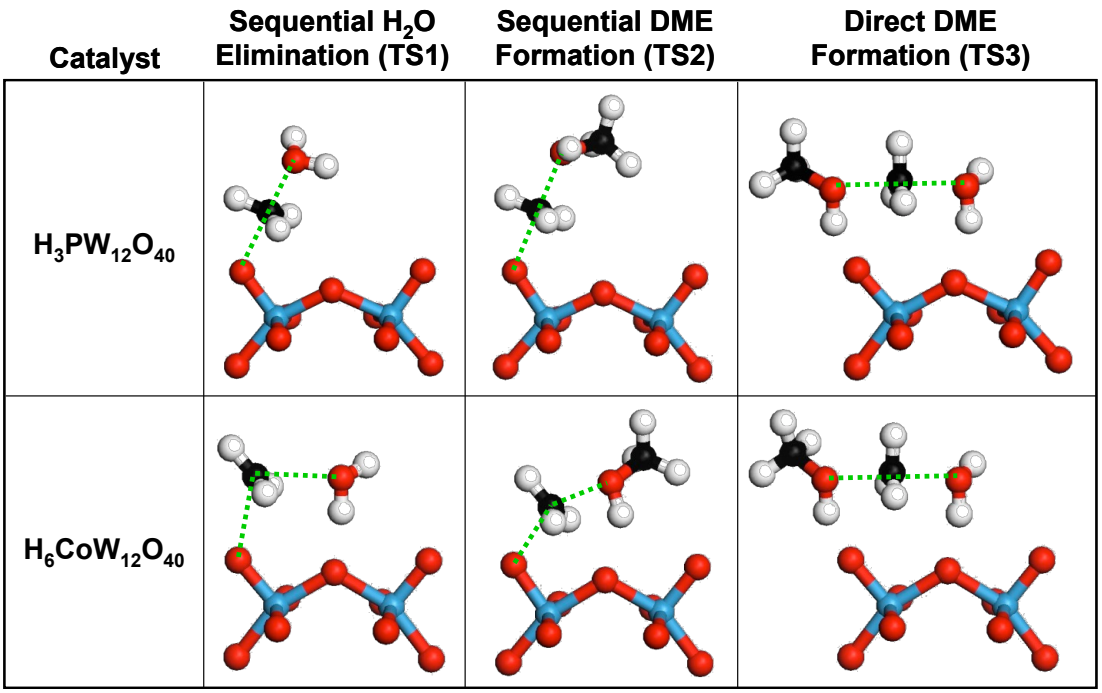

Figure 2.6. Structures of transition states involved in sequential and direct paths of CH_3OH dehydration on $H_3PW_{12}O_{40}$ and $H_6CoW_{12}O_{40}$ clusters. All transition states on $H_3PW_{12}O_{40}$ and the direct DME formation transition state on $H_6CoW_{12}O_{40}$ have methyl cations arranged in linear structures (shown by the dotted lines) appropriate for S_N2 reactions. Transition states for the sequential route on $H_6CoW_{12}O_{40}$ have methyl cations in bent conformations (shown by the dotted lines).

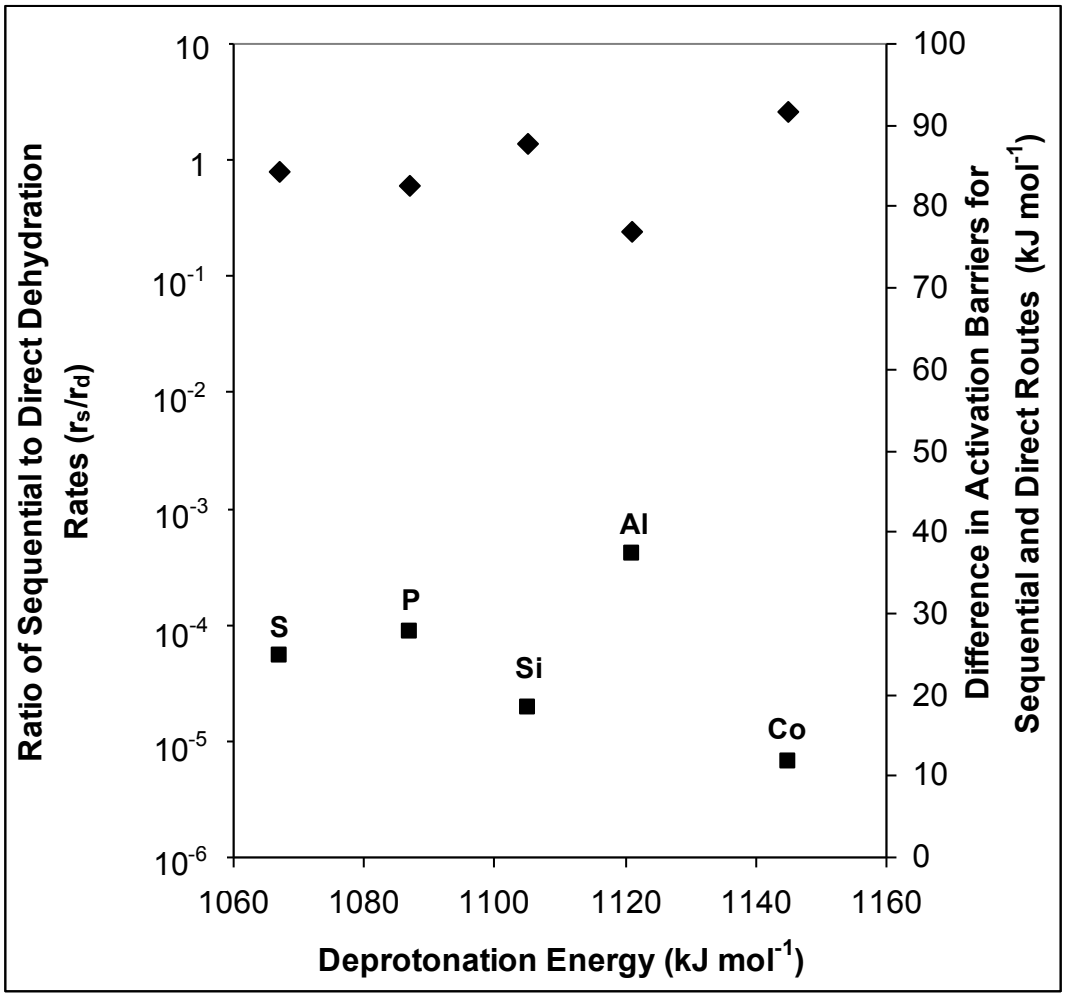

Figure 2.7. Comparisons of sequential and direct route contributions to CH_3OH dehydration as ratios of rates (■) and differences in activation barriers (♦) for Keggin clusters with different central atoms (S, P, Si, Al, Co). Predicted ratios of sequential to direct dehydration rates (0.01 kPa CH_3OH) were calculated from Eq. (2.8), with rate and equilibrium constants estimated from DFT-derived energies of intermediates and transition states and statistical descriptions of entropy. Ratios are far below unity for all Keggin catalysts. Activation barriers for the sequential route were calculated as H_2O elimination (TS1 in Figure 2.3a) from monomers and activation barriers for the direct route were calculated as DME formation (TS3 in Figure 2.3b) from a monomer and gas-phase CH_3OH. Differences in activation barriers were calculated as $E_{a,seq} - E_{a,direct}$.

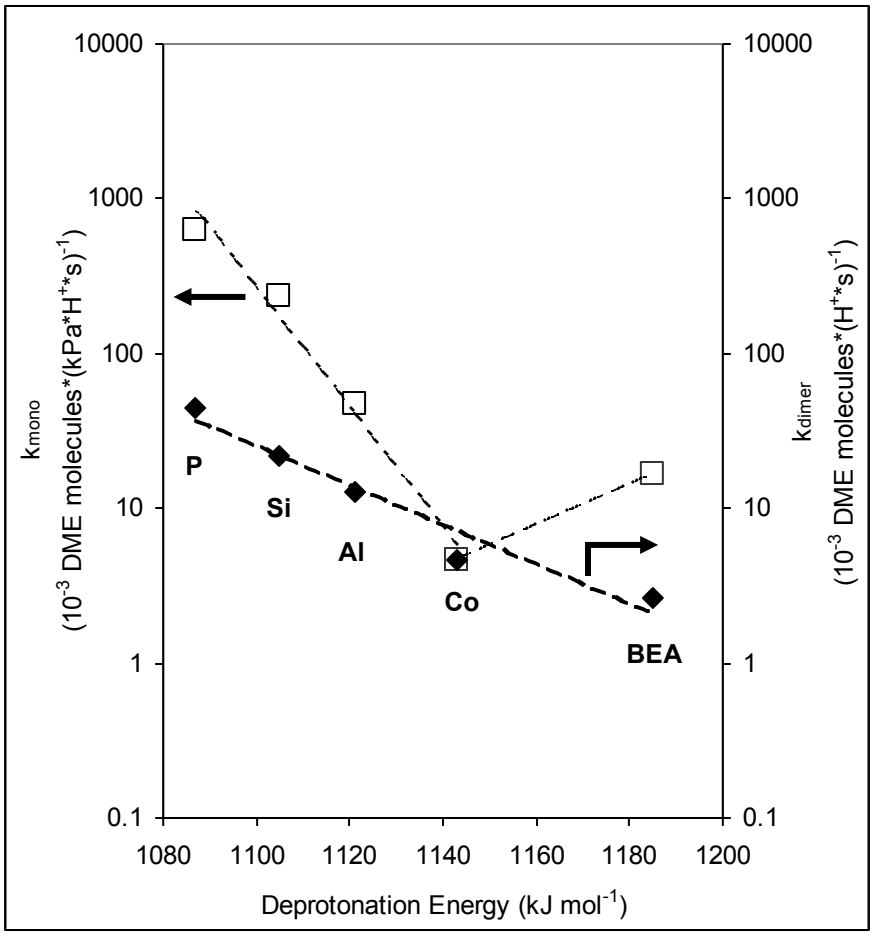

Figure 2.8. Measured first-order rate constants (k_{mono}, □; Eq. (2.9)) and zero-order rate constants (k_{dimer}, ♦; Eq. (2.10)) of CH_3OH dehydration to DME (433 K) as a function of DPE values for $H_{8-n}X^{n+}W_{12}O_{40}/SiO_2$ (X = P, Si, Al, Co) and H-BEA.

2.5.3. Schemes

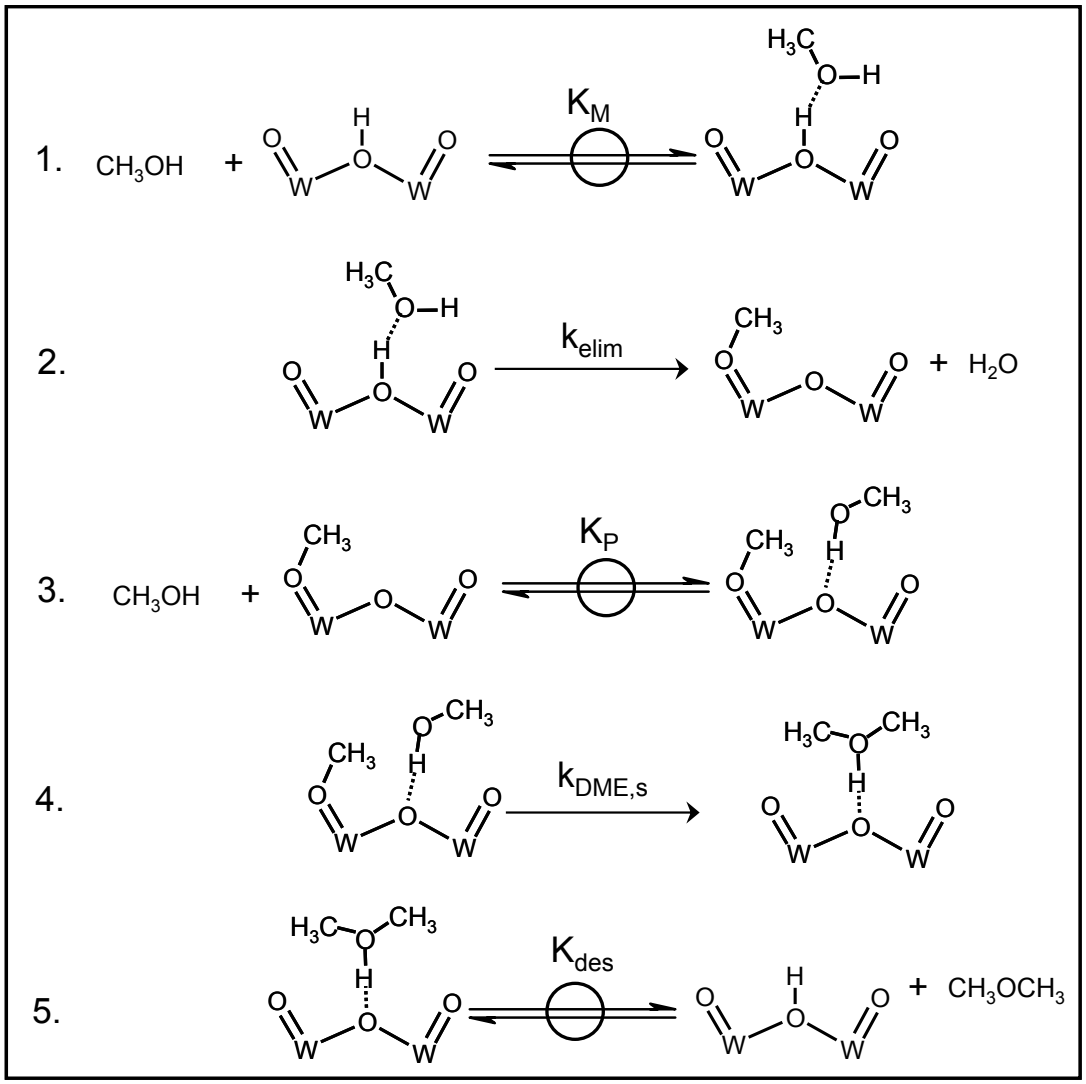

Scheme 2.1. Elementary steps in the sequential CH_3OH dehydration route. Dashed lines represent H-bonding interactions.

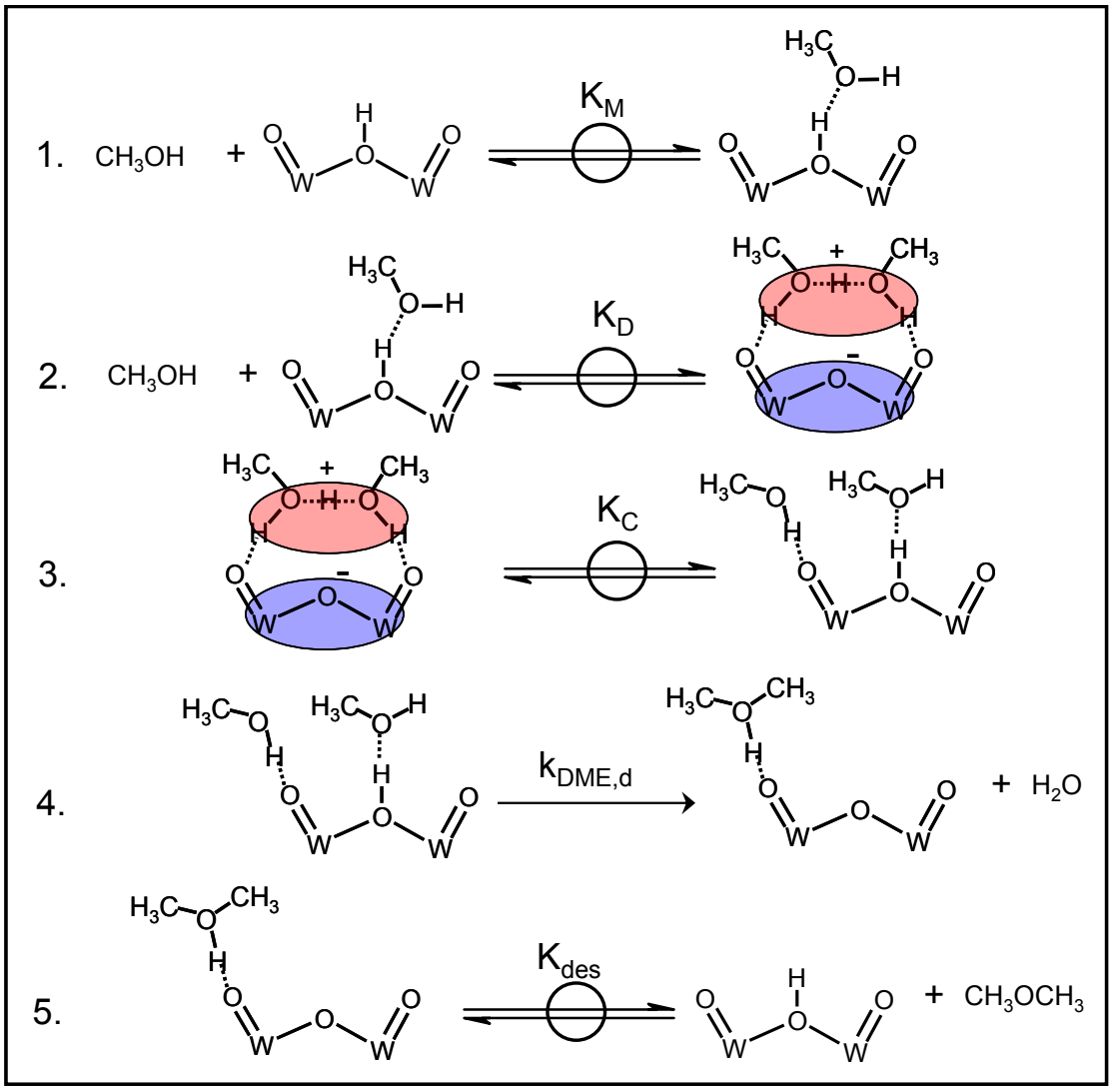

Scheme 2.2. Elementary steps in the direct CH_3OH dehydration route. Dashed lines represent H-bonding interactions.

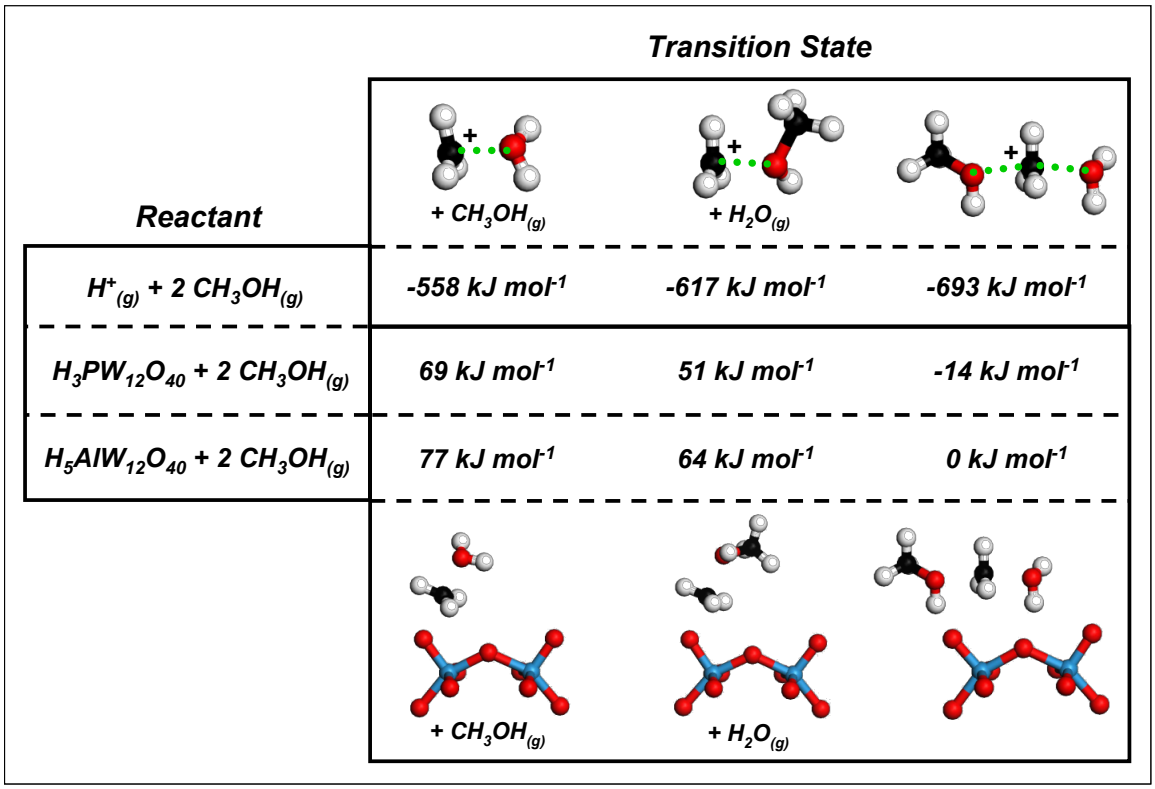

Scheme 2.3. Energies and structures of transition states and their gas-phase analogs in sequential and direct dehydration routes. Energies of transition states are reported relative to two gas-phase CH_3OH and the bare acid (or a gas-phase proton for the gas-phase transition states). Energies decrease in the order: sequential H_2O elimination, sequential DME formation, and direct DME formation for all cases.

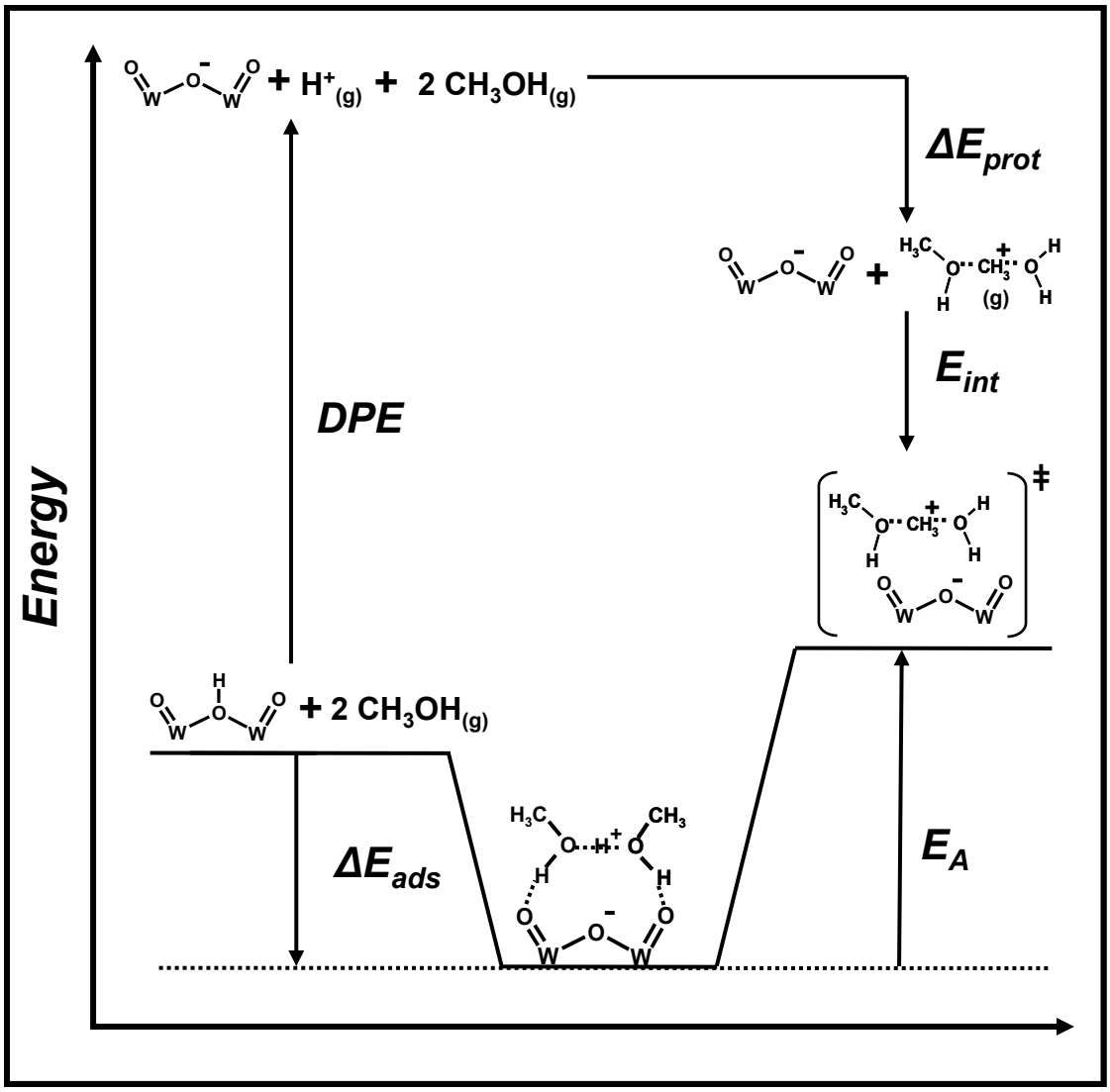

Scheme 2.4. Thermochemical cycle description of the activation barrier for k_{dimer} in the direct route (Scheme 2.2 and Eq. (2.12)). The activation energy (E_A) depends on the catalyst deprotonation energy (DPE), reactant proton affinity (ΔE_{prot}), transition state stabilization energy (E_{int}), and reactant adsorption energy as a protonated dimer (ΔE_{ads}).

2.6. Supporting Information

2.6.1. MAS-^{31}P-NMR of Silica-Supported $H_3PW_{12}O_{40}$

Solid-state MAS-^{31}P-NMR spectra of SiO_2-supported $H_3PW_{12}O_{40}$ ($H_3PW_{12}O_{40}/SiO_2$) were recorded on a Bruker DSX-500 spectrometer equipped with a Bruker 4mm CPMAS probe. Samples were loaded into a ZrO_2 rotor at ambient conditions and spun at 14 kHz at ambient temperature. An operating frequency of 202.2 MHz was used for ^{31}P nuclei and small angle rf pulses (1 ms-15 degree) were used with a recycle time of 100 s because of the long spin-lattice relaxation of ^{31}P nuclei in Keggin clusters. MAS-^{31}P-NMR signals were also examined with delay times up to 3000 s to check for the presence of slow relaxing components. Chemical shifts are referenced to 85% H_3PO_4 for ^{31}P nuclei.

The MAS-^{31}P-NMR spectrum of $H_3PW_{12}O_{40}/SiO_2$, prepared by the methods described in Section 2.2.1, is shown in Figure S.2.1. This spectrum has a single sharp peak located at -14.9 ppm. The chemical shift of this peak is in excellent agreement with the ^{31}P nucleus signal for Keggin $[PW_{12}O_{40}]^{3-}$ anions in the aqueous-phase ($\delta(^{31}P)$ = -14.9 ppm).[60] There are also no peaks at chemical shifts that have been reported for non-Keggin (Wells-Dawson $[P_2W_{18}O_{62}]^{6-}$, $\delta(^{31}P)$ = -12.7 ppm)[60] or lacunary Keggin ($[PW_{11}O_{39}]^{7-}$, $\delta(^{31}P)$ = -10.4 ppm) structures. Thus, we conclude that the Keggin structure persists on the silica support and is not degraded during grafting procedures.

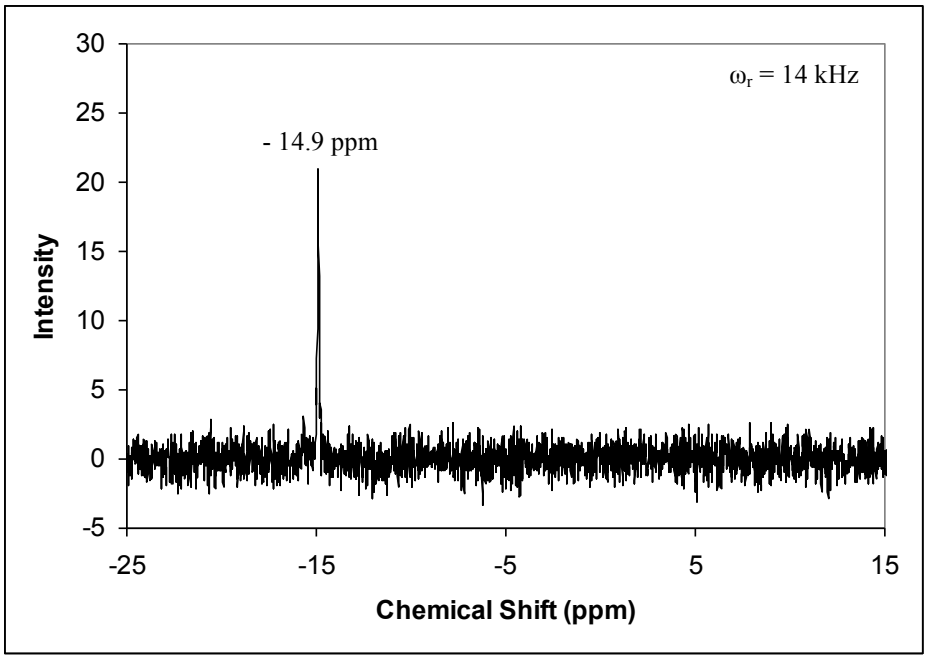

Figure S.2.1. MAS-^{31}P-NMR of 0.04 POM nm^{-2} $H_3PW_{12}O_{40}/SiO_2$ referenced to 85wt% H_3PO_4.

2.6.2. Transmission Electron Micrographs (TEM) of Silica-Supported $H_4SiW_{12}O_{40}$

TEM samples were prepared by grinding $H_4SiW_{12}O_{40}/SiO_2$ (as prepared in Section 2.2.1) into a fine powder (< 50 μm) using a mortal and pestle. Approximately

0.002 g of powder was suspended in 1 cm^3 of $CHCl_3$ (Sigma-Aldrich, >99%) by sonication for 1 min before evaporating the mixture onto an ultrathin carbon film on a 400 mesh copper TEM grid (Ted Pella, Inc.). TEM images were obtained on FEI Tecnai 12 (120 kV accelerating voltage, bright field) transmission electron microscope using an internal charge-coupled device (CCD) camera. Figure S.2.2 shows a typical TEM image of $H_4SiW_{12}O_{40}$ (small dark circular features approximately 1-5 nm in diameter) supported on amorphous silica particles (medium gray) at 0.04 POM nm^{-2} surface density. The size of these features relative to the diameter of a single Keggin cluster (~1.2 nm) indicates that supported POM clusters exist as isolated clusters or as small aggregates (< 15 POM clusters). Edges of silica particles do not reveal large multi-layer structures; thus, small aggregates of clusters are only two-dimensional.

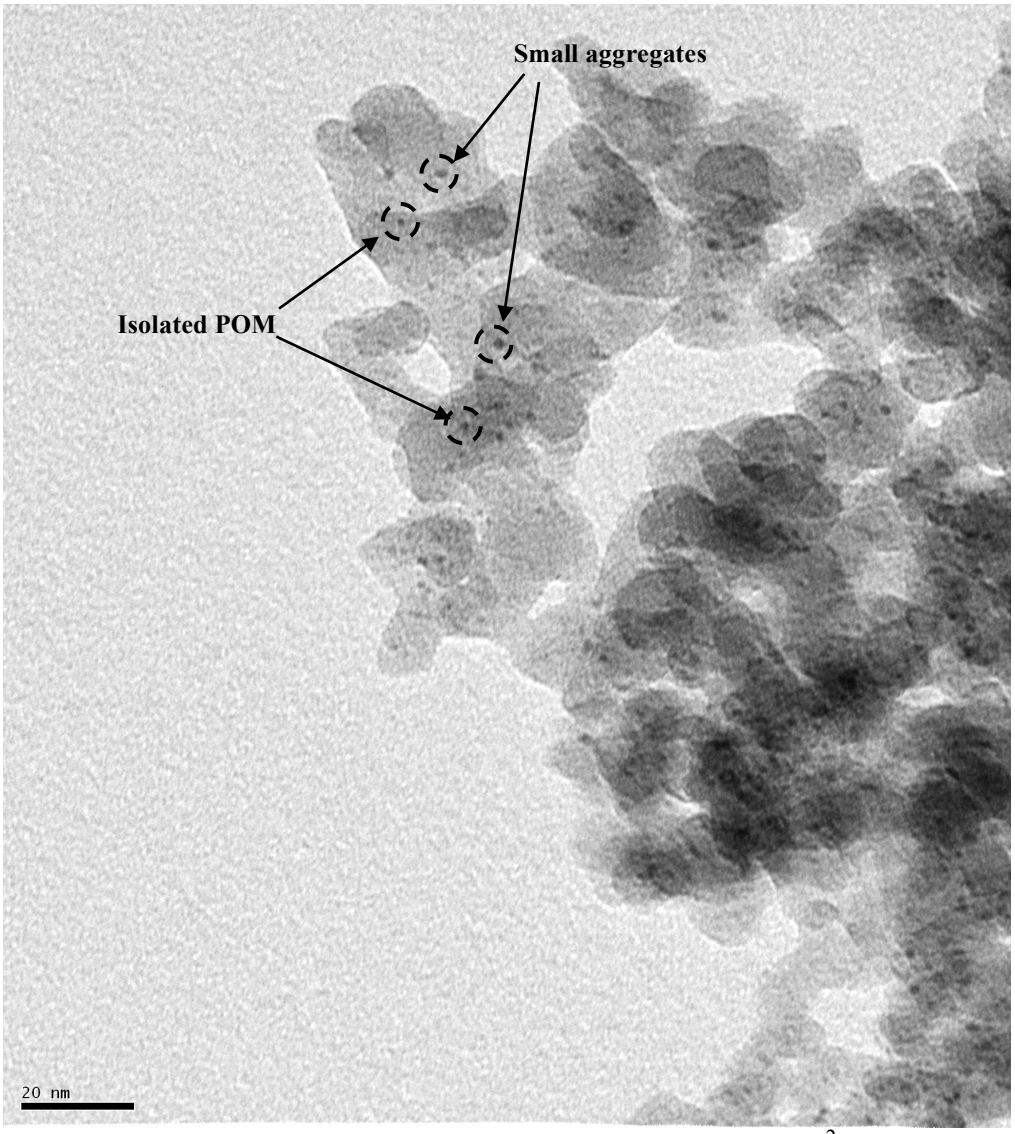

Figure S.2.2. Transmission electron micrograph of 0.04 POM nm^{-2} $H_4SiW_{12}O_{40}/SiO_2$. Dark circular features are isolated or small two-dimensional aggregates of Keggin POM on the silica support, examples of which are indicated in the micrograph.

2.6.3. Optimized Structures of Full Keggin Clusters

All calculations of intermediates and transition states were completed on full Keggin clusters. As seen in Figure S.2.3, the optimized structures of Keggin clusters were nearly identical for different central atoms, and only differed in the number of protons. Proton locations were chosen to minimize interactions between proton sites.[49] All intermediates and transition states were calculated at the same proton location (H_{C1}) which is labeled in Figure S.2.3, along with the nearby O-atoms that constitute the active site.

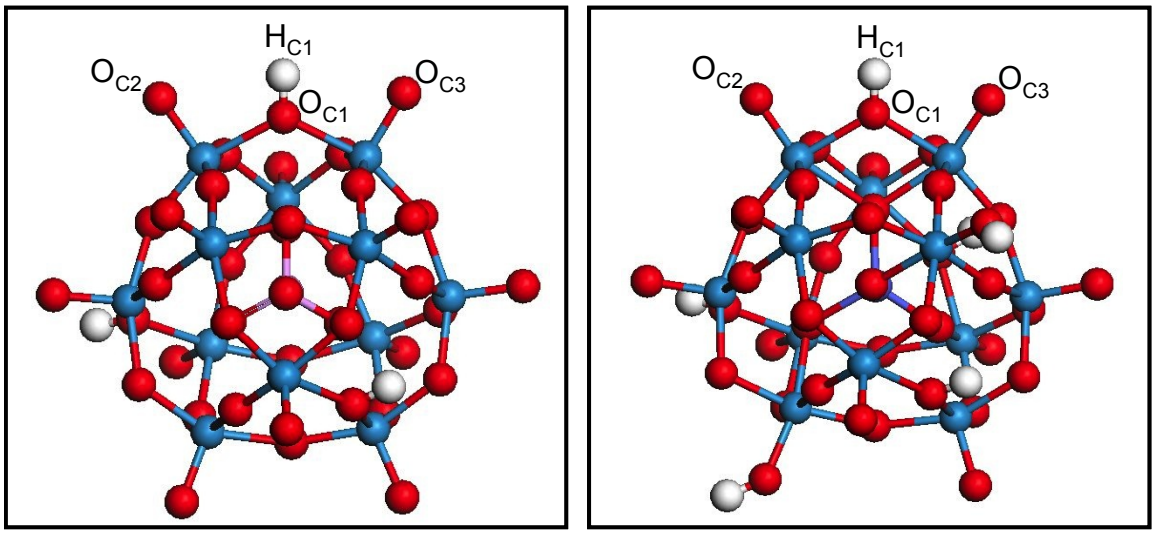

Figure S.2.3. Optimized structures of full Keggin $H_3PW_{12}O_{40}$ and $H_6CoW_{12}O_{40}$ clusters. The proton (H_{C1}) and local O-atoms that constitute the active site in calculations are labeled and correspond to those in Figure 2.3.

2.6.4. Methanol Pressure Effects on Proton Accessibility

Proton accessibility was measured as a function of CH_3OH pressure by titration with 2,6 di-*tert*-butyl pyridine during reaction on $H_4SiW_{12}O_{40}/SiO_2$ at 413 K (Figure S.2.4). The number of protons titrated was nearly constant (~ 2.5 H^+/POM) over a wide range of CH_3OH pressures (0.22 – 10 kPa) and indicates that pressure effects on CH_3OH dehydration rates reflect kinetic changes and not commensurate changes in proton accessibility. CH_3OH reactants can swell secondary structures of POM clusters, rendering protons located in interstitial spaces accessible for reaction. The extent of this swelling can significantly change the number of accessible protons for unsupported POM or supported POM with high surface densities where the fraction of clusters located within aggregates is large; however, for low surface density samples used here, clusters are isolated or reside in small two-dimensional structures (transmission electron micrograph in Section 2.6.2). Thus, small effects of swelling are expected, consistent with titration values that are independent of CH_3OH pressure (Figure S.2.4). The numbers of accessible protons are near the stoichiometric value under all conditions and

also indicate that POM clusters are well-dispersed on supports and most protons are accessible and reactive for CH_3OH dehydration.

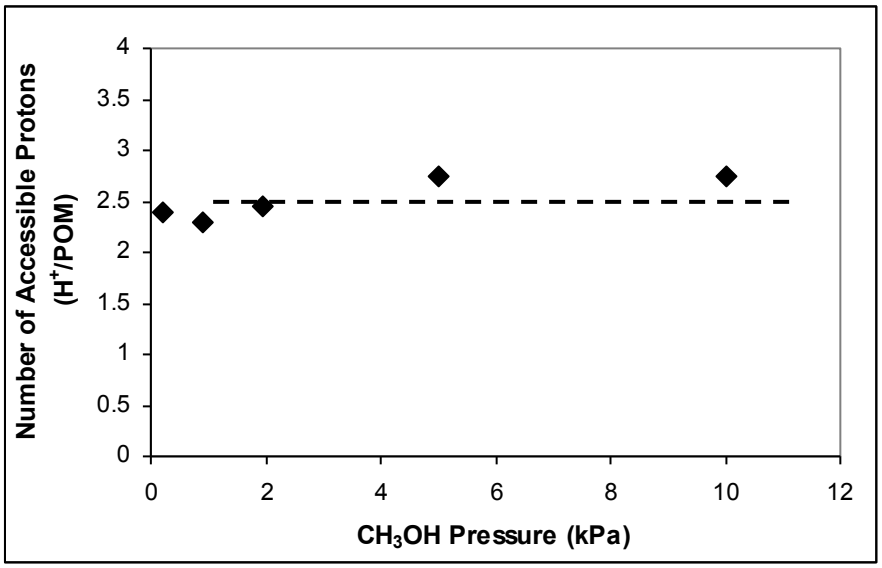

Figure S.2.4. Number of accessible protons (per Keggin cluster) as a function of CH_3OH pressure on $H_4SiW_{12}O_{40}/SiO_2$ measured by titration during dehydration catalysis (1.4 Pa 2,6-di-*tert*-butylpyridine, 413 K).

2.6.5. MAS-^{27}Al-NMR of H-BEA

H-BEA samples (Zeolyst, Si/Al = 11.8) were prepared for MAS-^{27}Al-NMR by packing into a 4mm ZrO_2 rotor, followed by complete hydration in a desiccator containing a 1.0 M KCl aqueous solution for at least 48 h prior to sealing the rotors with a kel-F cap. Solid-state MAS-^{27}Al-NMR spectra were recorded on a Bruker Avance 500 MHz spectrometer using a 4 mm CPMAS probe at ambient temperature and an operating frequency of 130.35 MHz with strong proton decoupling and spinning of the rotor at 14 kHz. 512 scans with a 0.5 μs pulse and a 6 s delay were averaged to produce the final spectrum (Figure S.2.5). The relative amounts of ^{27}Al nuclei in framework and extra-framework locations were determined from integrated areas of peaks centered at chemical shifts (referenced to a 1.0 M aqueous solution of $Al(NO_3)_3$) of 53 ppm and 0 ppm, respectively, corresponding to tetrahedral and octahedral coordinated Al-atoms. The normalized areas of tetrahedral and octahedral NMR peaks are 1.00 and 0.376, respectively, and indicate that 73% of Al-atoms are in zeolite framework positions.

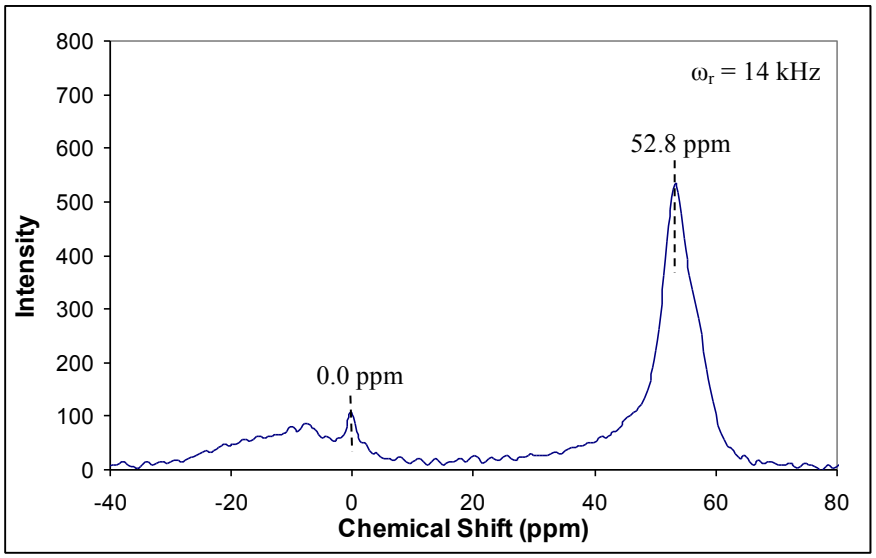

Figure S.2.5. MAS-^{27}Al-NMR of H-BEA referenced to a 1.0 M aqueous solution of $Al(NO_3)_3$.

2.6.6. Titrations of H-BEA by 2,6-di-*tert*-butyl pyridine and pyridine

The number of reactive, accessible protons in H-BEA was measured by chemical titration with 2,6-di-*tert*-butyl pyridine and pyridine during CH_3OH dehydration. Dehydration rates were not fully suppressed by titration with 2,6-di-*tert*-butyl pyridine and at saturation uptakes of the titrant, residual rates were 15% of their initial values (Figure 2.2b). The cumulative titrant uptake (Figure 2.2b, 0.35 titrant molecules (total Al sites)$^{-1}$) and the and the fraction of Al sites in framework locations (0.73, Section 2.6.5) indicate that only 50% of protons associated with framework Al are titrated by 2,6-di-*tert*-butyl pyridine at saturation.

Saturated titration values below one titrant molecule per framework Al and residual rates may indicate that adsorbed hindered pyridine molecules occlude neighboring protons from other titrant molecules, but not smaller CH_3OH molecules, by size exclusion or blocking channels. The latter of these is unexpected because of H-BEA's two interconnecting 12-member ring channels with large apertures (5.6 Å x 5.6 Å and 6.6 Å x 6.7 Å) that give it three-dimensional connectivity. The plausibility for an adsorbed titrant obstructing the titration of neighboring proton was determined from the number of hindered pyridines that could fit theoretically in a unit cell of H-BEA relative to the average number of framework Al per unit cell. Micropore volumes [61] and the molecular weight for BEA, 0.23 cm^3 g^{-1} and 3840 g mol^{-1}, respectively, and molecular properties of hindered pyridine (0.852 g cm^{-3} bulk liquid density and 191.3 g mol^{-1} molecular weight) predict a maximum packing of 3.9 titrant molecules per unit cell. This value is only slightly larger than the proton density at this Si/Al_f ratio (16.2), 3.6 H^+/unit cell, so that all protons can be simultaneously titrated. Inefficient packing of titrant molecules inside zeolites caused by the channel shape and size and non-uniform Al site distributions would easily reduce the fraction of protons that can be titrated at saturation below unity.

Residual rates after saturation with 2,6-di-*tert*-butyl pyridine indicate that CH_3OH reactants are able to reach reactive protons that are not accessible to hindered pyridine and/or they react at extra-framework Lewis acid sites present on H-BEA samples. The latter of these possibilities was examined by titration during dehydration catalysis with pyridine (non-hindered) which titrates both protons and Lewis acid sites because it lacks bulky substituents near the N-atom that prevent hindered pyridine from coordinating to Lewis sites. Titration with pyridine also did not fully suppress rates; residual rates equal to 10% of the initial rate were present at a saturation adsorption of 0.45 pyridine per total Al (Figure S.2.6). By comparison to the titration with hindered pyridine, Lewis acid site contributions to dehydration rates are minimal (~ 5% of the total rate) and are therefore neglected.

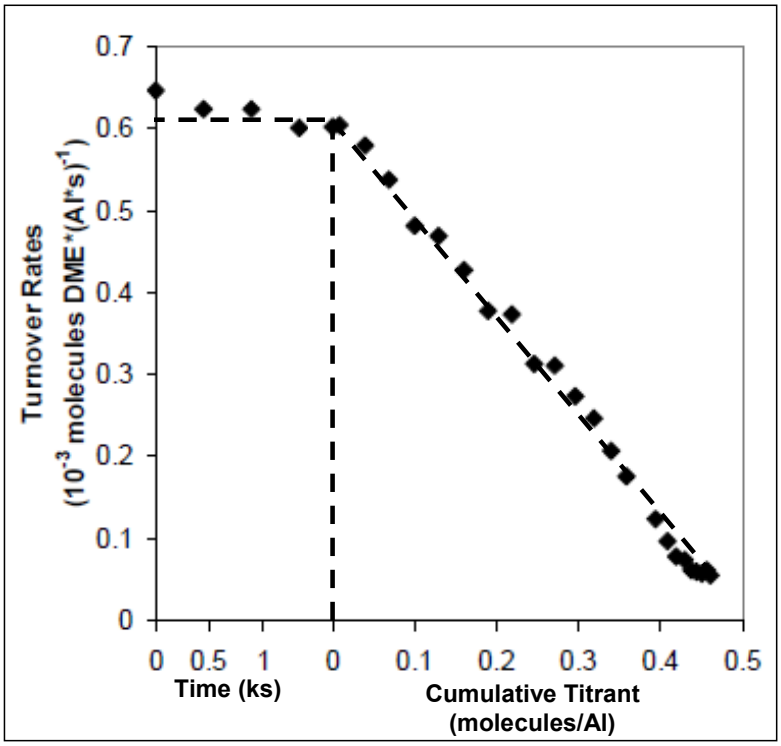

Figure S.2.6. DME formation rates (per total Al) on H-BEA as a function of time before titrant injection (0.3 kPa CH_3OH, 433 K) and as a function of cumulative titrant uptake (0.3 kPa CH_3OH, 1.4 Pa pyridine, 433K) during titration.

Reactive protons that are accessible to CH_3OH reactants, but not to hindered pyridine, were taken into account by extrapolating the titration curve in Figure 2.2b to zero rates. Thus, the final measured value for the total number of reactive and accessible protons is 0.55 H^+ per framework Al. This value indicates half of the framework Al-atoms have protons that are either unreactive or inaccessible. Unreactive protons in zeolites may be caused by paired sites that are weaker acids or are removed by dehydroxylation reactions. Inaccessible protons may be caused by pyrolysis products that evolve from organic templates during thermal pretreatment and block channels. H-BEA samples were treated at 773 K in dry air for 2.5 h to remove organic species,

however, during this procedure some pyrolyze into stable species that cannot be removed at temperatures that do not harm the zeolite structure. The saturation uptake for H-BEA pretreated in the manner above was twice the value of a sample heated to reaction temperature (433 K) in dry He, indicating the effects on accessibility by removing organic compounds by pretreatment are quite dramatic.

2.6.7. Derivations of the Rate Expressions for Sequential and Direct Methanol Dehydration Routes

Here we derive in detail, the rate expressions for the sequential and direct routes from the elementary steps outlined in Schemes 2.1 and 2.2. Assumptions of quasi-equilibrium and irreversibility of elementary steps shown in these schemes are applied in the following derivations and are justified by the rate constant calculations within Section 2.6.14. Concentrations of all surface intermediates (indicated by the use of square brackets) are calculated from the pseudo-steady-state hypothesis (PSSH).

$$\left|\frac{d[C_i *]}{dt}\right| \approx 0 \qquad \text{(S.2.1)}$$

2.6.7.1. Derivation of the Rate Expression for the Sequential Route

The sequential route proceeds through adsorption of CH_3OH at a proton ([*]) to form a monomer ([M*]), which irreversibly eliminates H_2O and forms a covalently-bound methoxide species ([Me*]). Methoxide/CH_3OH pairs ([P*]) are formed subsequently by CH_3OH adsorption near the methoxide and react to DME and re-form the proton. Eqs. (S.2.2) to (S.2.4) are the PSSH for these surface species based upon the elementary steps in Scheme 2.1.

$$\left|\frac{d[M *]}{dt}\right| = k_M(CH_3OH)[*] - k_{-M}[M*] - k_{elim}[M*] \approx 0 \qquad \text{(S.2.2)}$$

$$\left|\frac{d[Me *]}{dt}\right| = k_{elim}[M*] - k_P(CH_3OH)[Me*] + k_{-P}[P*] \approx 0 \qquad \text{(S.2.3)}$$

$$\left|\frac{d[P *]}{dt}\right| = k_P(CH_3OH)[Me*] - k_{-P}[P*] - k_{DME,s}[P*] \approx 0 \qquad \text{(S.2.4)}$$

Desorption of CH_3OH from monomers is significantly faster than the subsequent elimination ($k_{-M} >> k_{elim}$; see values listed in Table S.2.8), therefore monomers are in quasi-equilibrium with gas-phase CH_3OH. Likewise, desorption of CH_3OH from methoxide/CH_3OH pairs is much faster than the formation of DME ($k_{-P} >> k_{DME,s}$; see values listed in Table S.2.8) so that methoxide/CH_3OH pairs are at quasi-equilibrium. The equilibrated adsorption of CH_3OH at methoxides and their reaction is faster than the reaction between H_2O and a methoxide ($K_P k_{DME,s} >> k_{-elim}$; see values in Table S.2.8), thus, H_2O elimination is irreversible. Finally, DME desorption is faster than its

decomposition to methoxide/CH_3OH pairs (k_{des} >> $k_{-DME,s}$; see values listed in Table S.2.8) so that DME formation is also irreversible.

Steady-state concentrations of surface intermediates were evaluated by applying these simplifications to the PSSH above (Eqs. (S.2.2) to (S.2.4)) and solving the system of equations.

$$[M^*] = \frac{k_M}{k_{-M}}(CH_3OH)[^*] = K_M(CH_3OH)[^*] \quad \text{(S.2.5)}$$

$$[Me^*] = \frac{k_{elim}}{k_{DME,s}} K_M \frac{k_{-P}}{k_P}[^*] = \frac{k_{elim}}{k_{DME,s}} \frac{K_M}{K_P}[^*] \quad \text{(S.2.6)}$$

$$[P^*] = \frac{k_{elim}}{k_{DME,s}} K_M(CH_3OH)[^*] \quad \text{(S.2.7)}$$

The concentration of bare protons in these equations is determined from the total site balance, which states that the summation of all surface intermediates must add to the total site concentration ([L]). By substituting the values of K_M, K_P, k_{elim} and $k_{DME,s}$ (Table S.2.8) into the terms that precede "[*]" in Eqs. (S.2.5) to (S.2.7), it is shown that active sites are primarily occupied as methoxides and monomers at reaction conditions.

$$[L] = [^*] + [Me^*] + [M^*] + [P^*] \approx [Me^*] + [M^*] \quad \text{(S.2.8)}$$

Turnover rates for DME formation are equal to the rate at which methoxide/CH_3OH pairs react.

$$\frac{r_s}{[L]} = \frac{d([DME])}{dt}\frac{1}{[L]} = k_{DME,s}\frac{[P^*]}{[L]} \quad \text{(S.2.9)}$$

Thus, the rate expression for CH_3OH dehydration is evaluated by combining Eq. (S.2.9) with the site balance (Eq. (S.2.8)) and the equations for steady-state concentrations of surface intermediates (Eqs. (S.2.5) to (S.2.7)).

$$\frac{r_s}{[L]} = \frac{k_{DME,s}K_P(CH_3OH)}{1 + \frac{k_{DME,s}}{k_{elim}}K_P(CH_3OH)} \quad \text{(S.2.10)}$$

The presence of protonated dimers as unreactive, but prevalent surface species that occupy protons requires their inclusion in site balances. Dimers form by the adsorption of CH_3OH at monomers (Scheme 2.2, Step 2). The PSSH for monomers and protonated dimers, including this new elementary step, are:

$$\left|\frac{d[M*]}{dt}\right| = k_M(CH_3OH)[*] - k_{-M}[M*] - k_D[M*](CH_3OH) + k_{-D}[D*] - k_{elim}[M*] \approx 0 \quad \text{(S.2.11)}$$

$$\left|\frac{d[D*]}{dt}\right| = k_D[M*](CH_3OH) - k_{-D}[D*] \approx 0 \quad \text{(S.2.12)}$$

The assumptions of irreversibility and quasi-equilibrium are unaffected by dimer formation, so that steady-state concentrations of surface species are calculated by solving this new the system of equations (Eqs. (S.2.3), (S.2.4), (S.2.11), and (S.2.12)). The solutions for [M*], [Me*], and [P*] are the same as above (Eqs. (S.2.5) to (S.2.7)) and [D*] is given by:

$$[D*] = \frac{k_D}{k_{-D}} K_M (CH_3OH)^2 [*] = K_D K_M (CH_3OH)^2 [*] \quad \text{(S.2.13)}$$

Protonated dimers are present at significant coverages over the range of CH_3OH pressures examined here (0.01 kPa to 1.0 kPa) and need to be included in the total site balance.

$$[L] = [Me*] + [M*] + [D*] \quad \text{(S.2.14)}$$

Rates of the sequential route with dimer formation are calculated from Eq. (S.2.9) using the same method as above, except that the new site balance (Eq. (S.2.14)) is used.

$$\frac{r_s}{[H^+]} = \frac{k_{DME,s} K_P (CH_3OH)}{1 + \frac{k_{DME,s}}{k_{elim}} K_P (CH_3OH) + \frac{k_{DME,s}}{k_{elim}} K_P K_D (CH_3OH)^2} \quad \text{(S.2.15)}$$

2.6.7.2. Derivation of the Rate Expression for the Direct Route

CH_3OH dehydration via the direct route proceeds through multiple adsorptions of CH_3OH at protons to form monomers ([M*]) and protonated dimers ([D*]). Protonated dimers rearrange to co-adsorbed species ([C*]), which have the correct orientation to react to DME. Eqs. (S.2.16) to (S.2.18) are the PSSH for these surface intermediates based upon the set of elementary steps in Scheme 2.2.

$$\left|\frac{d[M*]}{dt}\right| = k_M(CH_3OH)[*] - k_{-M}[M*] - k_D[M*](CH_3OH) + k_{-D}[D*] \approx 0 \quad \text{(S.2.16)}$$

$$\left|\frac{d[D*]}{dt}\right| = k_D[M*](CH_3OH) - k_{-D}[D*] - k_C[D*] + k_{-C}[C*] \approx 0 \qquad \text{(S.2.17)}$$

$$\left|\frac{d[C*]}{dt}\right| = k_C[D*] - k_{-C}[C*] - k_{DME,d}[C*] \approx 0 \qquad \text{(S.2.18)}$$

Rearrangement of co-adsorbed species to protonated dimers and CH_3OH desorption from protonated dimers and monomers are all much faster than concerted DME formation and H_2O elimination from co-adsorbed species ($k_{-C} >> k_{DME,d}$; $k_{-D} >> K_C k_{DME,d}$; $k_{-M} >> K_D K_C k_{DME,d}$; see values in Tables S.2.8 and S.2.9). Thus, monomers, protonated dimers, and co-adsorbed species are in quasi-equilibrium with each other and gas-phase CH_3OH and have steady-state concentrations that are given by their respective equilibrium constants.

$$[M*] = \frac{k_M}{k_{-M}}(CH_3OH)[*] = K_M(CH_3OH)[*] \qquad \text{(S.2.19)}$$

$$[D*] = K_M \frac{k_D}{k_{-D}}(CH_3OH)^2[*] = K_M K_D (CH_3OH)^2[*] \qquad \text{(S.2.20)}$$

$$[C*] = K_M K_D \frac{k_C}{k_{-C}}(CH_3OH)^2[*] = K_M K_D K_C (CH_3OH)^2[*] \qquad \text{(S.2.21)}$$

The concentration of vacant protons ([*]) in Eqs. (S.2.19) to (S.2.21) is solved using a site balance. Concentrations of co-adsorbed species are always negligibly small relative to those for protonated dimers ($K_C/K_D << 1$; see values in Table S.2.9) and never have significant contributions to site balances. Additionally, vacant protons do not have appreciable concentrations at the temperatures and CH_3OH pressures examined here ($K_M >> 1$; see values in Table S.2.8).

$$[L] = [*] + [M*] + [C*] + [D*] \approx [M*] + [D*] \qquad \text{(S.2.22)}$$

DME formation rates from co-adsorbed CH_3OH molecules are given by:

$$\frac{r_d}{[L]} = \frac{d(DME)}{dt}\frac{1}{[L]} = k_{DME,d}\frac{[C*]}{[L]} \qquad \text{(S.2.23)}$$

which is evaluated by substituting in the site balance (Eq. (S.2.22)) and the steady-state concentrations of surface intermediates (Eqs. (S.2.19) to (S.2.21)).

$$\frac{r_d}{[L]} = \frac{k_{DME,d} K_C K_D (CH_3OH)}{1 + K_D (CH_3OH)} \quad \text{(S.2.24)}$$

2.6.7.3. Derivation of the Ratio of Sequential and Direct Methanol Dehydration Rates

The relative contributions from the sequential and direct routes were calculated from the ratio of their rate expressions (Eqs. (S.2.9) and (S.2.23)).

$$\frac{r_s}{r_d} = \frac{k_{DME,s}[P^*]}{k_{DME,d}[C^*]} \quad \text{(S.2.25)}$$

Concentrations of methoxide/CH_3OH pairs ([P*]) and co-adsorbed species ([C*]) were put in terms of monomers ([M*]), using the steady-state concentrations derived above for the two routes and were substituted into Eq. (S.2.25)

$$\frac{r_s}{r_d} = \frac{k_{DME,s} \frac{k_{elim}}{k_{DME,s}} [M^*]}{k_{DME,d} K_D K_C (CH_3OH)[M^*]} \quad \text{(S.2.26)}$$

The dependence on monomer concentrations cancels out since both routes are referred to the monomer. Simplification leads to the equation used to calculate the ratios of rates.

$$\frac{r_s}{r_d} = \frac{k_{elim}}{k_{DME,d} K_C K_D (CH_3OH)} \quad \text{(S.2.27)}$$

2.6.8. Calculations of Proton Locations and Movement by "Proton-Hopping"

All intermediates and transition states were calculated at a proton located on a bridging O-atom (O_{C1}), however, protons on POM clusters can also be located a terminal O-atoms (e.g. O_{C3}). The effect of proton location and CH_3OH-assisted proton-hopping reactions, which facilitate proton movement, were examined by their calculations on a $H_3PW_{12}O_{40}$ cluster. Figure S.2.7 shows the energies and structures of intermediates and the transition state along the proton-hopping reaction coordinate, which moves a proton from a bridging O-atom (O_{C1}) to a terminal O-atom (O_{C3}). Energies, atomic separations, and Bader charges for these species are listed in Table S.2.1.

Proton hopping begins with adsorption of CH_3OH at a proton located on a bridging O-atom (A in Figure S.2.7) to form the same monomer as discussed in Section 3.3.1 (A in Figure 2.3a and B in Figure S.2.7). The adsorption energy for this species (-74.6 kJ mol^{-1} on $H_3PW_{12}O_{40}$; Table 2.4) and the small O-atom separation (O_{C1}-O_{M1} = 0.247 nm on $H_3PW_{12}O_{40}$; Table 2.2) signify this is a strong adsorption, largely because of electrostatic interactions between the proton and the CH_3OH. The proton has not been transferred from the POM cluster to the CH_3OH in this intermediate; the proton remains closer to the POM O-atom than the CH_3OH O-atom (O_{C1}-H_{C1} = 0.107 nm and O_{M1}-H_{C1} =

0.139 nm on $H_3PW_{12}O_{40}$) and the Bader charge on the CH_3OH (0.12 e) is small. These observations are in agreement with the weak dependence of monomer adsorption energies on Keggin cluster DPE (Figure 2.4).

CH_3OH adsorption facilitates proton movement by proton-hopping reactions that transfer the proton location from bridging (O_{C1}) to terminal (O_{C3}) O-atoms (Figure S.2.7) and its reverse. Such reactions change the identity of the proton; the proton in the final location is initially the CH_3OH hydroxyl H-atom (Figure S.2.7). The transition state for CH_3OH-assisted proton hopping resembles a methoxonium ion ($[CH_3OH_2]^+$) interacting with the proton-donating and receiving O-atoms in the POM cluster (TS in Figure S.2.7). The locations of the involved H-atoms at the transition state indicate that the initial proton (H_{C1}) is transferred to CH_3OH (O_{C1}-H_{C1} = 0.181 nm and O_{M1}-H_{C1} = 0.100 nm) before the CH_3OH H-atom (H_{M1}) is transferred to the cluster (O_{M1}-H_{M1} = 0.112 nm and O_{C3}-H_{M1} = 0.134 nm). The Bader charge of the CH_3OH_2 at the transition state (+0.81 e) is significantly larger than for the monomer and suggests it is a full ion-pair, in accordance with the H-atom positions. The energy of the transition state is 11 kJ mol^{-1} higher than the bridging monomer reactant (B in Figure S.2.7) and is nearly the same as the terminal monomer product (C in Figure S.2.7), indicating this is a late transition state. This activation barrier for CH_3OH-assisted proton-hopping from a bridging location is in good agreement with previous calculations of activation barriers for H_2O-assisted proton-hopping on $H_3PW_{12}O_{40}$ (11.2 kJ mol^{-1}).[35] Barriers for assisted proton-hopping are much lower than that for unassisted hopping (103.3 kJ mol^{-1}) because H_2O and CH_3OH stabilize protons as they move and circumvent the deformation of catalyst bonds that occurs in unassisted pathways.

Monomers at terminal proton locations (C in Figure S.2.7) are 11 kJ mol^{-1} higher in energy than those at bridging proton locations. The proton (O_{M1}) in this intermediate resides closer to the cluster than the CH_3OH (H_{M1}-O_{C3} = 0.108 nm and H_{M1}-O_{M1} = 0.139 nm) and, with the CH_3OH Bader charge (0.12 e), suggests that terminal monomers are also not protonated. The adsorption energy of CH_3OH at a terminal proton is -71 kJ mol^{-1} on $H_3PW_{12}O_{40}$, which is similar to adsorption at bridging locations. Thus, the difference in energy for bridging and terminal monomers mostly reflects the lower stability of protons at terminal locations (by 7.2 kJ mol^{-1}). For CH_3OH dehydration reactions, where CH_3OH adsorption is quasi-equilibrated and proton-hopping reactions are significantly faster than DME formation rates, monomers and protons will have thermodynamic distributions. The relative energies of bare protons and monomers at bridging and terminal O-atom locations, indicates that bridging locations are favored for both species (by factors of 7 and 21 for bare protons and monomers, respectively).

Table S.2.1. Atomic distances (listed in nm), Bader charges (listed in electron charges), and energies (listed in kJ mol^{-1}) of intermediates and the transition state for proton hopping reactions on $H_3PW_{12}O_{40}$ (Figure S.2.7).

Species [a]	***Energy*** [b] ***(kJ mol^{-1})***	***H_{C1}-O_{C1} (nm)***	***H_{C1}-O_{M1} (nm)***	***H_{M1}-O_{M1} (nm)***	***H_{M1}-O_{C3} (nm)***	***Bader Charge***
Bare Cluster (Bridging Proton) (A)	0.0	0.098	- - -	0.097	- - -	- - -
Monomer (Bridging Proton) (B)	-74.6	0.107	0.139	0.098	0.277	0.116
Proton Hopping TS (TS)	-63.2	0.181	0.100	0.112	0.134	0.814
Monomer (Terminal Proton) (C)	-63.7	0.253	0.098	0.139	0.108	0.119
Bare Cluster (Terminal Proton) (D)	7.2	- - -	0.097	- - -	0.098	- - -

[a]Atomic and structural labels correspond to structures shown in Figure S.2.7.
[b] Energies are listed with respect to one gas-phase CH_3OH and a bare POM cluster with the proton located on a bridging O-atom (O_{C1}) (A in Figure S.2.7).

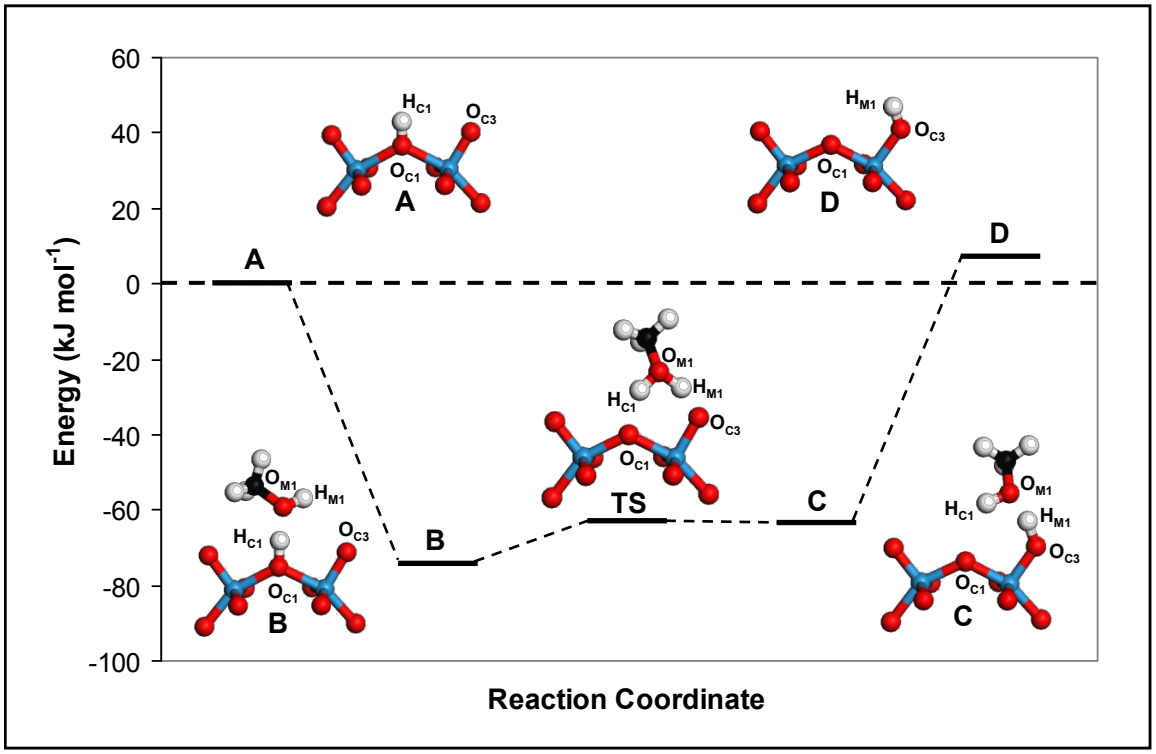

Figure S.2.7. Structures and energies of intermediates and the transition state for proton hopping reactions calculated on $H_3PW_{12}O_{40}$. Atomic labels correspond to those used to report the distances listed in Table S.2.1 and colors correspond to elemental identity (blue = W, red = O, white = H, black = C).

2.6.9. Complete List of Distances and Bader Charges for Direct and Sequential Methanol Dehydration Routes on Keggin Clusters

Here we list the complete set of relevant distances and Bader charges of intermediates and transition states calculated for the direct and sequential CH_3OH dehydration routes on Keggin POM clusters with varying central atoms (S, P, Si, Al, Co). Structures for these intermediates on $H_3PW_{12}O_{40}$ can be found in Figures 2.3a and 2.3b and were similar for all central atoms. Labels for intermediates and transition states and for their atoms are shown in these figures and are used in the tables below. Methods used to optimize structures of intermediates and transition states and to calculate Bader charges are detailed in Section 2.2.3.

Table S.2.2. Atomic distances (listed in nm) and Bader charges (listed as electron charges) of intermediates and transition states in the sequential route of CH_3OH dehydration (Scheme 2.1).

	Central Atom				
Species[a]	**S**	**P**	**Si**	**Al**	**Co**
Bare Cluster					
H_{C1}-O_{C1}	0.098	0.097	0.097	0.097	0.097
Monomer (A)					
H_{C1}-O_{C1}	0.108	0.107	0.107	0.108	0.104
H_{C1}-O_{M1}	0.141	0.140	0.140	0.139	0.149
C_{M1}-O_{M1}	0.146	0.146	0.146	0.146	0.145
C_{M1}-O_{C2}	0.324	0.333	0.326	0.337	0.350
O_{M1}-H_{M1}	0.098	0.098	0.098	0.098	0.097
H_{M1}-O_{C3}	0.289	0.277	0.288	0.283	0.301
H_{C1} Bader Charge	0.730	0.730	0.644	0.662	0.750
CH_3OH Bader Charge	0.000	0.116	0.000	0.084	0.089
H_2O Elimination TS (TS1)					
H_{C1}-O_{C1}	0.404	0.398	0.367	0.371	0.182
H_{C1}-O_{M1}	0.098	0.098	0.098	0.098	0.099
C_{M1}-O_{M1}	0.186	0.184	0.183	0.181	0.253
C_{M1}-O_{C2}	0.207	0.208	0.210	0.213	0.250
O_{M1}-H_{M1}	0.098	0.098	0.098	0.098	0.097
H_{M1}-O_{C3}	0.547	0.566	0.542	0.546	0.334
Methyl Bader Charge	0.580	0.590	0.590	0.580	0.596
Water Bader Charge	0.190	0.200	0.230	0.210	0.250
Methoxide + H_2O_{ads}					
H_{C1}-O_{C1}	0.221	0.201	0.202	0.202	0.194
H_{C1}-O_{M1}	0.098	0.098	0.098	0.098	0.098
C_{M1}-O_{M1}	0.320	0.314	0.325	0.327	0.314
C_{M1}-O_{C2}	0.144	0.144	0.143	0.143	0.142
O_{M1}-H_{M1}	0.097	0.097	0.097	0.097	0.097

H_{M1}-O_{C3}	0.349	0.329	0.312	0.331	0.338
Water Bader Charge	-0.004	-0.011	-0.008	-0.011	-0.015
Methoxide					
C_{M1}-O_{C2}	0.143	0.143	0.143	0.142	0.142
Methoxide/CH_3OH Pairs (B)					
H_{M2}-O_{C1}	0.205	0.204	0.201	0.213	0.208
H_{M2}-O_{M2}	0.097	0.098	0.098	0.097	0.097
C_{M1}-O_{M2}	0.317	0.327	0.320	0.327	0.331
C_{M1}-O_{C2}	0.144	0.143	0.143	0.143	0.142
O_{M2}-C_{M2}	0.144	0.144	0.144	0.144	0.144
C_{M2}-O_{C3}	0.338	0.344	0.342	0.360	0.348
CH_3OH Bader Charge	0.001	-0.001	0.000	-0.034	-0.026
DME Formation TS (TS2)					
H_{M2}-O_{C1}	0.473	0.470	0.482	0.395	0.208
H_{M2}-O_{M2}	0.098	0.098	0.098	0.098	0.099
C_{M1}-O_{M2}	0.193	0.192	0.189	0.189	0.202
C_{M1}-O_{C2}	0.199	0.200	0.201	0.203	0.205
O_{M2}-C_{M2}	0.146	0.146	0.146	0.146	0.145
C_{M2}-O_{C3}	0.500	0.499	0.537	0.510	0.362
Methyl Bader Charge	0.571	0.570	0.570	0.570	0.560
CH_3OH Bader Charge	0.221	0.190	0.230	0.200	0.200
Adsorbed DME (C)					
C_{M1}-O_{M2}	0.144	0.145	0.144	0.144	0.144
C_{M1}-O_{C2}	0.323	0.323	0.323	0.329	0.324
H_{M2}-O_{C1}	0.105	0.110	0.103	0.107	0.106
H_{M2}-O_{M2}	0.147	0.137	0.151	0.142	0.142
O_{M2}-C_{M2}	0.144	0.145	0.144	0.143	0.144
C_{M2}-O_{C3}	0.316	0.310	0.313	0.318	0.321
DME Bader Charge	0.170	0.108	0.217	0.105	0.097

[a]Atomic and structural labels correspond to diagrams in Figure 2.3a

Table S.2.3. Atomic distances (listed in nm) and Bader charges (listed as electron charges) of intermediates and transition states in the direct route of CH_3OH dehydration (Scheme 2.2).

	Central Atom				
Species[a]	**S**	**P**	**Si**	**Al**	**Co**
Protonated Dimer D (D)					
H_{C1}-O_{C1}	0.295	0.284	0.275	0.271	0.267
H_{M1}-O_{C3}	0.162	0.154	0.160	0.157	0.148
H_{M2}-O_{C2}	0.173	0.187	0.179	0.181	0.185
H_{M1}-O_{M1}	0.101	0.103	0.102	0.103	0.105
H_{C1}-O_{M1}	0.116	0.111	0.116	0.114	0.110
H_{C1}-O_{M2}	0.127	0.134	0.127	0.130	0.136
H_{M2}-O_{M2}	0.100	0.099	0.100	0.099	0.099
O_{M1}-C_{M1}	0.146	0.146	0.146	0.146	0.146
O_{M2}-C_{M2}	0.146	0.145	0.145	0.145	0.145
Dimer Bader Charge	0.882	0.875	0.876	0.869	0.856
Protonated Dimer E (E)					
H_{C1}-O_{C1}	0.158	0.148	0.148	0.150	0.139
H_{C1}-O_{M1}	0.103	0.105	0.104	0.104	0.108
H_{M2}-O_{C3}	0.175	0.184	0.177	0.169	0.176
O_{M1}-H_{M1}	0.113	0.108	0.111	0.113	0.108
H_{M1}-O_{M2}	0.130	0.139	0.134	0.132	0.139
O_{M2}-H_{M2}	0.100	0.099	0.100	0.100	0.100
O_{M1}-C_{M1}	0.146	0.146	0.146	0.146	0.145
O_{M2}-C_{M2}	0.145	0.145	0.145	0.145	0.145
Dimer Bader Charge	0.883	0.871	0.866	0.856	0.838
Co-Adsorbed CH_3OH (F)					
H_{C1}-O_{C1}	0.112	0.110	0.110	0.108	0.105
H_{C1}-O_{M1}	0.132	0.134	0.134	0.139	0.144
C_{M1}-O_{M1}	0.147	0.146	0.146	0.146	0.146
C_{M1}-O_{M2}	0.295	0.326	0.289	0.312	0.327
O_{M2}-C_{M2}	0.143	0.143	0.143	0.143	0.143
O_{M1}-H_{M1}	0.098	0.098	0.098	0.098	0.098
H_{M1}-O_{C3}	0.271	0.262	0.276	0.224	0.271
O_{M2}-H_{M2}	0.098	0.098	0.098	0.098	0.098
H_{M2}-O_{C2}	0.222	0.208	0.215	0.203	0.223
CH_3OH_{bridge} Bader Charge	0.133	0.118	0.119	0.107	0.094
$CH_3OH_{terminal}$ Bader Charge	0.003	0.008	0.001	0.007	-0.001
DME Formation TS (TS3)					
H_{C1}-O_{C1}	0.181	0.188	0.180	0.170	0.171

H_{C1}-O_{M1}	0.100	0.099	0.100	0.101	0.101
C_{M1}-O_{M1}	0.193	0.193	0.192	0.193	0.195
C_{M1}-O_{M2}	0.200	0.201	0.199	0.198	0.198
O_{M2}-C_{M2}	0.145	0.145	0.145	0.145	0.144
O_{M1}-H_{M1}	0.098	0.098	0.098	0.098	0.098
H_{M1}-O_{C3}	0.325	0.333	0.337	0.328	0.344
O_{M2}-H_{M2}	0.099	0.100	0.100	0.100	0.100
H_{M2}-O_{C2}	0.183	0.172	0.174	0.179	0.170
Methyl Bader Charge	0.561	0.559	0.546	0.541	0.538
Water Bader Charge	0.170	0.181	0.181	0.171	0.168
CH_3OH Bader Charge	0.180	0.169	0.171	0.181	0.178
Adsorbed DME + H_2O (G)					
H_{C1}-O_{C1}	0.219	0.211	0.219	0.212	0.209
H_{C1}-O_{M1}	0.098	0.098	0.098	0.098	0.098
H_{M2}-O_{C2}	0.130	0.125	0.119	0.115	0.110
C_{M1}-O_{M1}	0.305	0.302	0.306	0.319	0.312
C_{M1}-O_{M2}	0.147	0.147	0.146	0.146	0.145
O_{M2}-C_{M2}	0.146	0.145	0.145	0.145	0.144
O_{M1}-H_{M1}	0.097	0.097	0.097	0.097	0.097
H_{M1}-O_{C3}	0.319	0.303	0.293	0.306	0.310
O_{M2}-H_{M2}	0.111	0.115	0.121	0.126	0.132
DME Bader Charge	0.170	0.158	0.158	0.140	0.129
Water Bader Charge	-0.012	-0.002	-0.004	-0.004	-0.006

[a]Atomic and structural labels correspond to diagrams in Figure 2.3b

2.6.10. Comparisons of 2-Butanol and Methanol Dehydration Activation Barriers by Thermochemical Cycles

Activation barriers for Brønsted acid catalyzed reactions involving late, ion-pair transition states are accurately described by thermochemical cycles, which take advantage of the path independence of thermodynamic functions to construct a series of hypothetical steps that form the transition state from a reacting intermediate (Section 2.3.5). Thermochemical descriptions of activation barriers for H_2O elimination ($E_{a,elim}$) from H-bonded alkanols to form alkoxides via carbenium-like transition states depend on the adsorption energy of the alkanol at a proton (ΔE_{ads}, relative to the gas-phase alkanol), the DPE of the acid, the proton affinity of gas-phase reactants to form the gas-phase analogue of the transition state (ΔE_{prot}), and the interaction energy between the transition state and catalyst conjugate base (E_{int}) (Scheme 2.4).

$$E_{a,elim} = DPE + \Delta E_{prot} + E_{int} - \Delta E_{ads} \quad \text{(S.2.28)}$$

Adsorption energies for alkanols at protons have contributions from strong H-bonds ($E_{H\text{-}Bond}$) and van der Waals interactions (E_{vdW}). Alkanol H-bonding at protons is stronger

than typical H-bonds among alkanols or H_2O, because charges on the proton lend addition electrostatic stabilization to the interaction. Transition states for H_2O elimination from alkanols resemble carbenium ions interacting with the nearby H_2O molecule. Therefore, proton affinities include contributions from the gas-phase dehydration energy of the alkanol (E_{dehy}; $ROH_{(g)} + H^+_{(g)} \rightarrow R^+_{(g)} + H_2O_{(g)}$), which forms non-interacting carbenium and H_2O fragments, and the interaction energy between the carbenium ion and H_2O (E_{water}; estimated in Section 2.6.11). The transition state interaction energy primarily reflects electrostatic stabilization between the cationic transition state and the anionic cluster ($E_{ES,POM}$), but also contains contributions from van der Waals forces. The contributions from van der Waals interactions at the transition state are similar to those in the H-bonded alkanol so that they tend to cancel out in the equation for activation barriers. Using these simplifications, activation barriers for H_2O elimination reactions become:

$$E_{a,elim} = DPE + E_{dehy} + E_{water} + E_{ES,POM} - E_{H\text{-}bond} \quad \text{(S.2.29)}$$

Differences in elimination activation barriers for CH_3OH ($E_{a,MeOH}$) and 2-butanol ($E_{a,BuOH}$) reflect the different contributions from the terms in Eq. (S.2.29) for the two alkanols. The contributions from DPE will cancel out for a given acid. The dehydration energy for CH_3OH (-485 kJ mol^{-1}) is much less exothermic than that for 2-butanol (-720 kJ mol^{-1}) and primarily reflects the lower stability of methyl ions relative to butyl ions in the gas-phase (calculations in Section 2.6.11). The disparity in dehydration energies of CH_3OH and 2-butanol is largely attenuated by the water stabilization energies because methyl cations coordinate more strongly to water than butyl cations as a result of their instability. Distances between the sp^2 hybridized C-atoms in the organic cations and O-atoms in H_2O are much shorter in CH_3OH transition states (0.193 nm; Table 2.2), relative to those for 2-butanol (0.264 nm)[49]; the effects of water coordination are modeled as ion-dipole interactions in Section 2.6.11. The stabilization of transition states by a given conjugate base is determined by the charge distribution in the respective cation, where a localized charge is stabilized more effectively than a diffuse one. H-Bonding energies for 2-butanol and CH_3OH at protons are determined by their gas-phase proton affinities (i.e. $ROH_{(g)} + H^+_{(g)} \rightarrow [ROH_2]^+_{(g)}$). (**Note:** The proton affinity used here is not the same as the proton affinity used in the thermochemical cycle for activation barriers (ΔE_{prot} in Eq. (S.2.28)). This proton affinity is merely the energy to protonate an alkanol in the gas-phase, forming an oxonium ion. Proton affinities used in thermochemical cycles also include the energy for gas-phase water elimination from oxonium ions (i.e. $[ROH_2]^+_{(g)} \rightarrow R^+_{(g)} + H_2O_{(g)}$) and water stabilization energies (E_{water}).) Proton affinities for CH_3OH (754.3 kJ mol^{-1}) and 2-butanol (793.7 kJ mol^{-1}) are similar;[54] thus, the strengths of their H-bonding energies are expected to be similar and will cancel out in differences between CH_3OH and 2-butanol activation barriers. This is also supported by calculated adsorption energies for CH_3OH and 2-butanol on Keggin protons, which are nearly equivalent for the same central atom (-75 kJ mol^{-1} and -77 kJ mol^{-1}, respectively, on $H_3PW_{12}O_{40}$).[49,62] Thus, differences in H_2O elimination activation barriers for CH_3OH and 2-butanol are:

$$E_{a,MeOH} - E_{a,BuOH} = (E_{dehy} + E_{water} + E_{ES,POM})_{MeOH} - (E_{dehy} + E_{water} + E_{ES,POM})_{BuOH} \quad \text{(S.2.30)}$$

2.6.11. Calculations of Proton Affinities and Ion-Dipole Interactions

Here we show the calculations of proton affinities that are used in thermochemical cycles of activation barriers (ΔE_{prot} in Eq. (S.2.28)) and describe the reaction between gas-phase alkanols and a proton to form the gas-phase analog of the transition state. Proton affinities include the dehydration energies of gas-phase alkanols (E_{dehy}) and the interaction between the resulting carbenium ion and H_2O or CH_3OH molecules at the transition state (E_{sol}).

$$\Delta E_{prot} = E_{dehy} + E_{sol} \quad \text{(S.2.31)}$$

(**Note:** E_{sol} in Eq. (S.2.31) is equal to E_{water} in Section 2.6.10 when the solvating molecule is H_2O.)

2.6.11.1 Gas-Phase Alkanol Dehydration Energies

Alkanol dehydration energies are defined by the gas-phase reaction between a proton and an alkanol molecule (ROH) to form H_2O and a non-interacting carbenium ion (R^+).

$$ROH_{(g)} + H^+_{(g)} \rightarrow H_2O_{(g)} + R^+_{(g)};\ E_{dehy} \quad \text{(S.2.32)}$$

Values of E_{dehy} for CH_3OH and 2-butanol were calculated from tabulated standard enthalpies of formation for these species. [46, 51]

$$E_{dehy} = \Delta H_f^0(R^+) + \Delta H_f^0(H_2O) - \Delta H_f^0(H^+) - \Delta H_f^0(ROH) \quad \text{(S.2.33)}$$

Table S.2.4 contains these standard enthalpies of formation and the calculated dehydration energies. The dehydration of 2-butanol (-720 kJ mol^{-1}) is much more exothermic than the dehydration of CH_3OH (-485 kJ mol^{-1}) because the alkyl groups of 2-butyl carbenium ions stabilize the positive charge.

Table S.2.4. Standard enthalpies of formation (in kJ mol^{-1}) involved in alkanol dehydration energies

	CH_3OH	**2-Butanol**
$\Delta H_f^0(R^+)$[a]	1092	766
$\Delta H_f^0(H_2O)$[b]	-242	-242
$\Delta H_f^0(H^+)$[a]	1536	1536
$\Delta H_f^0(ROH)$[b]	-201	-292
E_{dehy}	-485	-720

[a] Values taken from ref. [51]
[b] Values taken from ref. [46]

2.6.11.2 Carbenium Ion Stabilization Energies

Carbenium ions at dehydration transition states are stabilized by long-range ion-dipole interactions with nearby H_2O and alkanol molecules. Stabilization energies from these interactions are calculated from:

$$V(r) = \frac{-\alpha e^2}{8\pi\varepsilon_0 r^4} \qquad \text{(S.2.34)}$$

where α is the polarizability of the stabilizing molecule[50], e is an electron's charge (1.6 $x10^{-19}$ C), ε_0 is the permittivity of a vacuum (8.85 x 10^{-12} F m^{-1}) and r is the separation distance between the ion and molecule at the transition state (Tables 2.2 and 2.3). A sample of this calculation is shown below for the interaction between the H_2O and the methyl cation at the H_2O elimination transition state (TS1 in Figure 2.3a). The results for the remaining transition states are summarized in Table S.2.5.

$$V(r) = \frac{-(1.45x10^{-30}\,m^3)(1.6x10^{-19}\,C)^2}{8\pi(8.85x10^{-12}\,Fm^{-1})(1.93x10^{-10}\,m)^4} = 1.20 \text{ x } 10^{-19} \text{ J} = 72.4 \text{ kJ mol}^{-1}$$

Proton affinities for each transition state are calculated from the sum of the stabilization energy and the appropriate dehydration energy. For the DME formation transition state in the direct route (TS3 in Figure 2.3b), the stabilization energy is the sum of the interactions from both the H_2O and CH_3OH.

Table S.2.5. Ion-dipole interactions at alkanol dehydration transition states

Transition State	Stabilizing Molecule	α (10^{-30} m^3)[a]	r (10^{-10} m)[b]	E_{sol} (kJ mol^{-1})
Sequential H_2O Elimination (TS1)	H_2O	1.45	1.93	72
Sequential DME Formation (TS2)	CH_3OH	3.29	2.04	132
Direct DME Formation (TS3)	H_2O	1.45	1.92	74
Direct DME Formation (TS3)	CH_3OH	3.29	2.03	134
2-Butanol H_2O Elimination	H_2O	1.45	2.64	21

[a] Molecular polarizabilities taken from ref [50].

[b] Ion-dipole separations were taken from the optimized transition geometries calculated on $H_3PW_{12}O_{40}$ for CH_3OH dehydration. They correspond to the O_{M1}-C_{M1} and O_{M2}-C_{M1} distances in Tables 2.2 and 2.3. The separation for the 2-butanol H_2O elimination was taken from ref. [49].

2.6.11.3 Protonated Dimer Formation Energy

The protonated dimer formation energy ($\Delta E_f([CH_3OH)_2H]^+)$) is calculated from the reaction between two-gas phase CH_3OH and a proton:

$$2\ CH_3OH_{(g)} + H^+_{(g)} \rightarrow [(CH_3OH)_2H]^+_{(g)} \qquad \text{(S.2.35)}$$

The energy of this reaction is calculated from the proton affinity of a CH_3OH molecule, followed by the "clustering energy" of the resulting $[CH_3OH_2]^+$ ion with another CH_3OH molecule. Values for these quantities were obtained from tabulated thermodynamic data.[54,63]

$$\Delta E_f([CH_3OH)_2H]^+) = PA(CH_3OH) + CE([CH_3OH_2]^+) \quad \text{(S.2.36)}$$
$$\Delta E_f([CH_3OH)_2H]^+) = -754 \text{ kJ mol}^{-1} - 136 \text{ kJ mol}^{-1} = -890 \text{ kJ mol}^{-1}$$

2.6.12. Rearrangements Between Co-Adsorbed Species and Protonated Dimers

The rearrangement of a co-adsorbed species (F in Figure S.2.8 and Figure 2.3b) to a protonated dimer (D in Figure S.2.8 and Figure 2.3b) was calculated on a $H_3PW_{12}O_{40}$ cluster. Figure S.2.8 shows the energy of intermediate structures along the reaction path as function of the H_{C1}-O_{M2} distance, which is used here to denote the reaction coordinate. Atomic separations and energies of these species are located in Table S.2.6. The H_{C1}-O_{M1} distance decreases monotonically along the reaction coordinate as the proton becomes stabilized by ion-dipole interactions with the O-atoms of both CH_3OH molecules. The O_{C1}-H_{C1} distance increases concurrently as the proton is transferred from the catalyst to the dimer, which is consistent with the smaller Bader charge in the co-adsorbed species (+0.13 e) than in the protonated dimer (+0.87 e). The transition state of this reaction coordinate resembles a methoxonium ion, similar to the proton hopping reactions (Section 2.6.8), but with another CH_3OH present. The energy of this transition state is <1 kJ mol^{-1} higher than the co-adsorbed species (Table S.2.6). Thus, this rearrangement has no barrier above the difference in energies of these species and they will always be quasi-equilibrated.

Table S.2.6. Atomic distances (listed in nm) and energies (in kJ mol^{-1}) of intermediates and the transition state for rearrangements between co-adsorbed species and protonated dimers on $H_3PW_{12}O_{40}$ (Figure S.2.8).

***Species*[a]**	***Energy (kJ mol^{-1})*[b]**	***H_{C1}-O_{C1} (nm)***	***H_{C1}-O_{M1} (nm)***	***H_{C1}-O_{M2} (nm)***	***H_{M1}-O_{C3} (nm)***	***H_{M2}-O_{C2} (nm)***
Co-Adsorbed Species (F)	0.0	0.110	0.134	0.429	0.262	0.208
Rearrangement Transition State (TS)	0.0	0.158	0.104	0.290	0.168	0.176
Protonated Dimer (D)	-66.3	0.284	0.111	0.134	0.154	0.187

[a] Atomic and structural labels correspond to diagrams in Figure S.2.8.
[b] Energies are listed with respect to the co-adsorbed species (F in Figure S.2.8).

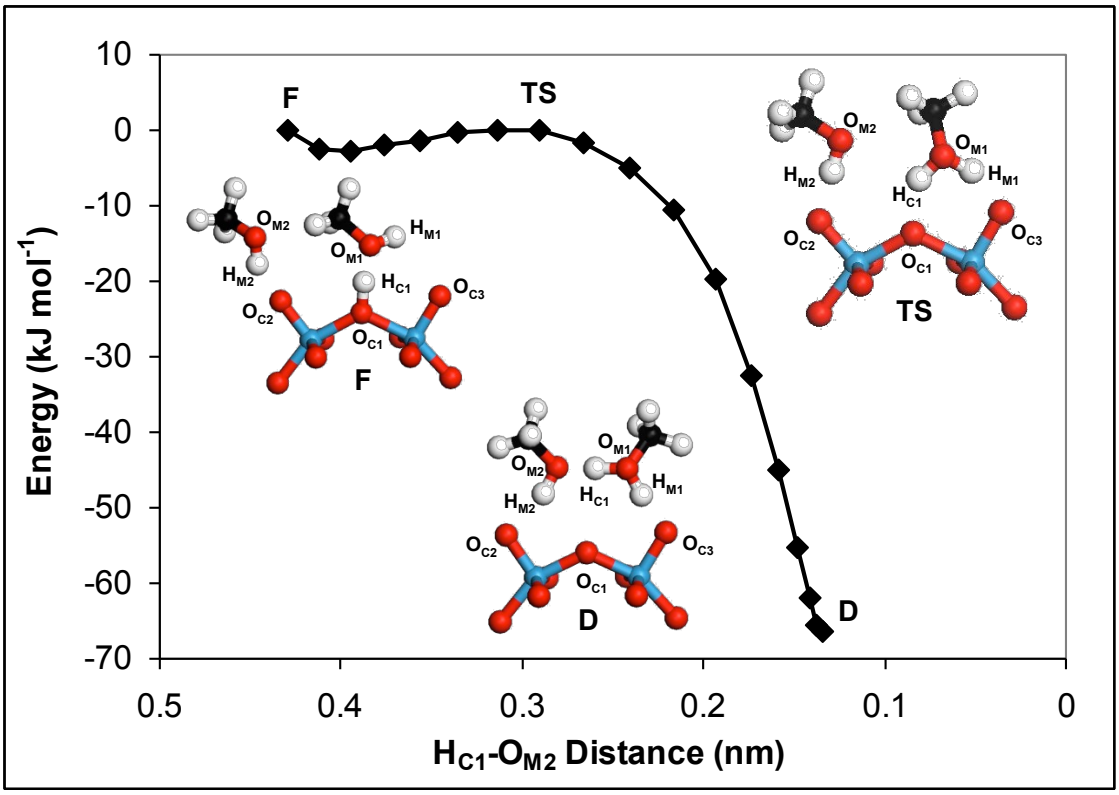

Figure S.2.8. Structures and energies of intermediates and the transition state calculated on $H_3PW_{12}O_{40}$ for rearrangements between co-adsorbed species and protonated dimers. Atomic labels correspond to those used to report the distances listed in Table S.2.6 and colors correspond to elemental identity (blue = W, red = O, white = H, black = C).

2.6.13. Formation and Reactions of Methanol Trimers

Structures of intermediates and transition states involving three CH_3OH molecules, referred to as trimers (T in Figure S.2.9), were calculated for comparison with DME formation via the sequential and direct routes. Figure S.2.9 shows the structures and energies of intermediates and the transition state for this path. Atomic labels in Figure S.2.9 are used in Table S.2.7, which lists the atomic separations in these structures and their energies (relative to the protonated dimer E and a gas-phase CH_3OH). For the ease of discussion, the positions of the three CH_3OH will be referred to as CH_3OH T-1, T-2, and T-3; these positions are labeled on structure T in Figure S.2.9. Trimers are formed from protonated dimers by adsorption of a third CH_3OH (T-3) at an adjacent POM O-atom. Protonated dimer "E" was used as the reactant for this reaction (E in Figure S.2.9) for reasons that will become apparent. The third CH_3OH adsorbs at a terminal POM O-atom (O_{C2}) vicinal to the protonated dimer by H-bonding through its hydroxyl H-atom (H_{M3}). Combined Bader charges for CH_3OH T-1 and T-2 in the trimer (+0.87 e) are equal their charges in protonated dimer E (+0.87 e), indicating that the proton remains fully transferred in the trimer, while the Bader charge on CH_3OH T-3 (+0.01 e) indicates it is neutral. The adsorption energy of CH_3OH T-3 (-18.7 kJ mol^{-1} on $H_3PW_{12}O_{40}$; Table S.2.7) is typical for H-bonds among CH_3OH (13 to 30 kJ mol^{-1})[42,

43], but is less than for T-1 and T-2 (-75 and -79 kJ mol^{-1}, respectively; Table 2.4) because of the absence of stabilizing electrostatic interactions.

The position of CH_3OH T-3 relative to CH_3OH T-1 resembles co-adsorbed species in the direct route (F in Figure 2.3b), which have the appropriate orientation for methyl transfer; the methyl group of CH_3OH T-1 is directed towards the O-atom in CH_3OH T-3 (C_{M1}-O_{M3} = 0.322 nm) because of the dipole-dipole interaction between them. Trimer structures with geometries appropriate for methyl transfer were not found for protonated dimer D (D in Figure 2.3b) because the methyl groups of its CH_3OH molecules point away from the POM surface. DME formation from trimers resembles direct methyl transfer within co-adsorbed species, as suggested above, where the C-O bond in CH_3OH T-1 elongates as the C-O bond in DME forms (C_{M1}-O_{M1} = 0.146 nm and C_{M1}-O_{M3} = 0.322 nm in trimers vs. 0.202 nm and 0.195 nm, respectively, at TS in Figure S.2.9) and as the methyl inverts to form a planar methyl at the transition state (TS in Figure S.2.9). The H-atom shared between CH_3OH T-1 and T-2 (H_{M1}) in the trimer is fully transferred to O_{M1} to form H_2O (O_{M1}-H_{M1} = 0.111 nm and O_{M3}-H_{M1} = 0.133 nm in trimers vs. 0.099 nm and 0.183 nm, respectively, in the product). Bader charges confirm this transition state as an ion-pair; the methyl cation (+0.55 e) is solvated by the O-atoms in H_2O and CH_3OH T-3 (+0.12 e and +0.19 e, respectively) via ion-dipole interactions and is stabilized by electrostatic interactions with the conjugate catalyst anion (-0.91 e). Similar to the transition state for the direct route (TS3 in Figure 2.3b), the O-atom of T-3, the methyl C-atom, and the H_2O O-atom are positioned along a line that is conducive to orbital overlap required for S_N2 reactions.

The activation barrier for this reaction (with respect to trimers) is 105 kJ mol^{-1} on $H_3PW_{12}O_{40}$ (Table S.2.7), which is approximately 30 kJ mol^{-1} higher than the activation barrier for the direct DME formation step (with respect to co-adsorbed species). DME formation from trimers is more demanding than from co-adsorbed species because electrostatic interactions in the trimers make them more stable relative to co-adsorbed species and increase their activation barrier. Thus, trimers do not stabilize transition states more than in the direct route, however, they convert protonated dimers into reactive intermediates without high energy rearrangements (Section 2.6.12). The adsorption equilibrium constant between trimers and protonated dimers (K_T) was calculated according to the methods described in Section 2.6.14. The value of the equilibrium constant (K_T = 2 x 10^{-2} kPa^{-1}) is much less than unity and indicates that trimers never reach significant surface concentrations at the CH_3OH pressures used here.

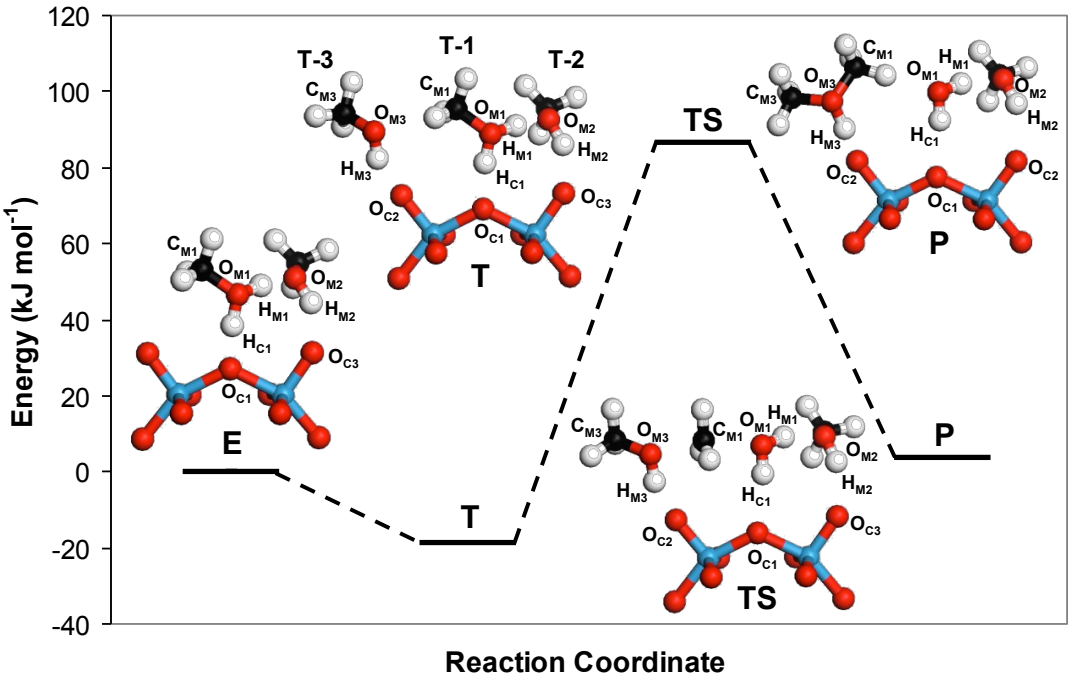

Figure S.2.9. Structures and energies of intermediates and the transition state for the formation and reaction of CH_3OH trimers on $H_3PW_{12}O_{40}$. Atomic labels correspond to those used to report the distances listed in Table S.2.7 and colors correspond to elemental identity (blue = W, red = O, white = H, black = C).

Table S.2.7. Atomic distances (listed in nm) and energies (in kJ mol^{-1}) of intermediates and the transition state for the formation and reaction of CH_3OH trimers on $H_3PW_{12}O_{40}$ (Figure S.2.9).

	Neutral Dimer (E)	*Trimer (T)*	*DME Formation Transition State (TS)*	*Adsorbed DME, H_2O, and CH_3OH (P)*
Energy (kJ mol^{-1})[a]	0.0	-18.7	86.4	3.3
H_{C1}-O_{C1}	0.148	0.161	0.210	0.210
H_{C1}-O_{M1}	0.105	0.102	0.098	0.098
O_{M1}-C_{M1}	0.146	0.146	0.202	0.305
C_{M1}-O_{M3}	- - -	0.322	0.195	0.147
O_{M3}-H_{M3}	- - -	0.098	0.100	0.111
H_{M3}-O_{C2}	- - -	0.207	0.170	0.131
O_{M1}-H_{M1}	0.108	0.111	0.102	0.099
H_{M1}-O_{M2}	0.139	0.133	0.160	0.183
O_{M2}-H_{M2}	0.099	0.100	0.098	0.098
H_{M2}-O_{C2}	0.184	0.177	0.196	0.208

[a]Atomic and structural labels correspond to diagrams in Figure S.2.9.

[b] Energies are listed with respect to protonated dimer E (E in Figure S.2.9) and a gas-phase CH_3OH.

2.6.14. Calculations of Rate and Equilibrium Constants in Sequential and Direct Dehydration Routes

Here we show details of the calculations for rate and equilibrium constants involved in the direct and sequential routes for CH_3OH dehydration using statistical descriptions of entropy and DFT-derived energies of intermediates and transition states. All calculations shown here are done at 433 K where most of the rate data was measured. Equilibrium constants for the reaction between *M* reactants to form *N* products were calculated from statistical mechanics:

$$K_{eq} = \frac{\prod_{j=1}^{N} (Q/V)_j}{\prod_{i=1}^{M} (Q/V)_i} \exp\left(\frac{-\Delta E_{rxn}}{RT}\right) \tag{S.2.37}$$

where Q/V is the total partition function per unit volume, ΔE_{rxn} is the change in energy of the reaction, R is the universal gas constant (8.314 J mol^{-1} K^{-1}), and T is the absolute temperature. The total partition function for a given species is the product of the translational (q_{trans}/V), rotational (q_{rot}), and vibrational (q_{vib}) partition functions:

$$(Q/V) = \frac{q_{trans}}{V} q_{rot} q_{vib} \tag{S.2.38}$$

The partition function (per unit volume) for three degrees of translational freedom is:

$$\frac{q_{trans}}{V} = \frac{(2\pi m k_B T)^{3/2}}{h^3} \tag{S.2.39}$$

where m is the mass of the species, k_B is the Boltzmann constant (1.38 x 10^{-23} J K^{-1}), and h is Planck's constant (6.63 x 10^{-34} J s). The partition function of a degree of rotational freedom for a non-linear molecule is:

$$q_{rot,i} = \frac{k_B T}{hcB_i} \tag{S.2.40}$$

where B_i is the rotational constant and c is the speed of light (3 x 10^8 m s^{-1}). The partition function for a degree of vibrational freedom is:

$$q_{vib,i} = \frac{1}{1 - \exp\left(\frac{-h\nu_i}{k_B T}\right)} \tag{S.2.41}$$

where ν_i is the frequency of the vibration. The values of these individual partition functions are calculated in Sections 2.6.14.3. Rate constants for the reaction between *M* reactants leading to the transition state (TS) were calculated from transition state theory [55]:

$$k = \frac{k_B T}{h} \frac{(Q/V)_{TS}'}{\prod_{i=1}^{M} (Q/V)_i} \exp\left(\frac{-E_a}{RT}\right) \tag{S.2.42}$$

The prime in the numerator of the second term is used to denote that the weak vibrational mode corresponding to the reaction coordinate has been removed from the partition function.

2.6.14.1. Equilibrium Constants in Sequential and Direct CH_3OH Dehydration Routes

Equilibrium constants for the adsorption of CH_3OH molecules at acid sites were calculated by applying Eq. (S.2.37) to the reaction between a gas-phase CH_3OH molecule and bare POM to form an adsorbate-POM complex (ads-POM).

$$K_{ads} = \frac{\left(\frac{q_{trans}}{V} q_{rot} q_{vib}\right)_{ads-POM}}{\left(\frac{q_{trans}}{V} q_{rot} q_{vib}\right)_{POM} \left(\frac{q_{trans}}{V} q_{rot} q_{vib}\right)_{CH_3OH}} \exp\left(\frac{-\Delta E_{ads}}{RT}\right) \tag{S.2.43}$$

where ΔE_{ads} is the adsorption energy calculated by DFT. For the calculations reported here, we assume that the internal vibrations of the POM cluster and CH_3OH are not significantly perturbed by the adsorption of a CH_3OH molecule and therefore their partition functions cancel out in the numerator and denominator of Eq. (S.2.43). The translational and rotational partition functions for the POM and the adsorbate-POM complex also cancel out because the mass of the POM is much larger than that of the adsorbate. These simplifications reduce Eq. (S.2.43) and show that CH_3OH adsorption transforms 3 translational and 3 rotational degrees of freedom for gas-phase CH_3OH into 6 vibrations relative to the surface.

$$K_{ads} = \frac{\left(q_{vib}^6\right)_{ads-POM}}{\left(\frac{q_{trans}^3}{V} q_{rot}^3\right)_{CH_3OH}} \exp\left(\frac{-\Delta E_{ads}}{RT}\right) \tag{S.2.44}$$

Although this derivation was done for CH_3OH adsorption at bare proton, the results are general for CH_3OH adsorption to sites that already occupied by other surface intermediates (i.e. adsorption at monomers to form dimers or at methoxides to form methoxide/CH_3OH pairs). The only difference is that the bare POM partition functions

are replaced by those for the reactant intermediate and the adsorbate-POM partition functions are replaced by the product intermediate. Eq. (S.2.44) was used to calculate the adsorption equilibrium constant for an immobile surface species (i.e. methoxide/CH_3OH pairs), however, many of the intermediates in dehydration pathways (i.e. monomers) have significant surface mobility because of proton hopping reactions (Section 2.6.8). In these cases, two of the vibrations in the adsorbate-POM complex are modeled as two-dimensional hindered translations across the surface [55] (q'_{trans}; calculations in Section 2.6.14.3).

$$K_{ads} = \frac{\left(q'^{2}_{trans}\, q^{4}_{vib}\right)_{ads-POM}}{\left(\frac{q^{3}_{trans}}{V} q^{3}_{rot}\right)_{CH_3OH}} \exp\left(\frac{-\Delta E_{ads}}{RT}\right) \qquad \text{(S.2.45)}$$

2.6.14.2. Rate Constants in Sequential and Direct CH_3OH Dehydration Routes

All rate constants calculated for sequential and direct rates were calculated from the transition state theory equation for a unimolecular reaction [55]:

$$k = \frac{k_B T}{h}\left(\frac{1}{q_{vib}}\right)\exp\left(\frac{-E_a}{RT}\right) \qquad \text{(S.2.46)}$$

where q_{vib} is the partition function of the vibration in the reacting intermediate that will become the imaginary vibration along the reaction coordinate at the transition state. This equation assumes that the vibrations normal to the reaction coordinate are unchanged between the reacting intermediate and transition state. For elimination and DME formation rate constants, E_a is the activation barrier calculated from DFT that is measured relative to the reacting intermediate that directly proceeds the transition state along the reaction coordinate. For CH_3OH desorption rate constants, E_a is assumed as the full adsorption energy of that CH_3OH molecule.

2.6.14.3. Calculations of Partition Functions

The translational and rotational partition functions for gas-phase CH_3OH molecules can be calculated exactly because of their known mass (5.3×10^{-26} kg) and rotational constants (4.2 cm^{-1}, 0.82 cm^{-1}, and 0.79 cm^{-1}).[64] The partition function (per unit volume) for three degrees of translation freedom at 433 K is:

$$\frac{q_{trans}}{V} = \frac{(2\pi * 5.3\text{x}10^{-26}\,\text{kg} * 1.38\text{x}10^{-23}\,\text{JK}^{-1} * 433\text{K})^{3/2}}{(6.63\text{x}10^{-34}\,\text{Js})^{3}} = 3.0 \text{ x } 10^{32}$$

The partition function for the degree of rotational freedom corresponding to $B_i = 4.2$ cm^{-1} is:

$$q_{rot} = \frac{1.38x10^{-23}\,JK^{-1} * 433K}{6.63x10^{-34}\,Js * 3x10^{10}\,cms^{-1} * 4.2cm^{-1}} = 72$$

The partition functions for B_i = 0.82 cm^{-1} and 0.79 cm^{-1} are 370 and 380, respectively.

Vibrational partition functions are more difficult to calculate because they require sophisticated calculations of structures to obtain the vibrational frequencies. Order of magnitude estimates have been used in lieu of these frequency calculations so that each degree of vibrational freedom is equal to 1.[55] The values of vibrational partition functions corresponding to hindered translations were estimated from the results of proton hopping reactions to calculate the frequencies of surface translations (ν_{st}).[55]

$$\nu_{st} = \sqrt{\frac{2E_d}{\lambda_d m}} \qquad \text{(S.2.47)}$$

where E_d is the diffusion activation barrier, λ_d is the jump length, and m is the mass of the diffusing species. The activation barrier for proton hopping was used as E_d (11 kJ mol^{-1}; Table S.2.1) and λ_d was taken as distance between bridging and terminal POM O-atoms (0.28 nm).

$$\nu_{st} = \sqrt{\frac{2 * 1.1x10^{4}\,Jmol^{-1}}{2.8x10^{-10}\,m * 3.3x10^{-2}\,kgmol^{-1}}} = 4.9 \text{ x } 10^{7}\ s^{-1}$$

The partition function for surface translation is estimated from this frequency by using Eq. (S.2.41). [55]

$$q'_{trans} = \frac{1}{1 - \exp\left(\frac{-6.63x10^{-34}\,Js * 4.9x10^{7}\,s^{-1}}{1.38x10^{-23}\,JK^{-1} * 433K}\right)} = 1.8 \text{ x } 10^{5}$$

For several of the adsorbate-POM complexes, one vibrational mode relative to the surface is a hindered rotation about an axis normal to the surface. This rotation was accounted for by replacing the partition function of one degree of vibrational freedom by the rotational partition function corresponding to B_i = 4.2 cm^{-1} (q_{rot} = 72).

2.6.14.4. Calculated Values for Rate and Equilibrium Constants

Below are sample calculations for each type of rate parameter estimation, using the aforementioned methods. All sample calculations are for $H_3PW_{12}O_{40}$ clusters at 433 K. The results of the remaining calculations are summarized in Tables S.2.8 and S.2.9 for the sequential and direct routes, respectively. The adsorption equilibrium constant for the monomer is calculated from Eq. (S.2.45):

$$K_M = \frac{(1.8x10^5)^2 * 72 * 1^3}{3.0x10^{32}\,m^{-3} * 72 * 370 * 380} \exp\left(\frac{-\Delta E_{ads}}{RT}\right) = 7.7x10^{-28} \exp\left(\frac{-\Delta E_{ads}}{RT}\right) m^3$$

This equilibrium constant is in terms of molecular concentration (molecules per volume) and must be converted to units of pressure to compare it to measured rate data. This is done by dividing the values above by the product k_BT according to the ideal gas law.

$$K_M = \frac{7.7x10^{-28}\,m^3}{1.38x10^{-23}\,JK^{-1} * 433K} \exp\left(\frac{74.6kJmol^{-1}}{8.31x10^{-3}\,kJmol^{-1}K^{-1} * 433K}\right)$$
$$= 1.3 \text{ x } 10^2 \text{ Pa}^{-1} = 1.3 \text{ x } 10^5 \text{ kPa}^{-1}$$

The equilibrium constant for the formation of methoxide/CH_3OH pairs was done similarly, except that they do not have hindered translations (Eq. (S.2.44)).

$$K_M = \frac{72 * 1^5}{3.0x10^{32}\,m^{-3} * 72 * 370 * 380} \exp\left(\frac{-\Delta E_{ads}}{RT}\right) = 2.2x10^{-38} \exp\left(\frac{-\Delta E_{ads}}{RT}\right) m^3$$

$$K_M = \frac{2.2x10^{-38}\,m^3}{1.38x10^{-23}\,JK^{-1} * 433K} \exp\left(\frac{17.4kJmol^{-1}}{8.31x10^{-3}\,kJmol^{-1}K^{-1} * 433K}\right)$$
$$= 4.6 \text{ x } 10^{-16} \text{ Pa}^{-1} = 4.6 \text{ x } 10^{-13} \text{ kPa}^{-1}$$

The H_2O elimination rate constant was calculated from the transition state theory equation for a unimolecular reaction (Eq. (S.2.46)).

$$k_{elim} = \frac{1.38x10^{-23}\,JK^{-1} * 433K}{6.63x10^{-34}\,Js}\left(\frac{1}{1}\right)\exp\left(\frac{-143.3kJmol^{-1}}{8.31x10^{-3}\,kJmol^{-1}K^{-1} * 433K}\right) = 4.6 \text{ x } 10^{-5} \text{ s}^{-1}$$

Table S.2.8. Calculated rate and equilibrium constants for the sequential CH_3OH dehydration route (Scheme 2.1)

		POM Central Atom				
Reaction Step[a]	**Partition Functions[b]**	**S**	**P**	**Si**	**Al**	**Co**
Monomer Adsorption (Step 1)						
ΔE_{ads} (kJ mol^{-1})	- - -	-72.5	-74.6	-66.4	-63.5	-61.7
K_M (kPa^{-1})	1.3 x 10^{-4}	7.2 x 10^{4}	1.3 x 10^{5}	1.3 x 10^{4}	5.9 x 10^{3}	3.6 x 10^{3}
$E_{a,des}$ (kJ mol^{-1})	- - -	72.5	74.6	66.4	63.5	61.7
k_{-M} (s^{-1})	9.0 x 10^{12}	1.6 x 10^{4}	9.0 x 10^{3}	8.9 x 10^{4}	2.0 x 10^{5}	3.3 x 10^{5}
H_2O Elimination (Step 2)						
$E_{a,elim}$ (kJ mol^{-1})	- - -	139.4	143.3	144.0	140.4	166.3
k_{elim} (s^{-1})	9.0 x 10^{12}	1.4 x 10^{-4}	4.6 x 10^{-5}	3.8 x 10^{-5}	1.0 x 10^{-4}	7.8 x 10^{-8}
$E_{a,-elim}$ (kJ mol^{-1})	- - -	77.3	85.9	96.8	92.4	122.8
k_{-elim} (kPa^{-1} s^{-1})	1.2 x 10^{-2}	5.6 x 10^{-12}	5.3 x 10^{-13}	2.5 x 10^{-14}	8.6 x 10^{-14}	1.9 x 10^{-17}
Methoxide/CH_3OH Pair Formation (Step 3)						
ΔE_{ads} (kJ mol^{-1})	- - -	-13.2	-17.4	-16.7	-20.4	-16.1
K_P (kPa^{-1})	3.7 x 10^{-15}	1.5 x 10^{-13}	4.6 x 10^{-13}	3.8 x 10^{-13}	1.1 x 10^{-12}	3.3 x 10^{-13}
$E_{a,des}$ (kJ mol^{-1})	- - -	13.2	17.4	16.7	20.4	16.1
k_{-P} (s^{-1})	9.0 x 10^{12}	2.3 x 10^{11}	7.2 x 10^{10}	8.7 x 10^{10}	3.1 x 10^{10}	1.0 x 10^{11}
DME Formation (Step 4)						
$E_{a,DME}$ (kJ mol^{-1})	- - -	72.9	85.4	89.4	99.7	118.6
$k_{DME,s}$ (s^{-1})	9.0 x 10^{12}	1.4 x 10^{4}	4.5 x 10^{2}	1.5 x 10^{2}	8.4	4.5 x 10^{-2}
$E_{a,-DME}$ (kJ mol^{-1})	- - -	134.7	136.1	138.5	145.0	160.1
$k_{-DME,s}$ (s^{-1})	9.0 x 10^{12}	5.1 x 10^{-4}	3.4 x 10^{-4}	1.8 x 10^{-4}	2.9 x 10^{-5}	4.3 x 10^{-7}
DME Desorption (Step 5)						
$E_{a,des}$ (kJ mol^{-1})	- - -	74.8	74.7	74.3	70.6	65.3
k_{des} (s^{-1})	9.0 x 10^{12}	8.5 x 10^{3}	8.8 x 10^{3}	9.7 x 10^{3}	2.7 x 10^{4}	1.2 x 10^{5}

[a] Rate constants, equilibrium constants, and reaction steps correspond to the elementary steps in Scheme 2.1.

[b] Partition functions correspond to the terms before the exponential in Eqs. (S.2.37) and (S.2.42).

Table S.2.9. Calculated rate and equilibrium constants for the direct CH_3OH dehydration route (Scheme 2.2)

Reaction Step[a]	Partition Functions[b]	POM Central Atom S	P	Si	Al	Co
Monomer Adsorption (Step 1)						
ΔE_{ads} (kJ mol^{-1})	- - -	-72.5	-74.6	-66.4	-63.5	-61.7
K_M (kPa^{-1})	1.3 x 10^{-4}	7.2 x 10^{4}	1.3 x 10^{5}	1.3 x 10^{4}	5.9 x 10^{3}	3.6 x 10^{3}
$E_{a,des}$ (kJ mol^{-1})	- - -	72.5	74.6	66.4	63.5	61.7
k_{-M} (s^{-1})	9.0 x 10^{12}	1.6 x 10^{4}	9.0 x 10^{3}	8.9 x 10^{4}	2.0 x 10^{5}	3.3 x 10^{5}
Dimer Formation (Step 2)						
ΔE_{ads} (kJ mol^{-1})	- - -	-82.8	-80.5	-77.2	-71.0	-61.6
K_D (kPa^{-1})	1.3 x 10^{-4}	1.3 x 10^{6}	6.6 x 10^{5}	2.7 x 10^{5}	4.8 x 10^{4}	3.5 x 10^{3}
$E_{a,des}$ (kJ mol^{-1})	- - -	82.8	80.5	77.2	71.0	61.6
k_{-D} (s^{-1})	9.0 x 10^{12}	9.1 x 10^{2}	1.8 x 10^{3}	4.3 x 10^{3}	2.4 x 10^{4}	3.4 x 10^{5}
Dimer Rearrangement (Step 3)						
ΔE (kJ mol^{-1})	- - -	66.7	66.3	56.0	35.0	40.4
K_C (unitless)	1	8.9 x 10^{-9}	1.0 x 10^{-8}	1.8 x 10^{-7}	6.0 x 10^{-5}	1.3 x 10^{-5}
$E_{a,des}$ (kJ mol^{-1})	- - -	-66.7	-66.3	-56.0	-35.0	-40.4
k_{-C} (s^{-1})	9.0 x 10^{12}	1.0 x 10^{21}	9.0 x 10^{20}	5.1 x 10^{19}	1.5 x 10^{17}	6.8 x 10^{17}
DME Formation (Step 4)						
$E_{a,DME}$ (kJ mol^{-1})	- - -	71.3	75.0	77.4	99.5	95.7
$k_{DME,d}$ (s^{-1})	9.0 x 10^{12}	2.3 x 10^{4}	8.0 x 10^{3}	4.1 x 10^{3}	8.8	26
$E_{a,-DME}$ (kJ mol^{-1})	- - -	68.1	71.5	74.7	81.2	88.7
$k_{-DME,d}$ (kPa^{-1} s^{-1})	1.2 x 10^{-2}	7.3x10^{-11}	2.8x10^{-11}	1.2x10^{-11}	1.9x10^{-12}	2.4x10^{-13}
DME Desorption (Step 5)						
$E_{a,des}$ (kJ mol^{-1})	- - -	74.8	74.7	74.3	70.6	65.3
k_{des} (s^{-1})	9.0 x 10^{12}	8.5 x 10^{3}	8.8 x 10^{3}	9.7 x 10^{3}	2.7 x 10^{4}	1.2 x 10^{5}
Apparent Rate Constants						
k_{mono} (kPa^{-1} s^{-1})	1.2 x 10^{9}	2.6 x 10^{2}	53	2.0 x 10^{2}	26	1.2
k_{dimer} (s^{-1})	9.0 x 10^{12}	2.0 x 10^{-4}	8.0 x 10^{-5}	7.2 x 10^{-4}	5.3 x 10^{-4}	3.4 x 10^{-4}

[a] Rate constants, equilibrium constants, and reaction steps correspond to the elementary steps in Scheme 2.2.

[b] Partition functions correspond to the terms before the exponential in Eqs. (S.2.37) and (S.2.42).

2.7. References

[1] D. S. Santilli, B. C. Gates. In *Handbook of Heterogeneous Catalysis,* G. Ertl, H. Knözinger, J. Weitkamp, Eds., Wiley-VCH, Weinheim, 1997, Vol.3, p. 1123.

[2] J. Macht, M.J. Janik, M. Neurock, E. Iglesia, Angew. Chem. Int., Ed. 46 (2007) 7864.

[3] M. Brändle and J. Sauer J. Am. Chem. Soc. 120 (1998) 1556.

[4] I.A. Koppel, P. Burk, I. Koppel, I. Leito, T. Sonoda, M. Mishima, J. Am. Chem. Soc. 122 (2000) 5114.
[5] A. Zecchina, S. Bordiga, G. Spoto, D. Scarano, G. Spano, F. Geobaldo, J. Chem. Soc., Faraday Trans. 92 (1996) 4863.
[6] M. Hunger, Catal. Rev. – Sci. Eng. 39 (1997) 345.
[7] H. Karge, V. Dondur, J. Phys. Chem. 94 (1990) 765.
[8] D. T. Chen, L. Zhang, C. Yi, J.A. Dumesic, J.Catal. 146 (1994) 257.
[9] J. Macht, R.T. Carr, E. Iglesia, J. Am. Chem. Soc. 131 (2009) 6554.
[10] E.G. Derouane, J.B. Nagy, P. Dejaifve, J.H.C. van Hooff, B. P. Spekman, J.C. Védrine, C. Naccache, J. Catal. 53 (1978) 40.
[11] P. Cheung, A. Bhan, G. Sunley, E. Iglesia, Angew. Chem., Int. Ed. 45 (2006) 1617.
[12] J. Ahn, B. Temel, E. Iglesia, Angew. Chem., Int. Ed. 48 (2009) 3814.
[13] J.J. Cowan, C.L. Hill, R.S. Reiner, I.A.Weinstock, Inorg. Synth. 33 (2002) 18.
[14] L.C. Baker, T.P. McCutcheon, J. Am. Chem. Soc. 78 (1956) 4503.
[15] L.C. Baker, T.P. McCutcheon, J. Am. Chem. Soc. 72 (1950) 2374.
[16] G. Kresse, J. Hafner, Phys. Rev. B. 47 (1993) 558; G. Kresse, J. Furthmuller, Comput. Mater. Sci. 6 (1996) 15; G .Kresse, J. Furthmuller, Phys. Rev. B 54 (1996) 11169.
[17] D. Vanderbilt, Phys. Rev. B 41 (1990) 7892.
[18] J.P. Perdew, J.A. Chevary, S.H. Vosko, K.A. Jackson, M.R. Pederson, D.J. Singh, C. Fiolhais, Phys. Rev. B 46 (1992) 6671.
[19] H. Jonsson, G. Mills, and K.W. Jacobsen, *Classical and Quantum Dynamics in Condensed Phase Simulations*, B.J. Berne, G. Coccotti, D.F. Coker, Eds., Kluwer Academic: New York, 1998, pp 385.
[20] G. Henkelman, H. Jonsson, J. Chem. Phys. 111 (1999) 7010.
[21] R. Bader, *Atoms in Molecules: A Quantum Theory*, Oxford University Press: New York, 1990.
[22] G. Henkelman, A. Arnaldsson, H. Jonsson, Comput. Mater. Sci. 36 (2006) 354.; E. Sanville, S.D. Kenny, R. Smith, G. Henkelman, J. Comput. Chem. 28 (2007) 899.
[23] C.D. Baertsch, K.T. Komala, Y.-H. Chua, E. Iglesia, J. Catal. 205 (2002) 44.
[24] M.V. Luzgin, M.S. Kazantsev, W. Wang, A. Stepanov, J. Phys. Chem. C 113 (2009) 19639.
[25] H. Hayashi, J.B. Moffat, J. Catal. 77 (1982) 473.; J.G. Highfield, J.B. Moffat, J. Catal. 95 (1985) 108.; J.G. Highfield, J.B . Moffat, J. Catal. 98 (1986) 245.
[26] Z. Qinwei, D. Jingfa, J. Catal. 116 (1989) 298.
[27] P. Salvador, W. Kladnig, J. Chem. Soc., Faraday Trans. I, 73 (1977) 1153.
[28] E.G. Derouane, P. Dejaifve, J.B. Nagy, J. Mol. Catal. 3 (1977/78) 453.
[29] Y. Ono, T. Mori, J. Chem. Soc., Faraday Trans. I, 77 (1981) 2209.
[30] S.R. Blaszkowski, R.A. van Santen, J. Phys. Chem. 99 (1995) 11728.
[31] C.M. Zicovich-Wilsom, P. Viruela, A. Corma, J. Phys. Chem. 99 (1995) 13224.
[32] P.E. Sinclair, C.R.A. Catlow, J. Chem. Soc. Faraday Trans. 92 (1996) 2099.
[33] S.R. Blaszkowski, R.A. van Santen, J. Am. Chem. Soc. 118 (1996) 5152.
[34] S.R. Blaszkowski, R.A. van Santen, J. Phys. Chem. B 101 (1997) 2292.

[35] M.J. Janik, R.J. Davis, M. Neurock, J. Am. Chem. Soc. 127 (2005) 5238.
[36] M. Anderson, J. Klinowski, J. Am. Chem. Soc. 112 (1990) 10.
[37] C. Tsiao, D. Corbin, C. Dybowski, J. Am. Chem. Soc. 112 (1990) 7140.
[38] A. Ison, R.J. Gorte, J. Catal. 89 (1984) 150
[39] G. C. Pimentel, A.L. McClellan, Annu. Rev. Phys. Chem. 22 (1971) 347.
[40] G. C. Pimentel, A.L. McClellan, *The Hydrogen Bond*, Freeman: San Francisco, 1960.
[41] J.S. Rowlinson. Trans. Farad. Soc. 45 (1949) 974.
[42] J.D. Lambert, Discussions Faraday Soc. 15 (1953) 226.
[43] J.D. Lambert, G.A.H. Roberts, J.S. Rowlinson, V.J. Wilkinson, Proc. Roy. Soc. (London) 196A (1949) 113.
[44] J.D. Gale, C.R Catlow, A.K. Cheetam, J. Chem. Soc., Chem. Commun. 31 (1991) 3083.
[45] V.I. Minkin, B. Ya. Simkin, R.M. Minyaev, *Quantum Chemistry of Organic Compounds – Mechanisms of Reactions,* Springer-Verlag: Berlin, 1990, p. 116.; S. Shaik, H.B. Schlegel, S. Wolfe, *Theoretical Aspects of Physical Organic Chemistry-the S_N2 Mechanism*, John Wiley & Sons: New York, 1992.; M.N. Glukhovtsev, A. Pross, L. Radom, J. Am. Chem. Soc. 117 (1995) 2024.
[46] D. R. Stull, E.F. Westrum, G.C. Sinke, *The Chemical Thermodynamics of Organic Compounds*, Wiley: New York, 1987.
[47] R.A. van Santen, M. Neurock, *Molecular Heterogeneous Catalysis: A Mechanistic and Computational Approach*, VCH-Wiley, Inc., 2006.
[48] J. Macht, M.J. Janik, M. Neurock, E. Iglesia, J. Am. Chem. Soc. 130 (2008) 10369.
[49] M.J. Janik, J. Macht, E. Iglesia, M. Neurock, J. Phys. Chem. C 113 (2009) 1872.
[50] T.M. Miller, *CRC Handbook of Chemistry and Physics*, 77th Ed., D.R. Lide, Ed., CRC Press, Inc.: Boca Raton, 1996, pp 10-199 -10-213 .
[51] D.H. Aue, M.T. Bowers, *Gas Phase Ion Chemistry*, Vol.2, Academic Press: New York, 1979, pp 1-51.
[52] P. Kebarle, *Ions and Ion Pairs in Organic Reactions*, Vol. 1, M. Szwarc, Ed., John Wiley & Sons: New York, 1972, pp 27-83.
[53] P. Kebarle, R.N. Haynes, J.G. Collins, J. Am. Chem. Soc. 89 (1967) 5753.
[54] E. Hunter, S. Lias, J. Phys. Chem. Ref. Data. 27 (1998) 413.
[55] J.A. Dumesic, D.F. Rudd, L.M. Aparicio, J.E. Rekoske, A.A. Treviño, *The Microkinetics of Heterogeneous Catalysis*, ACS Publishing: Washington, DC, 1993, p. 35.
[56] M.T. Aronson, R.J. Gorte, W.E. Farneth, J. Catal. 98 (1986) 434.
[57] P.W. Ayers, R.G. Carr, R.C. Pearson. J. Chem. Phys. 124 (2006) 194107.
[58] S. Svelle, C. Tuma, X. Rozanska, T. Kerber, J. Sauer, J. Am. Chem. Soc. 131 (2009) 816.
[59] J. Macht, R. Carr, E. Iglesia, J. Catal. 264 (2009) 54.
[60] R. Massart, R. Contant, J.M. Fruchart, J.P. Ciabrini, M. Fournier, Inorg. Chem. 16 (1977) 2916.
[61] K. Yoo, P. Smirniotis, Appl. Catal., A 227 (2002) 171.

[62] This assumes that calculated adsorption energies contain equal contributions from van der Waals interactions.
[63] M. Meot-Ner, J. Am. Chem. Soc. 114 (1992) 3312.
[64] Calculated Rotational Constants for CH_3OH. *National Institute of Standards and Technology*, *Computational Chemistry Comparison and Benchmark Database* [Online] 2002. http://cccbdb.nist.gov/rotcalc2.asp (accessed April 2010).

Chapter 3

Effects of Acid Strength and Solvation on the Isomerization of Hexane Isomers on Solid Brønsted Acids

Abstract

The effects of acid strength and confinement on reactivity are probed using 2-methylpentane (2MP), 3-methylpentane (3MP), 2,3-dimethylbutane (23DMB), and n-hexane (nH) isomerization routes on well-defined solid Brønsted acids, whose known structures permit reliable calculations of deprotonation energies (DPE) from theory as measures of acid strength. Isomerization rate data for each alkane reactant and titrations that count the number of reactive protons (H^+) were measured on Keggin polyoxometalate (POM) clusters and zeolite BEA in bifunctional mixtures with Pt/Al_2O_3 co-catalysts that equilibrate dehydrogenation-hydrogenation reactions. Mechanism-based interpretations of turnover rates suggest that alkenes interconvert at acid sites via analogous paths in which alkoxide backbone isomerization is kinetically-relevant and lead to similar rate expressions for the different reactants. Measured isomerization rate constants of alkenes ($k_{isom}K_{prot}$) decreased exponentially with increasing DPE on Keggin POM clusters for all reactants; their isomerization rate constants sensed DPE changes similarly despite having very different values. Deprotonation and the formation of ion-pair isomerization transition states both form less stable conjugate anions with higher anionic charge densities on weaker acids and cause larger activation energies and lower rate constants on weaker acids than stronger acids. Changes in activation energies inferred from $k_{isom}K_{prot}$ values suggest activation energies are strongly attenuated to DPE values because electrostatic interactions between the anionic and cationic moieties at ion-pair transition states recover most of the additional energy needed to deprotonate weaker acids. The similar charge distributions of cyclopropyl carbenium ions at all isomerization transition states recover electrostatic interactions equally well and lead to the equivalent effects of DPE for all reactants. Isomerization rate constants measured on zeolite BEA were at least a factor of 1.6 higher than the values predicted for a POM with the same DPE value for all reactants because van der Waals interactions stabilize transition states, but not unconfined gas-phase reactant alkenes. Confinement within BEA solvates alkyl shift transition states preferentially over those that change the number of alkyl groups and also stabilizes less branched transition states over more branched transition states. The results of this study suggest changing acid strength alone cannot lead to more selective isomerization conversions, because all isomerization transition states contain cations with similar charge distributions; however, tailoring microporous environments to solvate specific backbone rearrangements may make lead to more selective isomerizations.

3.1. Introduction

Catalysis by solid Brønsted acids is relevant in many industrial processes [1], but rigorous connections between the structure and strength of acid sites and their consequences for reactivity remain imprecise and often contradictory. The prevailing uncertainties about the number and structure of acid sites during catalysis, the challenges

in assessing acid strength unambiguously, and measured rates that are seldom interpreted in terms of chemical mechanisms have contributed to long-standing controversies about the consequences of acid strength and solvation, which reflect electrostatic and van der Waals interactions, respectively, for reactivity. Deprotonation energies (DPE) reflect the interactions between a proton (H^+) and the conjugate anion that must be overcome for H^+ removal and are a probe-independent measure of acid strength. DPE values can be estimated using density functional theory (DFT) for well-defined solid acids, such as Keggin polyoxometalate (POM) clusters (1087 – 1143 kJ mol^{-1} for P, Si, Al and Co central atoms) and zeolites (1171 -1200 kJ mol^{-1} for CHA, FAU, MOR, MFI), because of their known crystalline structures [2, 3, 4].

Alkanol dehydration [3, 5, 6] and n-hexene isomerization [7] rate constants (per accessible H^+) on Keggin polyoxometalates (POM) ($H_{8-n}X^{n+}W_{12}O_{40}$; X = P, Si, Al, Co in order of increasing DPE) and acid forms of zeolites showed that ion-pair transition states on stronger acids contain more stable conjugate anions than on weaker acids and lead to kinetically-relevant steps with lower activation energies. The sensitivities of these steps to acid strength depend on differences in the amount and localization of the cationic charges at transition states and in precursors involved in activation energies [6, 7]. Cations with localized charges and close proximities to anions resemble H^+ and interact most effectively with anions via electrostatic interactions. Proton-like transition states recover most of the electrostatic interactions lost during H^+ removal, which determine DPE values, and lead to reactions that are less sensitive to DPE. Reactions are less sensitive to acid strength when transition states are measured with respect to charged intermediates instead of uncharged intermediates, because the stabilities of charged intermediates and transition states depend similarly on the catalyst's ability to separate charges [6]. Confinement of acid sites within voids of molecular size stabilize preferentially those intermediates and transition states that fit within zeolite voids through van der Waals interactions; such effects cause zeolites to have lower activation energies than POM clusters with similar DPE values when transition states fit more precisely within such voids than their precursors [6]. The stabilities of gaseous analogs of transition state cations determine the demanding or facile nature of reactions and do not directly determine the sensitivity of such reactions to acid strength or confinement [7].

Here, we examine the implications of acid strength and of solvation by confinement for isomerization rates of C_6 alkanes with different backbone structures on bifunctional catalyst mixtures containing well-defined Brønsted acids. Pt/Al_2O_3 co-catalysts equilibrate alkanes and alkenes via rapid hydrogenation-dehydrogenation reactions and alkenes that subsequently isomerize at acid sites via backbone rearrangements [8, 9, 10]. Isomerization rate constants for 2-methylpentene, 3-methylpentene, 2,3-dimethylbutene, and n-hexene are obtained by interpreting rate data in mechanistic terms and by titrating Brønsted acid sites with organic bases during catalysis. The effects of acid strength on all isomerization rate constants suggest their activation energies increase with DPE on Keggin POM clusters because conjugate anions present at ion-pair isomerization transition states are less stable for weaker acids. Transition states that mediate 23DMB and nH isomerization are less stable than those required for 2MP-3MP interconversions because the cyclopropyl carbenium ions present in the former have less stable gas-phase analogs; however, the effects of DPE on

isomerization rate constants are equal for all reactants. Confinement of acid sites within BEA channels stabilizes isomerization transition states via van der Waals forces and lead to similar rate constants on BEA and $H_3PW_{12}O_{40}$ POM clusters, in spite of their marked differences in acid strength. Confinement within BEA preferentially stabilizes methyl shift transition states over those changing the degree of branching and also favors reactions whose transition states have less branching.

3.2. Experimental Methods

3.2.1. Catalyst synthesis and characterization

$H_3PW_{12}O_{40}$ (Sigma-Aldrich; reagent grade; CAS #12501-23-4), $H_4SiW_{12}O_{40}$ (Aldrich; >99.9 %; CAS #12027-43-9), and $H_5AlW_{12}O_{40}$ (as prepared in [11]) were supported on amorphous SiO_2 (Cab-O-Sil HS-5; 310 $m^2\ g^{-1}$; 1.5 $cm^3\ g^{-1}$ pore volume) by incipient wetness impregnation with their ethanolic solutions. SiO_2 was washed three times in 1M HNO_3 and treated in flowing dry air (UHP Praxair; 0.5 $cm^3\ g^{-1}\ s^{-1}$) at 573 K for 5 h before impregnation. Ethanolic POM solutions (ethanol, Sigma-Aldrich; >99.5%; anhydrous) were added to SiO_2 (1.5 cm^3 solution [g dry SiO_2]$^{-1}$) and samples were stored in closed vials for > 24 h before treatment in flowing dry air (UHP Praxair; 0.5 $cm^3\ g^{-1}\ s^{-1}$) at 323 K (0.033 K s^{-1} heating rate) for 24 h. The concentrations of POM clusters in impregnation solutions were controlled to give surface densities of 0.04 POM [nm-SiO_2]$^{-2}$ (~5.5 wt%), unless noted otherwise. ^{31}P-MAS-NMR spectra of H_3PW/SiO_2 (Chapter 2 Supporting Information) confirmed that the procedures used to disperse POM clusters on SiO_2 did not alter their Keggin structures. Transmission electron micrographs (Chapter 2 Supporting Information) showed that POM clusters were predominantly present as isolated clusters or as small two-dimensional oligomers on SiO_2 at the low surface densities used here.

H-BEA (Zeolyst; Si/Al = 11.8) was treated in flowing dry air (UHP Praxair; 0.5 $cm^3\ g^{-1}\ s^{-1}$) at 773 K (0.03 K s^{-1} heating rate) for 24 h before mixing with Pt/Al_2O_3 co-catalysts using procedures described below. H-BEA with encapsulated Pt clusters (Pt/H-BEA) was prepared by aqueous ion-exchange of H-BEA (treated in UHP air at 773 K for 24 h) with $Pt(NH_3)_4(NO_3)_2$ (Aldrich; 99.995 %; CAS# 20634-12-2) [12]. An aqueous solution of $Pt(NH_3)_4(NO_3)_2$ (7 x 10^{-3} mol L^{-1}; 30 cm^3) was added dropwise to a slurry of H-BEA in deionized water (4 g H-BEA; 10 [g H-BEA] L^{-1}) at 353 K with continuous stirring. The slurry was stirred at 353 K for 48 h and the solids were then collected by filtration and washed five times with 30 cm^3 of deionized water. The solids were treated in flowing dry air (UHP Praxair; 5.8 $cm^3\ g^{-1}\ s^{-1}$) at 393 K (0.017 K s^{-1} heating rate) for 3 h and then at 623 K (0.017 K s^{-1} heating rate) for 10 h. After cooling to 300 K in He (UHP Praxair; 5.8 $cm^3\ g^{-1}\ s^{-1}$), the sample was treated in 10 % mol H_2/He (UHP Praxair; 5.8 $cm^3\ g^{-1}\ s^{-1}$) at 393 K (0.017 K s^{-1} heating rate) for 3 h.

The Pt content of the Pt/H-BEA was 0.89 % wt as determined by ion-coupled plasma optical emission spectroscopy (ICP-OES; Galbraith Laboratories, Inc.). The Pt dispersion in Pt/H-BEA (0.77; defined as the fraction of Pt-atoms located at the surfaces of Pt particles) was determined by volumetric adsorption measurements of H_2 at 298 K on a manual glass chemisorption unit assuming a 1:1 H-atom:Pt_S adsorption stoichiometry (Pt_S, surface Pt-atom). Pt/H-BEA was treated in H_2 (99.999% Praxair) at

598 K for 1 h and then held under vacuum at 598 K for 0.5 h before chemisorption measurements. An H_2 adsorption isotherm (99.999% Praxair) was measured at 298 K and 0.1 - 50 kPa H_2. The cell was then evacuated for 0.25 h at 298 K and a second isotherm was measured at the same conditions. The amount of chemisorbed H_2 was calculated from the difference between the first and second isotherms after their respective extrapolations to zero pressure. Bright-field transmission electron microscope (TEM) micrographs of Pt/H-BEA were acquired using a JEOL 1200 EX transmission electron microscope at 80 kV accelerating voltage and imaged with an internal charge-coupled device (CCD) camera. TEM samples were ground into fine powders (< 100 μm) with a mortar and pestle, suspended in ethanol (Sigma-Aldrich; >99.5%; anhydrous, ~10 mg in 10 cm^3 ethanol), and deposited onto an ultrathin carbon film supported on a copper grid (400 mesh, Ted Pella Inc.).

Pt/Al_2O_3 (1.5 % wt), used as a co-catalyst in physical mixtures with POM/SiO_2 and BEA Brønsted acids, was prepared by incipient wetness impregnation of γ-Al_2O_3 (Sasol SBa-200; 193 m^2 g^{-1}, 0.57 cm^3 g^{-1} pore volume, treatment in dry air (UHP Praxair; 0.5 cm^3 g^{-1} s^{-1}) at 923 K for 5 h) with aqueous H_2PtCl_6 (Aldrich; CAS #16941-12-1; 0.57 cm^3 g^{-1} dried Al_2O_3). The impregnated sample was treated in dry air (Praxair UHP, 0.7 cm^3 g^{-1} s^{-1}) at 383 K for 10 h before heating to 823 K at 0.033 K s^{-1} and holding for 3 h in flowing dry air (Praxair UHP, 0.7 cm^3 g^{-1} s^{-1}). This sample was then treated in H_2 (Praxair 99.999%; 0.2 cm^3 g^{-1} s^{-1}) by heating to 723 K at 0.083 K s^{-1} and holding for 2 h. After cooling to 303 K in He (UHP Praxair; 0.7cm^3 g^{-1} s^{-1}), the Pt/Al_2O_3 was treated in a dry air/He mixture (2.1 % mol O_2, 7.9 % mol N_2, 90 % mol He, 0.7 cm^3g^{-1} s^{-1} total flow) for 2 h. The Pt dispersion was determined by H_2 chemisorption at 298 K using the same procedure as for Pt/H-BEA (0.92 Pt_S/Pt_{total}) and by CO chemisorption at 298 K using similar pretreatments, a single CO (99.5% Praxair) adsorption isotherm extrapolated to zero pressure, and assuming a 1:1 CO:Pt_S adsorption stoichiometry (0.78 Pt_S/Pt_{total}); their average (0.85) was used to calculate (Pt_S/H^+) ratios of acid-metal mixtures.

Pt/Al_2O_3 samples were mixed with POM/SiO_2 (P, Si, and Al central atoms), H-BEA, or Pt/H-BEA (< 100 μm Al_2O_3, SiO_2, and BEA particles) in a mortar and pestle and then pressed into wafers, crushed, and sieved to retain 125-180 μm aggregates. The compositions of these mixtures are reported here as the ratio of Pt_S (from H_2 and CO chemisorption) to accessible H^+ (measured by titration during catalysis; Section 3.3.1.1) (Pt_S/H^+); this ratio was varied between 2.9 and 22.5 to determine that the Pt amounts were sufficient to maintain alkane-alkene equilibrium during isomerization catalysis.

3.2.2. Alkane isomerization rates and selectivities

C_6 alkane isomerization rates and selectivities were measured on catalyst samples (0.01 - 0.3 g) held within a quartz tubular flow reactor (1.0 cm I.D.) using a porous quartz disk and held at 473 K by a resistively-heated furnace. The temperature was controlled electronically (Watlow Series 982 controller) and measured using a K-type thermocouple (Omega; ± 0.2K) held within a dimple at the reactor wall.

Mixtures of POM/SiO_2 and Pt/Al_2O_3 were heated to 473 K at 0.083 K s^{-1} in flowing He (UHP Praxair; 0.83 cm^3 s^{-1}) and held for 1 h before catalytic measurements. H-BEA-Pt/Al_2O_3 and Pt/H-BEA-Pt/Al_2O_3 mixtures were heated to 573 K (0.083 K s^{-1} heating rate) in flowing H_2/He (Praxair UHP; 75 % mol H_2; 0.83 cm^3 s^{-1}) and held for 1 h

before cooling to reaction temperatures. Catalyst samples were diluted with enough SiO_2 (washed with 1.0 M HNO_3 and pressed and sieved to 125-180 μm particles) to maintain least 0.07 g of sample in the reactor for good conductive contact between the catalyst bed and the thermocouple well. All transfer lines were kept at 423 K to prevent condensation of reactants, products, or titrants.

Liquid 2-methylpentane (2MP, Fluka; > 99.5 % analytical standard), 3-methylpentane (3MP, Fluka; > 99.5 % analytical standard), 2,3-dimethylbutane (23DMB, Fluka; > 99.5 % analytical standard), and n-hexane (nH, Fluka; > 99.0 % GC standard) reactants were added by evaporation into a flowing He (UHP Praxair) and H_2 (99.999 % Praxair) stream using a syringe pump (Cole-Palmer 74900 Series). Flow rates of He and H_2 were metered using electronic mass flow controllers (Porter, Model 201). Molar flow rates of alkanes, H_2, and He were controlled to give desired H_2 pressures and (alkane/H_2) molar ratios and to maintain low reactant conversions (< 7%). H_2 pressures between 60 and 90 kPa were used and (alkane/H_2) reactant ratios were varied between 0.01 and 0.3 (higher ratios led to detectable deactivation over the course of kinetic experiments). Reactant and product concentrations in the reactor effluent were measured by gas chromatography using flame ionization detection (Agilent 6890N GC; 50 m HP-1 column). All reactant alkanes contained one or more of the product alkanes as impurities (< 0.7% carbon selectivity); impurity concentrations were subtracted from those in the reactor effluent when calculating their formation rates. Formation rates of each product "P" were corrected for approach to equilibrium with each reactant "R" using:

$$r_{net} = r_{forward}\left(1 - \frac{\left(\frac{P}{R}\right)}{K_{eq}}\right) \tag{3.1}$$

in which (P/R) is the ratio of product and reactant pressures within the reactor effluent and K_{eq} is their equilibrium constant at 473 K obtained from tabulated thermodynamic data [13]. Moderate catalyst deactivation (< 20% after 36 h on stream) was observed on some catalysts. All rates were corrected for any intervening deactivation by periodic rate measurements at reference conditions (75 kPa H_2 and 1.9 kPa alkane).

Titration experiments were conducted by dissolving 2,6-di-*tert*-butylpyridine (DTBP, Aldrich; >97%; CAS #585-48-8) in liquid 2MP reactants (2.4×10^{-2} – 8.6×10^{-2} % mol) and evaporating this mixture into a flowing H_2/He stream (UHP Praxair; 75 % mol H_2) to give 0.45 – 2.6 Pa DTBP. Isomerization rates and DTBP uptakes were calculated from the concentrations of 2MP, its isomerization products, and DTBP in the reactor effluent. Isomerization rates were extrapolated to zero rates linearly to determine the number of DTBP molecules required to fully suppress isomerization rates, which was assumed to reflect the number of H^+ accessible during catalysis (using a 1:1 H^+: DTBP adsorption stoichiometry) [15].

3.3. Results and Discussion

3.3.1. 2-Methylpentane isomerization turnover rates and selectivities on POM/SiO_2 and BEA mixtures with Pt/Al_2O_3

2-Methylpentane (2MP) isomerization turnover rates were measured on SiO_2-supported POM clusters ($H_{8-n}X^{n+}W_{12}O_{40}/SiO_2$) with different central atoms (X^{n+} = P^{5+}, Si^{4+}, Al^{3+}), and on H-BEA and Pt/H-BEA, each present as physical mixtures with Pt/Al_2O_3 co-catalysts. 3-Methylpentane (3MP), 2,3-dimethylbutane (23DMB), and n-hexane (nH) were the predominant products at all conditions on all catalysts. 2MP isomerization selectivities to 3MP (79.9% - 97.0% for all conditions and catalyst mixtures) were much larger than selectivities to 23DMB or nH (0.1% - 14.5% and 2.3% - 5.4%, respectively, for all conditions and catalyst mixtures). Traces of 2,2-dimethylbutane (22DMB) were also detected (< 0.55 % carbon selectivity), but its selectivities extrapolated to zero at short residence times (Supporting Information), consistent with its exclusive formation via secondary reactions. Catalyst mixtures also formed small amounts of other products, such as C_1-C_5 alkanes and cyclic C_6 alkanes (< 0.4% selectivities). C_6 isomerization rates were higher on POM/SiO_2-Pt/Al_2O_3 mixtures than on Pt/Al_2O_3 (by factors > 100), indicating that isomerization products formed predominantly on acid sites in these mixtures.

2MP isomerization rates, defined as the sum of 3MP, 23DMB, and nH formation rates, are reported as turnovers (per H^+) using 2,6-di-*tert*-butylpyridine (DTBP) titrations to measure the number of accessible H^+ (Section 3.3.1.1). These turnover rates were measured on catalyst mixtures that equilibrated 2MP with all of its alkene isomers and allow alkene isomerization rate measurements at known alkene concentrations (Section 3.3.1.2). Secondary isomerization reactions of alkenes interconvert products before they hydrogenate to less reactive alkanes. They prevent accurate measurements of primary products, which are required to measure isomerization rate constants for 2MP conversion to *individual* products (i.e., 3MP, 23DMB, nH) (Section 3.3.1.3). Achieving conditions where secondary isomerization reactions are absent is beyond the scope of this study and will be pursued in a future communication [14] because the total 2MP isomerization rates, the subject of this study, are not influenced by the rates of these secondary reactions.

3.3.1.1. Titrations of protons by 2,6-di-tert-butylpyridine during 2-methylpentane isomerization catalysis

Turnover rates are normalized by the number of protons (H^+) titrated by DTBP, which adsorbed irreversibly on Brønsted acid sites, but not on Lewis acids because of steric constraints [15]. Isomerization rates (per POM) before and during titrations are shown in Figure 3.1a as a function of cumulative titrant uptakes (per POM) on H_3PW/SiO_2-Pt/Al_2O_3 and H_4SiW/SiO_2-Pt/Al_2O_3 mixtures. Rates were constant before the introduction of titrant, but decreased linearly with increasing titrant uptake and were completely suppressed by DTBP on both samples, indicating that 2MP isomerizes only on Brønsted acid sites and that DTBP titrates all reactive H^+ accessible to reactants.

The numbers of accessible H^+ (per POM; Table 3.1) were smaller than expected from the POM stoichiometry by factors of 2.5 to 3.5 for all central atoms. Secondary POM structures can block DTBP and nonpolar reactants from accessing H^+ located in

interstitial spaces [7, 16] and can cause DTBP uptakes below the H^+ stoichiometries of POM. The H^+ counts in Table 3.1 require POM secondary structures with average diameters between 15 to 20 nm [17], however, POM features visible in TEM images of samples with 0.04 POM (nm-SiO_2)$^{-2}$ show much smaller diameters (< 2 nm; TEM images in Chapter 2 Supporting Information). Substoichiometric uptakes may instead reflect intracluster dehydroxylation, which remove H^+ and POM O-atoms as H_2O, or similar reactions between POM H^+ and silanols on SiO_2 surfaces under anhydrous conditions [18,19]. Unsupported POM clusters lose H^+ as water at significantly higher temperatures (623 K for $H_3PW_{12}O_{40}$ [20]) than the reaction temperature here (473 K), suggesting that low H^+ counts (Table 3.1) are caused by dehydroxylation reactions with the SiO_2 support.

Titrations with DTBP also fully suppressed 2MP isomerization rates on H-BEA-Pt/Al_2O_3 and Pt/H-BEA-Pt/Al_2O_3 mixtures at adsorption stoichiometries of 0.25 and 0.26 H^+ per framework Al-atom (Al_f, from MAS-Al-NMR in the Chapter 2 Supporting Information) (Figure 3.1b), respectively, indicating that only Brønsted acid sites catalyze 2MP isomerization and that DTBP can adsorb at all H^+ that are accessible to reactants. The same H-BEA sample adsorbed nearly twice as much DTBP during CH_3OH dehydration as here (0.45 H^+ Al_f^{-1} [6]), indicating that BEA can accommodate more DTBP molecules within its channels than the titrant uptakes listed in Table 3.1. As a result, DTBP uptakes measured here do not reflect the packing threshold of DTBP in BEA channels. The numbers of H^+ in FAU zeolites measured from titrations with DTBP, Na^+, and CH_3 groups from dimethyl ether were recently found to be in agreement with each other, but much smaller than the number of Al_f atoms measured from NMR (0.35 H^+ Al_f^{-1} for H-USY) [21]. Hydration of FAU samples before taking NMR spectra, intended to sharpen NMR lines and to weaken Al quadrupolar interactions, causes unintended structural changes that are reversed during catalysis by dehydroxylation and dealumination processes [21]. The numbers of Al_f from NMR overestimate the numbers of H^+ under reaction conditions, because they are indirect proxies measured under *ex situ* conditions. We conclude that low DTBP adsorption stoichiometries (per Al_f) measured here on H-BEA and Pt/H-BEA reflect dealumination processes or the loss of H^+ as H_2O under anhydrous reaction conditions and that DTBP uptakes directly reflect the number of accessible Brønsted acid sites *during* catalysis needed to rigorously normalize rates.

3.3.1.2. 2-Methylpentane isomerization turnover rates on bifunctional metal-acid catalyst mixtures

Alkane isomerization rates on bifunctional metal-acid catalysts are limited solely by alkene isomerization rates on acid sites when metal sites establish alkane-alkene equilibrium [22]. H_3PW/SiO_2-Pt/Al_2O_3 mixtures with (Pt_S/H^+) ratios of 11.7 and 22.5 had similar 2MP isomerization turnover rates (per H^+) at all conditions (Figure 3.2; 0.75 – 22.5 kPa 2MP, 75 kPa H_2), indicating that Pt sites can maintain 2MP dehydrogenation-hydrogenation equilibrium in these mixtures. 2MP isomerization rates that are solely limited by 2MP alkene isomerization at acid sites require that alkene diffusion rates be sufficiently high to maintain equilibrium 2MP alkene concentrations throughout POM/SiO_2 particles in bifunctional mixtures. The Koros-Nowak criterion specifies that mass transport of reactants does not limit reaction rates when turnover rates (defined as the moles of reactant converted per active site per time) are invariant with the surface

concentration of catalyst sites [23]. 2MP isomerization turnover rates were the same on H_3PW/SiO_2-Pt/Al_2O_3 mixtures with 0.04 and 0.25 POM $(nm\text{-}SiO_2)^{-2}$ surface densities (Figure 3.2; Pt_S/H^+ = 11.7), indicating that 2MP alkene diffusion within H_3PW/SiO_2 particles does not limit 2MP isomerization rates. All kinetic experiments using H_3PW were conducted on 0.04 POM nm^{-2} samples with a (Pt_s/H^+) ratio of 11.7 (Figure 3.3) because 2MP isomerization rates on this mixture are solely limited by alkene isomerization at acid sites.

A pseudo-steady-state treatment of alkene concentrations (Supporting Information; Eq. (S.3.15)) shows that the approach to reactant dehydrogenation equilibrium is determined by the ratio of Pt_S to isomerization rate constants ($k_{isom}K_{prot}$ in Table 3.2, Eq. (3.3)). The value of this ratio (i.e., $Pt_S/k_{isom}K_{prot}$) on the H_3PW mixture used for kinetic experiments was 4.7×10^{-3}. Kinetic experiments were conducted on bifunctional mixtures with lower (Pt_S/H^+) ratios for weaker POM acids to minimize rates of Pt-catalyzed isomerization, however, $(Pt_S/k_{isom}K_{prot})$ ratios greater than 4.7×10^{-3} were used for all mixtures to ensure 2MP alkane-alkene equilibrium. Weaker POM acids, supported at 0.04 POM $(nm\text{-}SiO_2)^{-2}$, have lower reaction rates relative to diffusion rates than the 0.25 H_3PW $(nm\text{-}SiO_2)^{-2}$ sample so that they also have uniform 2MP alkene concentrations within acid aggregates (Supporting Information). As a result, 2MP isomerization rates on bifunctional mixtures containing weaker POM acids are also solely limited by alkene isomerization at acid sites.

Figure 3.3a shows 2MP isomerization turnover rates (per H^+) as a function of $(2MP/H_2)$ molar ratios on POM/SiO_2-Pt/Al_2O_3 mixtures with P, Si, and Al central atoms $((Pt_s/H^+)$ = 4.8 – 11.7). 2MP isomerization turnover rates increased with increasing valence of the POM central atom; they also increased with increasing $(2MP/H_2)$ ratios on all catalysts, linearly at first and then more gradually at higher ratios (Figure 3.3a). 2MP isomerization rates on all catalysts were independent of H_2 pressure (60 – 90 kPa H_2) and depended only on the $(2MP/H_2)$ ratio.

Next, we use the elementary steps depicted in Scheme 3.1 to derive an isomerization rate expression that describes the observed effects of $(2MP/H_2)$ ratios on isomerization rates, as shown previously for other bifunctional isomerization catalysts [7, 22, 24]. Pt sites equilibrate 2MP with all 2-methylpentene isomers (Scheme 3.1, Step 1 shown for 2-methylpent-2-ene) in these pathways; as a result, alkene pressures are proportional to $(2MP/H_2)$ ratios and to their respective dehydrogenation equilibrium constants (K_{dehy}). Quasi-equilibrated protonation of 2-methylpentene isomers at acid sites forms 2-methylpentoxide isomers attached to the catalyst at backbone locations prescribed by their thermodynamic stabilities (Scheme 3.1, Step 2 shown for 2-methylpent-2-ene and 2-methypent-3-oxide). 2-Methylpentoxides isomerize in irreversible steps to alkoxides with different backbone structures (Scheme 3.1, Step 3 shown for 3-methylpent-2-oxide). These backbone rearrangements are mediated by cationic transition states that resemble cyclopropyl carbenium ions and that cleave and form C-C and C-H bonds in concerted steps [25 - 29]. Product alkoxides deprotonate to form alkenes (Scheme 3.1, Step 4 shown for 3-methylpent-2-ene), which diffuse to Pt sites and hydrogenate to the respective alkanes (Scheme 3.1, Step 5 shown for 3MP). All alkene (and alkoxide) isomers can be rigorously lumped into chemical pseudo-species because equilibrium among them maintains their concentrations at constant ratios.

Alkene (and alkoxide) pseudo-species are denoted here by the superscript symbol "=" (and "*") throughout the text (e.g., 2-methylpentane, 2-methylpentene isomers, and 2-methylpentoxide isomers are denoted as 2MP, $2MP^{=}$, and 2MP*).

The assumptions of pseudo-steady-state for alkoxides, of equilibrated hydrogenation-dehydrogenation and protonation-deprotonation steps, of 2MP* and H^+ as the most abundant surface intermediates (MASI) at acid sites, and of irreversible skeletal isomerization of 2MP* lead to a rate equation for 2MP isomerization to each alkane product isomer "P" (r_P; P = 3MP, 23DMB, or nH; full derivation in Supporting Information):

$$\frac{r_{isom,P}}{\left[H^+\right]} = \frac{k_{isom,P}K_{prot,P}K_{dehy}\left(\frac{2MP}{H_2}\right)}{1+K_{surf}K_{dehy}\left(\frac{2MP}{H_2}\right)} \tag{3.2}$$

in which $[H^+]$ is the number of accessible H^+ (from DTBP titration data, Section 3.3.1.1). $K_{prot,P}$ is the $2MP^{=}$ protonation equilibrium constant for the 2-methylpentoxide isomer that forms product "P" (2-methylpent-3-oxide in Scheme 3.1), $k_{isom,P}$ is the alkoxide isomerization rate constant to form product "P", and K_{surf} is sum of K_{prot} for all 2MP* isomers. The first and second terms in the denominator of Eq. (3.2) reflect the relative numbers of active sites present as H^+ and 2MP*, respectively. All products have the same denominator in their formation rate expressions because they are formed by the same active sites. The sum of Eq. (3.2) for 3MP, 23DMB, and nH products therefore gives the equation for total 2MP isomerization rates (r_{isom}) at 2MP-$2MP^{=}$ equilibrium:

$$\frac{r_{isom}}{\left[H^+\right]} = \frac{\left(k_{isom}K_{prot}\right)K_{dehy}\left(\frac{2MP}{H_2}\right)}{1+K_{surf}K_{dehy}\left(\frac{2MP}{H_2}\right)} \tag{3.3a}$$

$$\left(k_{isom}K_{prot}\right) = k_{isom,3MP}K_{prot,3MP} + k_{isom,23DMB}K_{prot,23DMB} + k_{isom,nH}K_{prot,nH} \tag{3.3b}$$

2MP isomerization turnover rates in Figure 3.3 reflect the values of kinetic and thermodynamic parameters in Eq. (3.3a) because equilibrium $2MP^{=}$ concentrations are present at all acid sites throughout the reactor. 2MP isomerization rates that are inversely dependent on (H_2/2MP) ratios (Figure 3.3b) and that lie along a single curve at all H_2 pressures (60 - 90 kPa H_2; Figures 3.3a and 3.3b) are consistent with Eq. (3.3a) and with 2MP-$2MP^{=}$ equilibration:

$$\left(\frac{r_{isom}}{\left[H^{+}\right]}\right)^{-1} = \frac{1}{\left(k_{isom}K_{prot}\right)K_{dehy}}\left(\frac{H_2}{2MP}\right) + \frac{K_{surf}}{\left(k_{isom}K_{prot}\right)} \tag{3.4}$$

Table 3.2 shows $k_{isom}K_{prot}$, $k_{isom}K_{prot}K_{surf}^{-1}$, and K_{surf} values for each POM acid, obtained by least-squares linear regression of the data in Figure 3.3b to the functional form of Eq. (3.4) and by using thermodynamic data [13] to calculate and remove K_{dehy} values (K_{dehy} = 0.79 Pa at 473 K for 2-methylpent-2-ene as a reference alkene isomer. The choice of the reference alkene isomer is arbitrary when alkoxides are equilibrated with the alkane (justification provided in the Supporting Information). 2-Methylpent-2-ene was chosen because it has the highest equilibrium concentration.). These data provide accurate values for $k_{isom}K_{prot}$, but not for $k_{isom}K_{prot}K_{surf}^{-1}$ (e.g., the linear regression of rate data on POM give standard deviations of ± 0.8% - 1% for $k_{isom}K_{prot}$ and ± 13% -100% for $k_{isom}K_{prot}K_{surf}^{-1}$; Table 3.2); as a result, these parameters predict 2MP isomerization rates accurately for ($2MP/H_2$) ratios less than ~ 0.1 (i.e., when 1 is the dominant denominator term in Eq. (3.3a)), but less accurately at higher ($2MP/H_2$) ratios (dashed curves in Figure 3.3a). More accurate estimates of K_{surf} values require higher ($2MP/H_2$) ratios and concomitantly higher alkoxide coverages, which lead to bimolecular alkene-alkoxide oligomerization reactions that gradually deactivate acid sites.

2MP isomerization rate data were also collected on bifunctional mixtures containing zeolite BEA to measure the reactivities of alkenes at acid sites confined within zeolite voids. $2MP^{=}$ concentration gradients must be absent within BEA particles for measured 2MP isomerization rates to reflect only the kinetic and thermodynamic parameters in Eq. (3.3a). 2MP isomerization rates on H-BEA-Pt/Al_2O_3 and Pt/H-BEA-Pt/Al_2O_3 mixtures were compared to test for the presence of $2MP^{=}$ concentration gradients. Encapsulated Pt clusters of Pt/H-BEA dehydrogenate 2MP to $2MP^{=}$ within BEA channels to reduce $2MP^{=}$ concentration gradients if they exist. TEM micrographs of Pt/H-BEA (Figure 3.5) exhibit Pt clusters with average diameters of 1.1 nm within BEA particles and no large Pt clusters along the edges of BEA particles. Small clusters visible in TEM are similar to the sizes of Pt particles predicted from H_2 chemisorption (1.3 nm) and suggest that Pt is fully encapsulated within the channels of BEA. Figure 3.4a shows 2MP isomerization turnover rates measured on H-BEA-Pt/Al_2O_3 (Pt_S/H^+ = 3.2) and Pt/H-BEA-Pt/Al_2O_3 (Pt_S/H^+ = 2.9) mixtures as functions of ($2MP/H_2$) ratios (473 K, 75 kPa H_2). These rates were regressed to the functional form of Eq. (3.4) using least-squares to provide estimates of $k_{isom}K_{prot}$ and $k_{isom}K_{prot}K_{surf}^{-1}$ values on H-BEA and Pt/H-BEA (Table 3.2). 2MP isomerization rates measured on Pt/H-BEA increase more dramatically with ($2MP/H_2$) ratios than rates on H-BEA and result in a larger apparent $k_{isom}K_{prot}$ value on Pt/H-BEA (2740 and 990 x 10^{-3} molecules (Pa H^+ s)$^{-1}$, respectively). The two mixtures had similar turnover rates at high ($2MP/H_2$) ratios, as reflected by their similar estimates of $k_{isom}K_{prot}K_{surf}^{-1}$ (69 and 59 x 10^{-3} molecules (H^+ s)$^{-1}$ for Pt/H-BEA and H-BEA, respectively). Higher 2MP isomerization rates on Pt/H-BEA than H-BEA at low ($2MP/H_2$) ratios suggest that $2MP^{=}$ concentration gradients exist within H-BEA particles and are reduced by encapsulated Pt clusters that dehydrogenate 2MP within BEA voids. Encapsulated Pt clusters likely do not interact directly with reacting

molecules at acid sites at this low amount of encapsulated Pt (0.19 Pt-atoms H^{+-1} calculated from elemental analysis and DTBP titrations). Average distances between Pt clusters observed in TEM of Pt/H-BEA (ca. 10 nm, Figure 3.5), the apparent value of $k_{isom}K_{prot}$ measured on Pt/H-BEA (Table 3.1), and the diffusivity of n-hexane in MFI (2.9 x 10^{-9} m^2 s^{-1} [30]) predict a Thiele modulus 0.02 and an internal effectiveness factor of 1 (calculation in the Supporting Information); thus, $2MP^{=}$ concentration gradients are not expected in Pt/H-BEA particles. The addition of more Pt/Al_2O_3 to Pt/H-BEA-Pt/Al_2O_3 mixtures (Pt_S/H^+ = 8.7) did not increase turnover rates (Supporting Information), suggesting that Pt/H-BEA-Pt/Al_2O_3 mixtures contain sufficient Pt to maintain 2MP-$2MP^{=}$ equilibrium. Thus, we conclude that 2MP isomerization rates measured on Pt/H-BEA reflect the reactivity of equilibrium $2MP^{=}$ concentrations at acid sites confined with BEA channels only.

Isomerization rates measured on Pt/H-BEA at different H_2 pressures fall along a single curve at (H_2/2MP) ratios of 40 and 100 in Figure 3.4b (($2MP/H_2$) ratios of 0.025 and 0.01), consistent with the prediction of Eq. (3.4) and the 2MP-$2MP^{=}$ equilibrium achieved on this mixture. 2MP isomerization rates decrease slightly with increasing H_2 pressure at higher ($2MP/H_2$) ratios (0.1 and 0.3; Figure 3.4a). As a result, values of $k_{isom}K_{prot}$ are independent of the H_2 pressure (2640 - 2770 x 10^{-3} molecules (Pa H^+ s)$^{-1}$), while apparent $k_{isom}K_{prot}K_{surf}^{-1}$ values increase systematically with decreasing H_2 pressure by a factor of 1.4. 2MP physisorption at acid sites describe the dependence of isomerization rates on H_2 pressure at high, but not low, ($2MP/H_2$) ratios accurately by including physisorbed 2MP alkanes in acid site balances of isomerization rate expressions:

$$\frac{r_{isom}}{\left[H^+\right]} = \frac{k_{isom}K_{prot}K_{dehy}\left(\frac{2MP}{H_2}\right)}{1+K_{surf}K_{dehy}\left(\frac{2MP}{H_2}\right)+K_{alkane}\left(2MP\right)} \tag{3.5a}$$

The third term in the denominator of Eq. (3.5a) reflects the coverage of acid sites by physisorbed 2MP, where K_{alkane} is the 2MP physisorption equilibrium constant. Rearranging Eq. (3.5a):

$$\frac{r_{isom}}{\left[H^+\right]} = \frac{k_{isom}K_{prot}K_{dehy}\left(\frac{2MP}{H_2}\right)}{1+K_{surf}K_{dehy}\left(\frac{2MP}{H_2}\right)\left(1+\frac{K_{alkane}\left(H_2\right)}{K_{surf}K_{dehy}}\right)} \tag{3.5b}$$

and comparing it to Eq. (3.3a) shows that rate expressions that neglect and include 2MP physisorption (Eq. (3.3a) and Eq. (3.5b), respectively) are indistinguishable when acid sites are predominantly vacant (i.e., when 1 is the dominant term in the denominator) and when rates increase linearly with ($2MP/H_2$) ratios. As a result, rates on POM mixtures

(Figure 3.3) and rates on the Pt/H-BEA mixture below (2MP/H_2) ratios of 0.025 (Figure 3.4) are independent of H_2 pressure. Apparent values of K_{surf} ($K_{surf,app}$) on Pt/H-BEA at different H_2 pressures are obtained by regressing rate data in Figure 3.4b at 60, 75, and 90 kPa H_2 to Eq. (3.4) separately. The inset of Figure 3.4a shows that $K_{surf,app}$ values increase linearly with H_2 pressure. Eq. (3.5b) is obtained by substituting the linear equation for $K_{surf,app}$ in Eq. (3.6) below for K_{surf} in Eq. (3.3a) and rearranging:

$$K_{surf,app} = K_{surf} + \frac{K_{alkane}(H_2)}{K_{dehy}} \tag{3.6}$$

Thus, the linear dependence of $K_{surf,app}$ on H_2 pressure shown in the inset of Figure 3.4a is described accurately by 2MP physisorption at acid sites. The slope and intercept of the dashed line in the inset of Figure 3.4a define the values of K_{alkane}/K_{dehy} (0.48) and K_{surf} (3.4 Pa^{-1}), respectively, in Eq. (3.6). The value of $\frac{K_{alkane}(H_2)}{K_{surf}K_{dehy}}$ (8.5 to 13 for 60 – 90 kPa H_2) defines the relative concentrations of physisorbed alkanes to alkoxides at acid sites. This ratio is much larger than 1, indicating that acid sites become saturated predominantly by physisorbed 2MP at high 2MP pressures and cause isomerization rates to become independent to (2MP/H_2) ratios in Figure 3.4a. Isomerization rates at (2MP/H_2) ratios of 0.1 and 0.3 decrease with increasing H_2 pressure because increasing H_2 pressure (at a constant (2MP/H_2) ratio) increases the concentration of unreactive alkanes at acid sites relative to reactive alkenes and alkoxides.

DFT-derived adsorption energies of n-hexane (-62 kJ mol^{-1}) and 2-methylpent-2-ene (-115 kJ mol^{-1}) at acid sites of FAU [31] predict a K_{alkane}/K_{surf} ratio of 1.4 x10^{-6}, assuming alkanes and alkenes lose similar amounts of entropy upon adsorption. The strong enthalpic preference of acid sites to adsorb alkenes over alkanes is offset by the large differences in their concentrations at these H_2 pressures (given by K_{dehy} = 7.9 x 10^{-4} kPa) so that DFT adsorption energies predict $\frac{K_{alkane}(H_2)}{K_{surf}K_{dehy}}$ values of 0.11 - 0.16 for 60 – 90 kPa H_2. Measured $\frac{K_{alkane}(H_2)}{K_{surf}K_{dehy}}$ values are a factor of 75 higher than the prediction from DFT-derived energies because covalent bonds to acid sites prevent alkoxides from rotating freely relative to the surface and lead to more entropy loss for alkenes than alkanes upon adsorption.

We conclude that acid sites of Pt/H-BEA are predominantly covered by physisorbed 2MP at high 2MP pressures and cause 2MP isomerization rates to decrease with increasing H_2 pressure at a constant (2MP/H_2) ratio (Figure 3.4). Isomerization rates are independent of H_2 pressure when acid sites are predominantly vacant and lead to similar $k_{isom}K_{prot}$ values at 60 – 90 kPa H_2, the average of which is listed in Table 3.2. Values of $k_{isom}K_{prot}$ on POM and Pt/H-BEA are compared in Section 3.3.2 to examine the effects of acid strength and confinement on 2MP isomerization reactivity.

3.3.1.3. 2-Methylpentane isomerization selectivities on bifunctional metal-acid mixtures

Equations (3.3a) and (3.5a) and their underlying elementary steps (Scheme 3.1) describe the 2MP isomerization rates on all acid-metal mixtures shown in Figures 3.2 - 3.4, but do not accurately describe selectivities among primary products as we show next. Selectivities to 23DMB and nH (S_{23DMB} and S_{nH}, respectively) are defined here as ratios of 23DMB and nH formation rates ($r_{isom,23DMB}$ and $r_{isom,nH}$) to 3MP formation rates ($r_{isom,3MP}$):

$$S_{23DMB} = \frac{r_{isom,23DMB}}{r_{isom,3MP}} \tag{3.7a}$$

$$S_{nH} = \frac{r_{isom,nH}}{r_{isom,3MP}} \tag{3.7b}$$

Equation (3.2) predicts S_{23DMB} and S_{nH} values that are equal to the ratios of isomerization rate constants for the two products, regardless of the 2MP and H_2 pressures (e.g., $S_{23DMB} = \frac{k_{isom,23DMB} K_{prot,23DMB}}{k_{isom,3MP} K_{prot,3MP}}$). Figure 3.6a shows S_{23DMB} and S_{nH} values as functions of 2MP pressure on a H_3PW/SiO_2-Pt/Al_2O_3 mixture that achieved 2MP-$2MP^{=}$ equilibration (Pt_s/H^+ = 11.7) and whose H_3PW surface density (0.04 H_3PW [nm-SiO_2]$^{-2}$) did not cause $2MP^{=}$ concentration gradients within H_3PW/SiO_2 particles (Section 3.3.1.2). Selectivities measured at 60, 75, and 90 kPa H_2 lie along a single curve in Figure 3.6a for both S_{nH} and S_{23DMB}, consistent with predicted selectivities that are independent of H_2 pressure; however, measured S_{23DMB} and S_{nH} values decreased by factors of 0.52 and 0.61, respectively, as 2MP pressures increased from 0.6 to 25 kPa 2MP, which is inconsistent with the prediction of Eq. (3.2).

Varying S_{23DMB} and S_{nH} values on a catalyst mixture where $2MP^{=}$ diffusion and 2MP-$2MP^{=}$ interconversion do not influence measured rates indicate that secondary isomerization reactions interconvert product alkenes via steps that are kinetically-irrelevant for the total rate of 2MP isomerization. $3MP^{=}$, $23DMB^{=}$, and $nH^{=}$ interconvert via similar adsorption (Steps 4A and 4B in Scheme 3.2 shown for $3MP^{=}$ and $23DMB^{=}$) and backbone rearrangement (Steps 3C in Scheme 3.2 shown for 3MP* and 23DMB*) elementary steps as $2MP^{=}$, as we discuss in detail in Section 3.3.3.1. The net rates of isomerization reactions interconverting products are determined by the relative concentrations of product alkenes at acid sites and their respective isomerization rate constants (i.e., $k_{isom}K_{prot}$). Varying selectivities are not related to changing $2MP^{=}$ or 2MP* concentrations since the former change with H_2 pressures (but S_{23DMB} and S_{nH} values do not) and the latter are negligible under the reaction conditions here (i.e., isomerization rates in Figure 3.2 depend linearly on (2MP/H_2) ratios). The dependences of S_{23DMB} and S_{nH} values on 2MP pressure alone (Figure 3.6a) suggest that the 2MP pressure influences the net rates of product interconversion by changing the relative

concentrations of product alkenes. We propose that the dependence of S_{23DMB} and S_{nH} values on 2MP pressure derives from hydrogenation of product alkenes at acid sites via hydride transfer from 2MP (Scheme 3.2, Steps 6A and 6B for $3MP^{=}$ and $23DMB^{=}$, respectively), which is in direct competition with secondary isomerizations. Such reactions change the relative concentrations of product alkenes, and by inference the net rates of secondary isomerization reactions, according to their relative hydride transfer rate constants (i.e., $k_{HT,3MP}$ and $k_{HT,23DMB}$ Scheme 3.2, Steps 6A and 6B). Changes in product alkene concentrations do not influence the total rate of 2MP isomerization (i.e., 2MP pressures alone change S_{23DMB} and S_{nH} values, but not 2MP isomerization rates) because $2MP^{=}$ concentrations are much larger than product alkene concentrations, making 2MP* steps irreversible.

Figure 3.6b compares S_{23DMB} and S_{nH} values shown in Figure 3.6a with those measured on H_3PW/SiO_2-Pt/Al_2O_3 mixtures with higher (Pt_s/H^+) ratios (22.5) and with higher surface densities (0.25 H_3PW [nm-SiO_2]$^{-2}$). S_{23DMB} and S_{nH} values are independent of H_2 pressure for all mixtures (Figure S.3.3 in Supporting Information). Increasing 2MP pressure causes S_{23DMB} and S_{nH} values to decrease precipitously below ca. 10 kPa 2MP and more gradually at higher pressures on all catalyst mixtures. S_{23DMB} values increase with POM surface density and with (Pt_S/H^+) at 2MP pressures below ca. 20 kPa 2MP, above which S_{23DMB} values are similar for all H_3PW/SiO_2-Pt/Al_2O_3 mixtures. S_{nH} values decrease with increasing POM surface density and increase with increasing (Pt_S/H^+) over the entire 2MP pressure range examined (0.8 to 23.5 kPa 2MP).

Changes in S_{23DMB} and S_{nH} values with POM surface densities (at a given 2MP pressure) suggest that product alkenes interconvert before they diffuse out of POM/SiO_2 particles to Pt sites, which hydrogenate alkenes to less reactive alkanes. Dependences of S_{23DMB} and S_{nH} values on (Pt_S/H^+) ratios suggest that Pt sites in these mixtures do not equilibrate all product alkenes with their alkanes. The complicated effects of 2MP pressure, POM surface density, and (Pt_S/H^+) ratios on S_{23DMB} and S_{nH} make unequivocal interpretations of selectivities difficult. We only interpret total 2MP isomerization rates here because they are not influenced by these complexities and relegate finding reaction conditions where selectivities only reflect primary isomerizations (i.e., when POM surface density, Pt_S/H^+ ratios, and 2MP pressure do not influence S_{23DMB} and S_{nH} values) to a later communication [14].

3.3.2. Acid strength and solvation effects on total rate constants of 2-methylpentene isomerization

The values of $k_{isom}K_{prot}$ measured during 2MP isomerization decreased exponentially with increasing deprotonation energies (DPE) on Keggin POM (P, Si, Al central atoms; Figure 3.7). DPE values increase (and acids become weaker) as the number of H^+ per Keggin cluster increases, because deprotonation forms less stable conjugate anions from clusters that exhibit higher electron densities. These exponential effects of DPE on rate constants predominantly reflect increasing activation energies as acids weaken, rather than effects on pre-exponential factors (and activation entropies) [3, 7], because of the similar transition structures on POM clusters with different DPE. The change in activation energies of $k_{isom}K_{prot}$ (E_{meas}) for a given DPE change can be determined under this assumption from slope of the data in Figure 3.7 [7]:

$$\frac{d\left(\ln\left(k_{isom}K_{prot}\right)\right)}{d\left(DPE\right)} = -\frac{1}{RT}\frac{d\left(E_{meas}\right)}{d\left(DPE\right)} \tag{3.8}$$

The slope of the dashed line in Figure 3.7 (-0.025) corresponds to activation energies that change by much less than the concomitant changes in DPE ($d(E_{meas})/d(DPE) = 0.10 < 1$). A formalism for activation energies based on thermochemical cycles has proven useful in dissecting how catalyst and molecular properties influence alkanol dehydration [3,6] and n-hexane isomerization [7] activation energies, as well as protonation energies of molecules [32] on solid acids. Scheme 3.3 shows the reaction coordinate for 2-methylpent-2-ene isomerization (i.e., the reference alkene isomer used to calculate K_{dehy}) and the energy terms associated with E_{meas}. Selectivities of primary isomerizations could not be measured definitively (Section 3.3.1.3) and preclude the calculation of $k_{isom}K_{prot}$ values for *individual* product isomers (i.e., $k_{isom,P}K_{prot,P}$ in Eq. (3.2)); as a result, activation energies of measured $k_{isom}K_{prot}$ include contributions from 3MP, 23DMB, and nH formation, weighted by their relative formation rates. The reaction coordinate in Scheme 3.3 is illustrated for 3MP formation specifically because 3MP constitutes >80 % of 2MP isomerization products under all conditions and is therefore the largest contributor to measured activation energies. Measured activation energies (E_{meas}) include the energy for protonation of 2-methylpent-2-ene by acid sites (E_{prot} in Scheme 3.3 via K_{prot}) and the activation energy for 2MP* to form isomerization transition states (E_{isom} in Scheme 3.3 via k_{isom}). Activation energies, therefore, reflect differences in energy between the isomerization transition state and one gaseous 2-methylpent-2-ene molecule and an unoccupied acid site ($E_{meas} = E_{prot} + E_{isom}$ in Scheme 3.3). Activation energies can be expressed using an alternate hypothetical path (connecting gaseous 2-methylpent-2-ene reactants with transition states), which includes energy terms that are accessible to measurement or theoretical estimates. This thermochemical cycle (Scheme 3.3) includes DPE values, formation energies of gaseous cyclopropyl carbenium ions from gaseous H^+ and 2-methylpent-2-ene (E_{gas}), and interaction energies between organic cations and anionic clusters at the transition state (E_{int}):

$$E_{meas} = DPE + E_{gas} + E_{int} \tag{3.9}$$

E_{gas} is a property of the gas-phase reaction between a free H^+ and a 2-methylpent-ene to form a cyclopropyl carbenium ion as a gaseous analog of the isomerization transition state ($[C_6H_{13}^{\ddagger}]^+(g)$).

$$2MP^{=}(g) + H^+(g) \rightarrow [C_6H_{13}^{\ddagger}]^+(g) \qquad (E_{gas} < 0) \tag{3.10}$$

Scheme 3.4 shows cationic structures inferred from previous DFT calculations of gas-phase and surface isomerization steps likely to resemble 2MP isomerization transition states [26]. 3MP formation involves transition states that form and cleave C-C bonds in a concerted manner and shift methyl groups along a C_5 backbone (Scheme 3.4 (A)).

23DMB (Scheme 3.4 (B)) and nH (Scheme 3.4 (C)) require edge-protonated cyclopropyl cations for their formation, in which concerted C-C *and* C-H bond formation and cleavage increase or decrease, respectively, the number of methyl groups along the backbone. E_{gas} values differ among transition states forming 3MP, 23DMB, and nH paths because of differences in their respective gaseous cyclopropyl carbenium ion stabilities. Formation energies for cations mediating 3MP (Scheme 3.4 (A)) and 23DMB (Scheme 3.4 (B)) formation from gaseous 2-methylpent-2-ene and a free H^+ (E_{gas}) were -817 kJ mol^{-1} and -772 kJ mol^{-1} [26], respectively, indicating that methyl shifts are less demanding than routes that change the backbone length. More stable gaseous analogs of 3MP transition states account for the predominance of 3MP among isomerization products (Figure 3.6) by reducing its activation energy via E_{gas} in Eq. (3.9).

The sensitivity of each energy term in the thermochemical cycle (Eq. (3.9)) to DPE reflects the corresponding effects of DPE on $k_{isom}K_{prot}$ values (Figure 3.7):

$$\frac{d\left(E_{meas}\right)}{d\left(DPE\right)} = 1 + \frac{d\left(E_{int}\right)}{d\left(DPE\right)} \tag{3.11}$$

The $d(E_{gas})/d(DPE)$ term is absent in Eq. (3.11) because all catalysts form predominantly 3MP, the E_{gas} of which is a property of a gas-phase reaction (Eq. (3.10)) and insensitive to the catalyst. Changes in measured activation energies are a small fraction of the commensurate changes in DPE ($d(E_{meas})/d(DPE) = 0.10$), because weak acids, with strong interactions between H^+ and conjugate anions, also interact more strongly with cationic transition states via electrostatic interactions. Stronger forces for both H^+ (i.e., larger DPE) and transition states (i.e., more negative E_{int}) with more densely charged conjugate anions attenuate the effects of DPE on activation energies. Isomerization transition states do not fully recover the electrostatic interactions overcome during deprotonation between the H^+ and conjugate anion ($d(E_{int})/d(DPE) = -0.90$) because H^+ fulfill the criteria for strong electrostatic interactions better than isomerization transition states: close proximity to the anion and a localized charge. Proton-like transition states with localized cationic charges near the anion are the most effective at recovering the DPE and cause activation energies with weaker dependences on DPE. All POM clusters formed predominantly 3MP (80 – 94% carbon selectivity), with similar amounts of 23DMB and nH (3.1 – 14.5% and 3.2 – 5.4% carbon selectivities, respectively), indicating that selectivities do not change dramatically with acid strength. These results suggest, at least qualitatively, that transition states forming different products sense DPE to the same extent (i.e., $d(E_{int})/d(DPE)$ are similar for transition states forming 3MP, 23DMB, and nH) because they are all cyclopropyl carbenium ions with similar charge distributions. The results in Section 3.3.3 further support this notion by demonstrating equal effects of DPE on $3MP^=$, $23DMB^=$, and $nH^=$ isomerization rate constants.

The value of $k_{isom}K_{prot}$ for $2MP^=$ isomerization on Pt/H-BEA lies above the trend line defined by POM clusters when reported DFT-derived DPE values of zeolites are used as the abscissa (Figure 3.7) [3]. The ratio of the isomerization rate constant measured on Pt/H-BEA ($k_{isom,z}K_{prot,z}$) to the value predicted for a POM with same DPE

($k_{isom,POM}K_{prot,POM}$ ~ 215 x10^{-3} molecules (Pa H^+ s)$^{-1}$; dashed line in Figure 3.7) is given by:

$$\frac{k_{isom,z}K_{prot,z}}{k_{isom,POM}K_{prot,POM}} = \frac{A_z}{A_{POM}}\exp\left(-\frac{E_{meas,z}-E_{meas,POM}}{RT}\right) \tag{3.12a}$$

where A are the pre-exponential factors of $k_{isom}K_{prot}$ and subscripts "z" and "POM" denote zeolites and POM clusters with the same DPE values. Substituting Eq. (3.9) into Eq. (3.12a) shows that this ratio depends only on entropy (via A) and transition state interaction energy differences caused by confinement:

$$\frac{k_{isom,z}K_{prot,z}}{k_{isom,POM}K_{prot,POM}} = \frac{A_z}{A_{POM}}\exp\left(-\frac{E_{int,z}-E_{int,POM}}{RT}\right) \tag{3.12b}$$

because POM and BEA both form 3MP predominantly (> 80% selectivity), which leads to the same E_{gas} value in Eq. (3.9). Confinement of isomerization transition states within BEA channels restricts their degrees of freedom; thus, entropy losses upon formation of transition states from gaseous reactants are larger for zeolites than for unconfined POM clusters (A_z/A_{POM} < 1). The data in Figure 3.7 and Eq. (3.12b) suggest that transition state cations must interact more strongly with zeolite anions than POM anions of equal DPE to overcompensate for any additional entropy losses on BEA. The ratio $\frac{k_{isom,BEA}K_{prot,BEA}}{k_{isom,POM}K_{prot,POM}}$ (12.7) predicts that confinement of acid sites within BEA channels stabilizes 2MP isomerization transition states by a free energy of 10 kJ mol^{-1}. Interaction energies stabilize cations more with confined anions than with unconfined anions because the former stabilize isomerization transition state cations with stronger van der Waals forces (i.e., solvation by confinement) [33, 34, 35]. Van der Waals forces are unrelated to the electrostatic forces that determine the effects of DPE, but cause isomerization turnover rates on zeolites to be similar to those on H_3PW, the strongest POM acid.

3.3.3. Acid strength and solvation effects on the isomerization of 3-methylpentane, 2,3-dimethylbutane, and n-hexane

3.3.3.1. 3-Methylpentane, 2,3-dimethylbutane, and n-hexane isomerization turnover rates on bifunctional metal-acid catalyst mixtures

Next, we examine if the effects of acid strength and solvation by confinement are influenced by the structure of the reactant by measuring isomerization rate constants of 3-methylpentane (3MP), 2,3-dimethylbutane (23DMB), and n-hexane (nH) separately on POM/SiO_2-Pt/Al_2O_3 (P, Si, Al central atoms) and Pt/H-BEA-Pt/Al_2O_3 mixtures. 3MP reactants formed predominantly 2MP (> 85% carbon selectivity) with smaller amounts of 23DMB and nH on all catalysts and at all reaction conditions. Small amounts of 2,2-dimethylbutane (22DMB) were also formed (< 1.1% carbon selectivity). nH reactants

formed 2MP and 3MP in nearly equilibrium proportions (2MP/3MP = 1.4 - 1.6), smaller concentrations of 23DMB (< 6 % carbon selectivity), and trace amounts of 22DMB (< 0.5% carbon selectivity) on all catalysts. 23DMB also formed predominantly 2MP and 3MP at constant ratios (2MP/3MP = 2.0 – 2.2), and small concentrations of nH (< 3.3% carbon selectivity) and 22DMB (< 6 % carbon selectivity) on POM clusters. Pt/H-BEA mixtures formed 22DMB at significantly higher selectivities (ca. 73% carbon selectivity, respectively) than POM clusters. Contributions from 22DMB formation were removed from 23DMB isomerization rates to compare Pt/H-BEA and POM clusters since 2MP, 3MP, and nH did not form 22DMB with significant selectivities.

3MP, 23DMB, and nH isomerization rates were normalized as turnovers using the number of H^+ titrated with DTBP during 2MP isomerization (Table 3.1). Figure 3.8b shows 3MP, 23DMB, and nH isomerization turnover rates as functions of the (alkane/H_2) molar ratios on a H_3PW/SiO_2-Pt/Al_2O_3 mixture with a 0.04 POM nm^{-2} surface density and a (Pt_s/H^+) ratio of 11.7. 3MP, 23DMB, and nH isomerization turnover rates were independent of Pt content for H_3PW/SiO_2-Pt/Al_2O_3 mixtures with (Pt_S/H^+) ratios between 11.7 and 22.5 (Table 3.3) and indicate these mixtures equilibrate reactant alkanes and alkenes in all cases. Isomerization turnover rates for 3MP, 23DMB, and nH were also the same at H_3PW surface densities of 0.04 and 0.25 POM nm^{-2} (Table 3.3), indicating that reactant alkene concentration gradients do not exist within H_3PW/SiO_2 particles for all isomers and that the isomerization rates on these mixtures are limited only by alkene isomerization on acid sites.

Isomerization turnover rates measured at different H_2 pressures coincide along the same curves for all reactants in Figures 3.8a and 3.8b in agreement with mixtures that maintain reactant alkane-alkene equilibrium. Inverses of their isomerization rates increased linearly with (H_2/alkane) ratios (Figure 3.8b). These kinetic dependences are the same as for 2MP reactants and can be described accurately using analogous elementary steps as Scheme 3.1 depicts for 2MP. Pt sites establish dehydrogenation/hydrogenation equilibrium between reactant alkanes and alkenes. Alkenes isomerize at acid sites by quasi-equilibrated protonation of alkenes to form alkoxides, which subsequently rearrange to alkoxide isomers with different backbones in irreversible steps. The resulting product alkoxides deprotonate to form alkenes that are hydrogenated to alkanes at Pt sites. The isomerization rate expression for each reactant is analogous to the rate expression for 2MP isomerization:

$$\frac{r_{isom}}{\left[H^+\right]} = \frac{k_{isom} K_{prot} K_{dehy} \left(\frac{alkane}{H_2}\right)}{1 + K_{surf} K_{dehy} \left(\frac{alkane}{H_2}\right)} \tag{3.13}$$

where K_{dehy} is the dehydrogenation equilibrium constant to a reference alkene isomer (0.33 Pa for 3MP to *trans*-3-methylpent-2-ene, 0.051 Pa for 23DMB to 2,3-dimethylbut-2-ene, and 0.12 Pa for nH to *cis*-hex-2-ene) from tabulated thermodynamic data [13], K_{prot} is the protonation equilibrium constant for the reference alkene on acid sites forming the reactive alkoxide isomer, k_{isom} is the isomerization rate constant of the alkoxide, and

K_{surf} is the sum of K_{prot} for all alkoxide isomers. The dashed curves in Figures 3.8a and 3.8b are best fits of the data to the form of Eq. (3.4), but where the reactant alkane pressure replaces 2MP pressure. They provide $k_{isom}K_{prot}$ and $k_{isom}K_{prot}K_{surf}^{-1}$ values for all reactants after removing K_{dehy} values. Uncertainties in $k_{isom}K_{prot}$ were much less than in $k_{isom}K_{prot}K_{surf}^{-1}$ for 3MP, 23DMB, and nH reactants (e.g., ± 1 – 2 % for $k_{isom}K_{prot}$ and ± 15 – 270% for $k_{isom}K_{prot}K_{surf}^{-1}$ for the data in Figure 3.8) and predict rates at low (alkane/H_2) ratios more accurately than those at higher ratios.

Values of $k_{isom}K_{prot}$ for $3MP^{=}$, $23DMB^{=}$, and $nH^{=}$ were measured on other acid-metal mixtures by using rate data at low (alkane/H_2) only (75 kPa H_2, < 1.9 kPa alkane). The ($Pt_S/k_{isom}K_{prot}$) ratios for these catalyst mixtures were above their respective values on the H_3PW-Pt/Al_2O_3 mixture used for kinetic experiments and equilibrate reactant alkanes and alkenes (the justification of this criteria is given in Section 3.3.3.1 and Supporting Information). Next, we examine the effects of acid strength and solvation on values of $k_{isom}K_{prot}$ for $3MP^{=}$, $23DMB^{=}$, and $nH^{=}$.

3.3.3.2. Effects of acid strength and solvation on 3-methylpentene, 2,3-dimethylbutene, and n-hexene isomerization rate constants

Figure 3.9a shows the values of $k_{isom}K_{prot}$ for $2MP^{=}$, $3MP^{=}$, $23DMB^{=}$, and $nH^{=}$ reactants measured on POM/SiO_2-Pt/Al_2O_3 (P, Si, Al central atoms) and Pt/H-BEA-Pt/Al_2O_3 mixtures plotted at the deprotonation energy (DPE) of the acid [3, 4]. Values of $k_{isom}K_{prot}$ decrease exponentially with increasing DPE on Keggin POM clusters for $3MP^{=}$, $23DMB^{=}$, and $nH^{=}$ reactants, consistent with the paramount effects of DPE on measured activation energies, but not entropies, as discussed in Section 3.3.2 for $2MP^{=}$ reactants. Activation energies increase, and rate constants decrease, with increasing DPE because charge separation required to form cyclopropyl carbenium ion-pair transition states becomes more demanding as the conjugate anions become less stable. Values of $k_{isom}K_{prot}$ changed similarly with DPE of POM clusters for different reactants (slopes of -0.025 to -0.027 in Figure 3.9a), despite varying by a factor of 10 on all POM clusters. Applying Eq. (3.11) to these slopes suggests that measured activation energies for all reactants sense DPE weakly and equally (i.e., $d(E_{meas})/d(DPE) = 0.10 – 0.11$).

Measured activation energies of $k_{isom}K_{prot}$ for $3MP^{=}$, $23DMB^{=}$, and $nH^{=}$ are described by analogous thermochemical cycles (Eq. (3.9)) and reaction coordinate diagrams as Scheme 3.3 depicts for $2MP^{=}$ (where 2-methylpent-2-ene is replaced by the reference alkene for each reactant). Selectivities to the predominant products do not change significantly with POM composition for any of the reactants; 3MP isomerization is > 85% selective to 2MP on all POM acids, while nH and 23DMB isomerization form predominantly 2MP and 3MP (combined carbon selectivities of > 90% for nH and >85% for 23DMB) at nearly constant ratios (2MP/3MP = 1.4 – 1.6 for nH and 2.0 – 2.2 for 23DMB). Thus, the effects of DPE on measured activation energies are described by Eq. (3.11) for all reactants because the "reaction-weighted" value of E_{gas} for each reactant is the same for all POM. Similar slopes in Figure 3.9a indicate that interaction energies of all isomerization transition states change with DPE to the same extent (i.e., $d(E_{int})/d(DPE) = -0.90$ to -0.89), presumably because they all feature cyclopropyl carbenium ions with similar charge distributions, and consequently recover electrostatic interactions overcome during deprotonation equally. This conclusion is consistent with

2MP selectivities that do not change markedly with DPE on POM clusters (Section 3.3.2).

Measured activation energies for 2MP and 3MP isomerization predominantly reflect the stability of the methyl shift transition state that mediates their interconversion (Scheme 3.4 (A)). Measured activation energies for 23DMB and nH isomerization, however, reflect the reaction-weighted stabilities of transition states forming 2MP and 3MP, which resemble Scheme 3.4 (B) for 23DMB and Scheme 3.4 (C) for nH. The relative stabilities of transition states mediating the isomerizations of $2MP^{=}$, $3MP^{=}$, $23DMB^{=}$, and $nH^{=}$ cannot be determined by comparing their values of $k_{isom}K_{prot}$ directly because they are measured with respect to different alkenes (i.e., 2-methylpent-2-ene for 2MP, *trans*-3-methylpent-2-ene for 3MP, 2,3-dimethylbut-2-ene for 23DMB, and *cis*-hex-2-ene for nH), which have different gas-phase stabilities. Isomerization rate constants for all isomers ($k_{isom}K_{prot}$) were referred to 2-methylpent-2-ene (via $k_{isom}K_{prot}K_{ene}^{-1}$ values) to remove the dependence on the reactant alkene's stability using the data in Figure 3.9a and equilibrium constants between alkenes (K_{ene}) calculated from thermodynamic data [13]:

$$K_{ene} = \frac{[\text{reference alkene}]}{[\text{2-methylpent-2-ene}]} \tag{3.14}$$

where the reference alkene is determined by the isomer used to calculate the K_{dehy} value for a given reactant. Values of $k_{isom}K_{prot}K_{ene}^{-1}$ are the same for 2MP and 3MP on all POM clusters in Figure 3.9b, indicating that these reactants predominantly isomerize via the same kinetically-relevant transition state. This result is consistent with the microscopic reversibility of 2-methylpentoxide and 3-methylpentoxide isomerization elementary steps in pathways where alkoxide rearrangement is the sole kinetically-relevant step. Values of $k_{isom}K_{prot}K_{ene}^{-1}$ for 23DMB and nH reactants are factors of ca. 3.6 and 15 lower than for 2MP on all POM clusters, respectively, and suggest that the free energies of their isomerization transition states are 5.2 and 10.8 kJ mol^{-1} less stable than the transition state mediating 2MP-3MP interconversion (calculation in the Supporting Information) regardless of the POM anion. Values of $k_{isom}K_{prot}K_{ene}^{-1}$ that differ among reactants, but change similarly with DPE, clearly show that more demanding reactions are not necessarily more sensitive to acid strength than less demanding reactions. The essential role of E_{gas} in determining the activation energies of different isomers (Eq. (3.9)), but not in how they sense DPE (Eq. (3.11)), suggest that the stabilities of gaseous transition state cations cause differences in $k_{isom}K_{prot}K_{ene}^{-1}$ for the different reactants. DFT calculations predict that gas-phase protonation of 2-methylpent-2-ene to form cations mediating 2MP-3MP isomerization (Scheme 3.4 (A)) is more exothermic than forming cations mediating 2MP-23DMB isomerization (Scheme 3.4 (B)) (i.e., E_{gas} = -817 kJ mol^{-1} and -772 kJ mol^{-1} for 3MP and 23DMB cations [26], respectively, in Eq. (3.9)). The difference in these DFT-derived E_{gas} energies (45 kJ mol^{-1}) is significantly larger than the difference in transition state free energies calculated from $k_{isom}K_{prot}K_{ene}^{-1}$ for $2MP^{=}$ and $23DMB^{=}$ (5.2 kJ mol^{-1}). Entropies are not anticipated to cause this discrepancy since 23DMB transition state cations will have less entropy than

3MP transition state cations because formation of the former requires concerted C-C and C-H bond formation and cleavage, while the latter only requires C-C bond formation and cleavage. 23DMB and 3MP formation transition states have similar differences in DFT-calculated stabilities when they interact with H_2O (38 kJ mol^{-1}) and anions of aluminosilicate clusters (46 kJ mol^{-1}) [26] as the difference in the stabilities of their gas-phase analogs (45 kJ mol^{-1}). These observations are consistent with all isomerization transition state cations interacting equally effectively with bases, regardless of the reaction's difficulty, and suggest that DFT systematically over predicts the energies of edge-protonated cyclopropyl species in 23DMB isomerization relative to cyclopropyl species in 2MP-3MP interconversion.

Figures 3.9a and 3.9b also show the values of $k_{isom}K_{prot}$ and $k_{isom}K_{prot}K_{ene}^{-1}$, respectively, measured for each reactant on Pt/H-BEA. Values of $k_{isom}K_{prot}$ measured on Pt/H-BEA are above the trend defined by POM acids for all alkenes, suggesting entropic losses caused by confinement are more than compensated for by stronger enthalpic stabilization of transition states via van der Waals forces. Transition state stabilization by van der Waals forces reduces activation energies when they are measured with respect to unconfined alkenes (Eq. (3.12b)). Values of $k_{isom}K_{prot}K_{ene}^{-1}$ on Pt/H-BEA are the same for $2MP^{=}$ and $3MP^{=}$ (Figure 3.9b) and suggest these alkenes isomerize predominantly via the microscopic reverse of each other, and therefore sense solvation equally. Values of $k_{isom}K_{prot}K_{ene}^{-1}$ for 23DMB and nH on Pt/H-BEA suggest that the transition states mediating their rearrangements are respectively 13.2 and 13.7 kJ mol^{-1} higher in free energy than the 2MP-3MP methyl shift transition state (Supporting Information). Comparing these free energy differences to those calculated for POM clusters suggests that solvation preferentially stabilizes 2MP-3MP methyl shift transition states over those converting 23DMB and nH by 8 and 2.9 kJ mol^{-1}, respectively. We speculate that transition states mediating methyl shift reactions sense solvation most strongly because the entire C_5 backbone is able to maintain van der Waals contacts with the zeolite channel walls throughout the alkoxide isomerization reaction coordinate. Alkoxide isomerizations that change the number of methyl groups must contort their backbone to achieve the necessary geometry for concerted C-C and C-H bond rearrangements, and as a result, weaken van der Waals contacts at the transition state. Preferential solvation of methyl shift transition states also accounts for the significantly higher 22DMB selectivities measured on Pt/H-BEA compared to the POM clusters (Section 3.3.3.1). The preferential solvation of methyl shift transition states is less than the incremental van der Waals interactions per "CH_2" measured for linear alkanes in other large pore zeolites (enthalpies of 7 and 9 kJ mol^{-1} per CH_2 for FAU and MOR [36]); thus, the contortion of the alkoxide backbone at nH and 23DMB transition states likely only weakens van der Waals contacts and does not fully remove them. The preferential solvation of transition states from nH relative to those from 23DMB may be caused by the higher degree of branching in 23DMB, which reduces the number of van der Waals contacts at isomerization transition states, because 23DMB cannot lie flat along the walls of BEA channels.

These results suggest that changes in acid strength alone will not lead to more selective isomerization reactions, or any other reaction where transition state cations in competing pathways have similar charge distributions. More selective isomerizations can

be achieved by changing the microporous environments containing acid sites through structural features such as straight channels, cages, side pockets, and channel intersections. For example, selective isomerization of straight chain reactants may occur best in 1-dimesional straight channels because their backbones can lie flat along channel walls. Conversion of branched reactants, however, may occur selectively in cages because the curvature of zeolite walls can better accommodate the bulky structures of such reactants.

3.4. Conclusions

The effects of acid strength and confinement on reactivity are demonstrated using 2-methylpentane (2MP), 3-methylpentane (3MP), 2,3-dimethylbutane (23DMB), and n-hexane (nH) isomerization routes on well-defined solid Brønsted acids in mixtures with Pt/Al_2O_3 co-catalysts. Alkanes dehydrogenate at Pt sites and the resulting alkenes isomerize to one another through alkoxide backbone rearrangements at acid sites via similar elementary steps and with similar rate expressions when Pt/Al_2O_3 co-catalysts equilibrate reactant alkanes and alkenes. Isomerization rate constants for each reactant alkene ($k_{isom}K_{prot}$), which include the formation of all products, were measured on Keggin polyoxometalate (POM) clusters and zeolite BEA using mechanism-based interpretations of rate data and titrations that count the number of reactive H^+. Rate constants for the formation of individual products could not be separated from total isomerization rate constants because reactive product alkenes undergo secondary isomerizations rapidly before being hydrogenated at acid sites by hydride transfer with alkanes or at metal sites with H_2 and make unequivocal interpretations of selectivities difficult. Measured isomerization rate constants ($k_{isom}K_{prot}$) reflect the stabilities of cyclopropyl carbenium ion transition states, which mediate kinetically-relevant alkoxide isomerization steps, relative to gaseous reactant alkenes; rate constants decrease exponentially with increasing deprotonation energies (DPE) on Keggin POM for all reactants because ion-pair transition states contain less stable conjugate anions on weak acids. Activation energies of isomerization rate constants (E_{meas}) increase less than the commensurate changes in DPE because electrostatic interactions between the conjugate anion and cationic moieties at transition states recover most of the additional energy needed to deprotonate weaker acids. Rate constants for all reactants sense DPE equally because cyclopropyl carbenium ions with similar charge distributions mediate all transition states and lead to similar interactions with conjugate anions. Confinement of acid sites within BEA channel leads to higher isomerization reactivities than predicted from DPE alone, because preferential solvation of transition states (relative to gas-phase alkenes) reduces activation energies and overcompensates for larger entropic losses in zeolite voids. Confinement in BEA favors alkyl shifts relative to isomerizations changing the degree of branching and also favors reactions whose transition states have less branching because the transition states of preferred reactions presumably have more van der Waals contacts with the zeolite wall. The conclusions from this study suggest that strategies for improving selective isomerizations should focus on developing microporous containers of acid sites that solvate specific backbone arrangements, and not on changing catalyst acid strength, because of the similar charge distributions of cations mediating all isomerization reactions.

3.5. Tables, Figures, and Schemes

3.5.1. Tables

Table 3.1. Number of accessible H^+ per POM cluster or framework Al measured by chemical titration with 2,6-di-*tert*-butylpyridine[a] during 2-methylpentane isomerization[b] on $HXW_{12}O_{40}/SiO_2$-Pt/Al_2O_3 (X = P, Si, Al), H-BEA-Pt/Al_2O_3, and Pt/H-BEA-Pt/Al_2O_3 mixtures.

Catalyst	POM Content (% wt)	POM Surface Density (POM nm^{-2})	Accessible H^+ (per POM or framework Al)
$H_3PW_{12}O_{40}$	5	0.04	0.9
$H_4SiW_{12}O_{40}$	5	0.04	1.6
$H_5AlW_{12}O_{40}$	5	0.04	1.45
H-BEA (Si/Al = 11.8)	- - -	- - -	0.26[c]
Pt/H-BEA (Si/Al = 11.8)			0.25[c]

[a] Assuming a 1:1 DTBP:H^+ stoichiometry
[b] 1.9 kPa 2-methylpentane, 75 kPa H_2, 473 K
[c] Value listed per framework Al

Table 3.2. 2-Methylpentene isomerization rate constants ($k_{isom}K_{prot}$ and $k_{isom}K_{prot}K_{surf}^{-1}$) and the sums of protonation equilibrium constants (K_{surf}) measured on $HXW_{12}O_{40}/SiO_2$-Pt/Al_2O_3 (X = P, Si, Al), H-BEA-Pt/Al_2O_3, and Pt/H-BEA-Pt/Al_2O_3 mixtures (473 K)

Catalyst	$k_{isom}K_{prot}$ [a,d]	$k_{isom}K_{prot}K_{surf}^{-1}$ [b,d]	K_{surf} [c,d]
$H_3PW_{12}O_{40}$	2460 ± 20	1500 ± 400	1.7 ± 0.5
$H_4SiW_{12}O_{40}$	1610 ± 20	3000 ± 3000	0.6 ± 0.7
$H_5AlW_{12}O_{40}$	1070 ± 10	150 ± 20	7.3 ± 0.9
H-BEA	990 ± 10	59 ± 4	17 ± 1
Pt/H-BEA	2740 ± 60	69 ± 3	39 ± 2

[a] 10^{-3} molecules (Pa H^+ s)$^{-1}$
[b] 10^{-3} molecules (H^+ s)$^{-1}$
[c] Pa^{-1}
[d] Errors represent standard deviations of parameters in Eq. (3.4) from least-squares regression.

Table 3.3. 3MP, 23DMB, and nH isomerization rates measured on H_3PW/SiO_2-Pt/Al_2O_3 mixtures

Surface Density (POM nm^{-2})	Pt_s/H^+ Ratio	3MP Turnover Rate[a,b]	23DMB Turnover Rate[a,b]	nH Turnover Rate[a,b]
0.04	11.7	75	32	7.5
0.04	22.5	80	30	9.4
0.25	10.5	73	32	7.2

[a] 10^{-3} molecules (H^+ s)$^{-1}$
[b] 473 K, 1.9 kPa alkane, 75 kPa H_2

3.5.2. Figures

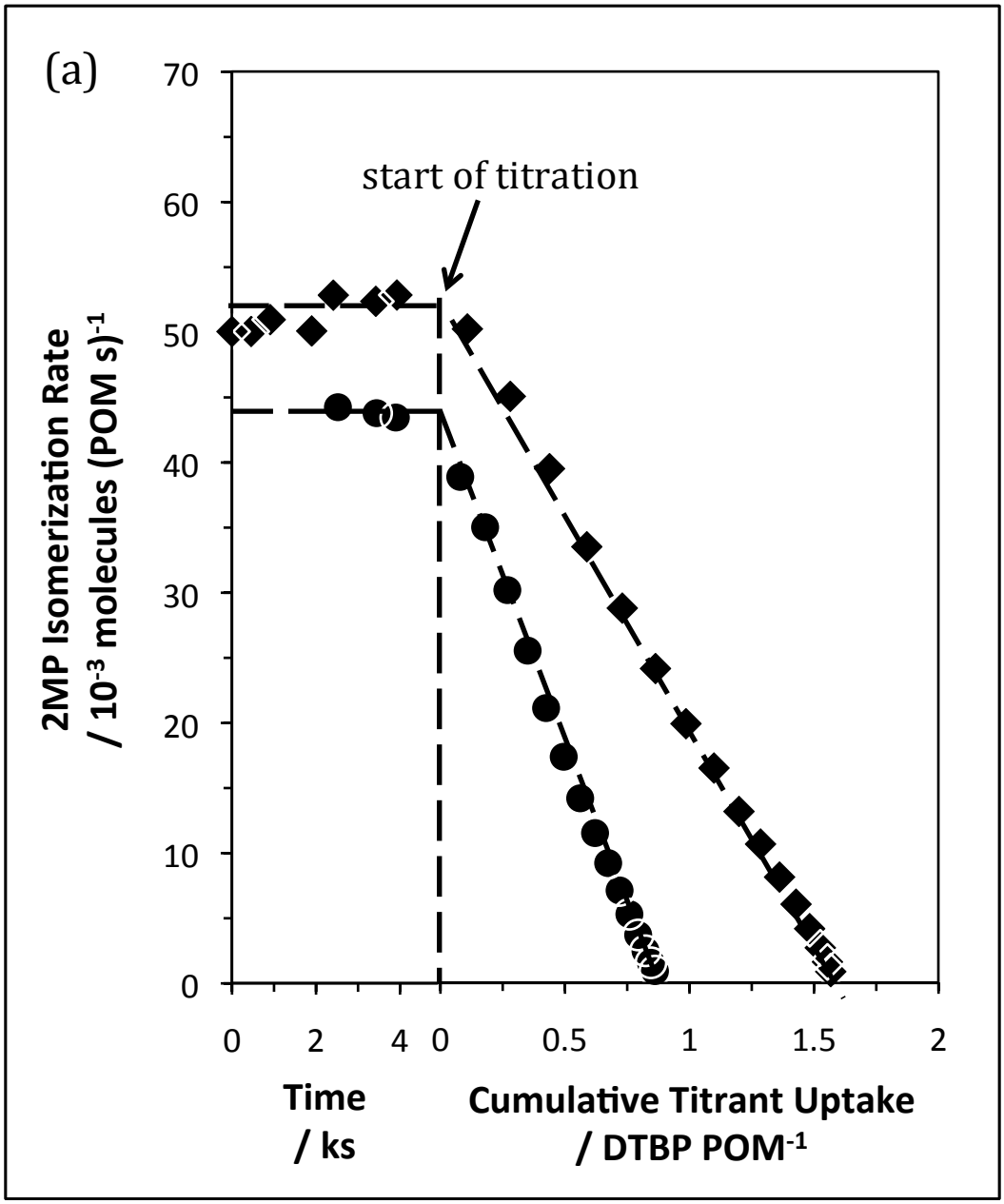

Figure 3.1. (a) 2-Methylpentane isomerization rates (per POM) on (●) H_3PW/SiO_2-Pt/Al_2O_3 (Pt_S/H^+ = 11.7) and (◆) H_4SiW/SiO_2-Pt/Al_2O_3 (Pt_S/H^+ = 4.8) as functions of time before 2,6-di-*tert*-butylpyridine injection (473 K, 1.9 kPa 2MP, 75 kPa H_2) and as functions of cumulative titrant uptake (473 K, 1.9 kPa 2MP, 75 kPa H_2, 0.45 Pa DTBP).

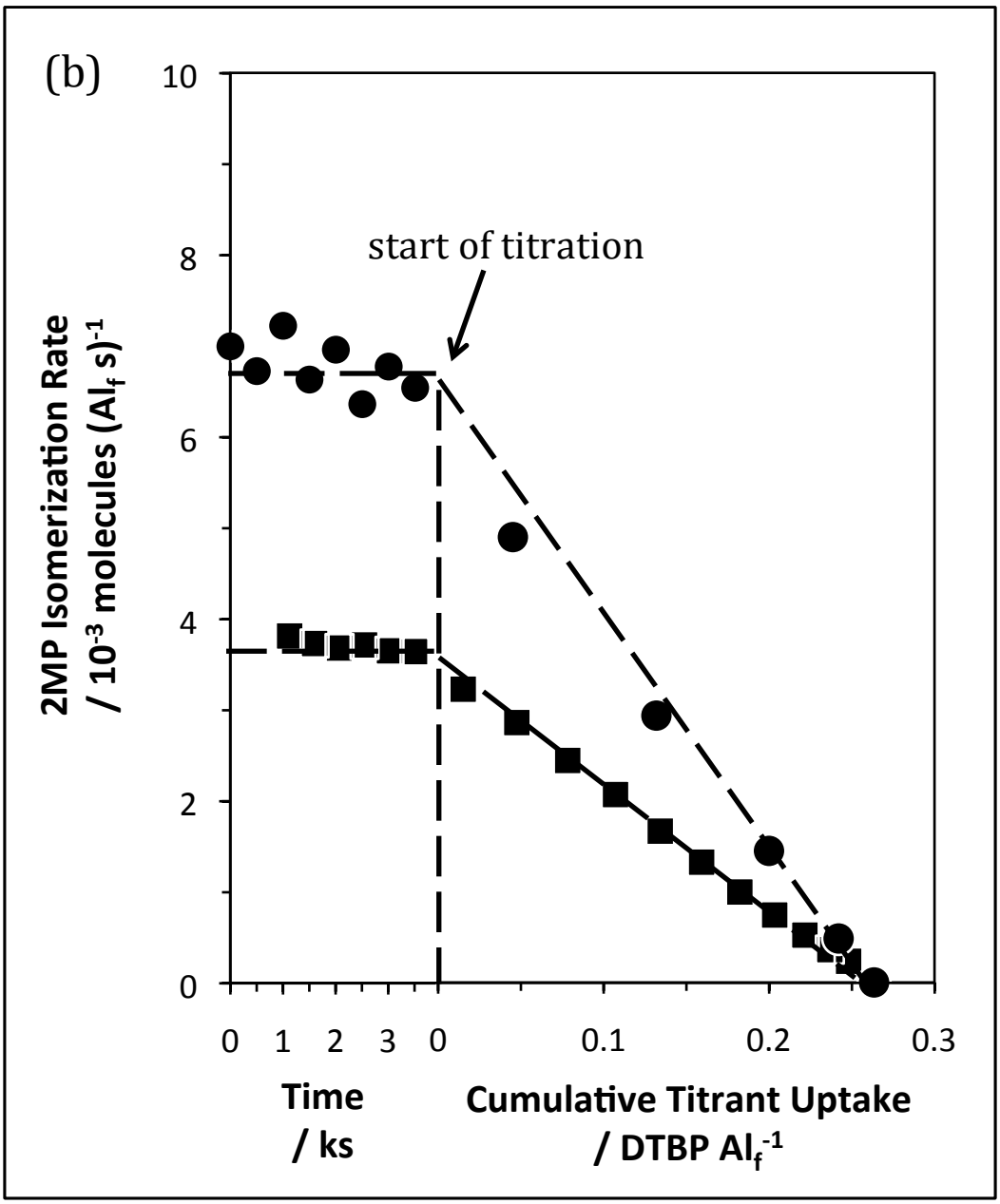

Figure 3.1. (b) 2-Methylpentane isomerization rates (per Al_f) on (■) H-BEA-Pt/Al_2O_3 (Pt_S/H^+ = 3.2) and (●) Pt/H-BEA-Pt/Al_2O_3 (Pt_S/H^+ = 2.9) as functions of time before 2,6-di-*tert*-butylpyridine injection (473 K, 1.9 kPa 2MP, 75 kPa H_2) and as functions of cumulative titrant uptake (473 K, 1.9 kPa 2MP, 75 kPa H_2, 2.5 Pa DTBP).

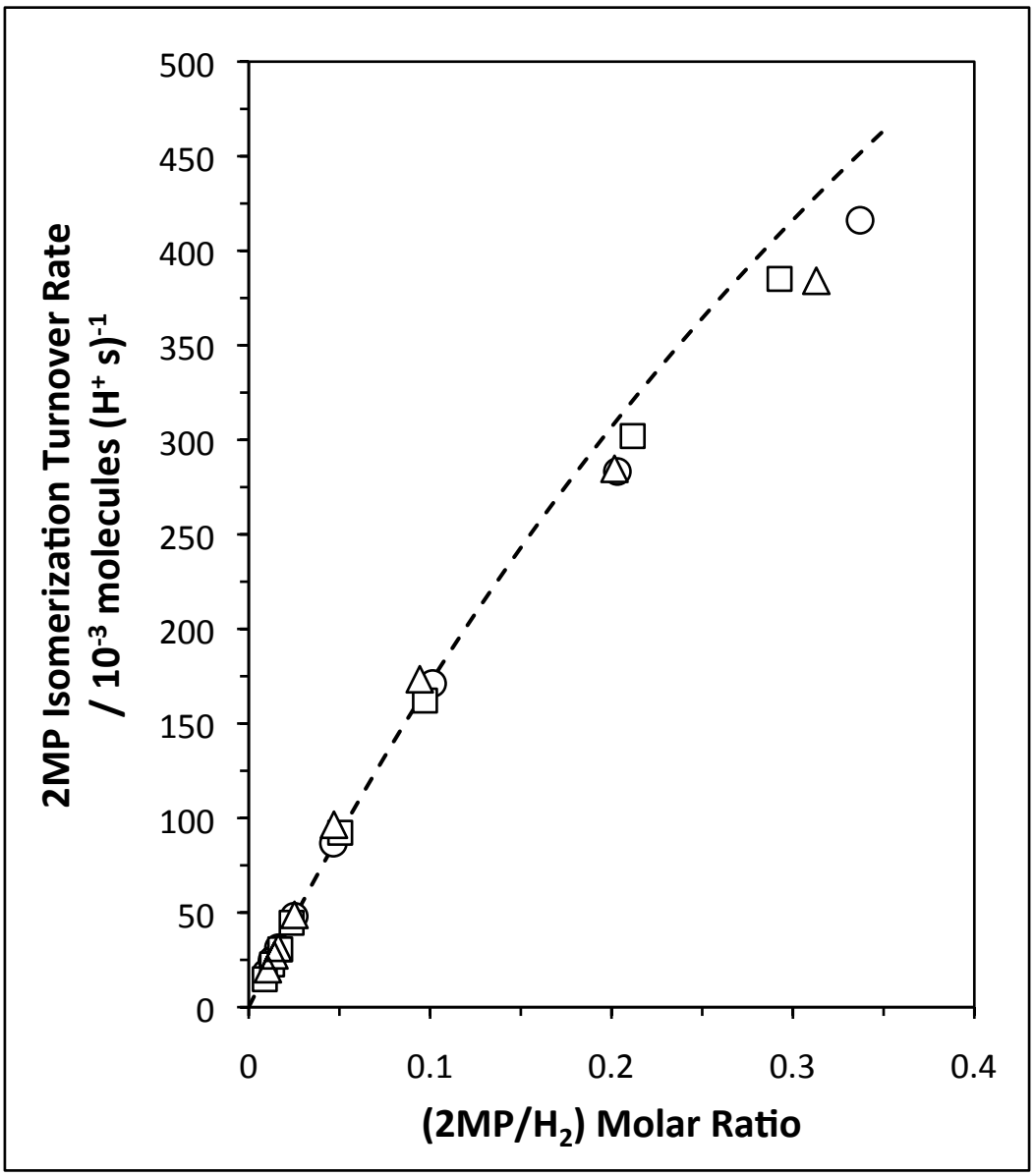

Figure 3.2. 2-Methylpentane isomerization turnover rates as functions of the ($2MP/H_2$) ratio on H_3PW/SiO_2-Pt/Al_2O_3 mixtures with (○) 0.04 H_3PW $[nm\text{-}SiO_2]^{-2}$ and Pt_S/H^+ = 11.7, (△) 0.04 H_3PW $[nm\text{-}SiO_2]^{-2}$ and Pt_S/H^+ = 22.5, and (□) 0.25 H_3PW $[nm\text{-}SiO_2]^{-2}$ and Pt_S/H^+ = 10.5 (reaction conditions: 473 K, 0.5 – 25 kPa 2MP, 75 kPa H_2). Dashed lines represent the regression of the data to Eq. (3.4).

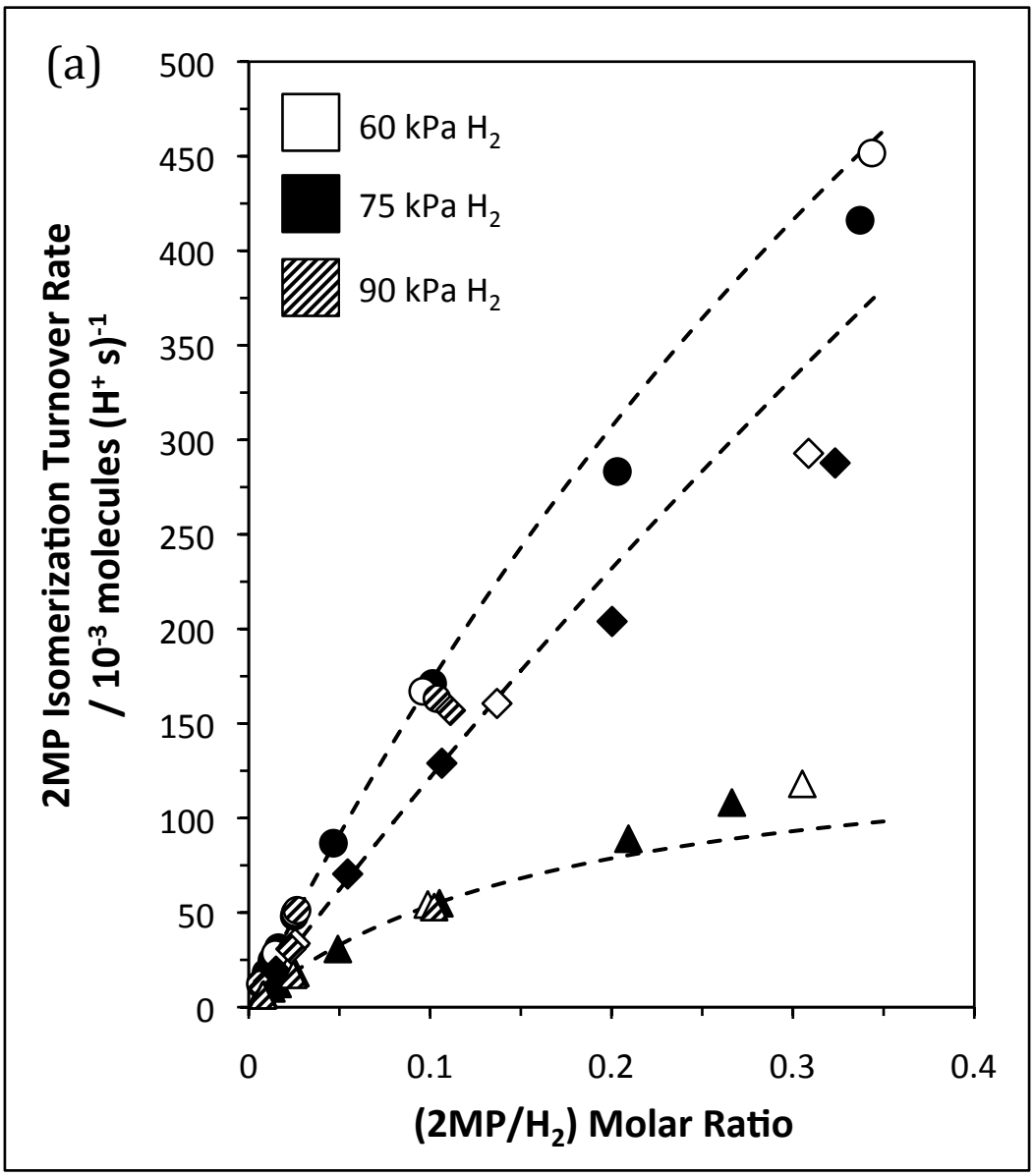

Figure 3.3. (a) Total 2-methylpentane isomerization turnover rates as functions of the (2MP/H_2) ratio on mixtures of Pt/Al_2O_3 with (●) H_3PW/SiO_2 (Pt_S/H^+ = 11.7), (◆) H_4SiW/SiO_2 (Pt_S/H^+ = 4.8), and (▲) H_5AlW/SiO_2 (Pt_S/H^+ = 5.0) (reaction conditions: 473 K, 0.5 – 25 kPa 2MP, 60 – 90 kPa H_2). Dashed lines represent the regression of the data to Eq. (3.4).

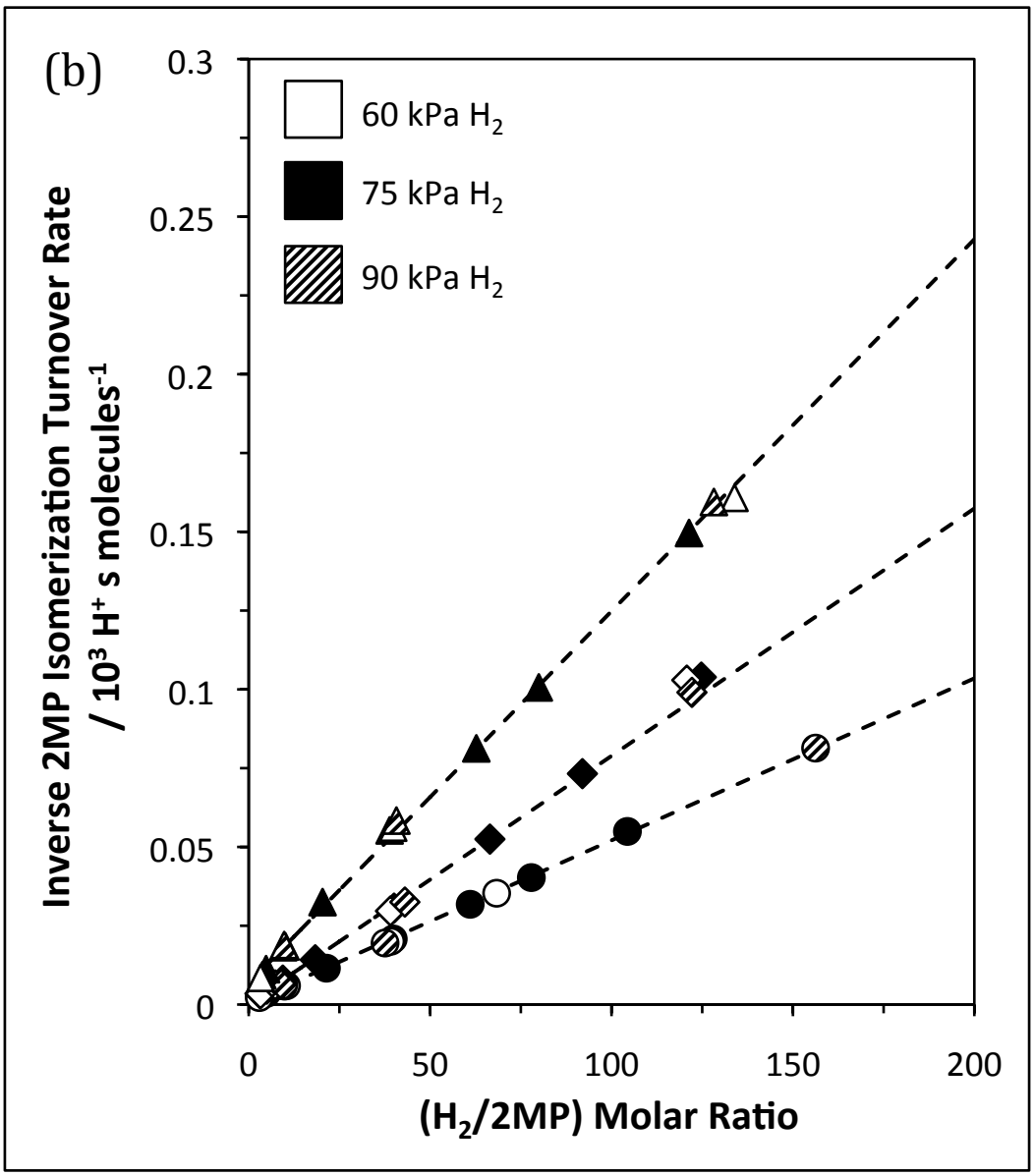

Figure 3.3. (b) Inverse 2-methylpentane isomerization turnover rates as a function of the (H_2/2MP) ratio on mixtures of Pt/Al_2O_3 with (●) H_3PW/SiO_2 (Pt_S/H^+ = 11.7), (◆) H_4SiW/SiO_2 (Pt_S/H^+ = 4.8), and (▲) H_5AlW/SiO_2 (Pt_S/H^+ = 5.0) (reaction conditions: 473 K, 0.5 – 25 kPa 2MP, 60 – 90 kPa H_2). Dashed lines represent the regression of the data to Eq. (3.4).

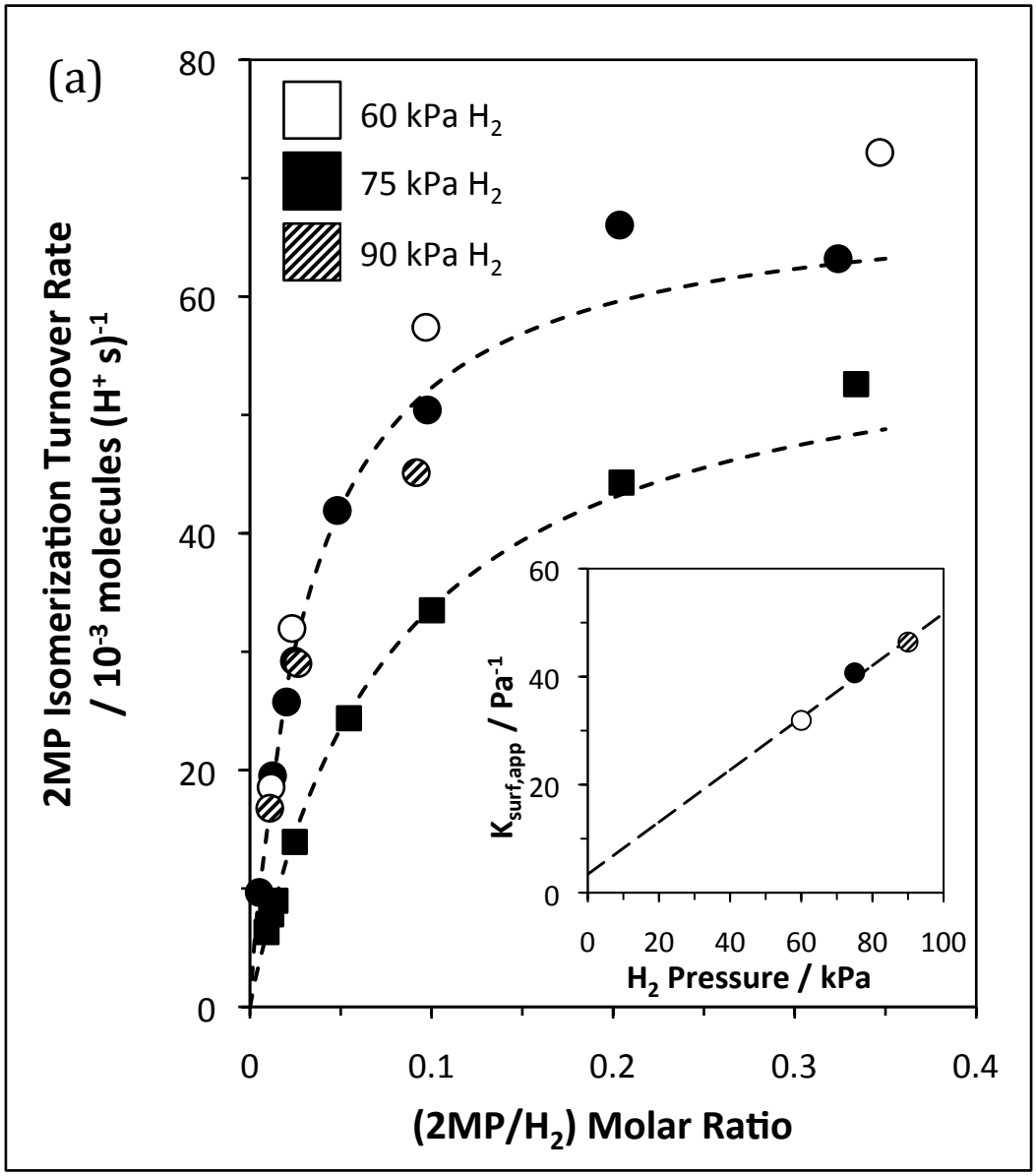

Figure 3.4. (a) 2-Methylpentane isomerization turnover rates as functions of the ($2MP/H_2$) ratio on mixtures of Pt/Al_2O_3 with (■) H-BEA (Pt_S/H^+ = 3.2) and (●) Pt/H-BEA (Pt_S/H^+ = 2.9) (reaction conditions: 473 K, 0.5 – 25 kPa 2MP, 60 – 90 kPa H_2). Dashed lines represent the regression of the data at 75 kPa H_2 to Eq. (3.4). The inset shows apparent values of K_{surf} on Pt/H-BEA ($K_{surf,app}$) fit using Eq. (3.4) as a function of the H_2 pressure. The dashed line in the inset is the regression of the data to Eq. (3.6).

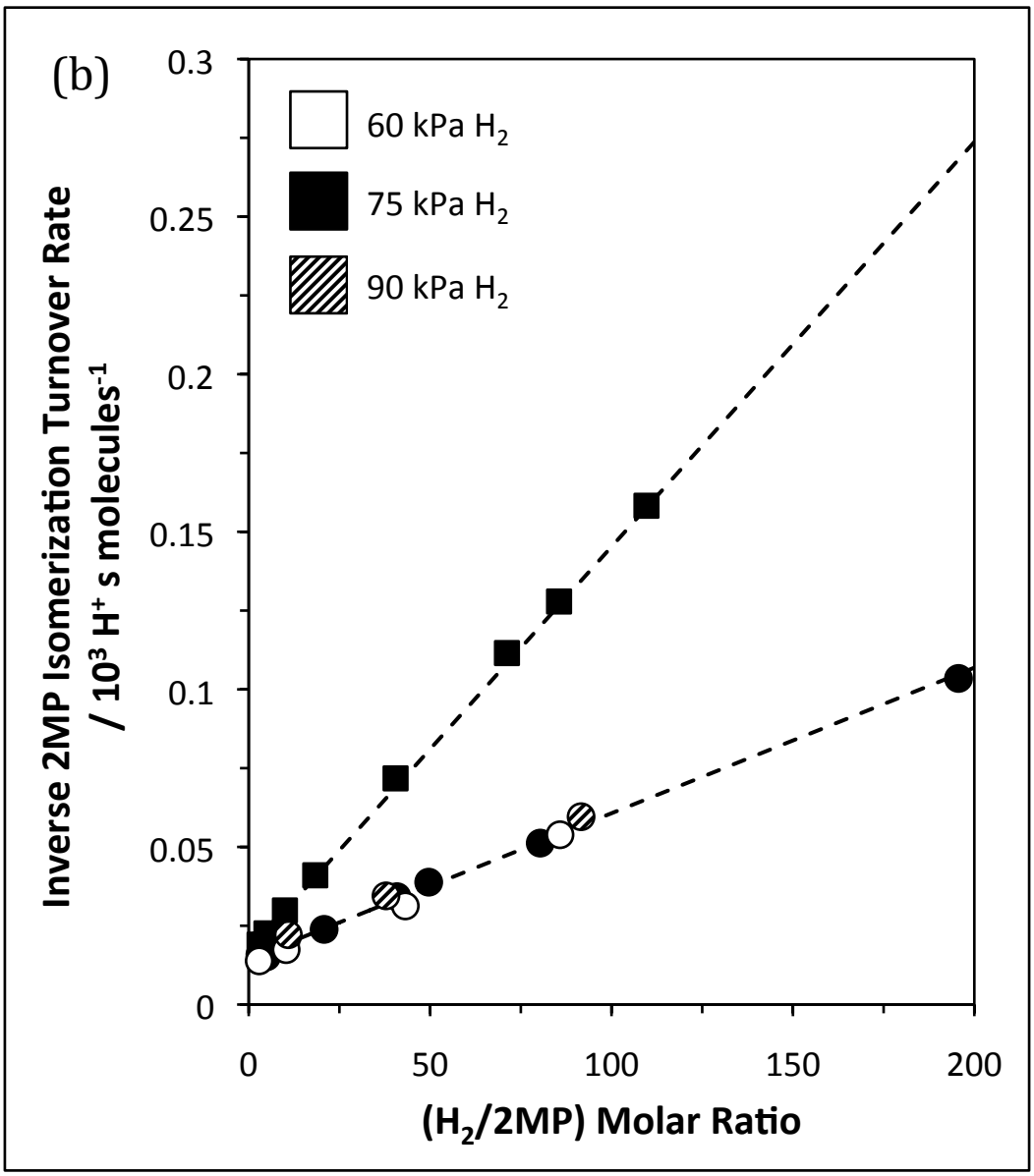

Figure 3.4. (b) Inverse 2-methylpentane isomerization turnover rates as a function of the (H_2/2MP) ratio on mixtures of Pt/Al_2O_3 with (■) H-BEA (Pt_S/H^+ = 3.2) and (●) Pt/H-BEA (Pt_S/H^+ = 2.9) (reaction conditions: 473 K, 0.5 – 25 kPa 2MP, 60 – 90 kPa H_2). Dashed lines represent the regression of the data at 75 kPa H_2 to Eq. (3.4).

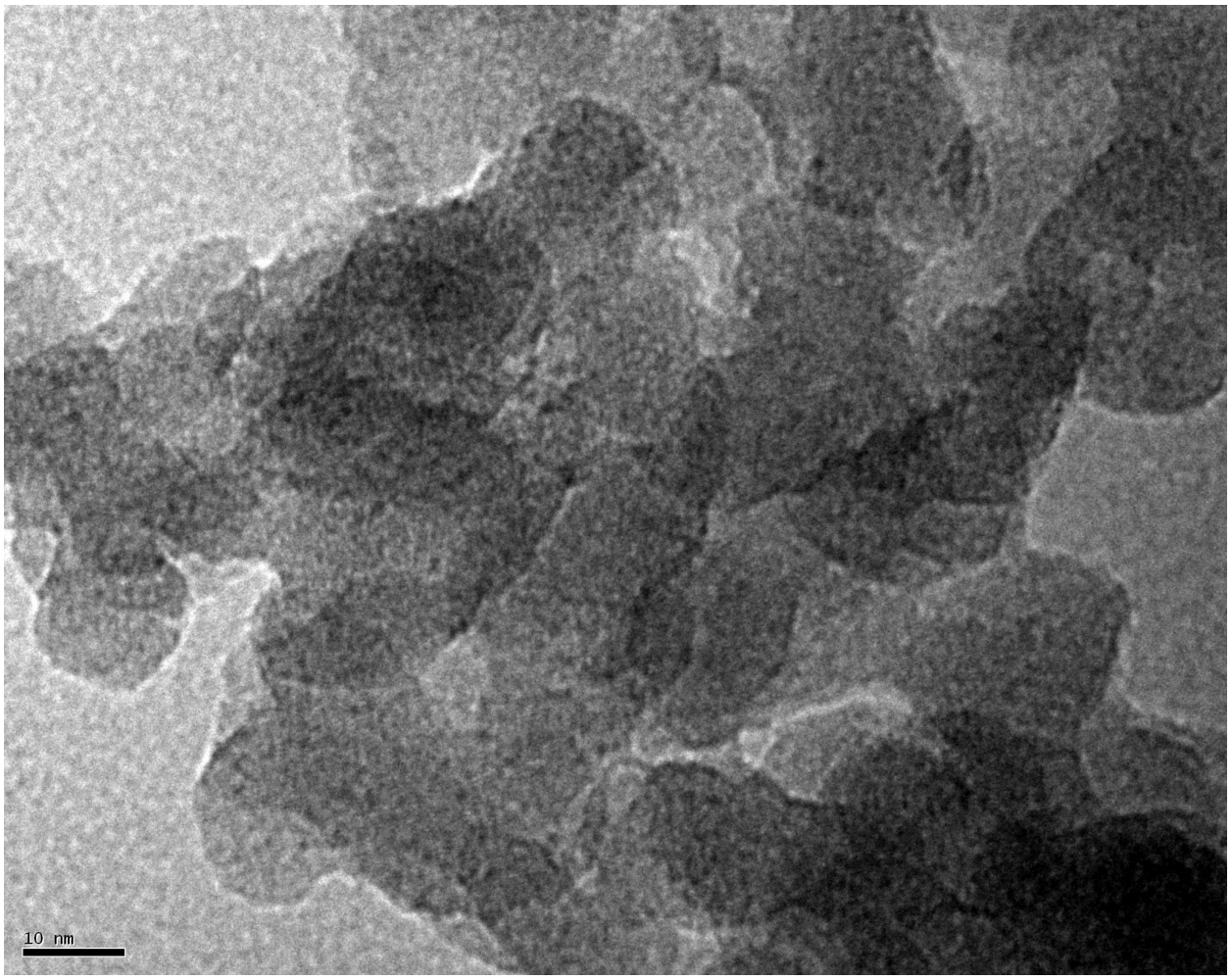

Figure 3.5. Transmission electron micrograph of Pt/H-BEA. Pt clusters are small dark features with diameters ca. 1 nm.

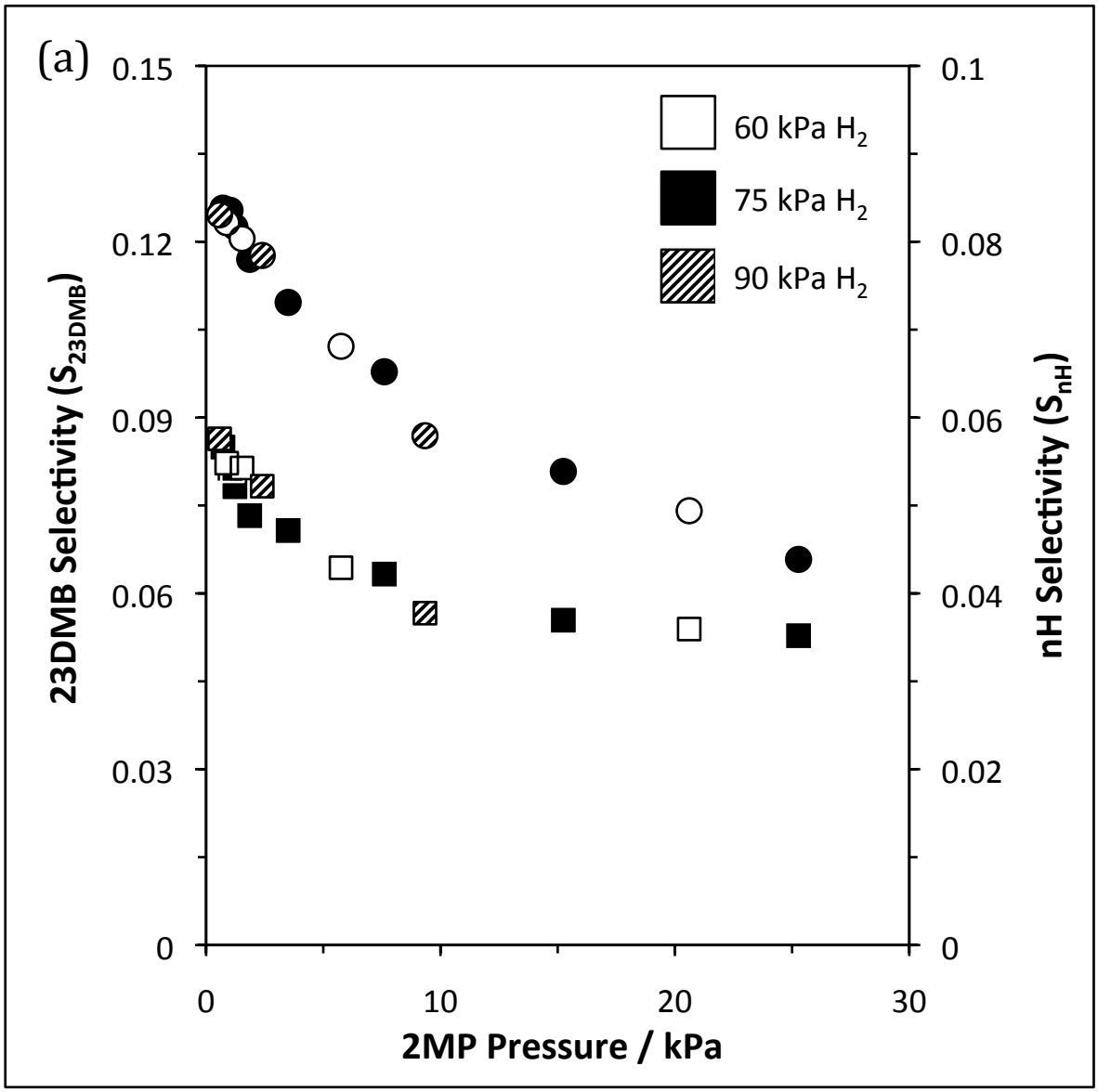

Figure 3.6. (a) 23DMB selectivities (S_{23DMB}; ●) and nH selectivities (S_{nH}; ■) as functions of 2MP pressure on a H_3PW/SiO_2-Pt/Al_2O_3 mixtures with 0.04 H_3PW [nm-SiO_2]$^{-2}$ and Pt_S/H^+ = 11.7 (reaction conditions: 473 K, 0.5 – 25 kPa 2MP, 60-90 kPa H_2).

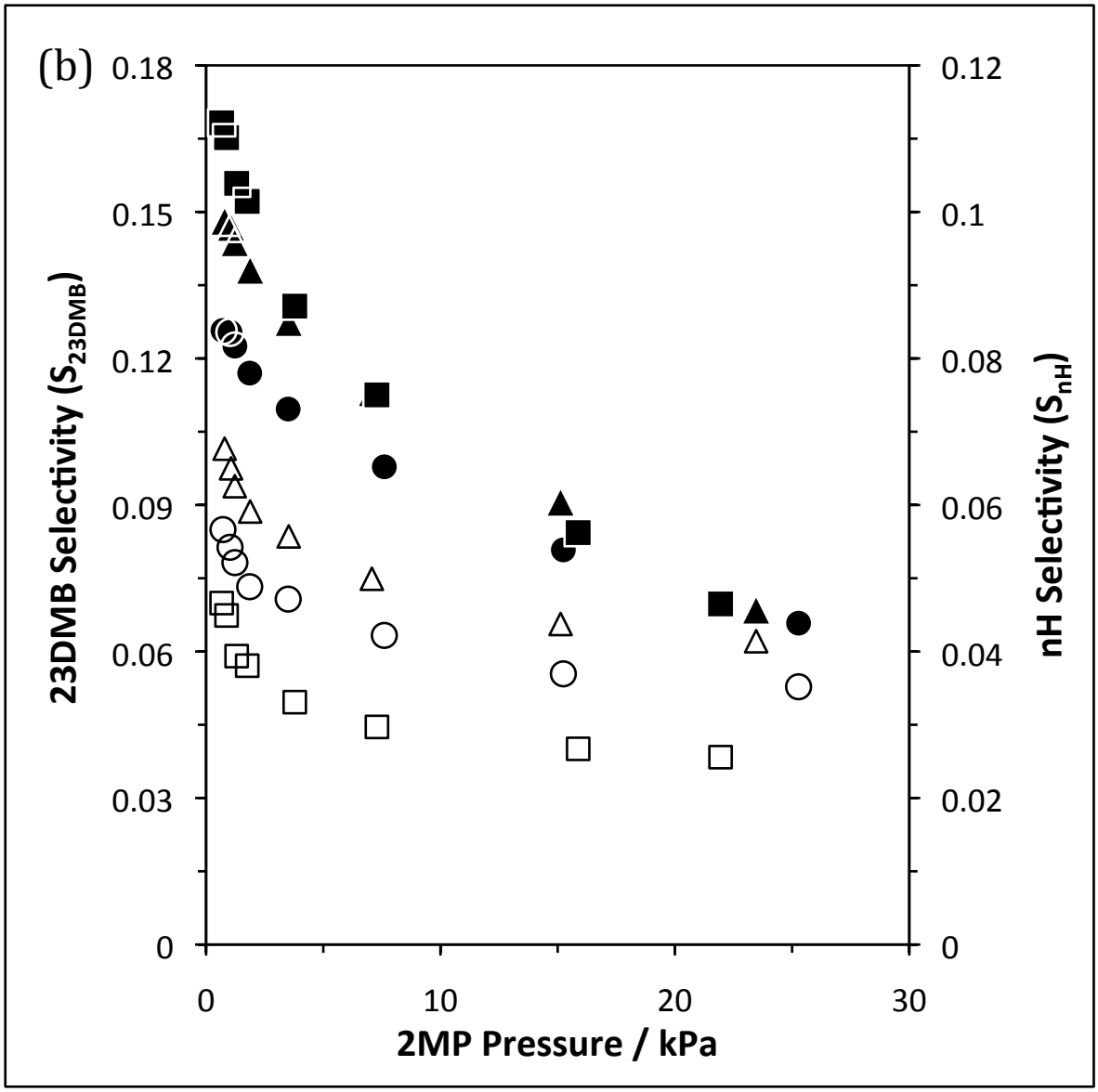

Figure 3.6. (b) 23DMB selectivities (S_{23DMB}; filled symbols) and nH selectivities (S_{nH}; open symbols) as functions of 2MP pressure on H_3PW/SiO_2-Pt/Al_2O_3 mixtures with (●) 0.04 H_3PW [nm-SiO_2]$^{-2}$ and Pt_S/H^+ = 11.7, (▲) 0.04 H_3PW [nm-SiO_2]$^{-2}$ and Pt_S/H^+ = 22.5, and (■) 0.25 H_3PW [nm-SiO_2]$^{-2}$ and Pt_S/H^+ = 10.5 (reaction conditions: 473 K, 0.5 – 25 kPa 2MP, 75 kPa H_2).

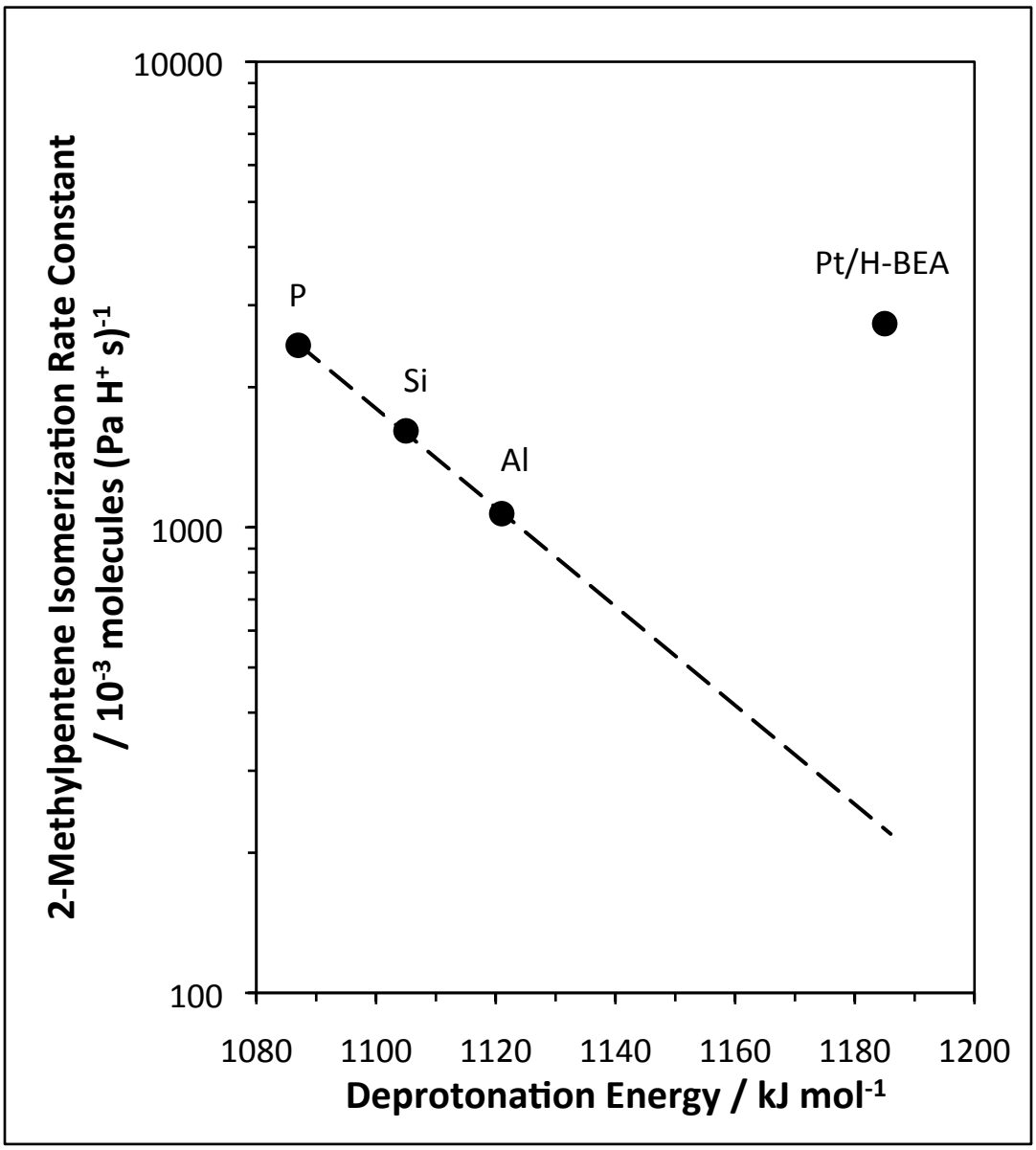

Figure 3.7. Total 2-methylpentene isomerization rate constants ($k_{isom}K_{prot}$; 473 K) as a function of deprotonation energy for $H_{8-n}X^{n+}W_{12}O_{40}$ (X = P, Si, Al) and BEA. The dashed line is an exponential fit of $k_{isom}K_{prot}$ values to deprotonation energies on Keggin clusters.

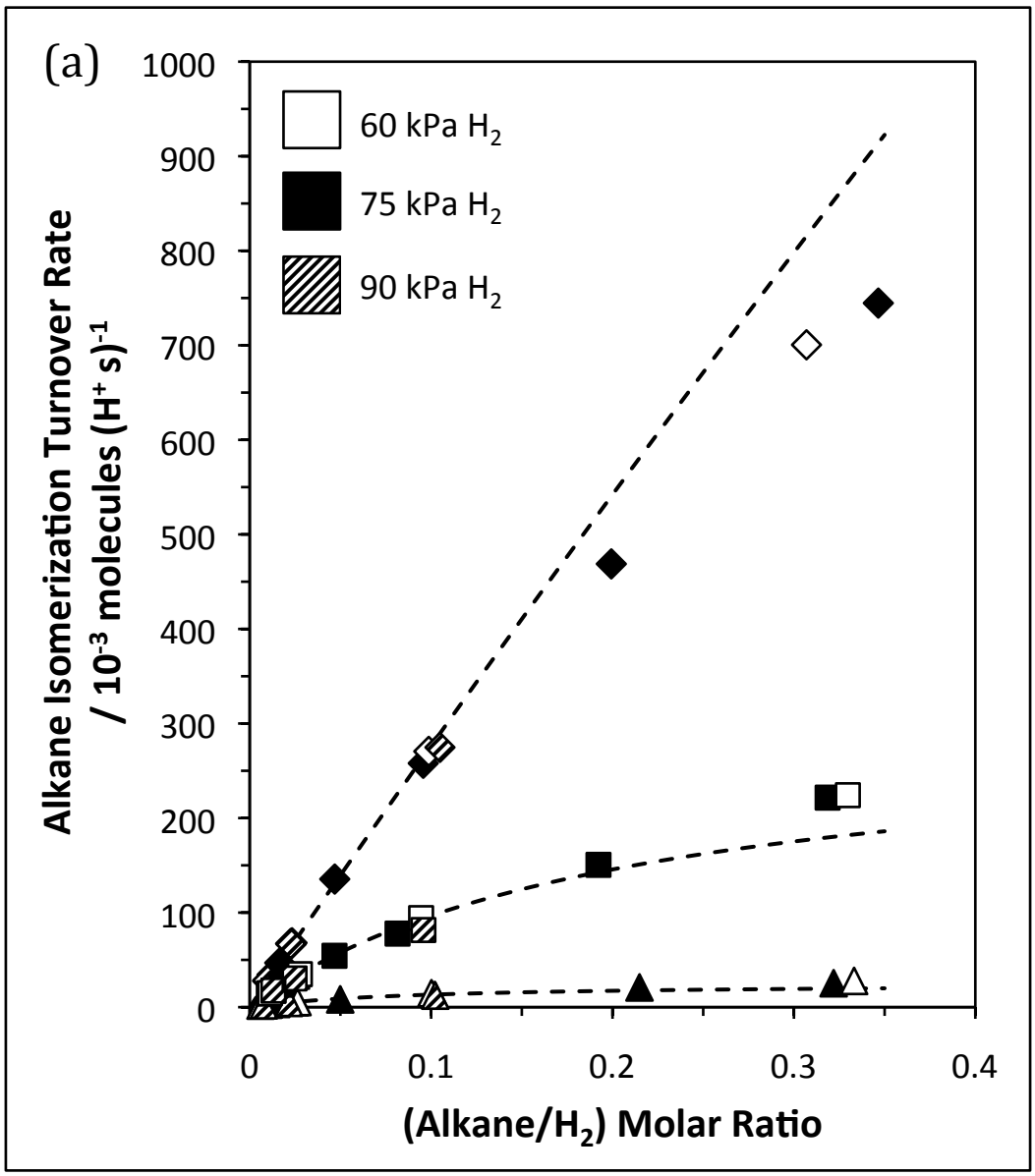

Figure 3.8. (a) (◆) 3-Methylpentane, (■) 2,3-dimethylbutane, and (▲) n-hexane isomerization turnover rates as functions of the (alkane/H_2) ratio on H_3PW/SiO_2-Pt/Al_2O_3 (Pt_S/H^+ = 11.7) (reaction conditions: 473 K, 0.5 – 25 kPa alkane, 60 – 90 kPa H_2). Dashed lines represent the regression of the data to Eq. (3.4).

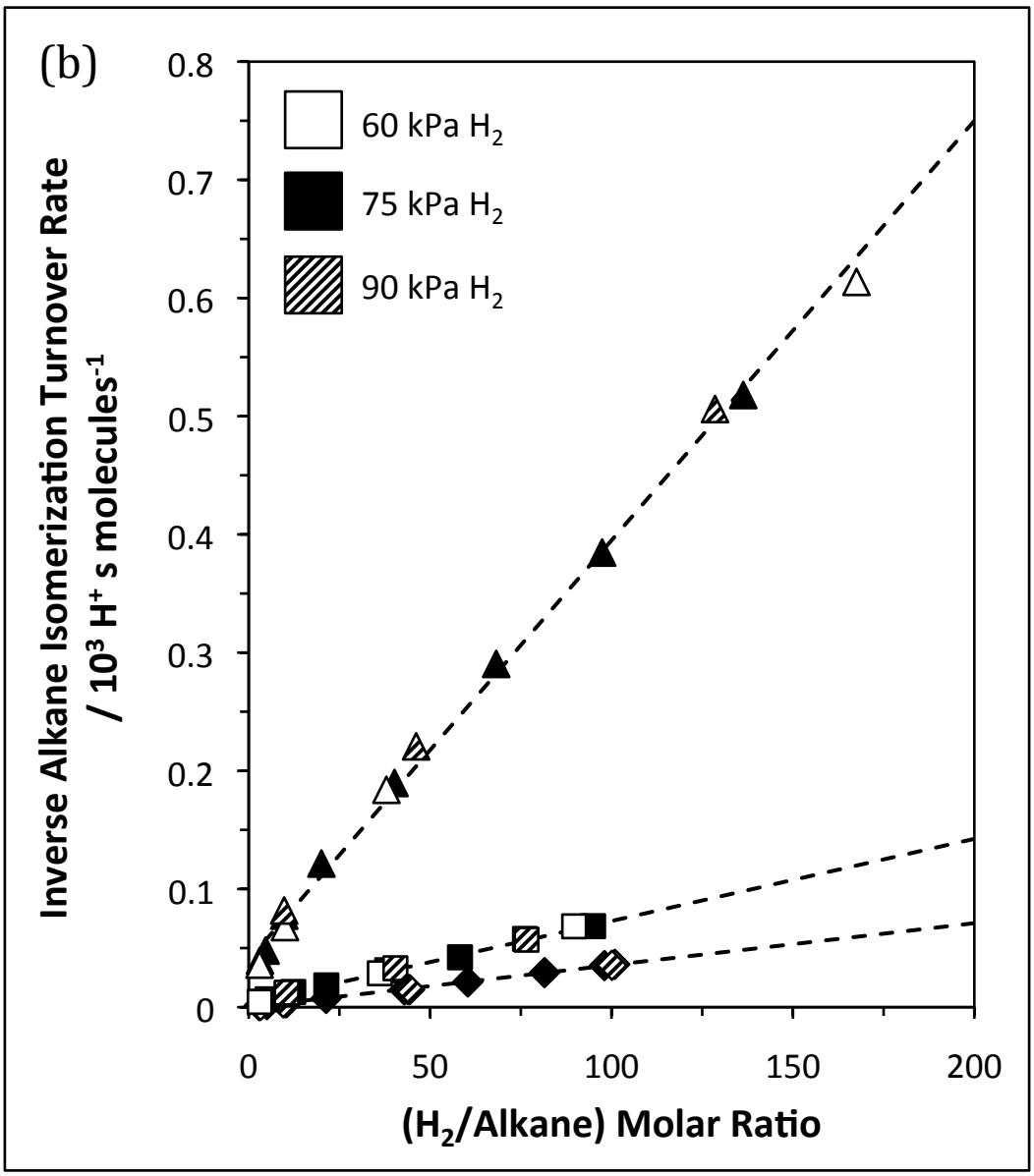

Figure 3.8. (b) Inverse (◆) 3-methylpentane, (■) 2,3-dimethylbutane, and (▲) n-hexane isomerization turnover rates as functions of the (H_2/alkane) ratio on H_3PW/SiO_2-Pt/Al_2O_3 (Pt_S/H^+ = 11.7) (reaction conditions: 473 K, 0.5 – 25 kPa alkane, 60 – 90 kPa H_2). Dashed lines represent the regression of the data to Eq. (3.4).

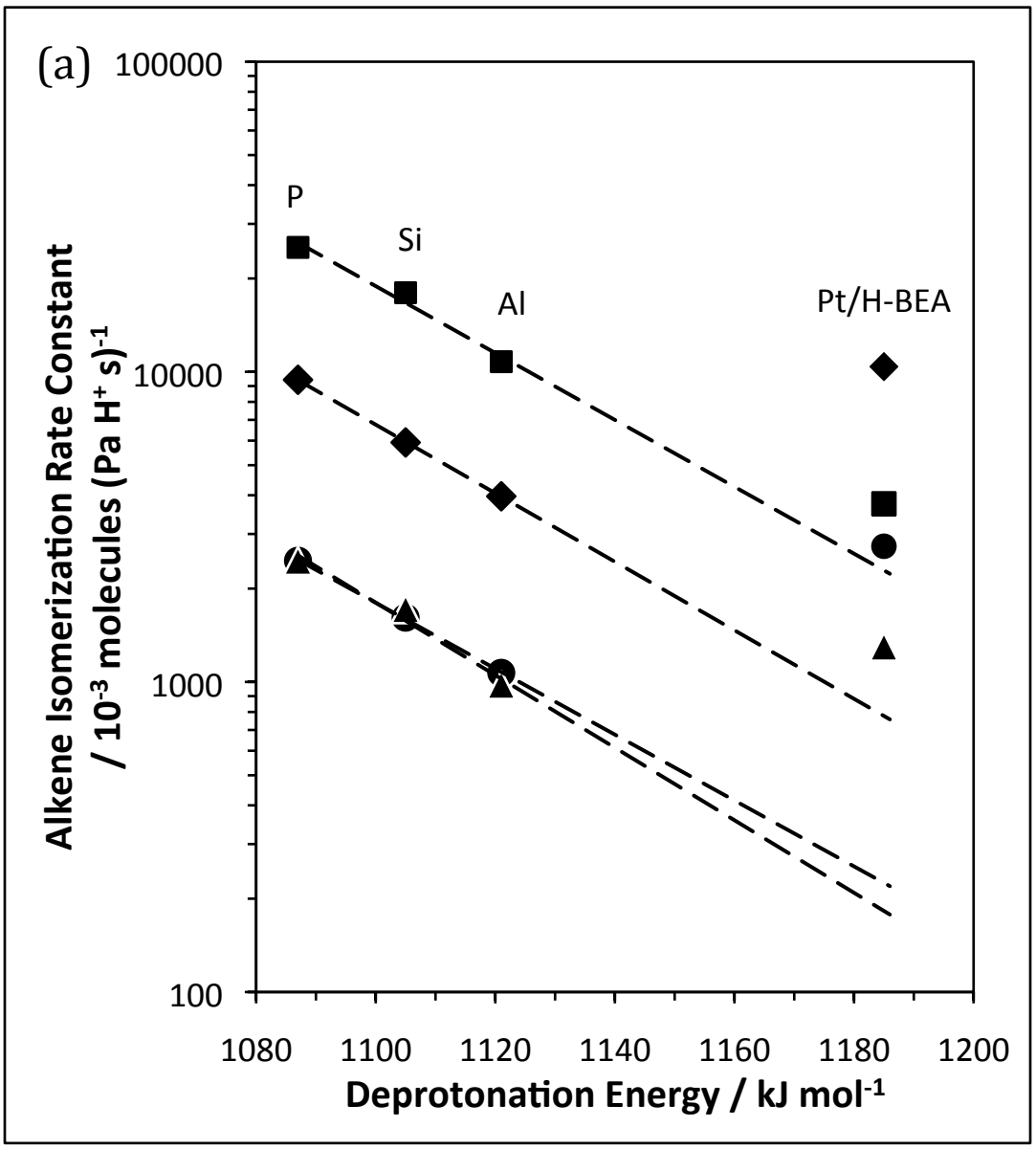

Figure 3.9. (a) Total (●) 2-methylpentene, (◆) 3-methylpentene, (■) 2,3-dimethylbutene, and (▲) n-hexene isomerization rate constants ($k_{isom}K_{prot}$; 473 K) as functions of deprotonation energy for $H_{8-n}X^{n+}W_{12}O_{40}$ (X = P, Si, Al) and BEA. The dashed lines are exponential fits of $k_{isom}K_{prot}$ values to deprotonation energies on Keggin clusters.

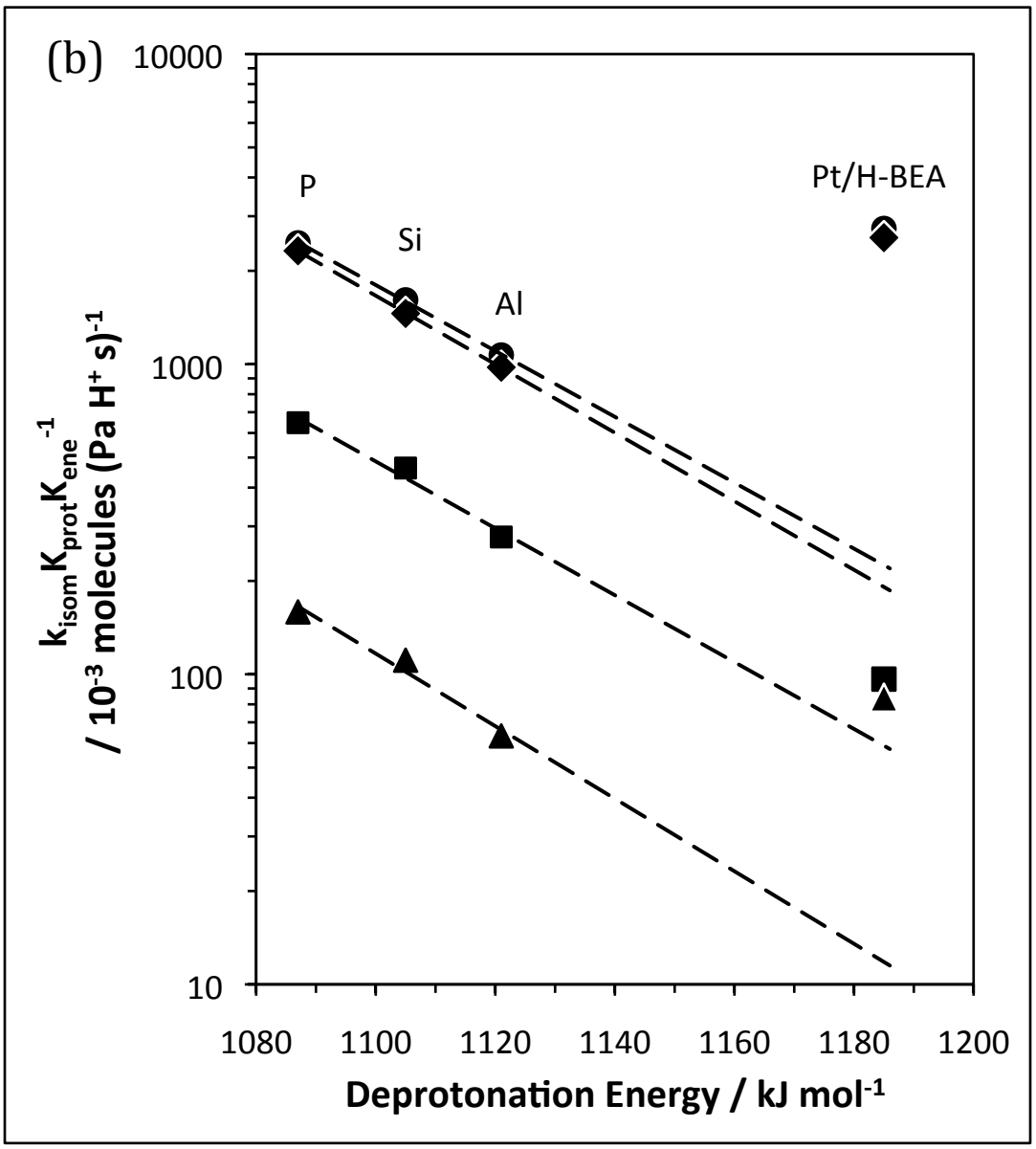

Figure 3.9. (b) Total (●) 2-methylpentene, (◆) 3-methylpentene, (■) 2,3-dimethylbutene, and (▲) n-hexene isomerization rate constants referenced to 2-methylpent-2-ene ($k_{isom}K_{prot}K_{ene}^{-1}$; 473 K) as functions of deprotonation energy for $H_{8-n}X^{n+}W_{12}O_{40}$ (X = P, Si, Al) and BEA. The dashed lines are exponential fits of $k_{isom}K_{prot}K_{ene}^{-1}$ values to deprotonation energies on Keggin clusters.

3.5.3. Schemes

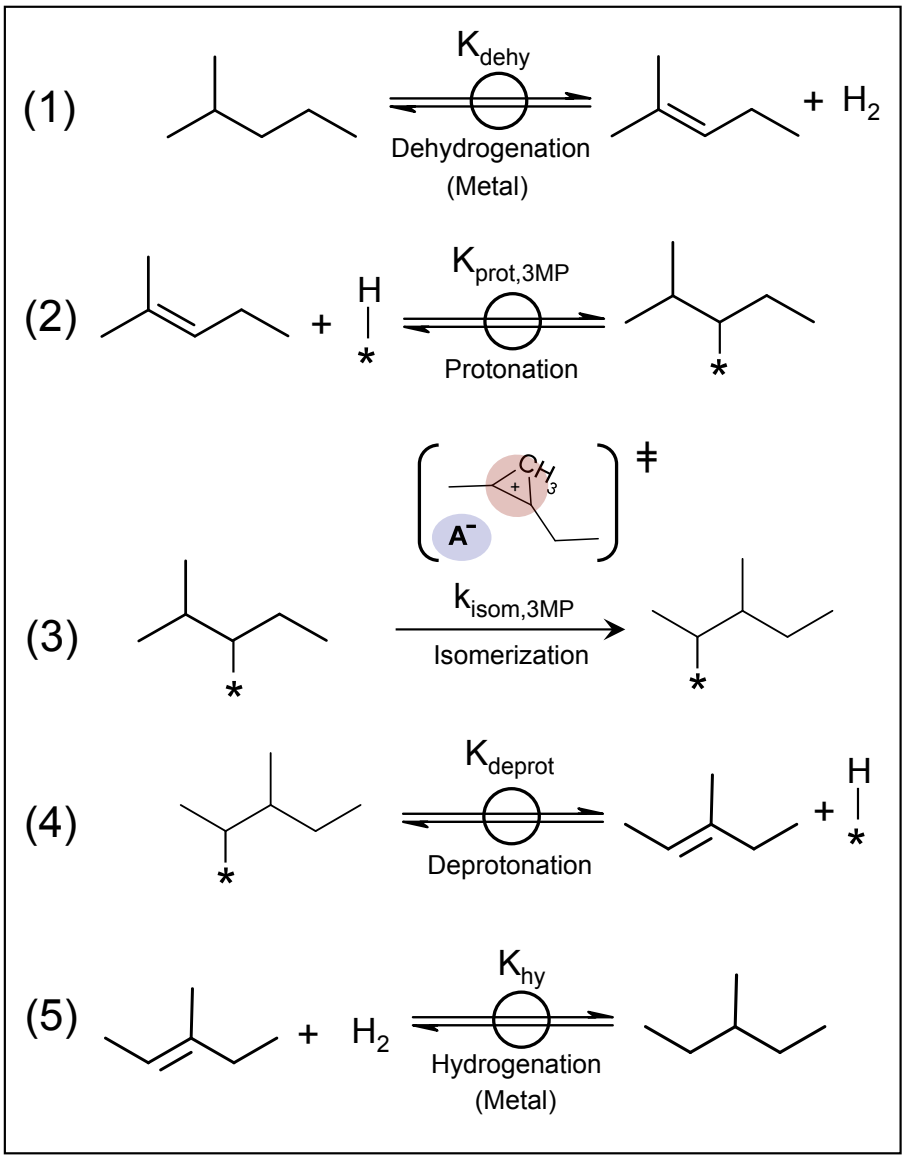

Scheme 3.1. Elementary steps and chemical reactions involved in 2-methylpentane isomerization on metal-acid mixtures that establish 2-methylpentane/2-methylpentene equilibrium. Chemical reactions are shown for the (de)hydrogenation on metal sites (Pt/Al_2O_3) and elementary steps are shown for acid-catalyzed routes on $H_{8-n}X^{n+}W_{12}O_{40}/SiO_2$ ($X = P^{5+}$, Si^{4+}, Al^{3+}) and BEA. Steps 3-5 are illustrated using 3-methylpentane as the product, but analogous steps are involved in 2,3-dimethylbutane and n-hexane formation. Bonds to the Brønsted active site are denoted as "*" in molecular structures.

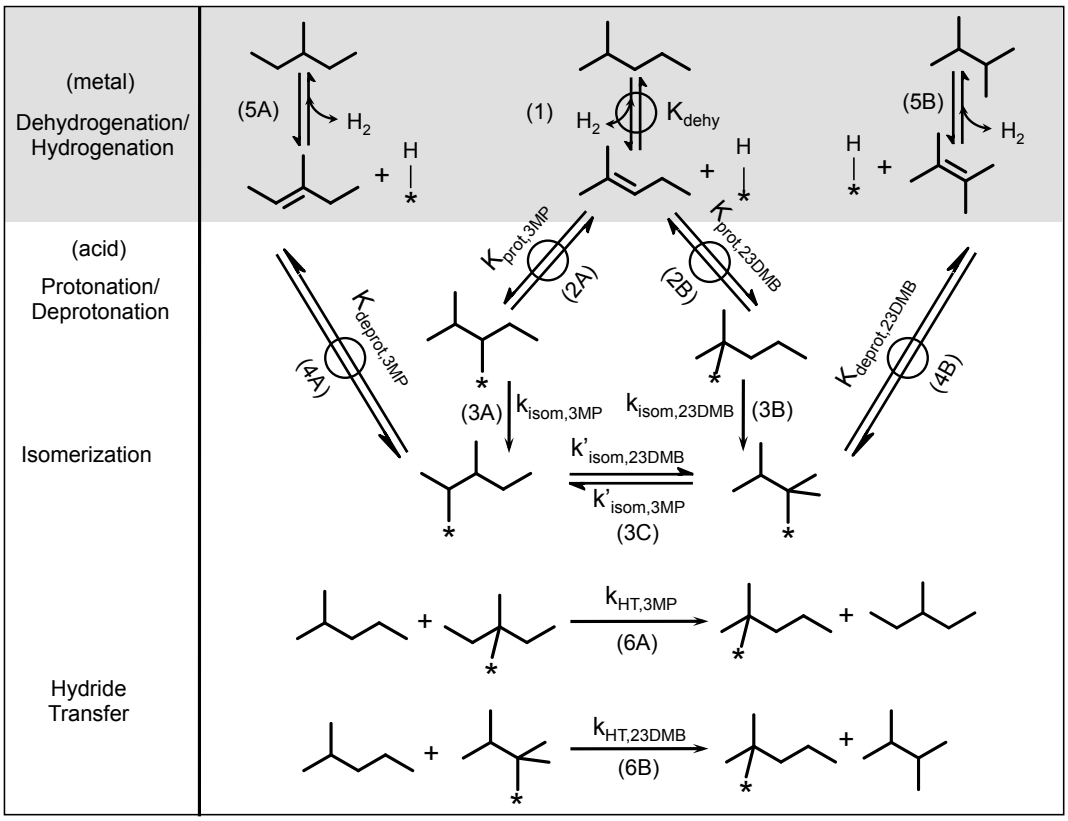

Scheme 3.2. 2-Methylpentane isomerization pathways on metal-acid mixtures, including secondary isomerizations of products and hydride transfer with 2-methylpentane. Elementary steps are shown for acid-catalyzed routes and chemical reactions are shown for metal-catalyzed reactions. Bonds to the acid active site are denoted as "*" in the molecular structures.

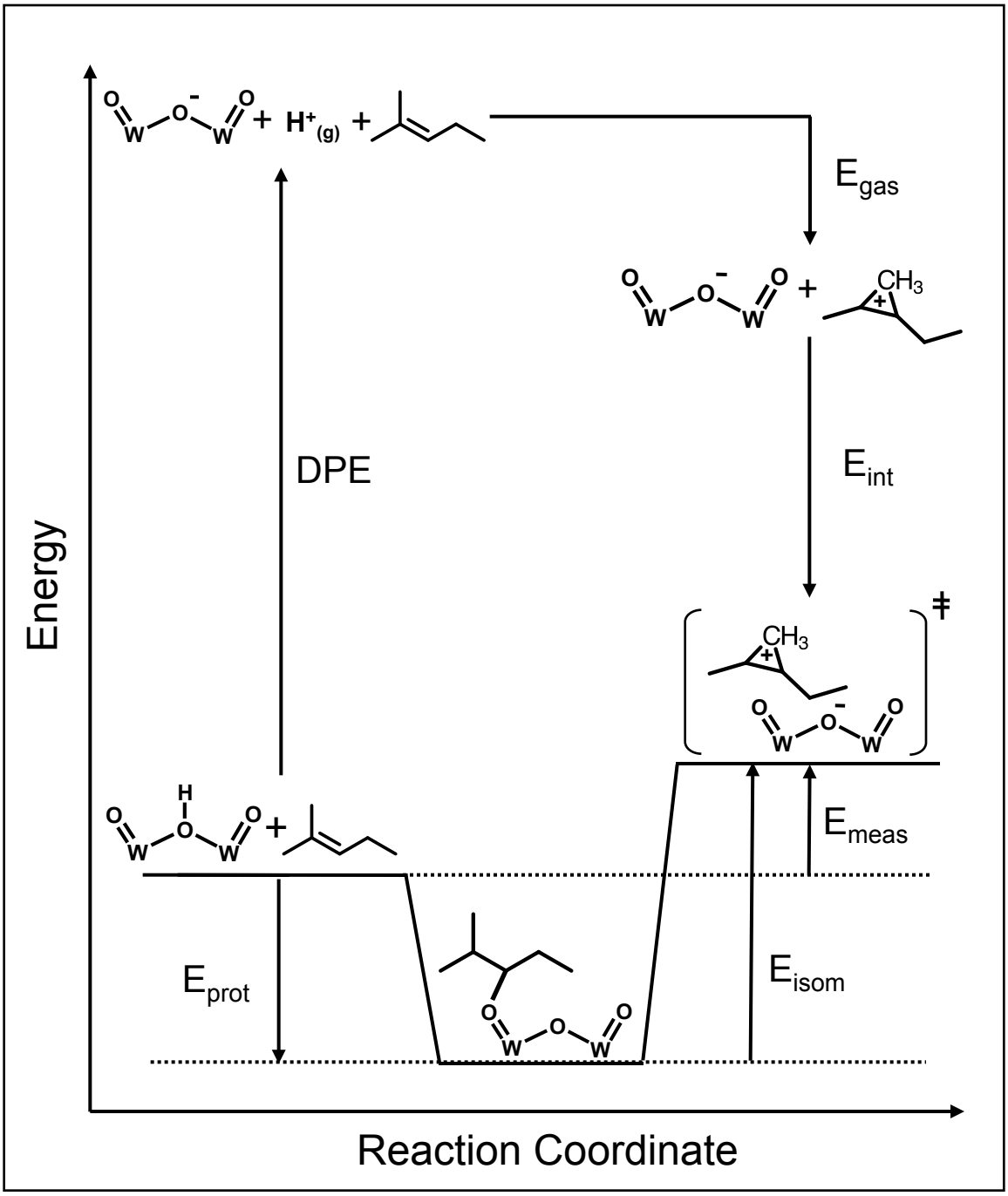

Scheme 3.3. Thermochemical cycle accounting for activation energies of Brønsted acid-catalyzed isomerization reactions (shown for 3MP products). Activation energies of $k_{isom}K_{prot}$ (E_{meas}) are the sum of the intrinsic isomerization activation energies (E_{isom}) and 2-methylpentene protonation energies at the acid site (E_{prot}). E_{meas} values depend on catalyst deprotonation energies (DPE), gas-phase protonation of the alkene to form the gaseous analog of the transition state (E_{gas}), and transition state interaction energies (E_{int}).

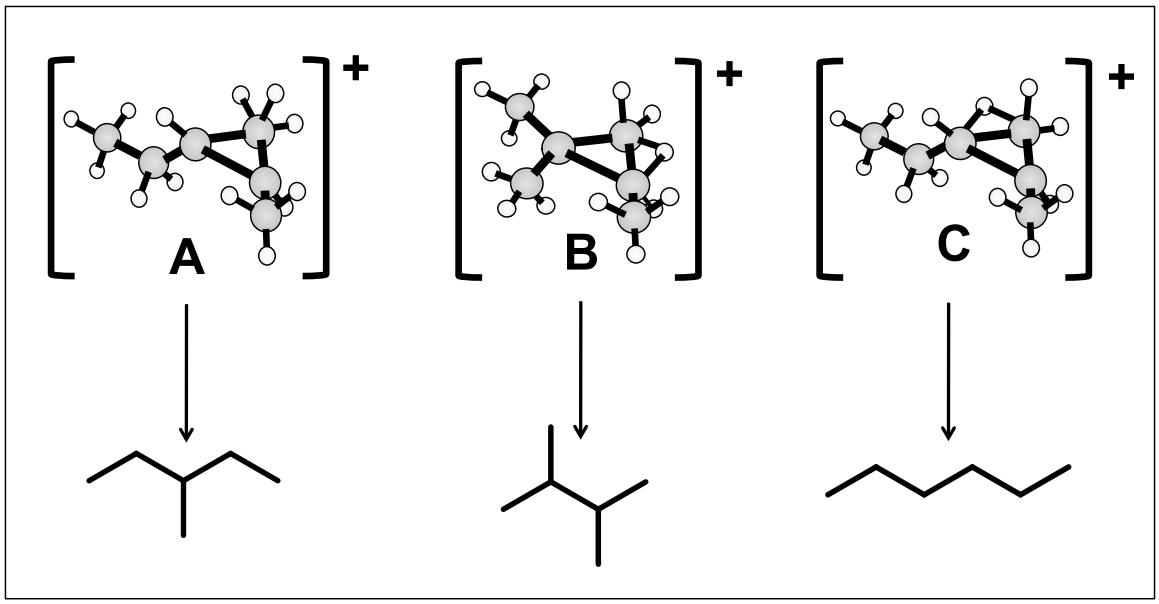

Scheme 3.4. Proposed cyclopropyl carbenium ions at isomerization transition states forming (A) 3-methylpentane, (B) 2,3-dimethylbutane, and (C) n-hexane [26]. 3-Methylpentane transition states involve cleavage and formation of C-C bonds to shift the methyl group along the C_5 backbone. 2,3-Dimethylbutane and n-hexane transition states involve concerted cleavage and formation of C-C and C-H bonds to rearrange the hydrocarbon backbone.

3.6. Supporting Information

3.6.1. Effects of Space Velocities on 2-Methylpentane Isomerization Rates

Figure S.3.1 shows formation rates of acyclic C_6 alkanes (per POM) as functions of 2-methylpentane (2MP) conversion (2 – 20%) on a H_3PW/SiO_2-Pt/Al_2O_3 mixture (Pt_s/H^+ = 4.9). Formation rates of 3-methylpentane (3MP), 2,3-dimethylbutane (23DMB), and n-hexane (nH) are independent of conversion below 20%. 2,2-Dimethylbutane (22DMB) formation rates increase monotonically with increasing conversion and nearly extrapolate to zero at low conversions, indicating that it is formed almost exclusively by secondary isomerizations. Methyl shift rates are significantly higher than those that change the extent of branching for 2MP (i.e., 3MP formation rates are much larger than 23DMB or nH formation rates); thus, 22DMB is likely formed from methyl shifts of 23DMB. These secondary reactions do not influence 23DMB rates, which are much larger than 22DMB formation rates (by factors > 20).

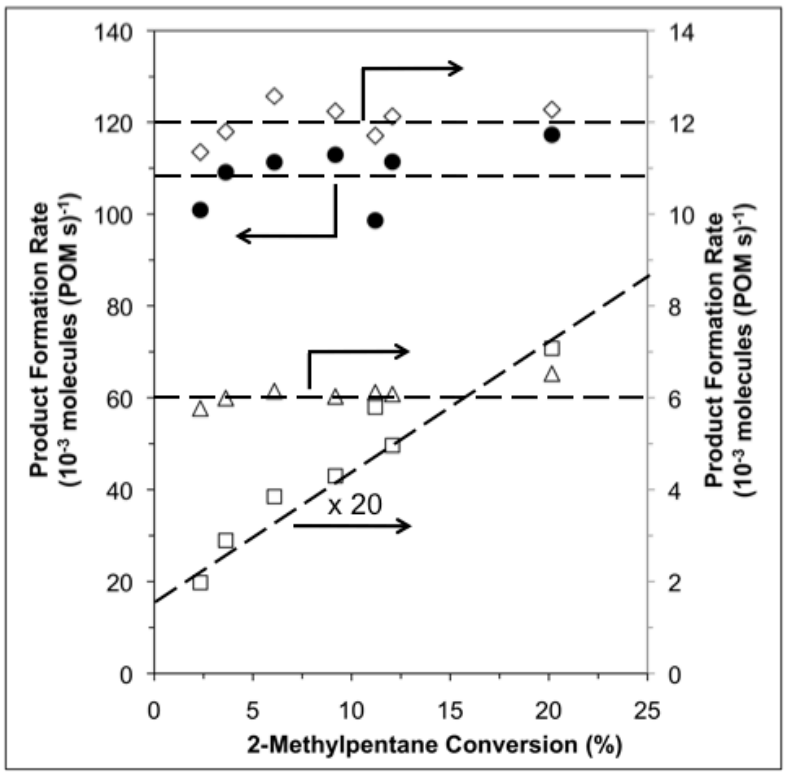

Figure S.3.1. Formation rates (per POM) of (●) 3-methylpentane, (◇) 2,3-dimethylbutane, (△) n-hexane, and (□) 2,2-dimethylbutane as functions of 2-methylpentane conversion on a H_3PW/SiO_2-Pt/Al_2O_3 (Pt_S/H^+ = 4.9) mixture (437 K, 30 kPa H_2, 3 kPa 2MP). Dashed lines show qualitative trends in the data.

3.6.2. Derivation of the 2-Methylpentane Isomerization Rate Expression

Here we derive the isomerization rate expression used throughout the main text (Eq. (3.2)), and additional equations used to justify our assumptions, by using kinetic analyses of elementary steps. The equations derived here assume 2MP reactants, however, derivations for other reactant alkanes (i.e., 3MP, 23DMB, and nH) are analogous. Throughout this section, concentrations of surface intermediates are denoted by square brackets and pressures of gas-phase species are denoted by parenthesis. Surface intermediates at metal and acid sites are denoted by "#" and "*", respectively.

3.6.2.1. Pseudo-steady-state Treatment of Alkenes

The pseudo-steady-state hypothesis (PSSH) may be applied to reactive intermediates when their concentrations (C_i) change by much less than reactant and/or product concentrations (C_r and C_p, respectively):

$$\left|\frac{dC_r}{dt}\right| \approx \left|\frac{dC_p}{dt}\right| >> \left|\frac{dC_i}{dt}\right| \approx 0 \qquad \text{(S.3.1)}$$

This assumption is valid for all surface intermediates because catalyst sites carry out many turnovers for detectable conversions. Alkenes may also be treated by PSSH according to Eq. (S.3.1), because they are produced at undetectable concentrations over conditions that cause detectable changes in reactant and product concentrations. Here we use PSSH to derive the concentrations of alkenes and their dependences on (Pt/H^+) ratios and on isomerization rates.

Metal sites dehydrogenate alkanes and hydrogenate alkenes by the proposed set of elementary steps shown in Scheme S.3.1. Alkanes (AH_2) adsorb dissociatively at vicinal vacant metal sites (#) to form chemisorbed hydrogen atoms (H#) and adsorbed alkyl fragments (AH#) (Scheme S.3.1, Step 1). Alkyl fragments lose another H-atom to form "adsorbed alkenes" (A#) (Scheme S.3.1, Step 2), which desorb as alkenes ($A^=$) (Scheme S.3.1, Step 3). Two H# desorb associatively as H_2 in quasi-equilibrated steps (Scheme S.3.1, Step 4).

Alkane dehydrogenation rates (r_{dehy}) are given by:

$$r_{dehy} = k_{des,AH_2}[A\#] \tag{S.3.2}$$

The PSSH for A#, AH#, and H# are:

$$\left|\frac{d[A\#]}{dt}\right| = k_{dehy,AH\#}[AH\#]\frac{[\#]}{[Pt]} - k_{hy,A\#}[A\#]\frac{[H\#]}{[Pt]} - k_{des,A\#}[A\#] + k_{ads,A=}[\#](A=) \approx 0 \tag{S.3.3}$$

$$\left|\frac{d[AH\#]}{dt}\right| = k_{dehy,AH_2}(AH_2)\frac{[\#]^2}{[Pt]} + k_{hy,A\#}[A\#]\frac{[H\#]}{[Pt]} - k_{hy,AH\#}[AH\#]\frac{[H\#]}{[Pt]} - k_{dehy,AH\#}[AH\#]\frac{[\#]}{[Pt]} \approx 0 \tag{S.3.4}$$

$$[H\#] = \sqrt{K_H(H_2)}[\#] \tag{S.3.5}$$

The solution for [A#] from this system of equations is substituted into Eq. (S.3.2). If all steps are reversible and equilibrated, except alkene desorption (i.e., $k_{des,A\#} << k_{hy,A\#}\sqrt{K_H(H_2)}\frac{[\#]}{[Pt]}$), Eq. (S.3.2) becomes:

$$\frac{r_{dehy}}{[Pt]} = \frac{k_{des,A\#}k_{dehy,AH\#}k_{dehy,AH_2}}{k_{hy,A\#}k_{hy,AH\#}K_H}\left(\frac{AH_2}{H_2}\right)\frac{[\#]}{[Pt]} \tag{S.3.6}$$

If alkane adsorption at metal sites is equilibrated (i.e., $k_{dehy,AH\#} << k_{hy,AH\#}\sqrt{K_H(H_2)}$) and the second H-atom abstraction is irreversible (i.e., $k_{des,A\#} >> k_{hy,A\#}\sqrt{K_H(H_2)}\frac{[\#]}{[Pt]}$), then Eq. (S.3.2) becomes:

$$\frac{r_{dehy}}{[Pt]} = \frac{k_{dehy,AH\#}k_{dehy,AH_2}}{k_{hy,AH\#}K_H}\frac{(AH_2)}{(H_2)^{1/2}}\left(\frac{[\#]}{[Pt]}\right)^2 \quad \text{(S.3.7)}$$

If alkane adsorption is irreversible (i.e., $k_{dehy,AH\#} >> k_{hy,AH\#}\sqrt{K_H(H_2)}$ and $k_{des,A\#} >> k_{hy,A\#}\sqrt{K_H(H_2)}\frac{[\#]}{[Pt]}$), the dehydrogenation rate is:

$$\frac{r_{dehy}}{[Pt]} = k_{dehy,AH_2}(AH_2)\left(\frac{[\#]}{[Pt]}\right)^2 \quad \text{(S.3.8)}$$

The fraction of metal sites that is vacant ([#]/[Pt]) in Eqs. (S.3.6) – (S.3.8) is determined by a surface Pt-atom site balance:

$$[Pt] = [\#] + [H\#] + [AH\#] + [A\#] \quad \text{(S.3.9)}$$

Surface species derived from alkanes and alkenes are reasonably presumed to be at low surface concentrations for the low alkene pressures used during this study (> 0.24 Pa), simplifying the site balance to:

$$[Pt] = [\#](1+\sqrt{K_H(H_2)}) \quad \text{(S.3.10)}$$

Substituting Eq. (S.3.10) into Eqs. (S.3.6) – (S.3.8) provides the dehydrogenation rate expressions for different kinetic-relevancies of elementary steps. Rigorous thermodynamic treatments of rates away from equilibrium [37] show that alkene hydrogenation rates (r_{hy}) are given by:

$$\frac{r_{hy}}{[Pt]} = r_{dehy}\left(\frac{\frac{(A=)(H_2)}{(AH_2)}}{\frac{k_{dehy,AH_2}k_{dehy,AH\#}k_{des,A\#}}{k_{ads,A=}k_{hy,A\#}k_{hy,AH\#}K_H}}\right) \quad \text{(S.3.11)}$$

Dehydrogenation rates are first-order in alkane pressure for all cases discussed above and have a H_2 pressure dependence (ranging from zero to inverse second order) that is determined by the kinetic-relevancies of the H-abstraction steps and the H# coverage. Alkene hydrogenation rates are therefore always first-order in alkene pressure. In the absence of further mechanistic knowledge regarding the kinetic-relevance of individual elementary steps for dehydrogenation-hydrogenation, we will assume that alkane dehydrogenation and alkene hydrogenation rates follow the rate expressions:

$$\frac{r_{dehy}}{[Pt]} = k_{dehy}\left(\frac{AH_2}{H_2}\right) \tag{S.3.12a}$$

$$\frac{r_{hy}}{[Pt]} = k_{hy}(A=) \tag{S.3.12b}$$

These results are used next to determine the pseudo-steady-state concentrations of $2MP^{=}$ under reaction conditions for POM/SiO_2-Pt/Al_2O_3 and BEA-Pt/Al_2O_3 mixtures. Isomerization rates are predominantly linear with $2MP^{=}$ pressures under the conditions used in this study (Figure 3.3) and are given by (derived in Section 3.6.2.2):

$$\frac{r_{isom}}{[H^+]} = k_{isom}K_{prot}(2MP=) \tag{S.3.13a}$$

$$k_{isom}K_{prot} = k_{isom,3MP}K_{prot,3MP} + k_{isom,23DMB}K_{prot,23DMB} + k_{isom,nH}K_{prot,nH} \tag{S.3.13b}$$

where the rate and equilibrium constants are defined by the elementary steps shown in Scheme 3.1. The PSSH for $2MP^{=}$ is therefore:

$$\left|\frac{d(2MP=)}{dt}\right| = k_{dehy}\left(\frac{2MP}{H_2}\right)[Pt] - k_{hy}(2MP=)[Pt] - k_{isom}K_{prot}(2MP=)[H^+] \approx 0 \tag{S.3.14}$$

and defines the pseudo-steady-state concentration of $2MP^{=}$:

$$(2MP=) = \frac{K_{dehy}\left(\frac{2MP}{H_2}\right)}{1+\frac{k_{isom}K_{prot}}{k_{hy}}\frac{[H^+]}{[Pt]}} \tag{S.3.15}$$

Saturation of protons by alkoxides causes isomerization rates that are zero-order in $2MP^{=}$ pressure so that Eq. (S.3.15) represents the lower bound of $2MP^{=}$ pressures. Pt sites equilibrate $2MP^{=}$ and 2MP at high (Pt_S/H^+) ratios and isomerization rates approach the dehydrogenation-hydrogenation equilibrium solution:

$$\frac{r_{isom}}{[H^+]} = k_{isom}K_{prot}K_{dehy}\left(\frac{2MP}{H_2}\right) \tag{S.3.16}$$

$2MP^{=}$ pressures approach asymptotic behavior (i.e., $\frac{k_{dehy}}{k_{isom}K_{prot}}\left(\frac{2MP}{H_2}\right)\frac{[Pt]}{[H^+]}$) in the limit of low ($Pt_S/H^+$) and alkane dehydrogenation at Pt sites limits isomerization rates:

$$\frac{r_{isom}}{[H^+]} = k_{dehy}\left(\frac{2MP}{H_2}\right)\frac{[Pt]}{[H^+]} \qquad \text{(S.3.17)}$$

Eq. (S.3.15) shows that proportional changes in isomerization rate constants ($k_{isom}K_{prot}$, Table 3.1) and (Pt/H^+) ratios do not change the extent of 2MP-2MP= equilibration. Such proportional changes are discussed in Section 3.3.1.2 to limit the effects of Pt-catalyzed isomerization routes, while maintaining equilibrium $2MP^=$ pressures.

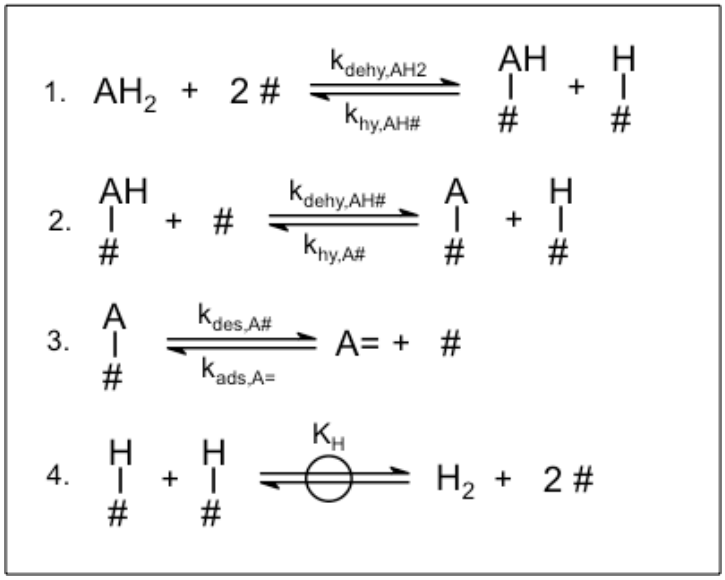

Scheme S.3.1. Elementary steps for alkane (AH_2) dehydrogenation and alkene ($A^=$) hydrogenation at metal sites (#).

3.6.2.2. Isomerization Rates at Alkane-Alkene Equilibrium

Here we derive the rate expression for the formation of product isomer "P" under conditions of alkane-alkene equilibrium (the criterion for which is derived and shown in Section 3.6.2.1). At high (Pt_S/H^+) ratios and low 2MP conversions, rapid deprotonation of product alkoxides and hydrogenation of the resulting alkenes make isomerization steps irreversible. The formation rate of product "P" (r_P) is then:

$$r_P = \sum_{i}^{\text{TS forming P}} k_{isom,iP}\left[2MP^*_i\right] \qquad \text{(S.3.18)}$$

where $2MP^*_i$ is the 2-methylpentoxide isomer that forms the *i*-th transition state (TS) (2-methylpent-3-oxide in Step 3 of Scheme 3.1), $k_{isom,iP}$ is the isomerization rate constant that forms product P via the *i*-th transition state, and the sum is over all transition states that form P. When alkene protonation and alkoxide deprotonation is equilibrated (Scheme 3.1, Step 2), [$2MP^*_i$] may be defined by its equilibrium with isomer "j" of $2MP^=$ (2-methylpent-2-ene in Scheme 3.1) in the contacting gas-phase:

$$\left[2MP*_i\right] = K_{prot,ij}\left(2MP=_j\right)[*] \tag{S.3.19}$$

where $K_{prot,ij}$ is the protonation equilibrium constant forming $2MP*_i$ from $2MP^{=}_j$. The concentration of unoccupied protons in Eq. (S.3.19) is given by the acid site balance:

$$\left[H^+\right] = [*] + \sum_{k}^{\substack{\text{all 2MP*}\\\text{isomers}}} \left[2MP*_k\right] = [*]\left(1 + \sum_{k}^{\substack{\text{all 2MP*}\\\text{isomers}}} K_{prot,kj}\left(2MP=_j\right)\right) \tag{S.3.20}$$

where the summation is over all *k* isomers of 2MP*. The complete expression for P formation is achieved by combining Eq. (S.3.18) – (S.3.20):

$$\frac{r_P}{\left[H^+\right]} = \frac{\sum_{\text{i}}^{\text{TS forming P}} k_{isom,iP} K_{prot,ij}\left(2MP=_j\right)}{1 + \sum_{k}^{\substack{\text{all 2MP*}\\\text{isomers}}} K_{prot,kj}\left(2MP=_j\right)} \tag{S.3.21}$$

Eq. (S.3.21) simplifies to Eq. (3.2) after a few additional simplifications. First, we note that the choice of the $2MP^{=}$ isomers are arbitrary when all $2MP^{=}$ isomers are in equilibrium proportions. By convention, we choose 2-methylpent-2-ene (2MP-2) as the $2MP^{=}$ isomer for all cases because it is present at the highest concentrations [13] so that Eq. (S.3.21) becomes:

$$\frac{r_P}{\left[H^+\right]} = \frac{\left(2MP-2\right)\sum_{\text{i}}^{\text{TS forming P}} k_{isom,iP} K_{prot,i}}{1 + \left(2MP-2\right)\sum_{k}^{\substack{\text{all 2MP*}\\\text{isomers}}} K_{prot,k}} \tag{S.3.22}$$

where all K_{prot} are with relation to 2MP-2. Eq. (3.2) is achieved by assuming a single transition state and alkoxide form the majority of P (i.e., the sum in the numerator is dominated by a single term, $k_{isom,P}K_{prot,P}$, in Eq. (3.2) and Scheme 3.1) and by adding the equilibrium constants in the denominator (to give K_{surf} in Eq. (3.2)).

$$\frac{r_P}{\left[H^+\right]} = \frac{k_{isom,P} K_{prot,P}\left(2MP-2\right)}{1 + K_{surf}\left(2MP-2\right)} \tag{S.3.23}$$

The $2MP^{=}$ pressure shown in Eq. (S.3.23) is rigorously the pressure of 2MP-2 only. Equation (3.2) is obtained from Eq. (S.3.23) by relating the 2MP-2 and 2MP pressures via the 2MP-2 dehydrogenation equilibrium constant (K_{dehy} in Eq. (3.2) and Scheme 3.1).

3.6.3. 2-Methylpentene Diffusion in Acid Aggregates

The mole balance for $2MP^{=}$ reactants diffusing in a spherical pellet of POM/SiO_2 is [38]:

$$\frac{d^2\theta}{d\lambda^2} + \frac{2}{\lambda}\frac{d\theta}{d\lambda} - \phi_n^2\theta^n = 0 \qquad \text{(S.3.24)}$$

where θ is the dimensionless $2MP^{=}$ concentration and is a function of the radial position in the pellet:

$$\theta = \frac{(2MP=)}{(2MP=)_{\text{pellet surface}}} = \frac{(2MP=)}{K_{dehy}\left(\frac{2MP}{H_2}\right)} \qquad \text{(S.3.25)}$$

λ is the dimensionless radial distance from the center of the pellet, and n is the kinetic reaction order (~1 for the data shown in Figure 3.2 and Figure 3.3). Dimensionless $2MP^{=}$ concentration profiles defined by Eq. (S.3.24) are solely determined by the Thiele modulus (ϕ_1^2):

$$\phi_1 = R_p\sqrt{\frac{k_{isom}K_{prot}RTS_w\rho_c}{N_{Av}D_{2MP=}}} \qquad \text{(S.3.26)}$$

where $k_{isom}K_{prot}$ is the total $2MP^{=}$ isomerization rate constant (molecules (Pa H^+ s)$^{-1}$; Eq. (3.3a)), R is the universal gas constant (8.314 m^3 Pa (mol K)$^{-1}$), T is the absolute temperature, S_w is the number of H^+ per g of catalyst, ρ_c is the density of the catalyst pellet (g m^{-3}), N_{av} is Avagadro's number (6.022 x 10^{23} molecules mol^{-1}), $D_{2MP=}$ is the diffusivity of $2MP^{=}$ in the pores of amorphous SiO_2 (m^2 s^{-1}), and R_p is the SiO_2 pellet radius (~10 μm). Larger values of ϕ_1 correspond to more severe diffusion limitations, which cause significant $2MP^{=}$ concentration gradients within SiO_2 particles. Isomerization rates that are unaffected by POM surface density (0.04 and 0.25 H_3PW nm^{-2}; Figure 3.2) indicating that samples used for kinetic experiments have low Thiele moduli and, as a result, uniform $2MP^{=}$ concentrations within POM/SiO_2 particles. Weaker acids supported at 0.04 POM (nm-SiO_2)$^{-2}$ surface densities have lower ϕ_1 values than the 0.25 H_3PW (nm-SiO_2)$^{-2}$ sample because of their lower $k_{isom}K_{prot}$ values (Table 3.2) and therefore also have uniform $2MP^{=}$ concentrations.

3.6.4. 2MP Isomerization Turnover Rates on Pt/H-BEA-Pt/Al_2O_3 Mixtures with Different (Pt_S/H^+) Ratios

Figure S.3.2 shows 2MP isomerization turnover rates measured on Pt/H-BEA-Pt/Al_2O_3 mixtures with different (Pt_S/H^+) ratios (2.9 and 8.9). 2MP isomerization turnover rates on both samples at 75 kPa were accurately described by the 2MP isomerization rate expression (Eq. (3.2)) as shown by the close agreement between the

predicted and measured rates shown in Figure S.3.2. Turnover rates were similar on the two mixtures under all conditions (within a factor of 1.2) and regressed values of $k_{isom}K_{prot}$ were nearly equivalent (i.e., $k_{isom}K_{prot}$ values of 2740 and 2630 x 10^{-3} molecules (Pa H^+ s)$^{-1}$ for (Pt_S/H^+) ratios of 2.9 and 8.4, respectively). Rates and rate constants that do not depend on the (Pt_S/H^+) ratios suggest that both mixtures contain sufficient Pt to equilibrate dehydrogenation and hydrogenation of 2MP reactants.

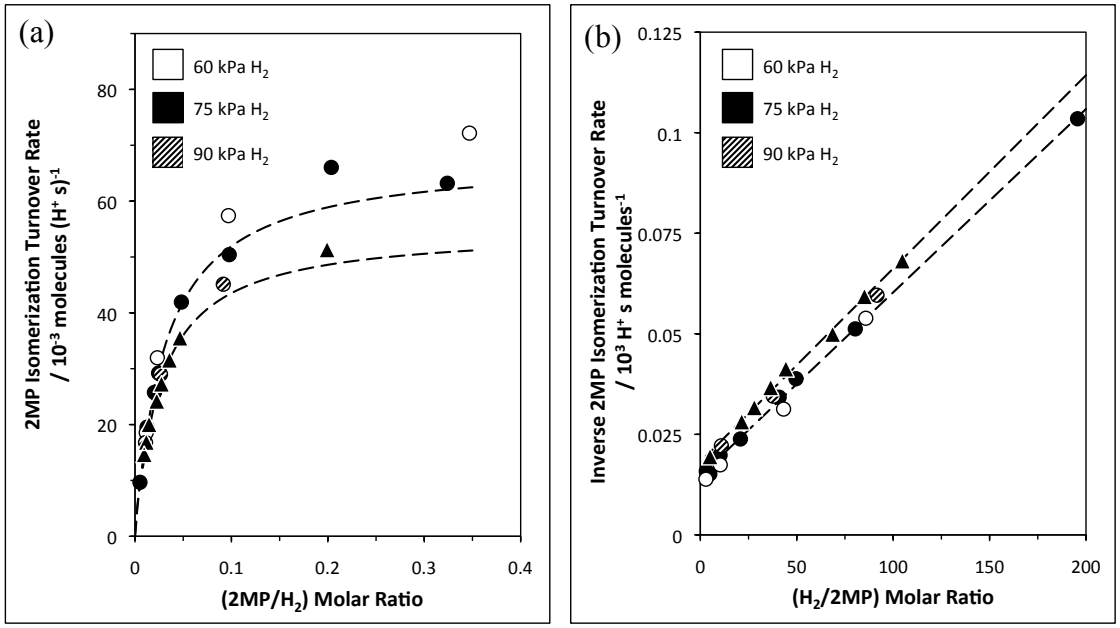

Figure S.3.2. (a) 2-Methylpentane isomerization turnover rates as a function of the ($2MP/H_2$) ratio and (b) inverse 2-methylpentane isomerization turnover rates as a function of the (H_2/2MP) ratio on Pt/H-BEA- Pt/Al_2O_3 mixtures with (●) Pt_S/H^+ = 2.9 and (▲) Pt_S/H^+ = 8.4 (reaction conditions: 473 K, 0.5 – 25 kPa 2MP, 60 – 90 kPa H_2). Dashed lines represent the regression of the data at 75 kPa to Eq. (3.4).

3.6.5. Calculation of the Thiele Modulus and Internal Effectiveness Factor of Pt/H-BEA

The first-order Thiele modulus and internal effectiveness factor were calculated for Pt/H-BEA using its measured value of $k_{isom}K_{prot}$ (2.74 molecules (Pa H^+ s)$^{-1}$) to estimate if transport within BEA pores limits 2MP isomerization rates. The first-order Thiele modulus is defined by Eq. (S.3.26) in Section 3.6.3 and was calculated for Pt/H-BEA using 3.3x10^{18} H^+ [g-BEA]$^{-1}$ from DTBP titrations, 1x10^6 g-BEA m^{-3}, the diffusivity of n-hexane in MFI (2.9 x 10^{-9} m^2 s^{-1} [30]) for $D_{2MP=}$, and 10 nm separations between Pt clusters from TEM micrographs (Figure 3.5):

$$\phi_1 = 5x10^{-9} m^2 \sqrt{\frac{\left(2.7 \frac{molecules}{Pa\ H^+ s}\right) * 473K * 8.314 \frac{m^3\ Pa}{mol\ K} * 3.3x10^{18} \frac{H^+}{g} * 1x10^6 \frac{g}{m^3}}{6.022x10^{23} \frac{molecules}{mol} * 2.9x10^{-9} \frac{m^2}{s}}} = 0.02$$

(S.3.27)

The internal effectiveness factor (η) is the value of the observed rate relative to the rate that would be observed if there were no concentration gradients within particles of Pt/H-BEA. The effectiveness factor can be calculated analytically for a first-order reaction occurring in a spherical particle according to [38]:

$$\eta = \frac{3}{\phi_1^2}\left(\phi_1 \coth \phi_1 - 1\right) \qquad \text{(S.3.28)}$$

The effectiveness factor for Pt/H-BEA is 0.99997 using Eq. (S.3.28) and φ_1 = 0.02, suggesting that $2MP^{=}$ transport inside of Pt/H-BEA particles does not limit isomerization rates.

3.6.6. Effects of 2MP and H_2 pressures on 23DMB and nH Selectivities on H_3PW/SiO_2-Pt/Al_2O_3 Mixtures

Figure S.3.3 shows the effects of 2MP pressure and H_2 pressure on 23DMB and nH selectivities on H_3PW/SiO_2-Pt/Al_2O_3 physical mixtures with different H_3PW surface densities and (Pt_S/H^+) ratios. 23DMB and nH selectivities are independent of H_2 pressure and decrease with increasing 2MP pressure on all physical mixtures under all conditions.

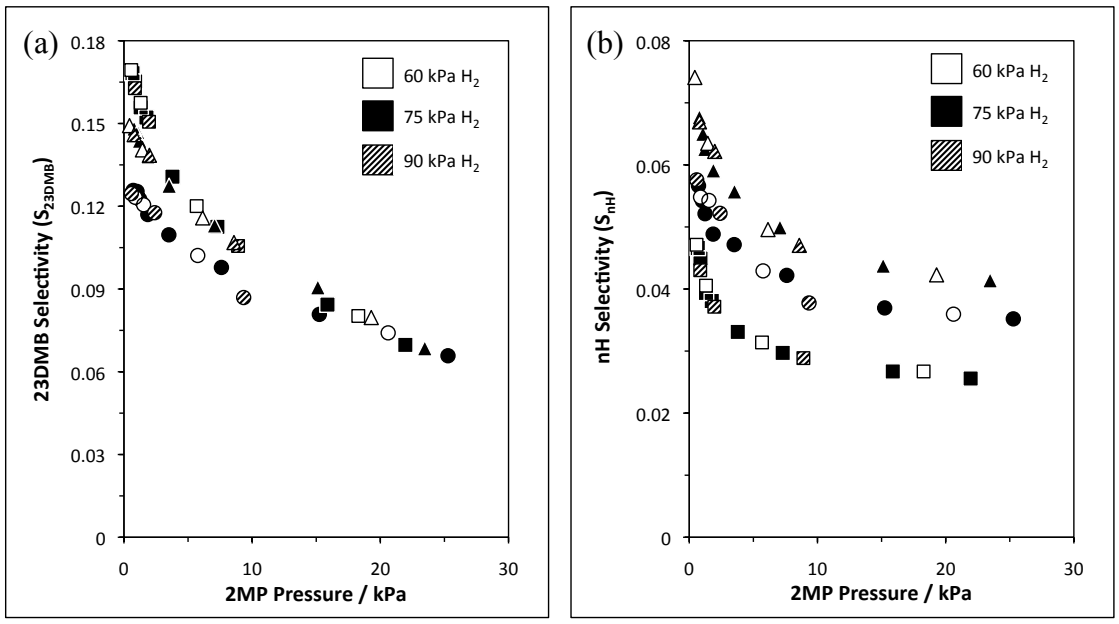

Figure S.3.3. (a) 23DMB selectivities (S_{23DMB}) and (b) nH selectivities (S_{nH}) as functions of 2MP pressure on H_3PW/SiO_2-Pt/Al_2O_3 mixtures with (●) 0.04 H_3PW [nm-SiO_2]$^{-2}$ and Pt_S/H^+ = 11.7, (▲) 0.04 H_3PW [nm-SiO_2]$^{-2}$ and Pt_S/H^+ = 22.9, and (■) 0.25 H_3PW [nm-SiO_2]$^{-2}$ and Pt_S/H^+ = 10.5 (reaction conditions: 473 K, 0.5 – 25 kPa 2MP, 60 - 90 kPa H_2).

3.6.7. Calculations of Relative Free Energies of Isomerization Transition States on Solid Acids

Activation free energies for each reactant alkene ($\Delta G_{a,I}$; Table S.3.1) were calculated from measured $k_{isom}K_{prot}$ values using the absolute rate theory formulation of rate constants:

$$k_{isom}K_{prot} = \exp(-\Delta G_{a,I}/RT) = \exp(-(\Delta G_{TS} - \Delta G_{alkene})/RT) \quad (S.3.29)$$

where ΔG_{TS} and ΔG_{alkene} are the free energies of formation for the transition states and reference alkenes (i.e., 2-methylpent-2-ene for 2MP, *trans*-3-methylpent-2-ene for 3MP, 2,3-dimethylbut-2-ene for 23DMB, and *cis*-hex-2-ene for nH), respectively. Differences in free energies of reference alkenes were accounted for by dividing all isomerization rate constants by K_{ene} (Eq. (3.14)) so that activation free energies of $k_{isom}K_{prot}K_{ene}^{-1}$ ($\Delta G'_{a,I}$; Table S.3.2) are measured with respect to 2-methylpent-2-ene, regardless of the reactant:

$$k_{isom}K_{prot}K_{ene}^{-1} = \exp(-\Delta G'_{a,I}/RT) = \exp(-(\Delta G_{TS} - \Delta G_{2\text{-methylpent-2-ene}})/RT) \quad (S.3.30)$$

Transition state free energies can be compared directly using values of $k_{isom}K_{prot}K_{ene}^{-1}$ (Table S.3.3).

Table S.3.1. Activation free energies of reacting alkenes ($\Delta G_{a,I}$ / kJ mol^{-1}) calculated from $k_{isom}K_{prot}$ values (473 K) and Eq. (S.3.29).

Catalyst	I = 2MP	I = 3MP	I = 23DMB	I = nH
H_3PW	-30.7	-36.0	-39.9	-30.7
H_4SiW	-29.0	-34.1	-38.5	-29.3
H_5AlW	-27.4	-32.6	-36.5	-27.1
Pt/H-BEA	-31.1	-36.4	-32.4	-28.2

Table S.3.2. Activation free energies measured with respect to 2-methylpent-2-ene ($\Delta G'_{a,I}$ / kJ mol^{-1}) calculated from $k_{isom}K_{prot}K_{ene}^{-1}$ values (473 K) and Eq. (S.3.30).

Catalyst	I = 2MP	I = 3MP	I = 23DMB	I = nH
H_3PW	-30.7	-30.5	-25.5	-19.9
H_4SiW	-29.0	-28.6	-24.1	-18.5
H_5AlW	-27.4	-27.0	-22.1	-16.3
Pt/H-BEA	-31.1	-30.9	-18.0	-17.4

Table S.3.3. Transition state free energy for reactant "I" (in kJ mol^{-1}) measured with respect to the 2MP isomerization transition state.

Catalyst	I = 3MP	I = 23DMB	I = nH
H_3PW	0.2	5.3	10.8
H_4SiW	0.4	4.9	10.5
H_5AlW	0.4	5.3	11.1
Pt/H-BEA	0.3	13.2	13.7

3.7. References

[1] A. Corma, Chem. Rev. 95 (1995) 559.
[2] M.J. Janik, J. Macht, E. Iglesia, M. Neurock, J. Phys. Chem. C. 113 (2009) 1872.
[3] J. Macht, M.J. Janik, M. Neurock, E. Iglesia, J. Am. Chem. Soc. 130 (2008) 10369.
[4] M. Brändle and J. Sauer J. Am. Chem. Soc. 120 (1998) 1556.
[5] J. Macht, M.J. Janik, M. Neurock, E. Iglesia, Angew. Chem., Int. Ed. 46 (2007) 7864.
[6] R. Carr, M. Neurock, E. Iglesia, J. Catal. 278 (2011) 78.
[7] J. Macht, R.T. Carr, E. Iglesia, J. Am. Chem. Soc. 131 (2009) 6554.
[8] P.B. Weisz, E.W. Swegler, Science 126 (1957) 31.
[9] M. Guisnet, F. Alvarez, G. Giannetto, G. Perot, Catal. Today 1 (1987) 415.
[10] G.D. Pirngruber, K. Seshan, J. Lercher, J. Catal. 186 (1999) 188.
[11] J.J. Cowan, C.L. Hill, R.S. Reiner, I.A.Weinstock, Inorg. Synth. 33 (2002) 18.
[12] E.J. Creyghton, J.A. Elings, R.S. Downing, R.A. Sheldon, H. van Bekkum, Microporous Mater. 5 (1996) 299.

[13] D. R. Stull, E. F. Westrum, G. C. Sinke, "The Chemical Thermodynamics of Organic Compounds." Robert E. Krieger Publishing Company, Malabar, 1987.
[14] R.T. Carr, W. Knaeble, E. Iglesia, *"Effects of Acid Strength and Solvation on 2-Methylpentane Isomerization Selectivity"* in Preparation.
[15] C.D. Baertsch, K.T. Komala, Y.-H. Chua, E. Iglesia, J. Catal. 205 (2002) 44.
[16] N. Mizuno and M. Misono, Chem. Rev. 98 (1998) 199.
[17] This estimation assumes POM anions with1.2 nm diameters form rhombic dodecahedron secondary structures with bcc crystal structure.
[18] B.B. Bardin, R.J. Davis, Appl. Cat. A. 200 (2000) 219.
[19] M. Janik, B. Bardin, R. Davis, M. Neurock, J. Phys. Chem. B. 110 (2006) 4170.
[20] T. Okuhara, N. Mizuno, M. Misono, Adv. Catal. 41 (1996) 113.
[21] R. Gounder, A. Jones, R.Carr, E. Iglesia, J.Catal. 286 (2012) 214.
[22] G. Djéga-Mariadassou, M. Boudart, J. Catal. 216 (2003) 89.
[23] R. Madon, M. Boudart, Ind. Eng. Chem. Fundam. 21 (1982) 438.
[24] J. Macht, R.T. Carr, E. Iglesia, J. Catal. 264 (2009) 54.
[25] V. B. Kazansky, Acc. Chem. Res. 24 (1991) 379.
[26] M. A. Natal-Santiago, R. Alcalá, J. A. Dumesic, J. Catal. 181 (1999) 124.
[27] M. Boronat, P. Viruela, A. Corma, J. Phys. Chem. 100 (1996) 16514.
[28] T. Demuth, X. Rozanska, L. Benco, J. Hafner, R.A. van Santen, H. Toulhoat, J. Catal. 214 (2003) 68.
[29] A. L. L East, T. Bucko, J. Hafner, J. Phys. Chem. A 111 (2007) 5945.
[30] F. Leroy, B. Rousseau, A.H. Fuchs, Phys. Chem. Chem. Phys. 6 (2004) 775.
[31] B.A. De Moor, M-.F. Reyniers, G.B. Marin. Phys. Chem. Chem. Phys. 11 (2009) 2939.
[32] M.T. Aronson, R.J. Gorte, W.E. Farneth, J. Catal. 98 (1986) 434.
[33] F.E.M. Stockenhuber, J. Lercher, J. Phys. Chem. B. 101 (1997) 5414.
[34] F. Eder, J. Lercher, J. Phys. Chem. B. 101 (1997) 1273.
[35] F. Eder, J. Lercher, Zeolites 18 (1997) 75.
[36] F. Eder, J. M. Stockenhuber, Lercher, J. Phys. Chem. B. 101 (1997) 5414.
[37] J.A. Dumesic, J. Catal. 185 (1999) 496.
[38] H.S. Fogler, "Elements of Chemical Reaction Engineering." Pearson Education, Inc., Upper Saddle River, 2006.

Chapter 4

Using Theory to Probe and Develop Accurate Descriptors of Reactivity for Acid and Oxidation Catalysis

Abstract

Deprotonation energies (DPE) and H-atom addition energies (HAE) are calculated from density functional theory (DFT) for Keggin polyoxometalate (POM) clusters with different central (S, P, Si, Al, Co) and addenda (W, Mo, V) atoms to develop these probes as accurate descriptors of reactivity for Brønsted acid and oxidation catalysis. The consequences of Keggin cluster composition for acid catalysis were examined using thermochemical cycles that dissect DPE values into components that reflect covalent and electrostatic interactions between protons and conjugate anions and similar cycles for the interaction energies between conjugate anions and organic cations present as transition states or intermediates during CH_3OH dehydration. These thermochemical cycles suggest that covalent interactions contribute significantly to bonds between protons and Keggin clusters, but have much smaller contributions in stabilizing DME formation transition states and protonated CH_3OH dimers because the latter species are full ion-pairs. Central atoms of Keggin clusters only influence the electrostatic stabilization of cations by the conjugate anion, while addenda atoms influence both electrostatic and covalent stabilization of protons. Covalent interactions must be overcome to deprotonate the catalyst, but are not recovered at ion-pair transition states; as a result, structure-function relations using DPE values as a descriptor of acid strength can only be used to compare materials when bonds between their protons and anions have similar covalent interactions. Electrostatic interactions between protons and conjugate anions determine the changes in DPE values for catalysts whose protons interact with anions via similar covalent interactions (e.g., W-POM clusters with different central atoms). Stabilities of ion-pair transition states and intermediates during CH_3OH dehydration on these catalysts also change predominantly according to electrostatic interactions between their respective cations and the conjugate anion, however, their electrostatic interactions represent only a fraction of those for protons. Ion-pair transition states that recover a portion of the electrostatic interactions overcome during deprotonation cause the attenuation of activation energies to DPE values measured previously in structure-function relations on W-POM clusters. Adsorbing CH_3OH at protons of Keggin clusters influences the DPE values of residual unoccupied protons on the same cluster because POM clusters are semiconducting materials. DPE values change to greater extents as more protons are occupied by CH_3OH and as adsorbed CH_3OH molecules separate protons from clusters to greater extents. Structure-function relations on POM must account for these changes in DPE, but do not for insulating solids, such as zeolites. The abilities of Keggin clusters to abstract H-atoms during CH bond activation steps in alkane and alkanol oxidative dehydrogenation (ODH) reactions are probed using DFT-derived HAE values. ODH rates, HAE values, and UV-visible absorption edge energies change markedly with the addenda atoms of metal oxides. ODH rates are higher on metal oxides whose unoccupied metal orbitals are lower in energy;

metals with unoccupied orbitals that are lower in energy lead to more negative HAE values and lower edge energies. HAE values vary with O-atom location on Keggin clusters with only Mo or W addenda atoms and with the proximity to V-atoms for V-substituted clusters, indicating that HAE values are probes of local redox properties. The effects of composition and reactant adsorption on DPE values suggest that electrons are delocalized across Keggin clusters, in contrast to the local effects of composition on HAE values, which suggest electrons are localized. DPE and HAE values probe different electronic properties of Keggin clusters because the electron transferred from H-atoms occupies a different orbital than the delocalized electrons that determine DPE values. These illustrative examples demonstrate that catalyst properties and their consequences for reactivity can be assessed quickly and reliably for well-defined materials by using theoretical treatments to calculate simple reaction probes that reflect the chemical processes occurring at kinetically-relevant transition states.

4.1. Introduction

Structure-function relations on solid catalysts indicate how their properties influence reactivity by stabilizing transition states and intermediates that determine activation energies of kinetically-relevant chemical steps and must be developed for well-defined solids to determine the most appropriate descriptors of reactivity. A recent set of communications used W-based Keggin polyoxometalate (POM) clusters in their proton forms ($H_{8-n}X^{n+}W_{12}O_{40}$) as Brønsted solid acids to explore the effects of their central atoms ($X^{n+} = P^{5+}$, Si^{4+}, Al^{3+}, Co^{2+}) on deprotonation energies (DPE) and on the rate constants for H_2O elimination in unimolecular and bimolecular alkanol dehydration reactions [1, 2, 3] and for alkoxide backbone rearrangements in alkene isomerization [4, 5]. DPE values represent the energy needed to fully remove a proton from an acid (forming a non-interacting proton and conjugate anion); they are probe-independent descriptors of acid strength and can be estimated from theory reliably for solids with known structure [6, 7]. These investigations suggest that DPE values describe the relative reactivities of solid Brønsted acids accurately because conjugate anions are also formed upon protonation of reactants at full ion-pair transition states, a ubiquitous feature of acid catalysis. Stronger acids have higher rate constants for alkanol dehydration and alkene isomerization because they require less energy to form the conjugate anions present in ion-pair transition states than on weaker acids. Cationic reactants interact with the conjugate anion via electrostatic interactions at transition states to recover a fraction of the DPE. The charge localization of the cation determines how much of the DPE is recovered and the reaction sensitivity to DPE. Transition state cations that are more "proton-like" recover more electrostatic interactions because of their localized charges and close proximities to the conjugate anions and lead to reactions that are less sensitive to DPE [4]. Ion-pair intermediates are also less stable on weaker acids than on stronger acids because they require full anions be formed. Activation barriers are less sensitive to DPE when transition states are measured with respect to ion-pair intermediates than with respect to uncharged intermediates, because the stabilities of transition states and ion-pair intermediates sense DPE values similarly [3].

Conclusions drawn from one class of well-defined solid acids (e.g., W-based Keggin POM) must apply to other acids (e.g., supported transition metal oxides or zeolites) to

exploit structure-function relations for practical applications. Changes in structures caused by reaction conditions and their effects on catalyst properties must also be taken into account in comparing the reactivities of different catalysts. The effects of catalyst structure and reaction conditions on their properties can be assessed rapidly for well-defined catalysts because theory is able to calculate descriptors of reactivity reliably. Appropriate descriptors of reactivity for different types of chemistry must be developed using theory based upon current knowledge of their kinetically-relevant steps. These descriptors can help discriminate among materials to find those that are suitable for development of new relations.

Here, we use theory to investigate the properties of Keggin POM solid acids and predict their consequences for reactivity in three examples by calculating deprotonation energies (DPE) and H-atom addition energies (HAE). In Section 4.3.1, DPE values for W-Keggin POM clusters are dissected into components that reflect covalent and electrostatic interactions to determine how central and addenda atoms dictate the energy required to form conjugate anions and to stabilize cations during deprotonation and in the formation of ion-pair transition states and intermediates. Proton removal requires overcoming significant electrostatic and covalent interactions. Transition state interactions partially recover the former, but not the latter, so that DPE values cannot be used to directly compare the reactivities of acids whose protons are stabilized to different extents by covalent interactions. DPE values of W-POM clusters increase when CH_3OH molecules adsorb at other protons on the same cluster (Section 4.3.2) and demonstrate the influence of reaction conditions on catalyst properties. Such changes are significant for POM clusters, because their semiconducting properties allow protons to sense the presence of other protons via changes in the cluster electronic structure, but such effects would be negligible for insulators, such as aluminosilicate acids. In Section 4.3.3, we develop HAE values as descriptors of oxidative dehydrogenation (ODH) reactions because electrons are transferred to unoccupied metal orbitals in both H-addition and the H-abstraction step of ODH reactions [8, 9,10, 11]. HAE values probe the local redox properties of POM clusters, which depend strongly on the addenda atom composition and are different than the properties of delocalized electrons probed by DPE values.

4.2. Computational Methods

The structures and energies of all transition states, intermediates, and species involved in the thermochemical cycles of DPE and HAE were calculated using periodic gradient-corrected density functional theory (DFT) via the Vienna ab initio Simulation Package (VASP) [12]. The wavefunction was represented using a periodic plane wave basis set expansion to a cutoff energy of 396.0 eV and Vanderbilt ultrasoft pseudopotentials [13] to describe electron-core interactions. Exchange and correlation energies were calculated within the generalized-gradient approximation using the Perdew-Wang (PW91) form of the exchange-correlation functional [14]. Full Keggin clusters were calculated at the center of a 20 Å x 20 Å x 20 Å unit cell to provide a sufficient vacuum region to prevent interactions between clusters in adjacent unit cells. The first Brillioun zone was sampled using A 1 x 1 x 1 Monkhorst-Pack k-point mesh.

Single-point calculations were converged self-consistently to energies < 1 x 10^{-4} eV. The structures of all stable intermediates were optimized until forces on all atoms

were < 0.05 eV A^{-1}. Structures and energies of Keggin clusters with Co central atoms and of clusters reduced by H-atom addition were calculated with spin-polarization. Structures and energies of charged species (e.g., conjugate anions and protons), required to calculate DPE values and interaction energies, were performed with uniform background charges (of opposite sign) to maintain neutral unit cells. Interactions between neighboring unit cells containing charged species were removed by calculating dipole and quadrupole interaction terms along the x, y, and z axis of the unit cell with the center of charge located at the central atom of the Keggin cluster. Structures of the dimethyl ether (DME) formation transition states were calculated by combining the nudged elastic band (NEB) [15] and dimer [16] methods, the details and convergence criteria of which have been reported previously [3]. Energies of intermediates, transition states, and single points were not corrected for zero-point vibrational energies (ZPVE) because such calculations are computationally prohibitive for full Keggin clusters.

Electronic structures of single point calculations used to generate charge distributions for electrostatic calculations were converged self-consistently to < 1 x 10^{-6} eV. Atomic nuclei and inner shell electrons were treated as "cores" with effective point charges equal to the sum of the nuclear and inner shell electronic charges due to the frozen-core approximation used in the calculations and valence electrons were distributed over a three-dimensional mesh. The electrostatic interactions (E_{es}) between two species include core-core repulsion (E_{nn}), repulsion among valence electron distributions (E_{ee}), and the attraction between cores and valence electrons (E_{en}):

$$E_{es} = E_{nn} + E_{ee} + E_{en} \tag{4.1}$$

The repulsion between the cores of cation "c" and the cores of anion "a" is given by:

$$E_{nn} = \sum_{c=1}^{N_c} \sum_{a=1}^{N_a} \frac{1}{4\pi\varepsilon_0} \frac{Z_a Z_c}{r_{ac}} \tag{4.1a}$$

where ε_0 is the permittivity of a vacuum, Z_a is the effective charge of a core in the anion, Z_c is the effective charge of a core in the cation, r_{ac} is the separation between the cores, and N_c and N_a are the total numbers of cores in the cation and anion, respectively. Valence electron distributions, consisting of charge densities distributed over a DFT unit cell with a 140 x 140 x 140 mesh, were divided into anionic and cationic electron distributions using the Bader partitioning method [17, 18]. E_{ee} and E_{nn} values were calculated from partitioned distributions assuming that all electronic charge within a given mesh cell (of size 0.143 Å x 0.143 Å x 0.143 Å) was a point charge located at the center of the mesh cell. The repulsion among the point charges comprising the valence electron distributions of anions and cations is given by:

$$E_{ee} = \sum_{c=1}^{V_c} \sum_{a=1}^{V_a} \frac{1}{4\pi\varepsilon_0} \frac{q_a q_c}{r_{ac}} \tag{4.1b}$$

where q_a is the charge of a point charge in the anion electron distribution, q_c is the charge of a point charge in the cation electron distribution, r_{ac} is the separation between the point charges, and V_a and V_c are the total number of point charges in the anion and cation valence electron distributions, respectively. Finally, the electron-nuclear interactions were calculated using:

$$E_{en} = \sum_{c=1}^{V_c}\sum_{a=1}^{N_a}\frac{1}{4\pi\varepsilon_0}\frac{Z_a q_c}{r_{ac}} + \sum_{a=1}^{V_a}\sum_{c=1}^{N_c}\frac{1}{4\pi\varepsilon_0}\frac{Z_c q_a}{r_{ac}} \quad (4.1c)$$

where the first term represents interactions between cores in the anion and valence electrons in the cation and the second term represents interactions between cores in the cation and valence electrons in the anion.

Electrostatic interaction energies between protons and conjugate anions ($E_{es,H+}$) used in DPE thermochemical cycles were calculated using Eq. (4.1) with the cation treated as a single point charge (+1 e) without an electron cloud and located at the same distance from the anion as in the neutral Keggin cluster (OH bond = 0.098 nm). Other components of the DPE thermochemical cycles were calculated from DFT-derived energies of species involved in **Scheme 4.1**. The energy to create non-interacting protons (H^+) and anions in their unrelaxed geometries (A_{prot}^-) from neutral clusters ($H\text{-}A_{prot}$) is equal to the sum of electrostatic interactions ($E_{es,H+}$) and reorganization energies (E_{reorg}):

$$E_{reorg,H+} + E_{es,H+} = E(A_{prot}^-) + E(H^+) - E(H\text{-}A_{prot}) \quad (4.2)$$

Therefore, E_{reorg} values were calculated by removing electrostatic interactions from the right hand side of Eq. (4.2). Relaxation energies of anions (E_{relax}) were taken from the difference in energies of anions in their unrelaxed (A_{prot}^-) and relaxed geometries (A_{relax}^-):

$$E_{relax} = E(A_{relax}^-) - E(A_{prot}^-) \quad (4.3)$$

Energies of components included in thermochemical cycles that describe interaction energies between anions and protonated CH_3OH dimer or DME formation transition state cations ($E_{int,dimer}$ and $E_{int,TS}$) were calculated using similar protocols as for protons. Single-point calculations of transition state and dimer cations in the gas-phase provided the electron distributions of these cations not interacting with anions (i.e., "isolated" cations). Single-point calculations also provided electron distributions of Keggin anions with geometries optimized while interacting with cations ("isolated" unrelaxed anions; A_{TS}^- and A_{dimer}^-). The cations and unrelaxed anions were then placed at separation distances present in optimized transition state and dimer structures to calculate electrostatic interaction energies according to Eq. (4.1). Reorganization and relaxation energies for transition state and dimer cycles were calculated by replacing $E_{es,H+}$ with $E_{es,TS}$ or $E_{es,dimer}$, replacing $E(A_{prot}^-)$ with $E(A_{TS}^-)$ or $E(A_{dimer}^-)$, and replacing $E(H\text{-}A_{prot})$ with the energies of the optimized structures for transition states or protonated dimers in Eqs. (4.2) and (4.3).

H-atom addition energies (HAE) for Keggin clusters were calculated by adding H radicals to different O-atom locations and allowing the entire cluster to optimize its structure. HAE values were calculated for 36 O-atom locations (12 terminal O-atoms, 12 edge-bridging O-atoms, and 12 corner-bridging O-atoms) for $H_3PW_{12}O_{40}$, $H_3PMo_{12}O_{40}$, $H_4PW_{11}VO_{40}$, and $H_4PMo_{11}VO_{40}$ clusters. HAE values were calculated from the difference in DFT-derived energies of reduced clusters (POM_{red}) and the combined energies of gas-phase H radicals (H•) and fully-oxidized clusters (POM_{ox}):

$$HAE = E(POM_{red}) - E(H\bullet) - E(POM_{ox}) \quad (4.4)$$

Protons locations for clusters containing 3 or 4 protons were taken to be the same as those prescribed previously on $H_3PW_{12}O_{40}$ and $H_4SiW_{12}O_{40}$, respectively [19, 20].

4.3. Results and Discussion

4.3.1. Effects of composition on deprotonation energies of Keggin POM clusters and their consequences for CH_3OH dehydration reactivity

The reactivities of solid Brønsted acids depend on deprotonation energies (DPE) because acids must fully transfer protons to organic bases (i.e., reactants) to form full ion-pairs at the kinetically-relevant transition states. Solid acids must separate charge in two ways to donate protons and these processes reflect the covalent and electrostatic interactions between protons and the conjugate anion. Reorganization of the electrons located in the OH bond of the starting acid is needed to form protons (+1 e) and conjugate anions (-1 e) and for any subsequent delocalization of electron density in the anion. The energies required for these processes reflect covalent interactions. Protons and anions must then be separated spatially, which requires overcoming their electrostatic attraction. Structure-function relations developed for W-POM clusters did not discern how each of these two processes cause the observed correlation between DPE values and activation energies, because the creation and separation of ion-pairs are both included in DPE calculations and experimental measurements of reactivity. The path-independent properties of energy allow us to construct thermochemical cycles of deprotonation energies (Scheme 4.1) that separate the stabilization of protons into covalent and electrostatic interactions with anions. DPE values of acids in the gas-phase depend on the energy required to reorganize electrons to form full protons and full anions (E_{reorg}), on the electrostatic interaction energy that must be overcome to separate them to non-interacting distances (E_{es}), and on the relaxation energy of the anion from its interacting structure to its non-interacting structure (E_{relax}):

$$DPE = E_{reorg} + E_{es} + E_{relax} \quad (4.5)$$

Next, we examine how the identity of the central atom and the concomitant changes in the number of protons per POM cluster influence each of the terms in Eq. (4.5). Energies, electron distributions, and structures of species involved in this thermochemical cycle (illustrated in Scheme 4.1) can be estimated by using density functional theory (DFT) or calculated classically from the DFT-derived electron distributions (details

included in Section 4.2). Table 4.1 includes the DFT-derived values of terms in Eq. (4.5) for W-Keggin POM clusters with S, P, Si, Al, and Co central atoms. The electron distribution of the non-interacting anion in its unrelaxed structure (A_{prot}^- in Scheme 4.1) defines the electronic structure of the anion that results from E_{reorg} (i.e., an E_{reorg} value of zero indicates that protons induce no change in the electron distribution of the conjugate anion). E_{reorg} is the largest contributor to DPE for all central atoms (909 – 924 kJ mol^{-1}; Table 4.1), indicating that protons induce strong changes in the electronic structure of anions, presumably by forming covalent OH bonds. Positive E_{reorg} values indicate that protons and anions form strong bonds because covalent interactions and electron-proton attraction prevail over any electron-electron repulsion associated with the localization of electron density required to form OH bonds. The values of E_{reorg} do not change systematically with central atom identity or DPE; thus, they do not account for differences in the strength or reactivity among these acids.

Separating protons from conjugate anions spatially (which requires an energy of E_{es}) does not cause further changes in charge distributions so that E_{es} can be calculated by integrating the Coulombic forces between the proton and the charge distribution in the non-interacting anion (details in Section 4.2). Values of E_{es} are positive (Table 4.1) because energy must be applied to overcome interactions between protons and anions. Figure 4.1 shows E_{es} values for protons as a function of DPE values for W-POM clusters with S, P, Si, Al, and Co central atoms. The slope of the regressed line is 0.92, indicating that changes in electrostatic energies between protons and anions account for nearly the entire differences in DPE values of these materials. These differences in E_{es} reflect, in turn, differences in *charge distributions* of anions, because all anions have charges of -1 e. Methods that construct quasiatomic orbitals from DFT-derived wave functions (e.g., QUAMBO [21]) are needed to determine the mechanism by which the central atom causes these different charge distributions. A decrease in the valence of the central atom causes the central tetrahedron to have a higher anionic charge (e.g., $[PO_4]^{3-} \rightarrow [SiO_4]^{4-}$). We speculate that clusters partially delocalize this higher anionic charge across the metal oxide cage and partially localize it in the covalent OH bond involving the additional proton needed to compensate for the lower valence of the central atom. DPE values increase monotonically with the total number of protons. The number of protons (p) and each of their partial charges (δ+) determine the number of delocalized electrons in Keggin clusters. Similar E_{reorg} values in Table 4.1 suggest that central atoms do not influence the electron sharing in OH bonds or by inference the partial charges on protons, so that the total amount of delocalized electrons scales with pδ. E_{es} and the total amount of delocalized electrons increase monotonically together because delocalized electrons can get closer to and interact more effectively with protons than electrons localized in the central tetrahedron. These results suggest that changes in E_{es} and DPE shown in Figure 4.1 are caused by changes in the amount of delocalized electrons. The amount and density of delocalized electrons are proportional for Keggin clusters because of their uniform size, so that their effects on E_{es} cannot be separated from each other. The incremental increase in DPE values with increasing numbers of protons does not correlate with the distance between the proton being removed and the proton added to compensate charge. These results suggest that the electron density localized in OH bonds does not

determine the E_{es} values in Figure 4.1 and that the effects of central atom identity on DPE primarily reflect changes in the amount of delocalized electrons.

The last components of the DPE thermochemical cycles are the anion relaxation energies (E_{relax}), which are similar for all central atoms (Table 4.1; -90 to -96 kJ mol^{-1}) and are similar in magnitude to typical reaction activation energies. Interactions with protons distort the positions of vicinal atoms, so that non-interacting anions relax their geometries and electron distributions to minimize their energies. These relaxation energies may not be relevant for reactivity, however, if anions do not undergo similar distortions when interacting with transition states and intermediates as when they interact with protons. DPE values using anions in their relaxed structures are more appropriate descriptors of reactivity if transition states and intermediates do not induce similar distortions as protons.

Higher-valent central atoms lead to stronger POM acids, because they exhibit lower densities (or amounts) of delocalized electrons, giving rise to weaker electrostatic interactions with protons (i.e., smaller E_{es} values). DPE values use protons as a probe cation to determine the ability of an acid to form ion-pairs from covalently-bound species and to separate the resulting cation and conjugate anion. Similar electron reorganization and ion separation processes must be calculated for organic cations present at transition states and in reactive intermediates to understand how composition directly influences reactivity. Interaction energies between organic cations and conjugate anions (E_{int}) can be described by the thermochemical cycle in Scheme 4.1 by reversing the direction of all arrows and replacing the proton with the organic cation that that is present in reactive intermediates or transition states. Elementary steps of CH_3OH dehydration were investigated previously by DFT calculations and kinetic experiments on W-POM clusters [3] and are shown in Scheme 4.2. CH_3OH dehydration proceeds by sequential adsorption of two CH_3OH molecules to form monomers (Step 1 in Scheme 4.2) and then protonated dimers (Step 2 in Scheme 4.2). Protonated dimers re-orient to direct the methyl group of one CH_3OH molecule towards the O-atom of the other CH_3OH molecule and transfer the methyl group in a single kinetically-relevant elementary step that simultaneously forms dimethyl ether (DME) and H_2O (Step 3 in Scheme 4.2).

Interactions between conjugate anions and protonated CH_3OH dimer or DME formation transition state cations ($E_{int,dimer}$ and $E_{int,TS}$, respectively) are given by:

$$E_{int,dimer} = E_{reorg,dimer} + E_{es,dimer} + E_{relax,dimer} \quad (4.6a)$$

$$E_{int,TS} = E_{reorg,TS} + E_{es,TS} + E_{relax,TS} \quad (4.6b)$$

where the "dimer" and "TS" subscripts denote energy terms of thermochemical cycles involving protonated dimers and transition states, respectively. The energies in Eqs. (4.6a) and (4.6b) were calculated by DFT methods using similar protocols as for protons (Section 4.2); their values are included in Table 4.2 for W-Keggin POM clusters with S, P, Si, Al, and Co central atoms.

First, we examine the effects of central atom composition on the interaction energies between protonated dimer cations and conjugate anions ($E_{int,dimer}$). The more negative $E_{int,dimer}$ values for weaker acids (Table 4.2) indicate that their conjugate anions

stabilize protons and protonated dimer cations more effectively than the conjugate anions of stronger acids. $E_{reorg,dimer}$ values change only slightly with central atom and are much smaller (in magnitude) than for protons (E_{reorg} = -125 to -139 kJ mol^{-1} for dimers in Table 4.2 and ca. 910 kJ mol^{-1} for protons in Table 4.1). E_{reorg} values that are smaller in magnitude for dimers suggest that protonated dimers and anions interact by bonds that are are less covalent than the OH bonds in the acid. Protons interact via stronger covalent bonds because they are unstable as cations with their highly localized charge, while O-atoms of CH_3OH solvate the proton in dimer intermediates and lead to more diffuse and stable cationic charge. The weak covalency of the interactions between protonated dimers and Keggin anions is consistent with their Bader charges on all POM clusters (+ 0.86 to + 0.88 e) [3], which suggest they exist as full ion-pairs. Figure 4.2 shows $E_{es,dimer}$ values as a function of the total interaction energy ($E_{int,dimer}$). The slope of the best-fit line through the data (0.89) indicates that electrostatic interactions account for nearly all changes in $E_{int,dimer}$ with changes in the POM central atom. A similar relation was found for proton stabilization (Figure 4.1) and suggests that the valence of the central atom in W-POM clusters determines how ion-pair intermediates sense acid strength through the density (or amount) of delocalized electrons. Relaxation energies of anions after removing protonated dimers are smaller than for protons because dimers are softer cations without covalent bonds to the anion that do not distort geometries of vicinal atoms in the anion.

Thermochemical cycles involving DME formation transition state cations (Table 4.2) have terms whose energies more closely resemble their counterparts for protonated dimers than for protons. $E_{reorg,TS}$ values are slightly less negative than $E_{reorg,dimer}$ values, indicating weak stabilization of transition states by covalent interactions, and depend only weakly on central POM atom (-83 to -100 kJ mol^{-1}). Electrostatic interactions contribute more than covalent interactions to $E_{int,TS}$ for these clusters (i.e., $|E_{reorg,TS}| < |E_{es,TS}|$ in Table 4.2) and also account for essentially all the differences in interaction energies for different central atoms ($\Delta E_{es,TS}/\Delta E_{int,TS}$ = 0.74 in Figure 4.2). $E_{reorg,TS}$ values have smaller magnitudes than $E_{es,TS}$ values and DME formation transition states have Bader charges of ca. +0.90 e [3], suggesting that these transitions states are full ion-pairs and interact with anions primarily through electrostatic and not covalent interactions.

DFT-derived energies of each term in DPE and interaction energy thermochemical cycles indicate that the central atom in W-POM clusters predominantly influences electrostatic interactions between the conjugate anion and cations. The activation energy for DME formation from protonated dimers (Step 3 in Scheme 4.2) reflects the difference between the energies of DME formation transition states and protonated CH_3OH dimers ($E_{a,dimer}$ in Scheme 4.3). The thermochemical cycle in Scheme 4.3 dissects the energy needed to carry out this chemical transformation into alternate steps whose energies are available from our calculations. The protonated dimer is first removed from the conjugate anion by overcoming its interaction energy ($-E_{int,dimer}$). The resulting gaseous dimer then restructures to form the transition state cation with a reaction energy equal to the difference in formation energies of the gas-phase cations from a free proton and two CH_3OH (g) ($E_{cation,TS} - E_{cation,dimer}$ in Scheme 4.3). The gaseous transition state analog interacts with the conjugate anion ($E_{int,TS}$) to complete the thermochemical cycle and to provide an equation for $E_{a,dimer}$:

$$E_{a,dimer} = -E_{int,dimer} + (E_{cation,TS} - E_{cation,dimer}) + E_{int,TS} \quad (4.7)$$

Structure-function relations for CH_3OH dehydration based on W-POM clusters indicate that activation energies increase weakly as the DPE values of acids increase ($dE_{a,dimer}/dDPE = 0.10$) [3]. The derivative of Eq. (4.7) with respect to DPE shows that the sensitivities of the dimer and transition state interaction energies to DPE determine the effects of DPE on $E_{a,dimer}$.

$$\frac{dE_{a,dimer}}{dDPE} = \frac{dE_{int,TS}}{dDPE} - \frac{dE_{int,dimer}}{dDPE} \quad (4.8)$$

Gas-phase formation energies of the dimer and transition state cations (E_{cation} in Table 4.2) do not vary with central atoms of POM clusters, because structures of dimers and transition states do not change among these catalysts and their energies are those of gaseous species; as a result, the terms corresponding to E_{cation} values are absent from Eq. (4.8). Changes in DPE, $E_{int,dimer}$, and $E_{int,TS}$ values with the central atom valence (n) are predominantly caused by changes in electrostatic interactions between conjugate anions and protons, dimer cations, and transition state cations, respectively (i.e., $dDPE/dn \sim dE_{es,H+}/dn$; $dE_{int,dimer}/dn \sim dE_{es,dimer}/dn$; $dE_{int,TS}/dn \sim dE_{es,TS}/dn$):

$$\frac{dE_{a,dimer}}{dDPE} \approx \frac{dE_{es,TS}}{dE_{es,H^+}} - \frac{dE_{es,dimer}}{dE_{es,H^+}} \quad (4.9)$$

The effects of acid strength on $E_{a,dimer}$ are predominantly defined by how effectively transition states and adsorbed species interact with the conjugate anion via electrostatic interactions relative to the electrostatic attraction between protons and the conjugate anion (i.e., $dE_{es,TS}/dE_{es,H+}$ and $dE_{es,dimer}/dE_{es,H+}$ in Eq. (4.9)). The slopes of the regressed lines in Figure 4.3 equal the values of the derivatives on the right hand side of Eq. (4.9) (-0.53 and -0.56 for transition states and dimers, respectively). These values indicate that organic cations present as intermediates and transition states only recover a portion of the electrostatic energy that must be overcome to deprotonate the POM clusters. Protons have stronger electrostatic interactions with conjugate anions than organic cations do because protons have more localized charges and closer proximities to the anions. The slopes of the lines regressed to $E_{es,dimer}$ and $E_{es,TS}$ data in Figure 4.3 predict that activation energies increase weakly with DPE ($dE_{a,dimer}/dDPE \sim 0.03$) because the effects of acid strength on transition state and dimer stabilities, which are similar, largely cancel out for activation energies. Similar calculations should be completed for organic cations present as transition states in other acid-catalyzed reactions (e.g., cyclopropyl carbenium ions for isomerization reactions and sp^2 hybridized secondary carbenium ions at 2-butanol dehydration transition states) to examine how the charge distributions in these cations influence the sensitivities of the reactions that they mediate to acid strength. Transition state cations that localize the majority of their charge near anion will have E_{es} values that are most similar to those for protons. Interactions between these cations and the

conjugate anion will recover most of the electrostatic interactions that are overcome during deprotonation and are predicted to result in reactions that are insensitive to DPE.

CH_3OH dehydration rate constants ($k_{DME}K_D$ and k_{DME}) were measured previously on W-POM clusters and acid forms of zeolites by regressing CH_3OH dehydration turnover rates ($r_{dehy}/[H^+]$) to the rate expression defined by the elementary steps in Scheme 4.2 [3]:

$$\frac{r_{dehy}}{\left[H^+\right]} = \frac{k_{DME}K_D\left(CH_3OH\right)}{1+K_D\left(CH_3OH\right)} \tag{4.10}$$

where the elementary steps in Scheme 4.2 define the reactions described by k_{DME} and K_D. Values of k_{DME} reflect the difference in free energy between DME formation transition states and protonated dimers [3]. Values of $k_{DME}K_D$ include additional chemical information about CH_3OH adsorption at monomers to form dimers (via K_D; Step 2 in Scheme 4.2), so that $k_{DME}K_D$ values reflect the difference in free energy between DME formation transition states and uncharged monomers (and a gas-phase CH_3OH). Experimental $k_{DME}K_D$ values depend more sensitively on DPE than values of k_{DME} [3]. Values of $k_{DME}K_D$ and k_{DME} only differ in the identity of the intermediate that DME formation transition states are measured with respect to in activation free energies (i.e., monomers for $k_{DME}K_D$ and dimers for k_{DME}); thus, the different sensitivities of $k_{DME}K_D$ and k_{DME} to DPE reflect the different effects of acid strength on the stabilization of dimer and monomer cations ($E_{int,dimer}$ and $E_{int,mono}$). Gas-phase monomer cations consist of a proton in ion-dipole interactions with the O-atom of a CH_3OH molecule at their separation distance in adsorbed monomers (0.140 nm [3]). The interaction energies between cationic monomers and anionic clusters are not yet calculated, but we speculate on their values and their role in determining the stronger sensitivity of $k_{DME}K_D$ values than kDME values to acid strength [3]. Protons are closer to Keggin O-atoms (0.107 nm) than to CH_3OH O-atoms (0.140 nm) in essentially uncharged monomers (+0.08 e), suggesting that protons are covalently-bound to the Keggin anion and H-bonded to CH_3OH. The separation between the proton and Keggin O-atom in monomers is only slightly longer than in unoccupied acid sites (by 0.010 nm). These structural features suggest that monomers incipiently remove protons, which are expected to weaken the covalent bond between protons and Keggin clusters and will be reflected in slightly smaller E_{reorg} values for monomers than for protons. Ion-dipole interactions between protons and CH_3OH molecules in monomers will strongly distort the charge distributions of protons and make predicting $E_{es,mono}$ values more difficult. Dimers delocalize the cationic charge of protons by solvating them between CH_3OH molecules; taken together with protons that are closer to Keggin O-atoms in monomers (0.107 nm) than in dimers (~ 0.28 nm) [3], this suggests that E_{es} values for monomers and their changes with central POM atom will more closely resemble those for protons than those for protonated dimers ($|E_{es,H+}| > |E_{es,mono}| > |E_{es,dimer}|$ and $-1 < \frac{dE_{es,mono}}{dE_{es,H^+}} < -0.56$). Replacing the value of $dE_{es,dimer}/dE_{es,H+}$ (-0.56) in Eq.

(4.9) with a value of $dE_{es,mono}/dE_{es,H+}$ that is closer to -1 will lead to more sensitive activation energies (i.e., $dE_{a,mono}/dDPE > 0.03$) .

We extend these calculations next to Mo-Keggin POM clusters with S, P, Si, Al, and Co central atoms. The results are shown in Table 4.3 for DPE values and illustrate the effects of addenda atoms on acid strength. DPE values of Mo-POM clusters are larger than for W-POM clusters with the same central atom. The $E_{reorg,H+}$ values for Mo-POM clusters are nearly independent of the central POM atom (Table 4.3; 945 – 963 kJ mol^{-1}), but ~ 40 kJ mol^{-1} larger than on W-POM clusters for each central atom (909 – 924 kJ mol^{-1}). These energies indicate that Mo-POM clusters bind protons more covalently than W-POM clusters. The origins of the effects of addenda atoms, but not of central atoms, on the extent of electron sharing in OH species remain unclear. Stronger contributions of covalent interactions to OH species also indicate that H-atoms on Mo-POM clusters have a smaller positive charges than on W-POM clusters. Relaxation energies ($E_{relax,H+}$) on Mo-POM clusters are also essentially independent of central POM atoms (Table 4.3; -80 to -91 kJ mol^{-1}) and their associated structural relaxations stabilize non-interacting anions slightly less than for W-POM clusters (by ca. 10 kJ mol^{-1}). The slope of the best-fit line through the data on Mo-POM clusters in Figure 4.1 (0.80) indicates that electrostatic interactions nearly account for all changes in DPE values with central atom identity on Mo-POM clusters. The trend on Mo-POM clusters in Figure 4.1 is, however, shifted to higher DPE values relative to the trend on W-POM clusters. Stronger covalent interactions on Mo-POM clusters than W-POM clusters lead to larger DPE values for the former (at a given $E_{es,H+}$ value) by contributing larger E_{reorg} values to DPE in Eq. (4.5). The more negative $E_{es,H+}$ values on W-POM clusters than on Mo-POM clusters of the same central atom, suggest each proton on Mo clusters delocalizes a smaller fraction of an electron than a proton on a W cluster. This is consistent with the greater amount of electron sharing in OH bonds of Mo-POM clusters predicted by their larger $E_{reorg,H+}$ values. W-POM clusters also have a larger range of $E_{es,H+}$ values than Mo-POM clusters (over the same central atoms) because each proton delocalizes more electron density.

Table 4.4 contains the energies of terms in the thermochemical cycle describing interactions between protonated dimer cations and Mo-POM anions. The slope of the best-fit line correlating $E_{int,dimer}$ and $E_{es,dimer}$ values on Mo-POM in Figure 4.2 (0.96) indicates that interaction energies of protonated dimers change with different central atoms entirely due to changes in electrostatic interactions between the ions. The data on Mo-POM are only shifted slightly to more negative $E_{int,dimer}$ values relative to the data on W-POM clusters in Figure 4.2. $E_{int,dimer}$ values on W and Mo clusters (at a given $E_{es,dimer}$) are closer than DPE values on W and Mo clusters (at a given $E_{es,H+}$) (Figure 4.1). Addenda atoms have a weaker effect on $E_{reorg,dimer}$ values (~5 kJ mol^{-1}) than on $E_{reorg,H+}$ values (~40 kJ mol^{-1}), because dimers are full cations and protons are covalently-bound to the anion.

Transition state interaction energies and energy terms in their thermochemical cycles have not been calculated for Mo-POM clusters, but transition states and protonated dimers that are both ion-pairs on W-POM and which have similar values for E_{reorg}, E_{es}, and E_{relax} in Table 4.2, suggest that addenda atoms will affect components of $E_{int,TS}$ and $E_{int,dimer}$ similarly. $E_{reorg,TS}$ will have slightly larger magnitudes on Mo clusters than W clusters and will be invariant with central atom. $E_{es,TS}$ will also account for the effects of

central atoms on $E_{int,TS}$ completely. The effects of metal atom composition on reactivity cannot be predicted using Eq. (4.9) because W and Mo clusters have different covalent contributions to DPE (i.e., $dDPE \neq dE_{int,H+}$). Eqs. (4.6a) and (4.6b) must be substituted into Eq. (4.7) instead to assess the consequences of addenda atoms for CH_3OH dehydration.

$$E_{a,dimer} = (E_{cation,TS} - E_{cation,dimer}) + (E_{reorg,TS} - E_{reorg,dimer}) + (E_{es,TS} - E_{es,dimer}) + (E_{relax,TS} - E_{relax,dimer}) \quad (4.11)$$

Dimer cations on Mo and W clusters have similar structures from DFT and structures of transition state cations are presumed to not change with addenda atom identity, so that E_{cation} terms will have constant values. Values of $E_{reorg,dimer}$ and $E_{relax,dimer}$ in Table 4.2 and Table 4.4 are similar for Mo and W clusters (values differ < 10 kJ mol^{-1} in all cases), because dimers are ion-pairs without strong covalent stabilization. DME formation transition states are also ion-pairs on W-POM clusters with small $E_{reorg,TS}$ and $E_{relax,TS}$ values, which are predicted to be similar on Mo-POM clusters. $E_{int,dimer}$ values on W and Mo clusters in Figure 4.3 fall along a similar correlation (for all but Co central atoms) when plotted versus $E_{int,H+}$ values. $E_{a,dimer}$ values will only be a function of $E_{int,H+}$ values if $E_{int,TS}$ values on W and Mo clusters also fall along a single correlation in Figure 4.3. Thus, values of k_{DME} on W and Mo clusters are predicted to lie along a single correlation when plotted versus catalyst $E_{int,H+}$ values. Values of $k_{DME}K_D$ on W and Mo clusters will not fall along a single correlation using DPE or $E_{es,H+}$ values because transition states do not recover the the energy needed to break the covalent OH bond in monomers (i.e., $E_{reorg,mono}$ values, but not $E_{reorg,TS}$ values, will depend on addenda atoms). These results suggest that structure-function relations cannot use DPE values to compare the reactivities of catalysts with OH bonds of different covalence directly. As a result, previous structure-function relations comparing zeolites and W-POM clusters must be revisited once $E_{reorg,H+}$ values for zeolites are calculated using the methods discussed in this section.

4.3.2. Effects of CH_3OH monomer and dimer formation on DPE values of W-Keggin POM clusters

The central atoms of Keggin clusters influence their DPE values via electrostatic attractions between protons and the density of delocalized electrons, which must be overcome to remove protons (Section 4.3.1). The identities of addenda atoms also influence the density of delocalized electrons via the partial charges on protons (i.e., Mo-POM clusters have a smaller DPE range than W-POM clusters for the same central atoms in Figure 4.1). DPE values of Keggin clusters are sensitive to the numbers of protons per cluster and their partial charges because protons located on the same cluster "communicate" via delocalized electrons. Adsorbing reactants at protons may also influence DPE values of POM clusters if reactant adsorption changes the density of delocalized electrons by partially or fully removing protons from the cluster. We investigate the effects of reactant adsorption on DPE values, and by inference the density of delocalized electrons, in this section by calculating DPE values of W-Keggin clusters

in which all acid sites, except the one being removed, are occupied by CH_3OH monomers or protonated CH_3OH dimers. The DFT-derived structures of these "monomer-saturated" and "dimer-saturated" clusters are shown in Scheme 4.4 for the P central atom (A and B, respectively), where the abstracted proton is labeled "H_{C1}".

Table 4.5 contains the DPE values of these monomer- and dimer-saturated W-POM clusters with S, P, Si, Al, and Co central atoms. Figure 4.4 plots these DPE values as a function of the number of protons per Keggin cluster. The DPE value of a monomer-saturated cluster is larger than a cluster with the same central atom where all protons are unoccupied. This indicates that the presence of CH_3OH monomers weakens residual unoccupied acid sites on that cluster. The lines regressed to the data on unoccupied and monomer-saturated clusters in Figure 4.4 have slopes of 19 and 27 kJ mol^{-1} H^{+-1}, respectively, indicating that the differences in DPE values between monomer-saturated and unoccupied clusters become larger as the number of protons per cluster increase. Adsorbing a second CH_3OH molecule at monomers to form protonated dimers increases DPE values for each central atom (Figure 4.4). The line regressed to the data on dimer-saturated clusters with S, P, Si, and Al central atoms in Figure 4.4 has a slope of 42 kJ mol^{-1} H^{+-1} (compared to 27 kJ mol^{-1} H^{+-1} for monomer-saturated clusters), indicating that DPE values of dimer-saturated clusters have the strongest dependence on the number of protons per cluster. The DPE value of the dimer saturated $H_6CoW_{12}O_{40}$ cluster is below the trend of the other central atoms in Figure 4.4, because one of the dimers on the $H_6CoW_{12}O_{40}$ cluster is not protonated (the non-protonated dimer is outlined in Scheme 4.4 C). Proton transfer to adsorbed CH_3OH molecules requires significant energy on dimer-saturated $H_6CoW_{12}O_{40}$ because they are weak acids (1252 kJ mol^{-1} vs. an average DPE value of 1185 kJ mol^{-1} for zeolites [6]); as a result, uncharged H-bonded dimers (outlined in Scheme 4.4C) are favored over protonated dimers, because the former do not require proton donation for their formation.

Next we use DFT-derived energies of components involved in DPE thermochemical cycles (Scheme 4.1) to investigate why DPE values of POM clusters increase upon adsorbing CH_3OH at protons. Table 4.5 contains the values of E_{es}, E_{reorg}, and E_{relax} in Eq. (4.5) for monomer- and dimer-saturated W-POM clusters with S, P, Si, and Al central atoms. Figure 4.5 shows $E_{es,H+}$ values (i.e., the electrostatic attraction between protons and conjugate anions) as a function of DPE for unoccupied, monomer-saturated, and dimer-saturated clusters. The lines regressed to the data on monomer- and dimer-saturated clusters in Figure 4.5 have slopes of 0.98 and 0.97, respectively, indicating that $E_{es,H+}$ values account for the effects of central atoms on DPE values of monomer- and dimer- saturated clusters, as was the case for unoccupied W-POM clusters (Section 4.3.1). The data for unoccupied, monomer-saturated, and dimer-saturated clusters are nearly superimposed in Figure 4.5 because E_{reorg} did not vary significantly among unoccupied clusters (909 – 924 kJ mol^{-1}; Table 4.1), monomer-saturated clusters, (916 – 921 kJ mol^{-1}; Table 4.5) or dimer-saturated clusters (902 – 916 kJ mol^{-1}; Table 4.5). These results indicate that changes in $E_{es,H+}$ account for changes in DPE values caused by the adsorption of CH_3OH at protons. DPE (and $E_{es,H+}$) values in Figure 4.4 depend most strongly on the number of protons per cluster for dimer-saturated clusters and more strongly for monomer-saturated clusters than unoccupied clusters. Densities of delocalized electrons in bare POM clusters, which depend on the valence of the central

atom, determine the electrostatic interactions between protons and their anions (Section 4.3.1). The data in Figure 4.4 therefore suggest that monomer formation increases the density of delocalized electrons and that dimer formation increases this density of delocalized electrons to an even greater extent. Structures calculated from DFT suggest that monomers "incipiently" remove protons from catalysts (e.g., catalyst OH bond = 0.098 nm and 0.107 nm for bare clusters and for those with monomers, respectively), which pushes electron density from the OH bond into the cluster. The delocalized electron density accumulates as more protons are occupied by monomers. Dimers delocalize more electron density than monomers because dimers fully break OH bonds (e.g., protons and Keggin O-atoms are separated by ca. 0.280 nm in protonated dimers) and are full cations (+0.87 e Bader charge). Future investigations should correlate adsorbate properties, such as their gas-phase protonation energies (i.e., $B + H^+ \rightarrow BH^+$), with their abilities to remove protons and to change DPE values. Future calculations also need to demonstrate the effects of CH_3OH adsorption on $E_{int,dimer}$ and $E_{int,TS}$ values using the methods described in Section 4.3.1. The results in Figure 4.3 predict that interaction energies of organic cations will change less than DPE values, because protons have more localized charges and are located closer to anions. Transition state and protonated dimer cation interactions with anions ultimately attenuate the effects of DPE on activation energies (according to Eq. (4.9) in Section 4.3.1); as a result, CH_3OH adsorption at protons is anticipated to cause smaller changes in activation energies than in DPE values.

The protons per cluster (i.e., the central atom valence) and the removal of protons by CH_3OH influence DPE values of POM clusters because the semiconducting properties of these materials delocalize electron density across the cluster. Structure-function relations that are based on POM clusters [1 - 5] must be adjusted in the future to account for the effects of reactant adsorption on DPE values, as we demonstrate next for CH_3OH dehydration. Such adjustments are necessary when protons are saturated with reactants under conditions used to measure kinetic parameters. Figure 4.6a and b show DME formation rate constants ($k_{DME}K_D$ and k_{DME}) measured on W-POM clusters and on zeolites with different framework structures as a function of DPE. The correlations of $k_{DME}K_D$ and k_{DME} with DPE for POM clusters shift markedly in Figure 4.6 when the DPE values of vacant POM clusters (filled symbols) are replaced by the DPE values of monomer- and dimer- saturated clusters (open symbols). Values of $k_{DME}K_D$ on zeolites were larger than the value predicted for a W-POM cluster with the same DPE value in previous correlations [3]. The higher dehydration reactivities on zeolites were attributed to van der Waals interactions that preferentially stabilize DME formation transition states over monomer intermediates because one of the CH_3OH molecules in the latter is not confined within zeolite voids. The values of $k_{DME}K_D$ and k_{DME} must be plotted at the DPE values of monomer- and dimer- saturated POM clusters, respectively, to take into account the effects of reactant adsorption on DPE values. This is because monomers are the most abundant surface intermediates (MASI) under reaction conditions where rates depend on $k_{DME}K_D$ values and dimers are the MASI under conditions where rates depend on k_{DME} values. DPE values of insulating materials such as zeolites do not change with reactant adsorption because these materials do not delocalize electrons like POM clusters. Values of $k_{DME}K_D$ on zeolites other than MFI and values of k_{DME} on all zeolites are below the relations for POM clusters when DPE values of POM clusters are adjusted for

CH_3OH adsorption. Transition states that have less entropy (relative to their precursors) upon being confined in zeolite voids or covalent interactions that contribute differently to OH bonds of zeolites and W-POM clusters may account for the lower values of $k_{DME}K_D$ and k_{DME} than predicted by POM clusters. The latter of these possibilities will be investigated in the future by applying the methods described in Section 4.3.1 to zeolites. The effects of reactant adsorption on DPE values discussed in this section have far-reaching consequences for structure-function relations developed on POM clusters and the interpretations about reaction sensitivity based on them. DPE values must account for the most abundant surface intermediate present under conditions used to measure kinetic parameters, however, even rate constants measured under reaction conditions where protons are unoccupied need to account for interactions with the support, dehydroxylation, and interactions between clusters in secondary structures if they exist.

4.3.3. H-atom addition energies as descriptors of the local redox properties of catalysts

Next we develop a descriptor for reactivity in oxidation catalysis using Keggin POM clusters because their well-defined structures permit reliable calculations of their properties by theoretical treatments. DPE values describe the relative reactivities of W-POM clusters in acid-catalyzed reactions accurately because they reflect the energy needed to separate charge, which is required to form ion-pair transition states that mediate these reactions (Section 4.3.1). The chemical processes occurring at kinetically-relevant transition states of oxidation reactions must be known before an appropriate descriptor can be proposed to probe the relevant catalyst properties for these reactions. Previous investigations have demonstrated that CH bond activation limits rates of alkane and alkanol oxidative dehydrogenation (ODH) on metal oxides [8-11], suggesting that their kinetically-relevant steps involve the catalyst abstracting H-atoms from hydrocarbons. The details of H-abstraction steps remain unresolved, including the identity of the catalyst atom that abstracts H-atoms and the nature of the abstracted H-atoms (i.e., proton, H-radical, hydride). Several theoretical investigations, however, suggest that O-atoms of metal oxides abstract the H-atom [10, 22]. Propane ODH turnover rates (per metal atom) depend strongly on the addenda atom of the oxide and increase as the UV-visible absorption edge energy of the oxide decreases [8]. UV-visible absorption edge energies reflect ligand-to-metal charge transfer from the highest occupied molecular orbital (HOMO) in a lattice O-atom to the lowest unoccupied molecular orbital (LUMO) in a metal atom [8]. Higher ODH turnover rates on oxides with lower edge energies suggest that H-abstraction transition states transfer electrons to metal atoms and this process proceeds at higher rates when electrons transfer to metal atoms with lower LUMO energies [8]. We propose HAE values as appropriate descriptors of H-abstraction processes in ODH reactions based on this mechanistic information. The H-atom addition energy (HAE) of a catalyst is the energy needed to add a gas-phase H-radical to a metal oxide O-atom (e.g., $H_3PMo_{12}O_{40} + H\bullet \rightarrow H_4PMo_{12}O_{40}$). The H-addition reaction forms OH bonds and transfers an electron to the catalyst, both of which are proposed features of H-abstraction transition states.

We first calculate HAE values for different O-atom locations on a single Keggin cluster composition before examining the effects of composition. Keggin clusters have

three "types" of O-atoms that are accessible to reactants (terminal, edge-bridging, and corner-bridging; 12 of each type), which may have different HAE values. Furthermore, protons may also influence to redox properties of O-atoms that they reside on or that they are nearby. We conduct these initial investigations on $H_3PMo_{12}O_{40}$ as a representative ODH catalyst, because it converts CH_3OH reactants to formaldehyde (HCHO), methylformate (MF), and dimethoxymethane (DMM) in the presence of O_2 (at 493 K), each of which require at least one ODH turnover [23]. Figure 4.7A shows a 2-dimensional projection of O-atom locations on $H_3PMo_{12}O_{40}$, where bridging and terminal O-atoms are represented as colored bars and circles, respectively. The color of the O-atom indicates the DFT-derived HAE value at that position according to the scale bar at the bottom of the figure. Reds and oranges indicate the most reducible locations (i.e., the most negative HAE values) and blues indicate the least reducible locations (i.e., the least negative HAE values). Edge- and corner-bridging O-atoms are distinguished from each other by the locations of central O-atoms, represented in Figure 4.7A as white triangles. The twelve edge-bridging O-atoms form four triangles around the central O-atoms in Figure 4.7A. Finally, the positions of protons in Figure 4.7A are denoted by white circles on O-atoms.

HAE values vary markedly with O-atom location on $H_3PMo_{12}O_{40}$, with values ranging from -254 to -317 kJ mol^{-1}. Terminal O-atoms in Figure 4.7A are all green, whereas bridging O-atoms are predominantly red, orange, or yellow, indicating that terminal O-atoms are generally less reducible than edge- or corner-bridging O-atoms. This is also reflected in the average HAE values of terminal, edge-bridging, and corner-bridging O-atoms (-270, -298, and -298 kJ mol^{-1}, respectively). These results suggest that bridging O-atoms are likely more reactive for H-abstractions than terminal O-atoms, assuming that the orientations of hydrocarbon species allow bridging O-atoms to access H-atoms. O-atoms occupied by protons are the least reducible bridging O-atoms (i.e., they are green in Figure 4.7A). Addition of H-atoms to O-atoms with protons causes elongation of Mo-O bonds (by ca. 0.156 nm) so that the final product resembles an H_2O molecule coordinated to two Mo-atoms. The low reducibilities of O-atoms with protons suggest that acid and oxidation turnovers occur at different sites on these bifunctional metal oxides. The causes for HAE values that change with O-atom location need to be investigated further in future calculations using thermochemical cycle methods that resemble those employed in Section 4.3.1. One potential thermochemical cycle that can be used to dissect H-atom addition into different processes would include the ionization energy of an H-atom (IE(H)), the protonation energy of a neutral Keggin cluster ($E_{prot,POM}$) at a given O-atom position, the electron affinity of the protonated cluster (E_{ea}), and the energy to relax the structure of the reduced cluster (E'_{relax}).

$$HAE = IE(H) + E_{prot,POM} + E_{ea} + E'_{relax} \quad (4.12)$$

The H-atom ionization energy is catalyst-independent because it is a gas-phase property of an H-atom. The relevance of each of the remaining terms for ODH reactivity depends on the features of the H-abstraction transition state. For example, the electron affinity will be more consequential for reactivity if the abstracted H-atom more closely resembles an H-radical than a proton.

Next we investigate the effects of addenda atoms on HAE values by comparing HAE values on $H_3PMo_{12}O_{40}$ and $H_3PW_{12}O_{40}$ clusters at different O-atom locations (Figure 4.7 A and B, respectively). HAE values on $H_3PW_{12}O_{40}$ range from -167 to -234 kJ mol^{-1} and have O-atoms in Figure 4.7B that are colored blue or green. Terminal O-atoms of $H_3PW_{12}O_{40}$ are less reducible than edge- or corner-bridging O-atoms (average HAE values of -210, -221, -215 kJ mol^{-1} for terminal, edge-bridging, and corner-bridging O-atoms, respectively). Comparing the colors of O-atom locations on $H_3PW_{12}O_{40}$ and $H_3PMo_{12}O_{40}$ in Figure 4.7 A and B shows that the most and least reducible O-atom locations are nearly the same for the two compositions (i.e., red O-atoms on $H_3PMo_{12}O_{40}$ are greenish blue O-atoms on $H_3PW_{12}O_{40}$ and green O-atoms on $H_3PMo_{12}O_{40}$ are dark blue O-atoms on $H_3PW_{12}O_{40}$). These results suggest that HAE values probe the local redox properties of oxidation catalysts, which are determined in part by O-atom location for Keggin clusters. O-atoms of $H_3PMo_{12}O_{40}$ are colored with more reds and oranges (Figure 4.7A) than O-atoms of $H_3PW_{12}O_{40}$ clusters (Figure 4.7B), indicating that W-POM clusters are less reducible than Mo-POM clusters. $H_3PW_{12}O_{40}$ clusters do not carry out CH_3OH ODH at 493 K in the presence of O_2, conditions under which $H_3PMo_{12}O_{40}$ clusters form ODH products at significant selectivities [23]. These results suggest that catalysts with more negative HAE values carry out ODH turnovers at higher rates. Supported MoO_x domains catalyze propane ODH at higher turnover rates and have lower edge energies than supported WO_x domains [8], suggesting that H-abstraction steps and their concomitant electron transfer to metal atoms occur at higher rates on oxides whose metals have lower LUMO energies. Higher CH_3OH and propane ODH rates on Mo-based oxides than on their W-based counterparts suggest that catalysts with lower LUMO energies better stabilize electrons transferred during H-abstraction steps. The same catalysts also stabilize electrons better in H-radical addition, leading to more negative HAE values.

One or more W or Mo addenda atoms in Keggin clusters can be substituted by other transition metals, the most common of which are V-atoms. Figure 4.7 C and D show the HAE values of different O-atom locations in $H_4PMo_{11}VO_{40}$ and $H_4PW_{11}VO_{40}$ clusters where the V-atoms are bonded to the terminal O-atom in the lower left hand corners of the projections. All O-atoms directly bonded to the V-atom (except the one with a proton) are red for $H_4PMo_{11}VO_{40}$ and green for $H_4PW_{11}VO_{40}$. The colors of these O-atoms locations in $H_3PMo_{12}O_{40}$ and $H_3PW_{12}O_{40}$ lie further to the right on the color scale, indicating that V-atom substitution makes vicinal O-atoms more reducible (by ca. 16 kJ mol^{-1} for $H_4PMo_{11}VO_{40}$ and 41 kJ mol^{-1} for $H_4PMo_{11}VO_{40}$). O-atoms located away from the V-atom become less reducible in several instances on $H_4PMo_{11}VO_{40}$ and $H_4PW_{11}VO_{40}$ clusters (Figure 4.7C and D). These results indicate that DFT-derived HAE values reflect the changes in local redox properties of Keggin clusters caused by V-atom substitution. O-atom locations that are vicinal to V-atoms and that have more negative HAE values are consistent with higher propane ODH rates and lower edge energies of supported VO_x than supported MoO_x [8]. CH_3OH ODH rates on $H_4PMo_{11}VO_{40}$, however, were similar to those on $H_3PMo_{12}O_{40}$ (at the same reaction conditions) [23]. V-atom substitution may not affect CH_3OH ODH rates because only the 5 O-atoms bonded to the V-atom become more reducible, while the remaining 31 O-atoms are unchanged or become slightly less reducible. An alternate explanation is that H-abstraction steps do not limit CH_3OH ODH

turnovers at O-atoms next to V-atoms at the reaction conditions used, and therefore HAE values are not the appropriate descriptor for reactivity. Instead, re-oxidation steps, which are needed to complete turnovers in Mars-van-Krevelen redox cycles, are kinetically-relevant for O-atoms bonded to V-atoms since the HAE values of these positions predict they abstract H-atoms very readily.

HAE values likely depend on metal atom composition because the electron from the H-radical transfers to a previously empty metal d-orbital. The occupation of metal d-orbitals by electrons is observable by the advent of pre-edge features in UV-visible spectra during ODH reactions on metal oxides [24]. Such pre-edge features arise from electronic transitions among d-orbitals of reduced metal atoms. The local properties of HAE values suggest that the H-atom must be within reasonable proximity to the metal atom for the electron to occupy its d-orbitals. The relationship between the location of the H-atom and the orbitals that the electron occupies may be investigated in the future by examining the dependence of electron affinities in Eq. (4.12) on the proximity between H-atoms and different metal atoms. Other theoretical methods that map the location of unpaired electrons may provide further insights in determining where added electrons reside in reduced clusters and whether they are localized or delocalized. The local properties of HAE values suggest that electrons added by H-addition are localized. This contrasts the effects of composition and reactant adsorption on DPE values, which suggest electrons in Keggin clusters are delocalized. These results suggest that DPE values and HAE values probe different electronic properties of Keggin clusters, which are consequential for different reactions. DPE values reflect the properties of delocalized electrons in fully-oxidized clusters, while HAE values reflect the properties of an electron located in a orbital that only becomes occupied as a result of reduction.

The significant effects of metal atom composition on HAE values suggest that different transition metals should be substituted into Mo or W based Keggin clusters to provide materials with a broad range of reactivities for ODH composition-function relations. The transition metals that lead to the largest changes in redox properties and ODH rates can be assessed by calculating HAE maps similar to those shown in Figure 4.7 and provide guidance for future synthetic efforts. The effects of V-atom substitution on HAE values indicate that transition metal substitution will form non-uniform redox sites, which complicates measuring the turnover rates of individual sites during kinetic experiments. The results presented here represent only the initial steps in developing HAE values as descriptors of oxidation catalysts for ODH reactions. Future investigations need to refine the relationships between the properties of metal atoms and HAE values of metal oxides and begin to correlate HAE values to experimental rate constants for H-abstraction steps in ODH mechanisms.

4.4. Conclusions

The consequences of composition for acid and oxidation catalysis were investigated by theoretical methods for Keggin POM clusters, because their well-defined structures permit reliable calculations of simple reaction probes that accurately describe their reactivities in these chemistries. Deprotonation energies (DPE), a probe independent measure of acid strength used previously in structure-function relations based on W-POM clusters, reflect both covalent and electrostatic stabilization of protons

by the conjugate anion. DPE values change with both central atom (S, P, Si, Al, Co) and addenda atom (W, Mo) compositions; the central atom influences predominantly electrostatic stabilization of protons, while addenda atoms influence covalent and electrostatic stabilization of protons. Interaction energies between conjugate anions and organic cations that are present at transition states and in reactive intermediates during CH_3OH dehydration are also described by thermochemical cycles that dissect interactions into electrostatic and covalent contributions. Stabilities of DME formation transition states and protonated dimer intermediates change with central atom identity predominantly via changes in the electrostatic stabilization of their respective cations by the conjugate anion. DME formation transition states and protonated dimers are full-ion pairs stabilized by weak covalent interactions; as a result, addenda atoms of Keggin clusters do not affect the stabilities of transition states and dimers as strongly as protons. Solid acids whose protons have different amounts of covalent stabilization cannot be compared directly using DPE values as the descriptor for acid strength in structure-function relations, because ion-pair transition states do not recover covalent interactions that must be overcome to deprotonate the catalyst. DPE values accurately relate the reactivities of catalysts with similar covalent contributions to OH bonds (e.g., W-POM clusters with different central atoms), because the distribution of electrons delocalized across conjugate anions determines the electrostatic stabilization of both protons and organic cations. Protons sense changes in the anion more sensitively than organic cations because their charges are more localized and they have closer proximities to anions. Adsorption of CH_3OH at protons increases the DPE values of residual unoccupied protons on the same cluster because the electron distributions of Keggin anions allow protons to "communicate" with each other. Protonated dimers remove protons fully, while monomer only incipiently remove protons; as a result, anionic electron densities increase more with protonated dimer formation and cause larger changes in DPE values than with monomer formation. H-atom addition energies (HAE) probe the local redox properties of Keggin clusters; their values depend on the O-atom location that accepts the H-atom for $H_3PW_{12}O_{40}$ and $H_3PMo_{12}O_{40}$ and the proximity to V-atoms for $H_4PW_{11}VO_{40}$ and $H_4PMo_{11}VO_{40}$. The local nature of HAE values suggest they probe different electronic properties than DPE values, which largely reflect delocalized electrons. HAE values and alkane and alkanol oxidative dehydrogenation (ODH) rates on metal oxides each depend strongly on the identities of metal atoms, suggesting that HAE values are accurate descriptors of reactivity in ODH reactions. Kinetically-relevant H-abstraction steps in ODH reactions and H-atom addition both transfer electrons to unoccupied metal orbitals; as a result, metal atoms with unoccupied metal orbitals that are lower in energy better stabilize transferred electrons and lead to higher ODH rates and more negative HAE values.

Prashant Deshlahra is gratefully acknowledged for developing the computer program used to calculate the values of electrostatic interactions between ion-pairs and for carrying out the calculations. William Kneable is also acknowledged with thanks for constructing the projections of H-atom addition energies on Keggin clusters.

4.5. Tables, Figures, and Schemes

4.5.1. Tables

Table 4.1. Components of thermochemical cycles (in kJ mol^{-1}) describing deprotonation energies of W-based Keggin POM with S, P, Si, Al, and Co central atoms.

	H_2SW	H_3PW	H_4SiW	H_5AlW	H_6CoW
E_{reorg} / kJ mol^{-1}	915	909	913	910	924
E_{es} / kJ mol^{-1}	249	261	284	306	313
E_{relax} / kJ mol^{-1}	-95	-90	-91	-96	-94
DPE / kJ mol^{-1}	1069	1080	1106	1120	1143

Table 4.2. Components of thermochemical cycles (in kJ mol^{-1}) describing interaction energies for protonated CH_3OH dimers and DME formation transition states on W-based Keggin POM with S, P, Si, Al, and Co central atoms.

		H_2SW	H_3PW	H_4SiW	H_5AlW	H_6CoW
Protonated Dimer	E_{reorg} / kJ mol^{-1}	-125	-129	-135	-136	-139
	E_{es} / kJ mol^{-1}	-200	-209	-218	-228	-241
	E_{relax} / kJ mol^{-1}	21	22	24	26	31
	E_{int} / kJ mol^{-1}	-304	-316	-329	-337	-349
	E_{cation} / kJ mol^{-1}	-917	-917	-917	-917	-915
Transition State	E_{reorg} / kJ mol^{-1}	-83	-85	-94	-100	-100
	E_{es} / kJ mol^{-1}	-220	-228	-242	-245	-260
	E_{relax} / kJ mol^{-1}	15	17	18	7	18
	E_{int} / kJ mol^{-1}	-288	-297	-319	-337	-341
	E_{cation} / kJ mol^{-1}	-797	-796	-793	-794	-792

Table 4.3. Components of thermochemical cycles (in kJ mol^{-1}) describing deprotonation energies of Mo-based Keggin POM with S, P, Si, Al, and Co central atoms.

	H_2SMo	H_3PMo	H_4SiMo	H_5AlMo	H_6CoMo
E_{reorg} / kJ mol^{-1}	951	945	947	950	963
E_{es} / kJ mol^{-1}	230	238	262	271	270
E_{relax} / kJ mol^{-1}	-86	-80	-83	-91	-82
DPE / kJ mol^{-1}	1095	1103	1125	1130	1150

Table 4.4. Components of thermochemical cycles (in kJ mol^{-1}) describing interaction energies for protonated CH_3OH dimers on Mo-based Keggin POM with S, P, Si, Al, and Co central atoms.

		H_2SMo	H_3PMo	H_4SiMo	H_5AlMo	H_6CoMo
Protonated Dimer	E_{reorg} / kJ mol^{-1}	-134	-135	-137	-137	-144
	E_{es} / kJ mol^{-1}	-187	-199	-213	-220	-228
	E_{relax} / kJ mol^{-1}	19	21	23	26	26
	E_{int} / kJ mol^{-1}	-302	-313	-326	-331	-346
	E_{cation} / kJ mol^{-1}	-918	-918	-917	-917	-914

Table 4.5. Components of thermochemical cycles (in kJ mol^{-1}) describing deprotonation energies for monomer-saturated and protonated-dimer saturated W-based Keggin POM clusters with S, P, Si, Al, and Co central atoms. The structures of monomer- and dimer-saturated $H_3PW_{12}O_{40}$ are shown in Scheme 4.4 A and B.

		H_2SW	H_3PW	H_4SiW	H_5AlW	H_6CoW
Monomer Saturated	E_{reorg} / kJ mol^{-1}	724	727	728	719	- - -
	E_{es} / kJ mol^{-1}	264	293	323	344	- - -
	E_{relax} / kJ mol^{-1}	96	94	96	101	- - -
	DPE / kJ mol^{-1}	1084	1113	1147	1164	1191
Dimer Saturated	E_{reorg} / kJ mol^{-1}	693	704	705	684	- - -
	E_{es} / kJ mol^{-1}	318	356	398	441	- - -
	E_{relax} / kJ mol^{-1}	104	102	104	116	- - -
	DPE / kJ mol^{-1}	1115	1163	1207	1241	1252

4.5.2. Figures

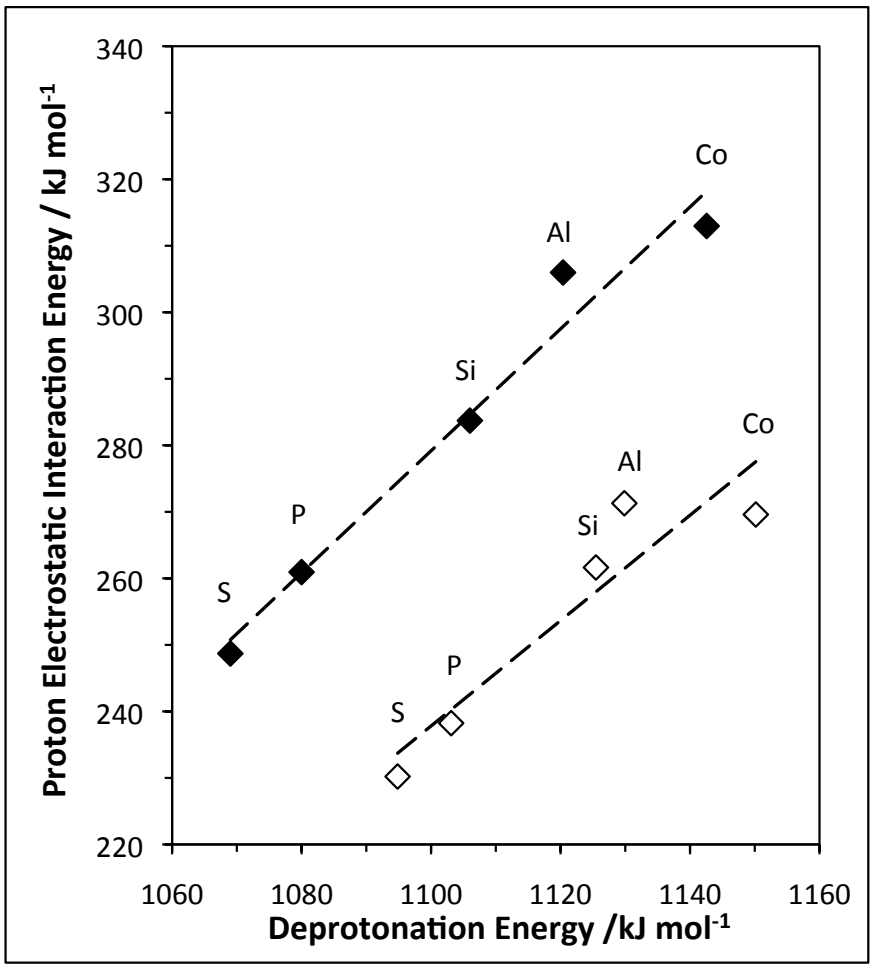

Figure 4.1. Electrostatic interaction energies (E_{es}) between protons and conjugate anions of W-based (closed symbols) and Mo-based (open symbols) Keggin POM clusters (S, P, Si, Al, and Co central atoms) as a function of the acid's deprotonation energy (DPE). Dashed lines represent linear best fits of the data.

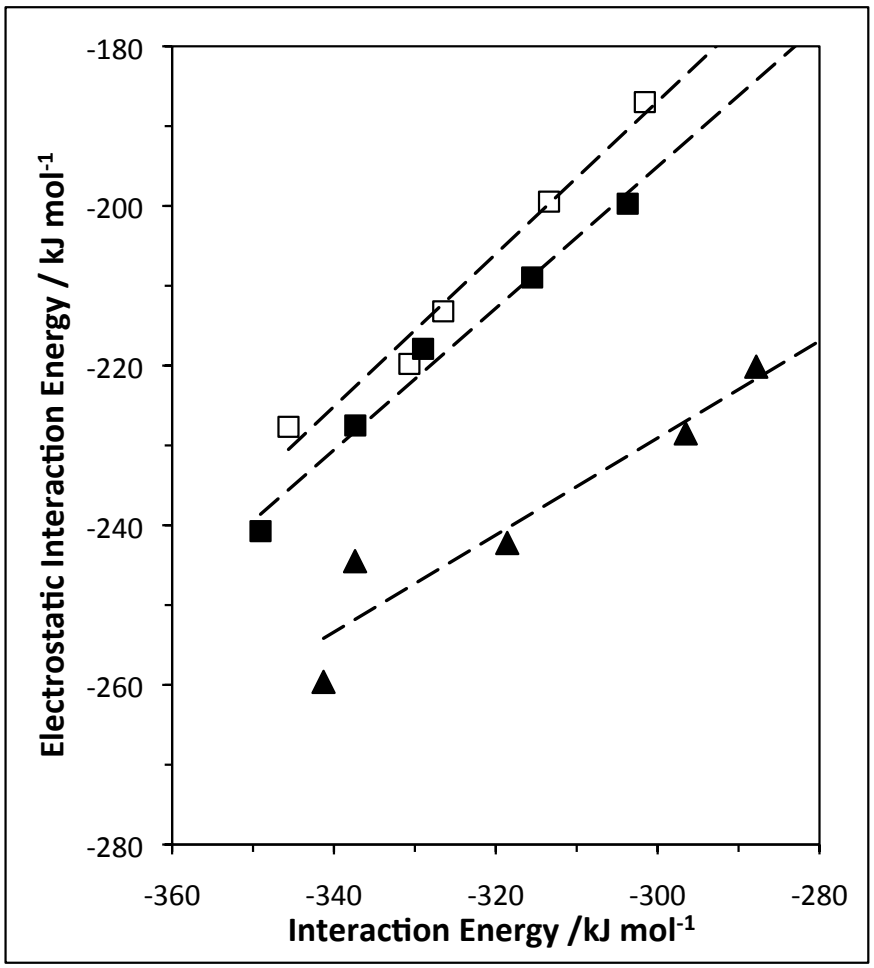

Figure 4.2. Electrostatic interaction energies (E_{es}) between conjugate anions of W-based (closed symbols) and Mo-based (open symbols) Keggin POM clusters (S, P, Si, Al, and Co central atoms) and (■) protonated dimer cations or (▲) DME formation transition state cations as functions of their interaction energies (E_{int}). Dashed lines represent linear best fits of the data.

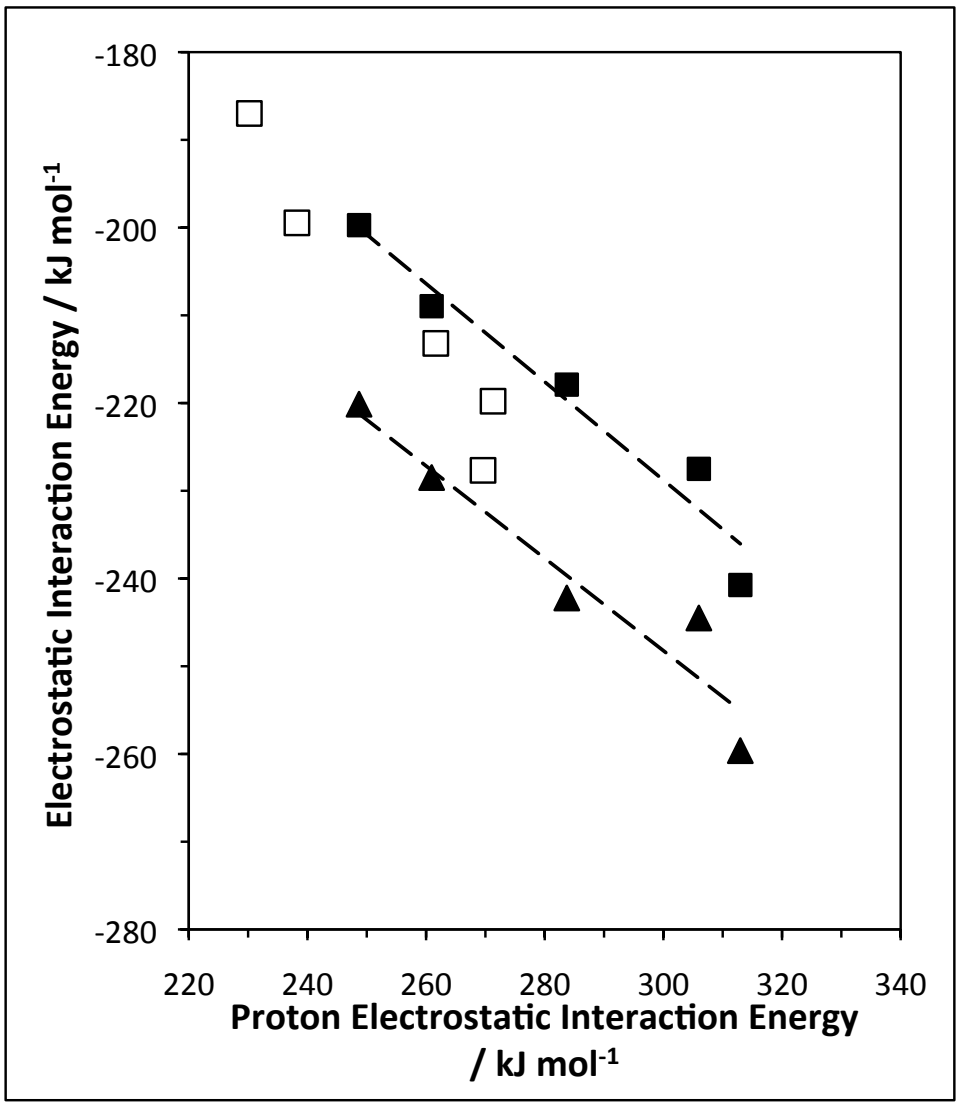

Figure 4.3. Electrostatic interactions between conjugate anions of W (closed symbols) and Mo (open symbols) Keggin clusters and (■) dimer cations or (▲) DME formation transition state cations as functions of the electrostatic interaction energies of protons. Dashed lines are best fits of the data and have slopes of 0.56 and 0.53 for protonated dimers and transition states on W clusters, respectively.

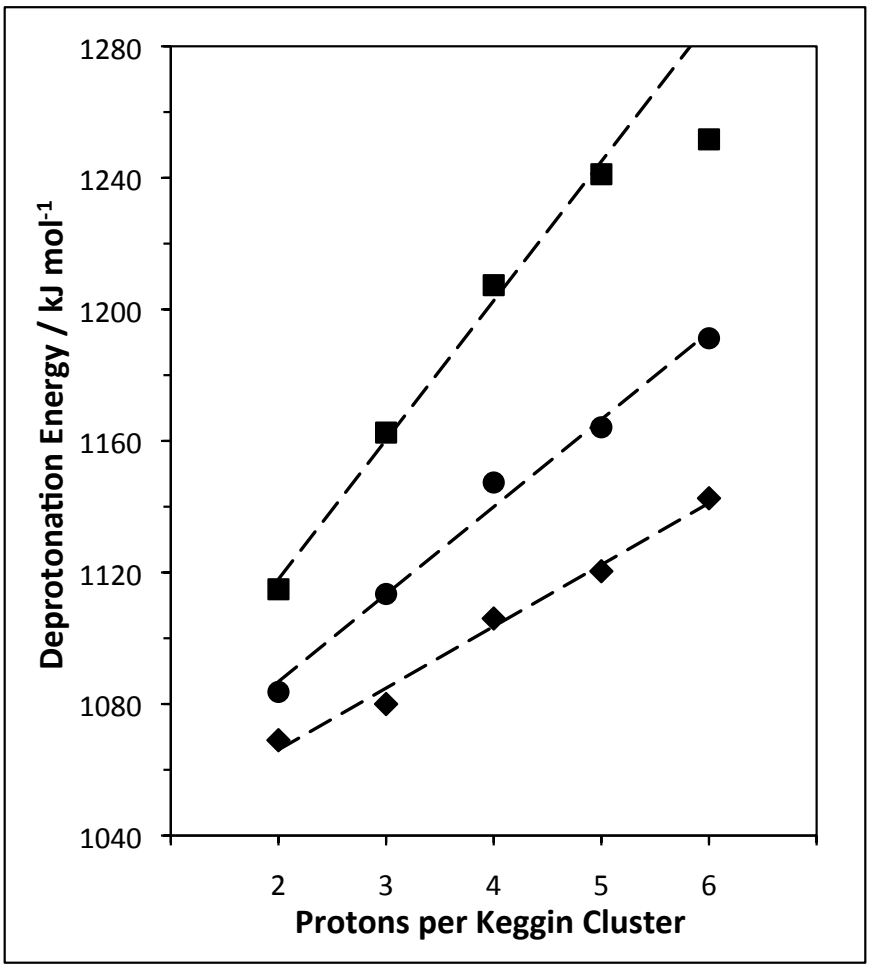

Figure 4.4. Deprotonation energies of W-Keggin POM clusters with S, P, Si, Al, and Co central atoms when (◆) all protons are vacant and when all protons other than the one being removed (H_{C1} in Scheme 4.4) are occupied with (●) CH_3OH monomers or (■) protonated dimers.

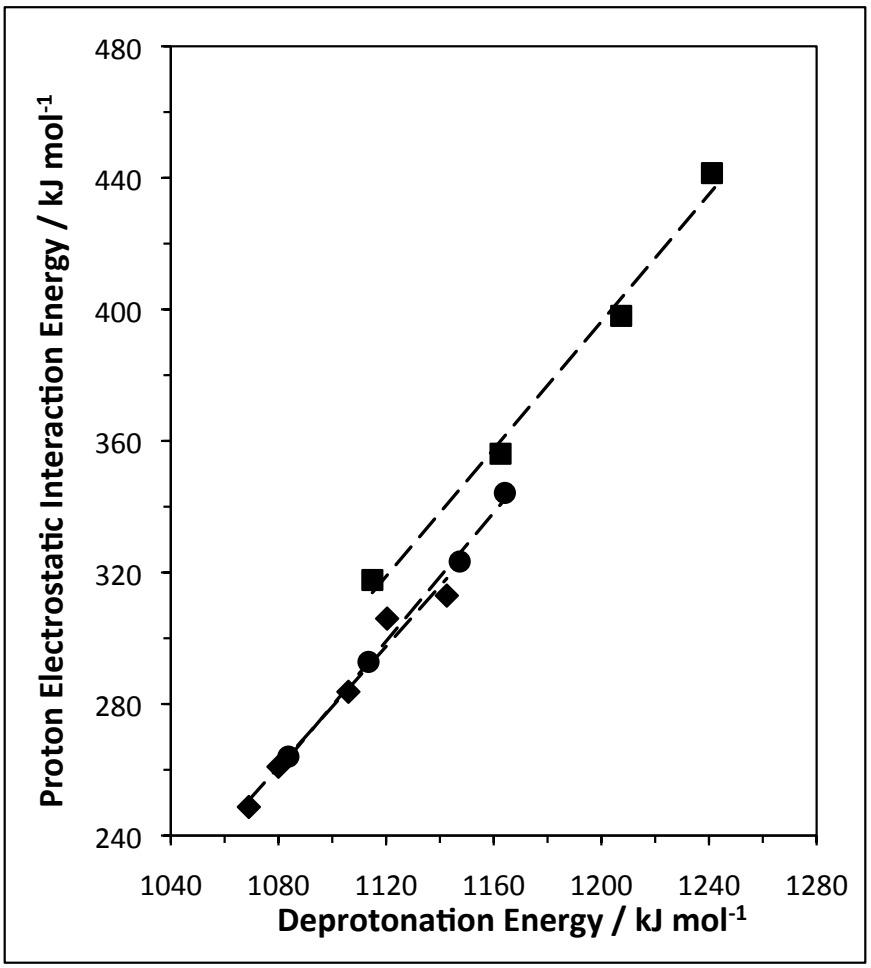

Figure 4.5. Electrostatic interaction energies (E_{es}) between protons and conjugate anions of W-based Keggin POM clusters (S, P, Si, Al, and Co central atoms) when (◆) all protons are vacant and when all protons other than the one being removed (H_{C1} in Scheme 4.4) are saturated with (●) CH_3OH monomers or (■) protonated dimers as functions of the acid's deprotonation energy (DPE). Dashed lines represent linear best fits of the data.

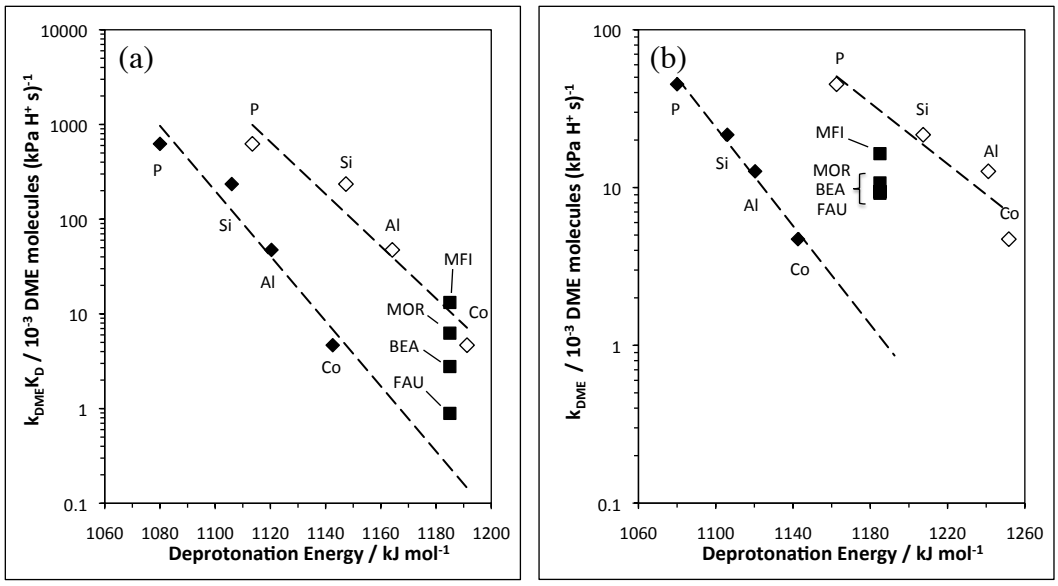

Figure 4.6. (a) CH_3OH dehydration rate constants measured from CH_3OH monomers (and a gas-phase CH_3OH) on (◆) W-Keggin POM (central atom listed) and (■) zeolites (framework type listed) as functions of their deprotonation energies. Closed symbols for POM use the DPE of unoccupied clusters and open symbols use the DPE of monomer-saturated clusters. (b) CH_3OH dehydration rate constants measured from protonated CH_3OH dimers on (◆) W-Keggin POM (central atom listed) and (■) zeolites (framework type listed) as functions of their deprotonation energies. Closed symbols for POM use the DPE of unoccupied clusters and open symbols use the DPE of dimer-saturated clusters.

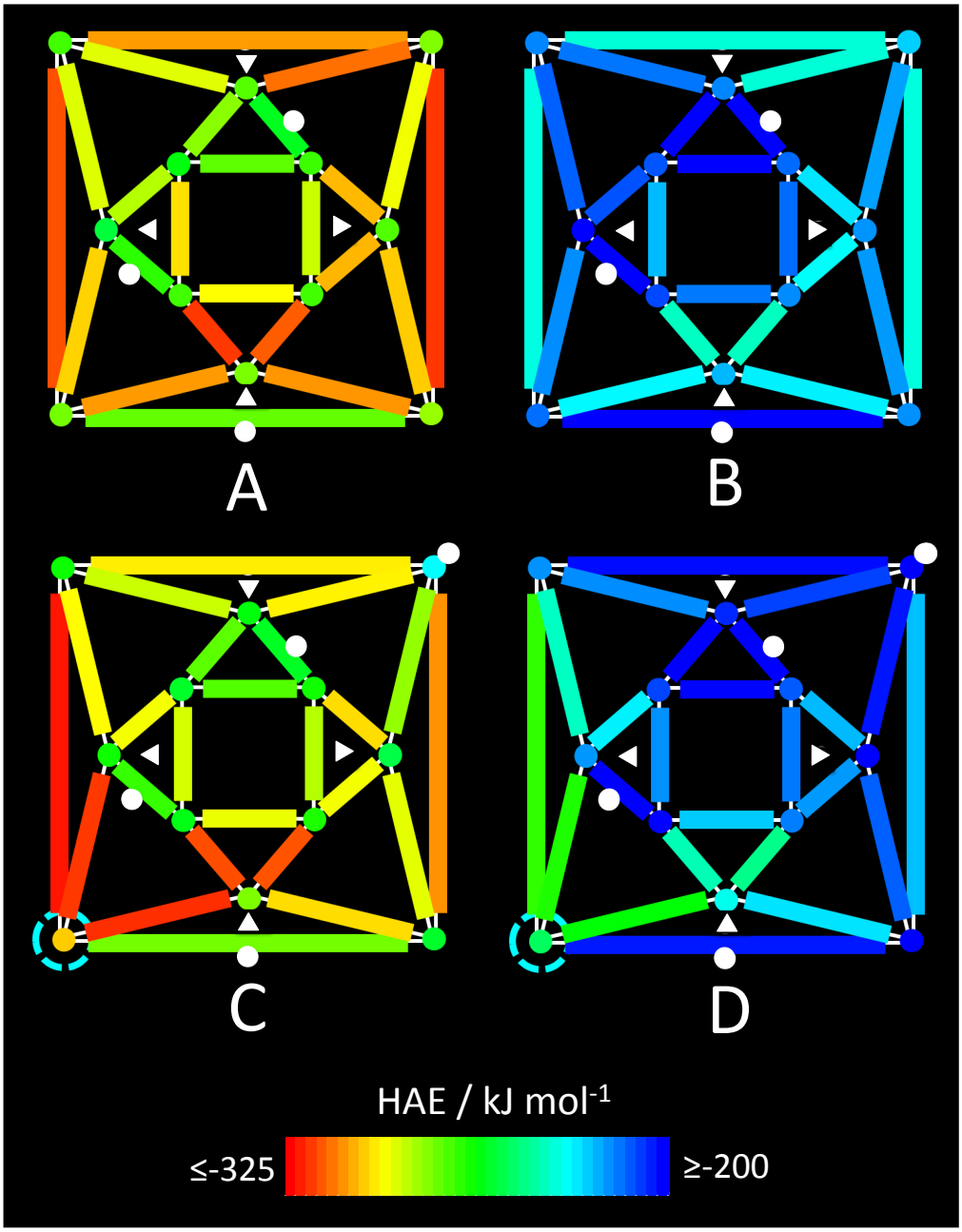

Figure 4.7. 2-Dimensional projections of O-atom locations in (A) $H_3PMo_{12}O_{40}$, (B) $H_3PW_{12}O_{40}$, (C) $H_4PMo_{11}VO_{40}$, and (D) $H_4PW_{11}VO_{40}$, colored according to their H-atom addition energies (HAE). Bridging and terminal O-atoms are depicted as colored bars and circles, respectively, and central O-atoms and protons are depicted as white triangles and circles, respectively. V-atoms in C and D are located at the lower left hand corners and are outlined by dashed circles.

4.5.3. Schemes

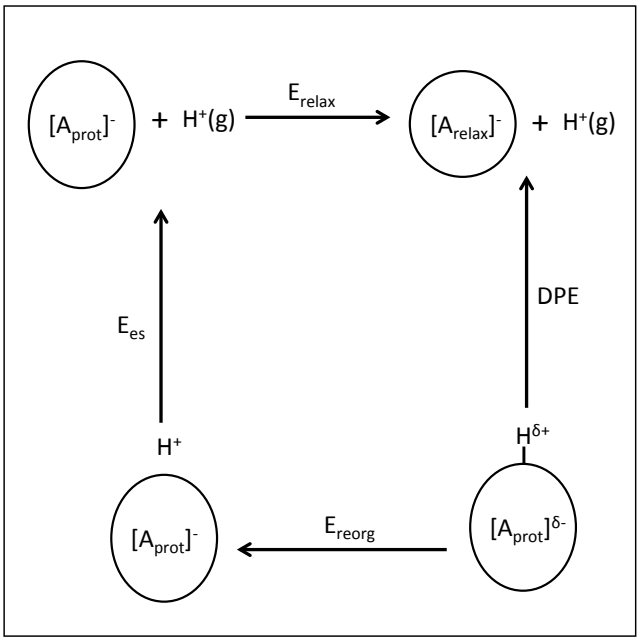

Scheme 4.1. Deprotonation energies (DPE) of Brønsted acid catalysts (HA_{prot}) depend on (i) the energy to form full ion-pairs (E_{reorg}) consisting of protons (H^+) and conjugate anions (A_{prot}^-), (ii) electrostatic interaction energies (E_{es}) between protons and the conjugate anions, and (iii) the energy for anions to relax (E_{relax}) to their non-interacting geometries (A_{relax}^-). Interaction anions (E_{int}) for other cations are described by the same thermochemical cycle as DPE by replacing the proton with the cation and reversing the directions of all processes (i.e., arrows in the schematic).

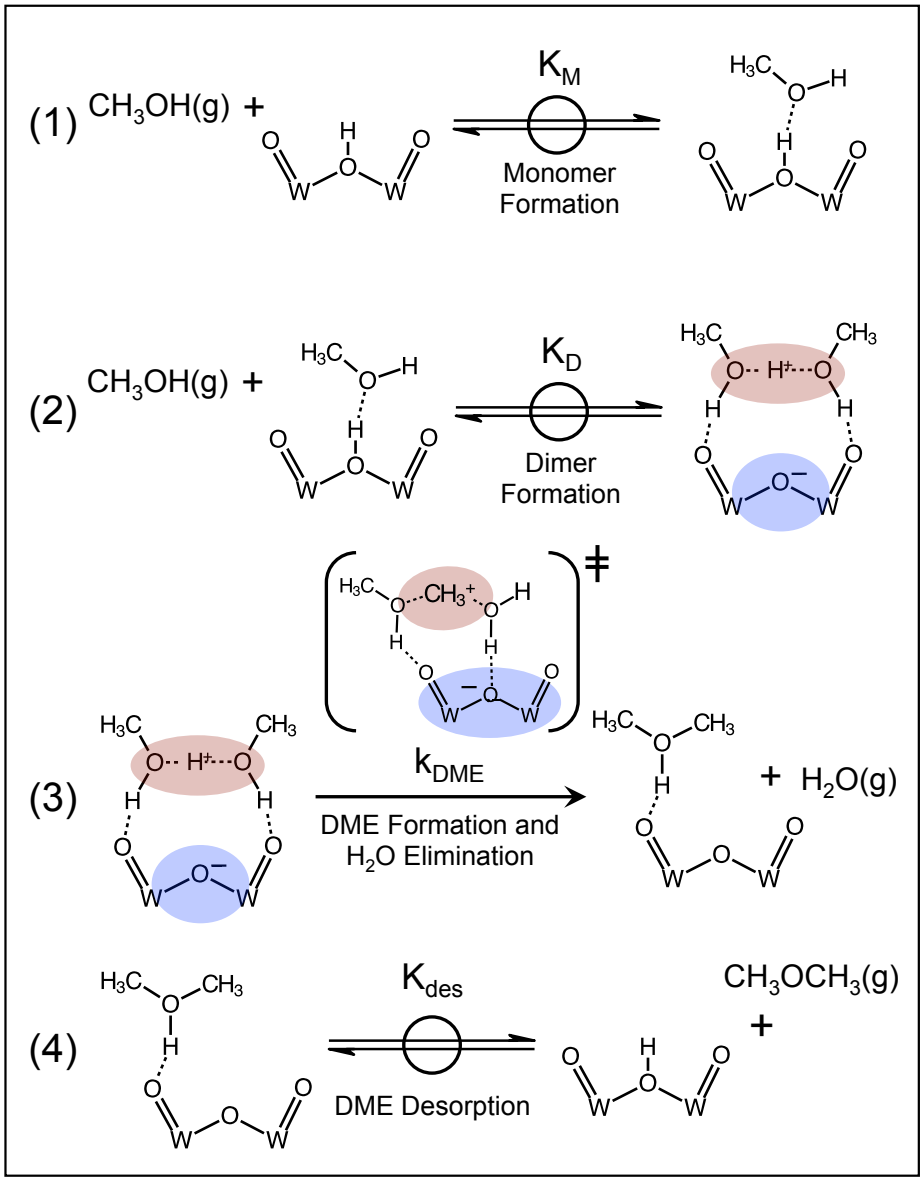

Scheme 4.2. Elementary steps for CH_3OH dehydration on W-based Keggin POM [3].

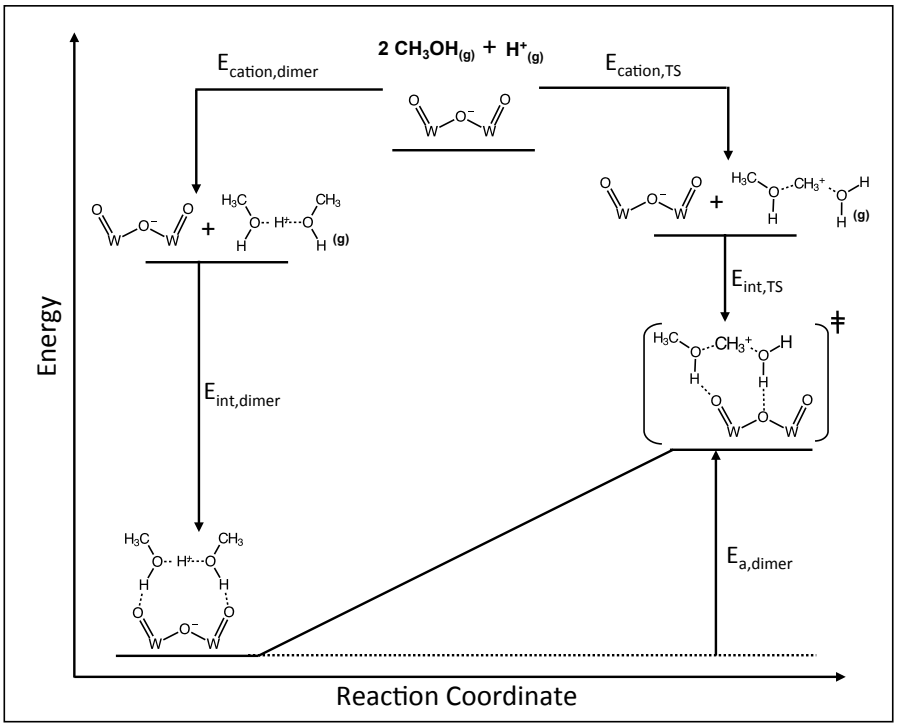

Scheme 4.3. Thermochemical cycle describing DME formation activation barriers measured from protonated dimers ($E_{a,dimer}$).

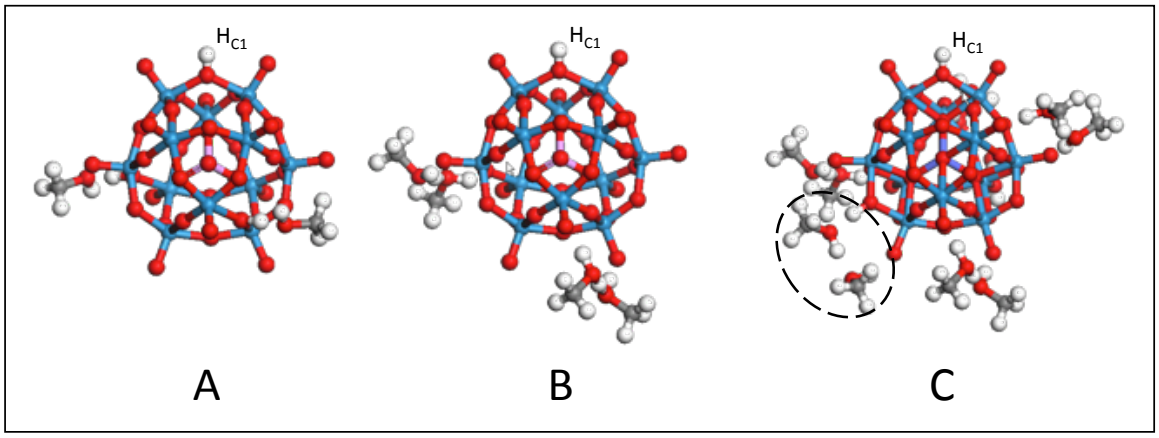

Scheme 4.4. DFT-calculated structures of (A) monomer and (B) dimer saturated $H_3PW_{12}O_{40}$ clusters. The structure of dimer saturated $H_6CoW_{12}O_{40}$ clusters is also shown (C) with the non-protonated dimer outlined by a dashed oval. The proton being removed in all calculations is labeled H_{C1}.

4.6. References

[1] J. Macht, M.J. Janik, M. Neurock, E. Iglesia, J. Am. Chem. Soc. 130 (2008) 10369.
[2] J. Macht, M.J. Janik, M. Neurock, E. Iglesia, Angew. Chem., Int. Ed. 46 (2007) 7864.
[3] R. Carr, M. Neurock, E. Iglesia, J. Catal. 278 (2011) 78.
[4] J. Macht, R.T. Carr, E. Iglesia, J. Am. Chem. Soc. 131 (2009) 6554.
[5] R.T. Carr, W. Knaeble, E. Iglesia, "*Effects of Acid Strength and Solvation on the Isomerization of Hexane Isomers on Solid Brønsted Acids*", in Preparation.
[6] M. Brändle, J. Sauer, J. Am. Chem. Soc. 120 (1998) 1556.
[7] R.A. van Santen, G.J. Kramer, Chem. Rev. 95 (1995) 637.
[8] K. Chen, A.T. Bell, E. Iglesia, J. Catal. 209 (2002) 35.
[9] B. Kilos, A. T. Bell, E. Iglesia, J. Phys. Chem. C 113 (2009) 2830
[10] A. Goodrow and A.T. Bell, J. Phys. Chem. C 111 (2007) 14753.
[11] R.S. Weber, J. Phys. Chem. 98 (1994) 2999.
[12] G. Kresse, J. Hafner, Phys. Rev. B. 47 (1993) 558; G. Kresse, J. Furthmuller, Comput. Mater. Sci. 6 (1996) 15; G .Kresse, J. Furthmuller, Phys. Rev. B 54 (1996) 11169.
[13] D. Vanderbilt, Phys. Rev. B 41 (1990) 7892.
[14] J.P. Perdew, J.A. Chevary, S.H. Vosko, K.A. Jackson, M.R. Pederson, D.J. Singh, C. Fiolhais, Phys. Rev. B 46 (1992) 6671.
[15] H. Jonsson, G. Mills, and K.W. Jacobsen, *Classical and Quantum Dynamics in Condensed Phase Simulations*, B.J. Berne, G. Coccotti, D.F. Coker, Eds., Kluwer Academic: New York, 1998, pp 385.
[16] G. Henkelman, H. Jonsson, J. Chem. Phys. 111 (1999) 7010.
[17] R. Bader, *Atoms in Molecules: A Quantum Theory*, Oxford University Press: New York, 1990.
[18] G. Henkelman, A. Arnaldsson, H. Jonsson, Comput. Mater. Sci. 36 (2006) 354.; E. Sanville, S.D. Kenny, R. Smith, G. Henkelman, J. Comput. Chem. 28 (2007) 899.
[19] M.J. Janik, K.A. Campbell, B.B. Bardin, R.J. Davis, M. Neurock, Appl. Catal. A 256 (2003) 51.
[20] M.J. Janik, B.B. Bardin, R.J. Davis, M. Neurock, J. Phys. Chem. B 110 (2006) 4170.
[21] X. Qian, J. Li, C.-Z. Wang, T.-L.Chan, Y.-X. Yao, K.-M. Ho, S. Yip, Phys. Rev. B 78 (2008) 245112.
[22] L.J. Gregoriades, J. Döbler, J. Sauer, J. Phys. Chem. C 114 (2010) 2967.
[23] H. Liu, E. Iglesia, J. Phys. Chem. B. 107 (2003) 10840.
[24] M.D. Argyle, K. Chen, C. Resini, C. Krebs, A.T. Bell, E. Iglesia, J. Phys. Chem. B 108 (2004) 2345.